

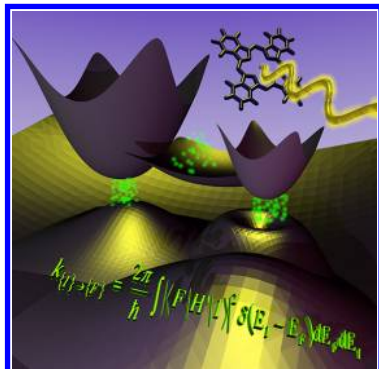
## Theoretical Insights into Photoinduced Charge Transfer and Catalysis at Oxide Interfaces

Alexey V. Akimov,<sup>†,‡</sup> Amanda J. Neukirch,<sup>§</sup> and Oleg V. Prezhdo<sup>\*,†</sup>

<sup>†</sup>Department of Chemistry, University of Rochester, Rochester, New York 14627, United States

<sup>‡</sup>Chemistry Department, Brookhaven National Laboratory, Upton, New York 11973-5000, United States

<sup>§</sup>Department of Physics and Astronomy, University of Rochester, Rochester, New York 14627, United States



### CONTENTS

1. Introduction	B	3.3.3. Inorganic Sensitizers – Quantum Dots (QD)	AD
2. Theory	E	3.3.4. Hybrid Structures, Nanoscale Carbon, and Polymers	AF
2.1. The Hierarchy of Approximations	E	3.4. Molecular and Electronic Structure of Sensitizer–Substrate Complexes	AG
2.1.1. Separation of Time and Spatial Coordinates	E	3.5. Donor and Acceptor States	AH
2.1.2. Separation of Electronic and Nuclear Coordinates	E	3.5.1. Weak Mixing	AH
2.1.3. Electronic Wave Functions	F	3.5.2. Strong Mixing	AI
2.1.4. Nuclear Wave Functions: Adiabatic Approximation	F	4. Interfacial Charge Transfer in Photovoltaic Cells	AI
2.1.5. Nuclear Wave Functions: Nonadiabatic Approximation	G	4.1. Kinetics of Electron Injection from Sensitizers to Oxide Substrates	AI
2.2. Electron Transfer Mechanisms	G	4.1.1. Electronic Structure of the Semiconductor and Chromophore	AI
2.2.1. Adiabatic ET	G	4.1.2. Modulation of the Conduction-Band Edge of the Semiconductor	AL
2.2.2. Nonadiabatic ET	H	4.1.3. Multiexponential Kinetics	AN
2.2.3. Direct Photoinduced ET	H	4.1.4. Role of the Anchor Group	AO
2.3. Analytic Models for Calculation of the Rate Constants	H	4.1.5. Role of the Linker Group – Sensitizer–Substrate Spatial Separation	AP
2.3.1. Adiabatic ET	H	4.1.6. Role of Vibrational Modes – Thermal Fluctuations	AQ
2.3.2. Nonadiabatic ET	L	4.1.7. Interaction with a Field	AR
2.3.3. Direct Injection Mechanism	P	4.1.8. Direct and Sequential Electron Injection	AR
2.4. Nonadiabatic Molecular Dynamics	P	4.2. Kinetics of Electron Transfer from Substrate to Electrolyte	AS
2.4.1. Surface Hopping and Related Quantum-Classical Methods	R	4.2.1. Electrolyte Equilibria	AS
2.4.2. Wave Function Propagation Methods	U	4.2.2. Electron Loss to Electrolytes	AT
3. Composition of the Photoactive Materials	X	5. Photocatalytic Processes	AX
3.1. Molecular and Electronic Structure of the Substrate	X	5.1. Photoexcitation	AX
3.2. Semiconductor Doping	AA	5.2. Charge Separation and Recombination	AZ
3.3. Molecular and Electronic Structure of Sensitizers	AC	5.2.1. Charge Carrier Diffusion	AZ
3.3.1. Metallo–Organic Sensitizers	AC	5.2.2. Charge Carrier Recombination	BA
3.3.2. Organic Molecular Sensitizers	AD	5.3. Photochemical Reactions on the Surface	BB
		5.3.1. Reaction Mechanisms	BB
		5.3.2. Overpotential	BD
		6. Conclusions and Outlook	BH
		Author Information	BI
		Corresponding Author	BI
		Notes	BI
		Biographies	BI
		Acknowledgments	BJ
		References	BJ

**Special Issue:** 2013 Surface Chemistry of Oxides

**Received:** December 11, 2012

## 1. INTRODUCTION

As the world's population increases and substantial industrial growth continues, the energy demands of society increase rapidly. Although the earth's oil, natural gas, and coal deposits constitute the main source of energy and fuel currently, their exploration and production are difficult and problematic. The byproducts and chemicals used in the extraction and refinement of fossil fuels can cause significant harm to the environment. The consumption of organic fuel is not sustainable and results in severe damage to the environment, causing pollution and other effects that lead to global warming. The energy produced by the sun and carried down to earth by its radiation provides an alternative and clean source of energy to meet and exceed the world's energy consumption demands.

A remaining fundamental challenge is in the development of efficient methods of harvesting solar energy that are accessible and cost-effective. This challenge has stimulated a large number of experimental<sup>1–15</sup> and theoretical<sup>2,16–26</sup> studies aimed at finding materials capable of either transforming solar energy into electricity (photovoltaics)<sup>1,10,27</sup> or inducing chemical reactions, such as water oxidation or hydrogen production (photocatalysis).<sup>4–6,28</sup> Silicon and germanium were some of the first materials used for transforming solar energy into electric current. Currently dominating the solar cell market, these materials are expensive, require excessive maintenance, are short-lived, and result in relatively low energy conversion efficiencies.

A number of alternative materials have been proposed for photovoltaic and photochemical systems, with the main focus aimed at lowering cost. Oxides are usually significantly cheaper than pure elements, that is, silicon versus silicon oxide. However, oxides function typically as wide-band gap semiconductors, transparent to solar light. An important breakthrough was achieved by Grätzel,<sup>29</sup> who proposed a novel photovoltaic cell, the dye-sensitized semiconductor solar cell (DSSC), that is composed of colloid titanium dioxide  $\text{TiO}_2$  coated with a light-sensitizer (dye) and sintered to an electrode to harvest solar energy (Figure 1a). This material is inexpensive, stable, and shows light-to-electric energy conversion efficiency comparable to those of the conventional silicon/germanium semiconductors (7.1–12%). The large surface area of the colloid  $\text{TiO}_2$  increases energy conversion efficiency by at least an order of magnitude over setups based on a monolayer of dye deposited on a flat or corrugated semiconductor surface.<sup>30</sup>

The photovoltaic Grätzel cell is designed to produce electric current by relaying the photoinduced electron via a semiconductor ( $\text{TiO}_2$ ) nanoparticle to the photoelectrode and then to the counter electrode (Figure 1a). In this process, the electron is formally extracted from the dye molecule and is put to work remotely in the form of electric current. In a photochemical cell (Figure 1b), the electron and hole, produced in the semiconductor–dye composite by photoexcitation, are used locally for completing a reduction/oxidation reaction. One of the first photochemical cells of this type was also developed by Grätzel,<sup>31</sup> for hydrogen generation. In that setup, photoelectrons in the conduction band (CB) of  $\text{TiO}_2$  were able to reduce a methylviologen compound. Adding a Pt catalyst to the  $\text{TiO}_2$  surface enabled direct hydrogen production, and the reaction was accelerated significantly by the presence of methylviologen. One of the first indications of the ability of  $\text{TiO}_2$  nanoparticles to produce oxygen by photocatalytic water oxidation was obtained by Fujishima and

Honda in 1972,<sup>32</sup> and since then this process has been developed significantly.<sup>33</sup>

Figure 2a shows the energy schematic of an operating Grätzel cell. Initially, the dye molecule is put into an excited state by absorbing a photon of energy,  $h\nu$ . In the simplest case, this excited state is represented by an electron promoted from the highest occupied molecular orbital (HOMO) to the lowest unoccupied molecular orbital (LUMO) of the dye molecule. Generally, the electron can be excited from any of the occupied orbitals to any of the unoccupied orbitals, giving rise to “hot” charge carriers possessing excess kinetic energy. The fate of the photoexcited electron includes the following possibilities:

- (a) Injection into the CB of the semiconductor, with the time  $\tau_{\text{inject}}$ .
- (b) Relaxation to one of the lower states of the chromophore,  $\tau_{\text{relax},1}$ , or to its ground state,  $\tau_{\text{relax},2}$ .
- (c) Quenching by the electrolyte, that is, the electron transfers to the electrolyte without performing useful work,  $\tau_{\text{quench}}$ .

To maximize the efficiency of the photovoltaic cell, the last two routes should be avoided.

Once injected into the CB of the semiconductor surface, the electron can experience a number of additional pathways:

- (a) Diffuse to the bulk CB of the semiconductor,  $\tau_{\text{diff}}$ , and subsequently be used for performing useful work; this pathway will maximize solar-to-electric energy conversion. Typically, the bulk CB edge is lower in energy than the surface CB edge, resulting in some energy and voltage loss.
- (b) Captured by the trap states at the surface of the semiconductor,  $\tau_{\text{trap}}$ .
- (c) Recombine with the positive charge by interacting with the electrolyte,  $\tau_{\text{recomb},1}$ , or with the chromophore,  $\tau_{\text{recomb},2}$ .

The latter two processes can happen in parallel with the other processes and decrease efficiency by reducing the number of charge carriers, that is, current, transported in the electrical circuit. In an ideal setup, all electrons from the excited chromophore are transferred to the bulk CB and perform useful work.

The electrolyte serves to close the electrical chain by transferring electrons from the opposite electrode to the chromophore. This process restores the chromophore to its neutral charge, making a new photoexcitation cycle possible. Diffusion of bulk electrolyte affects the chromophore regeneration,  $\tau_{\text{regen}}$ , and eventually the light-to-electric energy conversion ratio. However, the most important stages that define the productivity of the photovoltaic cell occur near the oxide surface and involve the dye–semiconductor as well as the solvent–semiconductor interfaces.

The basic principle of operation in the photocatalytic (photochemical) cell is similar to that of the photovoltaic cell in general, but there are some distinctive differences (Figure 2b). As with a photovoltaic cell, a photon,  $h\nu$ , must be absorbed and create an electron–hole pair (exciton) in the photocatalyst. In a simple photochemical setup, and in contrast to a photovoltaic cell, the charge carriers are formed in the same material and are not transferred across the interfaces. However, in more advanced setups (e.g., Z-, DSSC-, and compound schemes), such interfacial charge transfer is realized and often leads to improved photocatalytic performance. Once the electron–hole pair is formed in the semiconductor, several

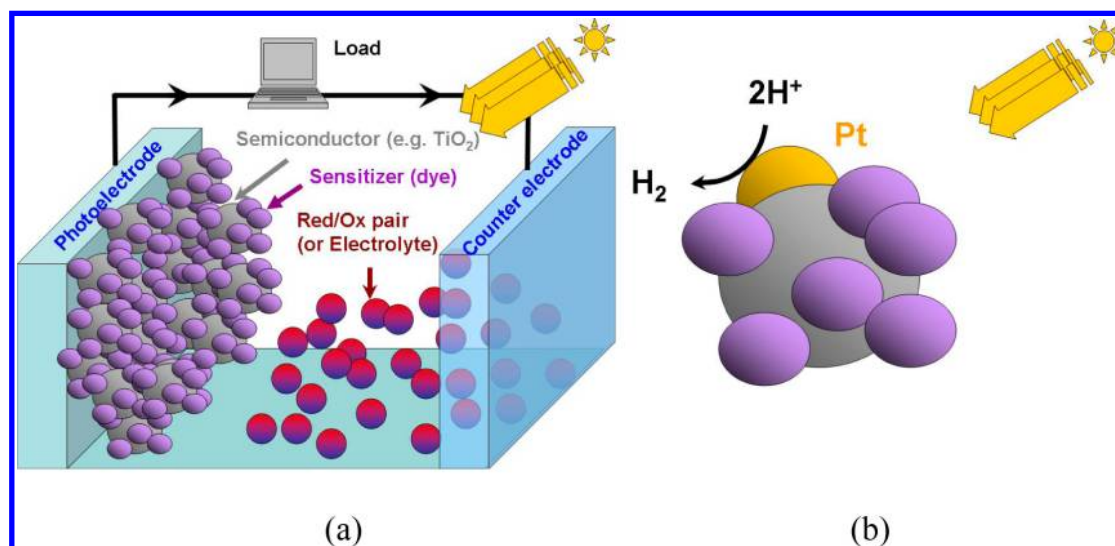


Figure 1. Schematic representation of photovoltaic (a) and photochemical (b) cells.

pathways become available for further transformations (Figure 2b):

- The electrons and holes residing in the CB and valence band (VB), respectively, can recombine,  $\tau_{\text{recomb},1}$ .
- The charge carriers can diffuse away from each other,  $\tau_{\text{diff},e}$  and  $\tau_{\text{diff},h}$ , leading to charge separation. Simultaneously, the electron and hole relax to the corresponding edges of the bulk CB and VB.
- During diffusion and charge separation, electrons ( $\tau_{\text{trap},e}$ ) and holes ( $\tau_{\text{trap},h}$ ) can be captured by trap states; this is mostly due to surface defects and vacancies, although it can occur in bulk as well.
- Trapped electron and holes can recombine with the VB holes and CB electrons, respectively,  $\tau_{\text{recomb},2}$  and  $\tau_{\text{recomb},3}$ . Trapped electrons can also recombine with the trapped holes; this process is slow, unless the electron and hole traps are located close to each other.

Finally, when the electrons and holes arrive at the surface reaction sites, they promote reduction and oxidation, respectively. The reaction sites are usually separated spatially, either by the use of cocatalysts, which direct the electron and hole movement in the nanoparticle, or by relaying the photoanode with the counter electrode, as in photovoltaic systems. In the first case, the reactions occur on the same nanoparticle or on the same electrode, producing a mixture of products (e.g.,  $\text{O}_2$  and  $\text{H}_2$  gases in the water splitting reaction). In the second case, products of the reduction and oxidation reactions are produced on different electrodes, simplifying their separation. There is no significant voltage difference between the anode and cathode, unlike in the photovoltaic cell.

The efficiency of the photovoltaic and photochemical cells can be characterized by the overall power conversion efficiency,  $\eta$ , and by the incident photon-to-current efficiency (IPCE).<sup>34</sup> The power conversion efficiency is determined by the photocurrent density, measured by the short circuit,  $J_{\text{sc}}$ , the open circuit voltage,  $V_{\text{oc}}$ , the fill factor of the cell,  $ff$ , and the intensity of the incident light,  $I_s$ , as follows:

$$\eta = \frac{J_{\text{sc}} \cdot V_{\text{oc}} \cdot ff}{I_s} \quad (1.1)$$

The fill factor is the ratio of the maximum power of the solar cell,  $P_{\text{max}}$ , and the product of the open circuit voltage,  $V_{\text{oc}}$ , and the short circuit current,  $I_{\text{sc}}$ :

$$ff = \frac{P_{\text{max}}}{I_{\text{sc}} \cdot V_{\text{oc}}} \quad (1.2)$$

Maximum power,  $P_{\text{max}}$ , is the product of the photocurrent and photovoltage, at the voltage in which the cell has maximal power output. The fill factor has a range from 0 to 1, and reflects the extent to which the power is lost during operation due to ohmic resistance and electrochemical phenomena, which require an overpotential.

The photocurrent density,  $J_{\text{sc}}$ , that enters the expression for the power conversion efficiency is defined by integrating IPCE( $\lambda$ ) over the solar spectral density,  $I_s(\lambda)$ :

$$J_{\text{sc}} = e \int \text{IPCE}(\lambda) I_s(\lambda) d\lambda \quad (1.3)$$

where  $e$  is the charge of an electron. IPCE( $\lambda$ ) defines the photocurrent density, produced in an external circuit under monochromatic irradiation per photon flux. This quantity is often used in conjunction with the power conversion efficiency to better characterize the properties of a solar cell device. IPCE can be high, even when the power conversion is low; however, if it is low, it is very unlikely that the power conversion will be high. Thus, the IPCE is useful for prescreening possible candidates for high-efficiency solar devices.

The IPCE can also be computed using the formula:<sup>35</sup>

$$\text{IPCE}(\lambda) = \text{LHE}(\lambda) \phi_{\text{inj}}(\lambda) \eta_{\text{coll}} \eta_{\text{reg}} \quad (1.4)$$

The light-harvesting efficiency, LHE( $\lambda$ ), at wavelength,  $\lambda$ , is given by  $\text{LHE}(\lambda) = (1 - 10^{-A})$ , where  $A$  is the film absorbance. The quantum yield for electron injection from the excited sensitizer into the CB of the semiconductor substrate is  $\phi_{\text{inj}}(\lambda)$ . The electron collection efficiency,  $\eta_{\text{coll}}$ , reflects electron losses due to back-electron transfer (ET) and related processes happening after electron injection occurs in the semiconductor. Dye regeneration efficiency is  $\eta_{\text{reg}}$ . The quantum yield for electron injection,  $\phi_{\text{inj}}(\lambda)$ , can, in principle, depend on the excitation wavelength, particularly for sensitizers with a dense manifold of unoccupied orbitals near the excitation level, such as quantum dots or graphene. In terms of the above kinetic



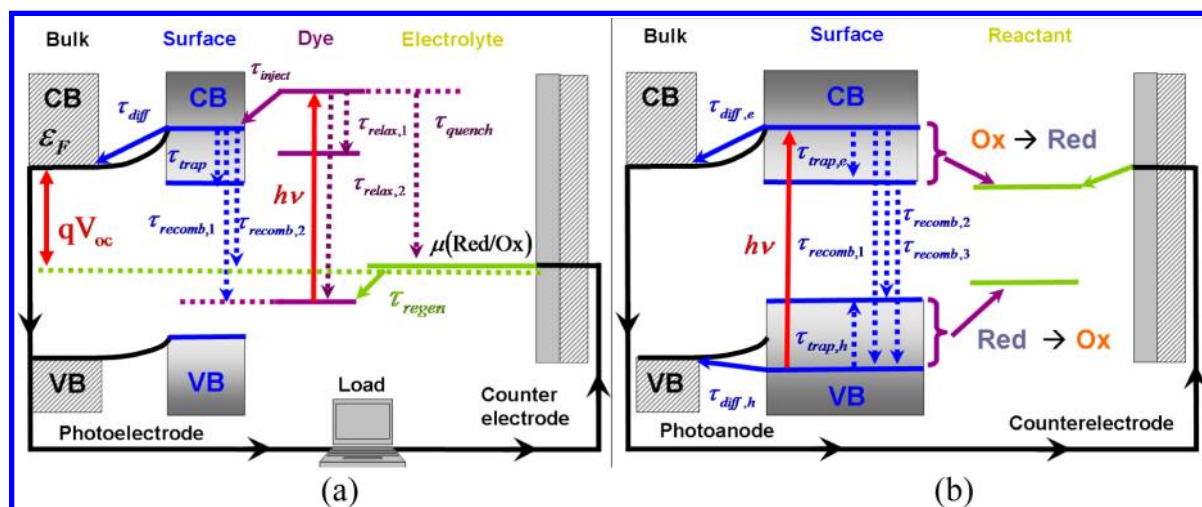


Figure 2. Energy diagram and competing processes in the photovoltaic (a) and photochemical (b) cells.

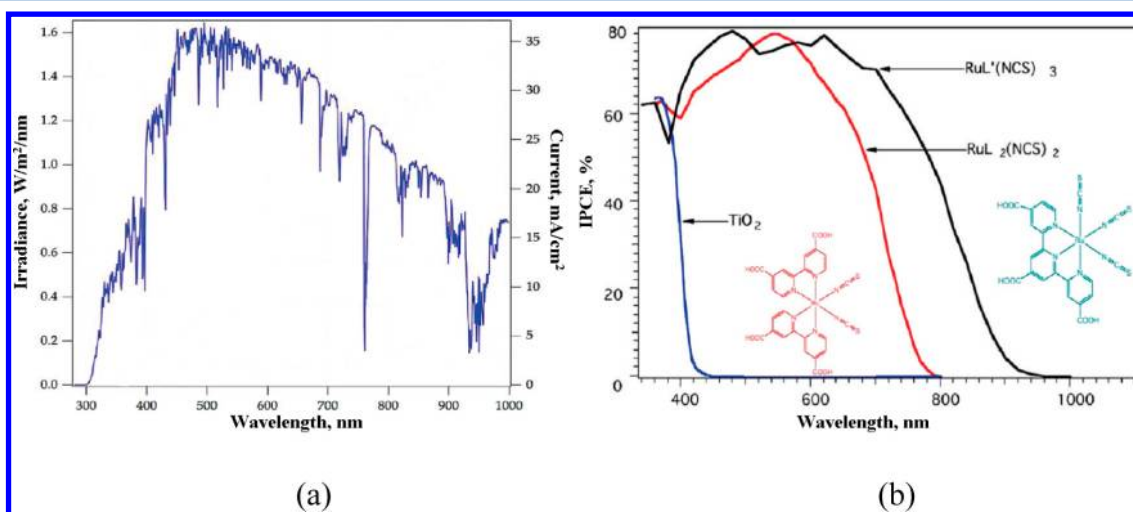


Figure 3. (a) Solar power spectrum; and (b) IPCE for Ru-based metallo–organic dyes. Adapted with permission from ref 34. Copyright 2009 American Chemical Society.

diagram (Figure 2a), the quantum yield of the electron injection can be estimated as:

$$\phi_{\text{inj}}(\lambda) \approx \frac{k_{\text{inject}}}{k_{\text{inject}} + k_{\text{quench}} + k_{\text{relax},1}} = \frac{\frac{1}{\tau_{\text{inject}}}}{\frac{1}{\tau_{\text{inject}}} + \frac{1}{\tau_{\text{quench}}} + \frac{1}{\tau_{\text{relax},1}}} \quad (1.5)$$

where  $k_i$  is the rate constant for process  $i$ .

Typical distributions of the solar radiation intensity and the IPCE for the two most efficient Ru-based dyes as functions of the wavelength,  $\lambda$ , are presented in Figure 3. To maximize the photocurrent density, the IPCE should be highest in the regions where the solar spectrum intensity is high. However, in many cases, the IPCE of organic and metallo–organic dyes is negligible for wavelengths above 700 nm. Thus, one of the promising research directions is to undertake a rational search for chromophores with wavelengths above 700 nm through a combination of theoretical and experimental tools.

This Review focuses on a theoretical description of ET processes that occur at the interface between metal oxide substrates and adsorbates, including organic, metallo–organic, and inorganic sensitizers, in photovoltaic and photocatalytic

cells. We combine the knowledge obtained from computational and experimental studies, and present it within a modern theoretical framework. We highlight the basic concepts behind the various processes that are involved in the operation of photovoltaic and photocatalytic cells. This work presents a wide and systematic description of the underlying principles and the complex relationships that are important for understanding these devices and improving their performance. Although we wish to cover a wide range of theoretical and experimental studies, it is not practical to discuss each topic in great detail in this Review. For this reason, we refer the reader to other reviews on this and related subjects.<sup>1,4,6,10,14,16,22,27,34,36–42</sup>

This Review is structured as follows. In section 2, we discuss the theoretical methods that are used to study the dynamics of charge separation, diffusion, relaxation, recombination, and related phenomena. Simultaneous consideration of these processes often requires special treatments, such as *ab initio* nonadiabatic molecular dynamics, which takes into account multiple electronic states and generates atomistic, time-domain representation, directly mimicking the processes as they occur in experiments. In section 3, we discuss the chemical and electronic structures of photoactive materials at oxide interfaces, focusing on their role in photovoltaic and photo-

chemical cells. In section 4, we consider the dynamics and mechanisms of ET processes in photovoltaic cells, following the above diagram (Figure 2a). Many of the processes taking place in photovoltaic cells are also encountered in photochemical cells. In section 5, we discuss the processes particularly relevant for photocatalytic applications; this discussion is also useful for a deeper understanding of the operation of photovoltaic devices. Finally, in section 6, we summarize the key points highlighted in this Review, by evaluating the progress made in the studies of photoexcited ET in oxide materials so far and outlining future research directions.

## 2. THEORY

### 2.1. The Hierarchy of Approximations

Electron transfer at an interface composed of two materials proceeds through one of two major mechanisms, adiabatic or nonadiabatic.<sup>14,41</sup> To understand the origins and properties of these mechanisms from a theoretical standpoint, let us briefly review the general scheme of solving the time-dependent Schrödinger equation (TD-SE):

$$i\hbar \frac{\partial \Psi(r, R, t)}{\partial t} = H(r, R, t) \Psi(r, R, t) \quad (2.1)$$

where  $\Psi(r, R, t)$  is the full wave function and  $H(r, R, t)$  is the total Hamiltonian of the system. They depend on the electronic ( $r$ ) and nuclear ( $R$ ) coordinates. The Hamiltonian can also depend explicitly on time ( $t$ ), for example, when the system interacts with an external electro-magnetic field. The total Hamiltonian can be separated into two terms:

$$H(r, R, t) = T_{\text{nuc}} + H_{\text{el}}(r, R(t)) \quad (2.2)$$

where  $T_{\text{nuc}} = -\sum_i \frac{\hbar^2}{2M_i} \nabla_{R,i}^2$  is the nuclear kinetic energy operator, and  $H_{\text{el}}$  is the electronic Hamiltonian of the system. The latter can be decomposed further:

$$H_{\text{el}}(r, R(t)) = T_{\text{el}} + V_{\text{el}}(r, R(t)) \quad (2.3)$$

where  $T_{\text{el}} = -\sum_i \frac{\hbar^2}{2m} \nabla_{r,i}^2$  is the kinetic energy of the electrons, and  $V_{\text{el}}$  includes electron–nuclear, electron–electron, and nuclear–nuclear interactions.

#### 2.1.1. Separation of Time and Spatial Coordinates.

Solutions of eq 2.1 are commonly obtained as linear combinations:

$$\Psi(r, R, t) = \sum_I c_I(t) \Psi_I(r, R(t)) \quad (2.4)$$

of the solutions for  $\Psi_I(r, R(t))$ , of the stationary Schrödinger equation:

$$[T_{\text{nuc}} + H_{\text{el}}(r, R(t))] \Psi_I(r, R(t)) = E_I(R(t)) \Psi_I(r, R(t)) \quad (2.5)$$

for the total Hamiltonian, eq 2.2.  $\Psi_I(r, R(t))$  are combined electron–nuclear (vibronic) wave functions. The functions may not depend on time explicitly, but they still evolve with time because of the parametric dependence on the nuclear coordinates  $R(t)$ , as discussed in detail below (see eq 2.7). The coefficients  $c_I(t)$  depend explicitly on time.

Substituting expansion 2.4 into eq 2.1 and projecting both sides of the resulting equation onto the electron–nuclear wave functions,  $\Psi_A(r, R(t))$ , gives the following set of equations for the time-dependent coefficients:

$$i\hbar \frac{\partial c_A(t)}{\partial t} = \sum_I \left[ E_I(R(t)) \delta_{A,I} - i\hbar \left\langle \Psi_A \left| \frac{\partial \Psi_I}{\partial t} \right. \right\rangle \right] c_I(t) \quad (2.6)$$

where  $E_I(R(t))$  is the total energy of the electron–nuclear state  $I$ , eq 2.5.

The quantity  $d_{AI} = \langle \Psi_A | (\partial \Psi_I / \partial t) \rangle$  is the nonadiabatic coupling (NAC) between states  $A$  and  $I$ . When the analytic expression of the wave function is known, it can be evaluated using the chain rule:

$$d_{AI} = \left\langle \Psi_A \left| \frac{\partial \Psi_I}{\partial t} \right. \right\rangle = \sum_{n=1}^{N_{\text{nuc}}} (\langle \Psi_A | \vec{\nabla}_{R,n} \Psi_I \rangle, \dot{\vec{R}}_n) \quad (2.7)$$

where the summation runs over all nuclei ( $N_{\text{nuc}}$ ),  $(\cdot, \cdot)$  is the scalar product of the two vectors, and the dot notation  $(\dot{\vec{R}}_n)$  is used for time derivatives,  $\dot{\vec{R}}_n = (d\vec{R}_n/dt)$ . If the analytic form of the wave function is not available, the following numerical approximation to the NAC can be used:<sup>43</sup>

$$d_{AI}(t) = \frac{\langle \Psi_A(t) | \Psi_I(t + \Delta t) \rangle - \langle \Psi_A(t + \Delta t) | \Psi_I(t) \rangle}{2 \cdot \Delta t} \quad (2.8)$$

In this case, a numerical representation of the wave function for each state  $A$  and  $I$  at adjacent time steps  $t$  and  $t + \Delta t$  is required.

**2.1.2. Separation of Electronic and Nuclear Coordinates.** Separation of the electronic and nuclear degrees of freedom is a commonly used approximation.<sup>44–47</sup> It is based on the fact that the mass of the electron is significantly smaller than the mass of the nuclei, so electrons move rapidly in the field created by static nuclei. The separation-of-variables assumption leads one to write the total wave function as a product of the electronic,  $\Phi_i(r; R(t))$ , and nuclear,  $\chi_{ia}(R(t))$ , components:

$$\Psi_I(r, R(t)) = \Phi_i(r; R(t)) \chi_{ia}(R(t)) \quad (2.9)$$

The double index,  $I = \{i, a\}$ , denotes the wave function corresponding to the  $i$ th electronic and  $a$ th nuclear state. Each electronic state has its own set of nuclear states, such that the nuclear wave function  $\chi_{ia}(R(t))$  carries both  $i$  and  $a$  indices. The semicolon in  $\Phi_i(r; R(t))$  emphasizes the fact that the electronic wave function is an explicit function of the electronic coordinates  $r$ , and that it depends on the nuclear coordinates  $R(t)$  parametrically. The basis functions,  $\Phi_i(r; R(t))$  and  $\chi_{ia}(R(t))$ , are not explicitly time-dependent and should be considered as static distributions for each nuclear configuration  $R(t)$ . For instance, the nuclear basis functions  $\chi_{ia}(R(t))$  can be harmonic oscillator eigenfunctions located on different centers. The explicit time-evolution of the total wave function of the system is determined by the time-dependent coefficient  $c_{ia}(t)$  in eq 2.4.

It is also useful to augment the time-dependent coefficients  $c_{ia}(t)$  with the nuclear wave functions  $\chi_{ia}(R(t))$ , which depend on time parametrically via nuclear positions. In a general case, the parametric dependence of  $\chi_{ia}(R(t))$  on time can also be relaxed, and the resulting nuclear wave function can be assumed to be truly time-dependent. In addition, it is convenient to sum all vibronic states in a single nuclear wave function, such that the result is indexed only by the electronic state:

$$\tilde{\chi}_i(t, R(t)) = \sum_a c_{ia}(t) \chi_{ia}(R(t)) \quad (2.10)$$

The total (time-dependent) wave function will then be given by inserting eq 2.9 into eq 2.4. In combination with eq 2.10, this gives:

$$\Psi(r, R, t) = \sum_i \tilde{\chi}_i(t, R(t)) \Phi_i(r; R(t)) \quad (2.11)$$

The squares of the amplitudes of the nuclear wave functions,  $|\tilde{\chi}_i(t, R(t))|^2$ , determine the probability of finding the system in the electronic state  $\Phi_i(r; R(t))$  at any given time,  $t$ .

**2.1.3. Electronic Wave Functions.** The electronic wave functions  $\Phi_i(r; R(t))$  in eq 2.9 are obtained as eigenfunctions of the stationary Schrödinger equation:

$$H_{\text{el}}(r; R(t)) \Phi_i(r; R(t)) = E_i(R(t)) \Phi_i(r; R(t)) \quad (2.12)$$

with the electronic Hamiltonian, eq 2.3.

Solving the electronic problem is an area of research that has received a lot of focus. A wide variety of methods have been developed to calculate the electronic energies, densities, and wave functions, while balancing the desired accuracy with computational cost. These methods range from semiempirical ones,<sup>48–52</sup> to various formulations of density functional theory (DFT),<sup>53–61</sup> to ab initio wave function-based approaches, including configuration interaction (CI),<sup>62–64</sup> coupled cluster theory (CC),<sup>65–69</sup> complete-active-space self-consistent-field (CASSCF),<sup>70–73</sup> along with more advanced techniques. Advanced methods, such as CASSCF, are only applicable to relatively small systems and become prohibitively expensive for large systems, while DFT approaches have gained popularity because of their computational efficiency and accuracy.

The Kohn–Sham formulation<sup>54,74</sup> of DFT is based on a variational minimization of the energy functional:

$$E(\{\phi_i\}) = \sum_{i=1}^{N_{\text{el}}} \langle \phi_i | h | \phi_i \rangle + \iint \frac{\rho(\vec{r}', R(t)) \rho(\vec{r}, R(t))}{|\vec{r}' - \vec{r}|} d\vec{r}' d\vec{r} + E_{\text{xc}}(\rho, \nabla \rho, \dots) \quad (2.13)$$

which yields a set of optimized single-particle Kohn–Sham orbitals  $\{\phi_i\}$ . The first term in eq 2.13 represents the kinetic energy of electrons and the energy of electron–nuclei attraction, the second term gives the classical-like energy of electron–electron repulsion, and the last term defines the exchange–correlation energy. The expressions for the electron exchange and correlation terms are extremely difficult to solve and constitute a key challenge in the development of DFT functionals. In the simplest local density approximation (LDA), the energy in eq 2.13 is defined as a function of the three-dimensional electron density,  $\rho(\vec{r}, R(t)) = \sum_{i=1}^{N_{\text{el}}} |\phi_i(\vec{r}, R(t))|^2$ . DFT functionals, which include density gradients, are known as the generalized gradient approximation (GGA). Second derivatives of the density lead to meta-GGAs. Explicit consideration of density currents results in nonadiabatic DFT functionals. There also are orbital-dependent functionals, among others.

In the wave function-based methods, the all-electron ground-state  $\Phi_0(r; R(t))$  is most frequently constructed as the Slater determinant build of one-particle orbitals:

$$\Phi_0(r; R(t)) = \hat{A}[\phi_1 \phi_2 \dots \phi_{N_{\text{el}}}] \quad (2.14)$$

where  $\hat{A}$  is an antisymmetrization operator. This leads to the Hartree–Fock (mean-field) approximation. Excited-state wave functions can then be obtained from  $\Phi_0(r; R(t))$  by applying the creation ( $a_i^\dagger$ ) and annihilation ( $a_i$ ) operators, which add or

remove orbitals ( $\phi_i$ ), respectively, from the Slater determinant. For instance, excited determinants up to the third-order of excitation can be represented as:

$$\Phi_i^a(r; R(t)) = a_a^\dagger a_i \Phi_0(r; R(t)) \quad (2.15a)$$

$$\Phi_{ij}^{ab}(r; R(t)) = a_b^\dagger a_j a_a^\dagger a_i \Phi_0(r; R(t)) \quad (2.15b)$$

$$\Phi_{ijk}^{abc}(r; R(t)) = a_c^\dagger a_k a_b^\dagger a_j a_a^\dagger a_i \Phi_0(r; R(t)) \quad (2.15c)$$

The electronic wave functions obtained for the ground and excited states, augmented with the corresponding nuclear wave functions, form the basis set in eq 2.9 for performing the time-dependent calculations in eq 2.6. Electronic excited-state wave function can be written as a linear combination of the excited determinants (eq 2.15) within the configuration interaction framework. In quantum-classical treatments, the nuclear degrees of freedom are treated classically. This formally corresponds to the nuclear wave functions being constants and may be taken as equal to unity. In such cases, the basis functions in eq 2.9 are purely electronic functions.<sup>75</sup> Depending on how the electronic wave function is obtained, some of the possible methods that may follow are the time-dependent Hartree–Fock (TD-HF) method, time-dependent density functional theory (TD-DFT), or time-dependent configuration interaction (TD-CI).

**2.1.4. Nuclear Wave Functions: Adiabatic Approximation.** In the adiabatic approximation, the system can be accurately described by a single electronic wave function. Formally, this means that the expansion 2.11 contains a single term. Substituting it into the time-dependent Schrödinger, eq 2.1 results in

$$i\hbar \frac{\partial}{\partial t} \tilde{\chi}_i(t, R(t)) \Phi_i(r; R(t)) = (T_{\text{nuc}} + H_{\text{el}}) \tilde{\chi}_i(t, R(t)) \Phi_i(r; R(t)) \quad (2.16)$$

For simplicity, we will assume that there is only one nuclear degree of freedom, such that the nuclear kinetic energy, eq 2.3, contains one term. The generalization for many degrees of freedom is straightforward. The right-hand side of eq 2.16 can further be reduced to:

$$\begin{aligned} & (T_{\text{nuc}} + H_{\text{el}}) \tilde{\chi}_i(t, R(t)) \Phi_i(r; R(t)) \\ &= \Phi_i(r; R(t)) T_{\text{nuc}} \tilde{\chi}_i(t, R(t)) + \tilde{\chi}_i(t, R(t)) T_{\text{nuc}} \Phi_i(r; R(t)) - \hbar^2 \frac{\nabla \tilde{\chi}_i(t, R(t)) \nabla \Phi_i(r; R(t))}{M} \\ &+ E_i(R) \Phi_i(r; R(t)) \tilde{\chi}_i(t, R(t)) \end{aligned} \quad (2.17)$$

Projecting both sides of eq 2.16 on the electronic state leads to:

$$\begin{aligned} & i\hbar \frac{\partial \tilde{\chi}_i(t, R(t))}{\partial t} \langle \Phi_i(r; R(t)) | \Phi_i(r; R(t)) \rangle \\ &= \langle \Phi_i(r; R(t)) | \Phi_i(r; R(t)) \rangle (T_{\text{nuc}} + E_i(R)) \tilde{\chi}_i(t, R(t)) \\ &+ \tilde{\chi}_i(t, R(t)) \langle \Phi_i(r; R(t)) | T_{\text{nuc}} \Phi_i(r; R(t)) \rangle \\ &- \hbar^2 \frac{\nabla \tilde{\chi}_i(t, R(t)) \langle \Phi_i(r; R(t)) | \nabla \Phi_i(r; R(t)) \rangle}{M} \end{aligned} \quad (2.18)$$

Because the electronic wave function is normalized,  $\langle \Phi_i(r; R(t)) | \Phi_i(r; R(t)) \rangle = 1$ , it is possible that  $\langle \Phi_i(r; R(t)) | \nabla \Phi_i(r; R(t)) \rangle = 0$ , and eq 2.18 can be simplified to:

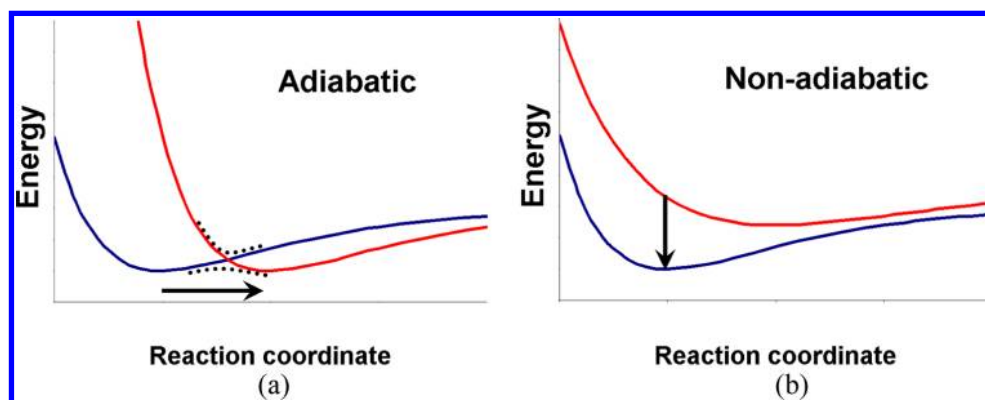


**Figure 4.** Adiabatic (a) and nonadiabatic (b) electron transfer mechanisms. The blue and red potential energy surfaces correspond to the reactant and product states, respectively.

$$i\hbar \frac{\partial \tilde{\chi}_i(t, R(t))}{\partial t} = (T_{\text{nucl}} + E_i(R) + \langle \Phi_i(r; R(t)) | T_{\text{nucl}} \Phi_i(r; R(t)) \rangle) \tilde{\chi}_i(t, R(t)) \quad (2.19)$$

The special case of adiabatic dynamic constitutes the Born–Oppenheimer approximation. It is based on the fact that the nuclear mass  $M$  is much larger than the mass of the electron, that is,  $M \gg 1$  in a.u., allowing one to neglect the term  $\langle \Phi_i(r; R(t)) | T_{\text{nucl}} \Phi_i(r; R(t)) \rangle$ . The resulting equation of motion for the nuclear degrees of freedom is:

$$i\hbar \frac{\partial \tilde{\chi}_i(t, R(t))}{\partial t} = (T_{\text{nucl}} + E_i(R)) \tilde{\chi}_i(t, R(t)) \quad (2.20)$$

The above equation allows for a simple interpretation of nuclei moving on a single potential energy surface,  $E_i(R)$ . If the quantum-mechanical kinetic energy operator  $T_{\text{nucl}}$  is replaced with the classical analogue, the nuclear wave function,  $\tilde{\chi}_i(t, R(t))$ , can be related to the classical probability density in the phase space,  $\rho_i(t, R(t), P(t))$ , and eq 2.20 can be reformulated into the classical Liouville, Hamilton–Jacobi, or Hamiltonian equations of motion.

**2.1.5. Nuclear Wave Functions: Nonadiabatic Approximation.** In a more general case, the wave function of a system cannot be described accurately by a single term in the expansion 2.11, for instance, when the kinetic energy of the nuclei is large as compared to the spacing between the electronic energy levels. This situation corresponds to avoided crossings (conical intersections), when the electronic energies of different states come to near-degeneracy. Here, a non-adiabatic treatment of the nuclear dynamics is required.

For simplicity, similar to the adiabatic case, we will consider only one classical degree of freedom. Repeating the steps similar to eqs 2.16–2.18, but using an arbitrary number of terms in expansion 2.11, we can arrive at a generalized, nonadiabatic equation for nuclear dynamics:

$$i\hbar \frac{\partial \tilde{\chi}_i(t, R(t))}{\partial t} = \sum_j \left\{ (T_{\text{nucl}} + E_j(R)) \delta_{ij} - \hbar^2 \frac{d_{ij}^{(1)}}{M} \nabla - \hbar^2 \frac{d_{ij}^{(2)}}{2M} \right\} \tilde{\chi}_j(t, R(t)) \quad (2.21)$$

where  $d_{ij}^{(n)}$  are the nonadiabatic couplings of  $n$ th order between states  $i$  and  $j$ :

$$d_{ij}^{(1)} = \langle \Phi_i(r; R(t)) | \nabla \Phi_j(r; R(t)) \rangle \quad (2.22a)$$

$$d_{ij}^{(2)} = \langle \Phi_i(r; R(t)) | \nabla^2 \Phi_j(r; R(t)) \rangle \quad (2.22b)$$

In a quantum-classical treatment, the quantum mechanical operators can be mapped onto the classical variables, leading to:

$$-\hbar^2 \frac{d_{ij}^{(1)}}{M} \nabla \rightarrow -i\hbar \frac{d_{ij}^{(1)}}{M} p \quad (2.23a)$$

$$-\hbar^2 \frac{d_{ij}^{(2)}}{2M} \rightarrow \frac{p^2}{2M} \delta_{ij} \quad (2.23b)$$

$$T_{\text{nucl}} \rightarrow \frac{p^2}{2M} \quad (2.23c)$$

As a result, eq 2.21 transforms into:

$$i\hbar \frac{\partial \tilde{\chi}_i(t, R(t))}{\partial t} = \sum_j \left\{ E_j(R) \delta_{ij} - i\hbar \frac{p}{M} d_{ij}^{(1)} \right\} \tilde{\chi}_j(t, R(t)) \quad (2.24)$$

which is exactly eq 2.6 with the nuclear wave function given by eq 2.10.

## 2.2. Electron Transfer Mechanisms

**2.2.1. Adiabatic ET.** As discussed in the previous section, a process that can be accurately described by a single electronic wave function is called an adiabatic process. Applied to ET, this situation defines the adiabatic ET mechanism. In this case, the system remains in the same electronic state at all times (Figure 4a), where the electronic state is an eigenstate of the electronic Hamiltonian, eq 2.12. In particular, it is the lowest energy (ground) state in Figure 4a. Even though the electronic state remains the same, the electron density does not have to be localized in the same place. Because the nuclear configuration changes with time and the electron density adjusts to the nuclear configuration, the density moves from one site to another. For instance, if an electron is initially localized on a donor (e.g., chromophore) and ends up on an acceptor (e.g., semiconductor), the overall process is seen as ET, induced by thermal fluctuations and configuration changes of the nuclear subsystem.

Adiabatic ET assumes that the electron instantaneously responds to nuclear motion, even if the latter occurs on a rapid (pico- to nanosecond) time-scale. Thus, the adiabatic ET rates are determined by the rates of nuclear rearrangements, and



hence they generally show Arrhenius-type temperature dependence.

**2.2.2. Nonadiabatic ET.** In contrast to adiabatic ET, nonadiabatic processes involve at least two electronic states, and hence they cannot be described by a single potential energy surface. Multiple surfaces are strongly coupled to each other, and may come into close contact or even intersect with each other. This scenario is most commonly found in photoactive systems where absorption of a photon induces a transition between electronic levels. In general, the wave function of the excited state is different from that of the ground state and may be localized in different parts of the system (Figure 4b). In this case, a change of the electronic state can result in ET from a donor (e.g., chromophore) to an acceptor (e.g., semiconductor). The potential energy surface for the excited state may be significantly different from that of the ground state, possibly inducing conformational changes that stabilize the system in the product.

The nonadiabatic mechanism implies that the ET process is governed by the electronic transition rather than through nuclear rearrangements. Nuclear relaxation usually takes place after the ET event, with the electronic wave function of the electron-acceptor state corresponding to the nuclear conformation of the reactant state. The nonadiabatic ET rates do not show Arrhenius temperature dependence; rather, the rates are determined by the nonadiabatic coupling between the electronic states involved in the process. The coupling arises from nuclear kinetic energy, and, therefore, it varies nearly linearly with temperature.<sup>76,77</sup> At the same time, the nonadiabatic ET rates depend exponentially on the energy gap between the donor and acceptor states. This dependence is known as the energy gap law.<sup>78–86</sup> Nonadiabatic ET also shows an exponential dependence on the length of the bridge between the donor and acceptor species. In this respect, nonadiabatic ET is similar to quantum-mechanical tunneling. Generally, the nonadiabatic mechanism applies when the donor–acceptor coupling is weak, such that after a donor–acceptor state crossing (Figure 4a), the electron remains in the donor state, and when the energy gap between the states is too large to allow crossings at all (Figure 4b). The nonadiabatic mechanism is also favored when there is a large density of acceptor states.

**2.2.3. Direct Photoinduced ET.** Photoinduced ET can occur through both adiabatic and nonadiabatic mechanisms. It is also possible that photon absorption will directly promote the electron from the donor to the acceptor. Direct ET may be considered a type of nonadiabatic ET. The direct mechanism can be predicted by quantum-mechanical calculations that include the interaction of the electronic subsystem with light. Both static optical absorption spectrum and dynamic optical response calculations can be performed for this purpose. To achieve the appreciable oscillator strength for an optical transition that promotes an electron from the donor to the acceptor species, the electronic donor–acceptor coupling must be very strong. Strong coupling implies that the electronic states are mixed and are partially delocalized between the donor and acceptor sites. In particular, the final (acceptor) state contains an admixture from the donor, and, therefore, one needs to consider subsequent steps in completing the ET process. Often, strong coupling leads to complex quantum dynamics, motivating an explicit time-domain simulation. The weak coupling limit can often be described using a rate theory.

## 2.3. Analytic Models for Calculation of the Rate Constants

A rate theory assumes a simple (typically, exponential) time-dependence of the ET process. In adiabatic ET, such dependence arises from the transition state theory assumption of the exponential (Boltzmann) probability of reaching the transition state, where the donor and acceptor states cross. The rate of nonadiabatic ET appears in low-orders in the time-dependent perturbation theory, which also leads to exponential time-dependence (for instance, in Fermi's golden rule).

**2.3.1. Adiabatic ET.** Adiabatic ET is strongly coupled to changes in the nuclear coordinates of the donor–acceptor system and its environment. Thus, the basic formulation is constructed on the ideas of the transition state theory, and, in general, the kinetic rates follow the phenomenological Arrhenius law:

$$k(T) = A(T) \exp\left(-\frac{\Delta G^*}{k_B T}\right) \quad (2.25)$$

where  $T$  is the temperature of the system,  $k_B$  is the Boltzmann constant,  $\Delta G^*$  is the activation free energy required to reach the transition state, and  $A(T)$  is a pre-exponential factor, which can also depend on temperature (although its dependence is much weaker than exponential). The pre-exponential factor can be estimated on the basis of the collision rate theory or from the partition function of the system studied. It can also include nonadiabatic corrections, if nonadiabatic effects are not too strong.

**2.3.1.1. Transition State Theory (TST).** One of the first comprehensive theories of chemical kinetics in general, and adiabatic electron transfer in particular, is the transition state theory (TST).<sup>87,88</sup> The theory allows both classical and quantum formulations. An extensive discussion of the TST can be found in the detailed reviews<sup>89–94</sup> and related developments.<sup>95–103</sup> Below, we emphasize the main points. According to the TST, the rate constant can be evaluated using partition functions calculated for the transition state (TS), also known as activated complex,  $Z^\#$ , and the reactant state,  $Z$ :

$$k_{\text{TST}}(T) = \frac{k_B T}{h} \frac{Z^\#}{Z} \quad (2.26)$$

where  $h$  is the Planck constant,  $k_B$  is the Boltzmann constant and  $T$  is temperature. Typically, the contributions to the ( $Z^\# / Z$ ) ratio from translational, electronic, internal rotational, and spin degrees of freedom are similar for the TS and the reactant. The main contribution making the above ratio different from unity arises from vibrations. In the harmonic approximation, such modes are represented, for the reactant state, by a collection of  $N$  harmonic oscillators with real frequencies:

$$V(q_i) = \frac{1}{2} m \omega_i^2 q_i^2 \quad (2.27)$$

and for the TS, by  $N - 1$  harmonic oscillators of type 2.27 and a single mode with a purely imaginary frequency  $\omega^\#$ :

$$V(q_\#) = V^\# - \frac{1}{2} m \omega_\#^2 (q_\# - \bar{q}_\#)^2 \quad (2.28)$$

For simplicity, we assumed that the masses of all oscillators are the same. With such assumptions, the above partition functions become:



$$Z = \prod_{i=0}^{N-1} \left[ \sinh \left( \frac{\hbar \Omega_i}{2k_B T} \right) \right]^{-1} \quad (2.29)$$

and

$$Z^\# = \frac{\hbar \Omega_0^\#}{2k_B T} \left[ \sin \left( \frac{\hbar \Omega_0^\#}{2k_B T} \right) \right]^{-1} \exp \left( -\frac{V^\#}{k_B T} \right) \prod_{i=1}^{N-1} \left[ \sinh \left( \frac{\hbar \Omega_i^\#}{2k_B T} \right) \right]^{-1} \quad (2.30)$$

Here,  $\Omega_i^\#$  denotes the frequencies of the nonreactive (bath) modes, while  $\Omega_0^\#$  denotes the frequency of the mode, along which the reaction takes place (reaction coordinate at the saddle point). The frequencies  $\Omega_i$  and  $\Omega_i^\#$  correspond to the normal modes of the entire system composed of interacting oscillators, while  $\omega_i$  are frequencies of individual oscillators representing bond, angle, torsional, and similar types of motion. Combining eqs 2.26–2.30, one obtains the reaction rate:

$$k(T) = \frac{\omega_0 \Omega_0^\#}{2\pi \omega_\#} \exp \left( -\frac{V^\#}{k_B T} \right) \rho \quad (2.31)$$

where

$$\rho = \frac{\omega_\#}{\omega_0} \frac{\sinh \left( \frac{\hbar \Omega_0}{2k_B T} \right)}{\sin \left( \frac{\hbar \Omega_0^\#}{2k_B T} \right)} \prod_{i=1}^{N-1} \frac{\sinh \left( \frac{\hbar \Omega_i}{2k_B T} \right)}{\sinh \left( \frac{\hbar \Omega_i^\#}{2k_B T} \right)} \quad (2.32)$$

As shown by Pollak,<sup>104,105</sup> the term  $((\omega_0 \Omega_0^\#)/(2\pi \omega_\#)) \exp(-(V^\#)/(k_B T))$  describes the classical Grote–Hynes rate.<sup>106</sup> Hence, the quantity  $\rho$  is a quantum correction to the classical rate. As temperature increases, the quantity  $\rho$  goes to unity, and the classical description of the reaction rates becomes valid. The quantum correction term was derived by Wolynes<sup>107</sup> and later rederived from different perspectives by Pollak,<sup>105</sup> Voth et al.<sup>94</sup> Summarizing, the correction eq 2.32 can be presented as:

$$\rho = \prod_{n=1}^{\infty} \left( \frac{M_n^2 + \omega_0^2 - 2\tilde{\alpha}_n/m}{M_n^2 - \omega_\#^2 - 2\tilde{\alpha}_n/m} \right) \quad (2.33)$$

where  $M_n = ((2\pi n)/(\hbar k_B T))$  is the Matsubara frequency,  $\omega_0$  is the harmonic frequency of the reaction coordinate in the reactant well,  $\omega_\#$  is the frequency of the parabolic activation barrier,  $m$  is the effective mass of the reaction coordinate, and  $\tilde{\alpha}_n$  is given by:

$$\tilde{\alpha}_n = \int_{-\infty}^{+\infty} d\tau \cdot \alpha(|\tau|) \cos(M_n \tau) \quad (2.34)$$

$$\alpha(|\tau|) = \frac{1}{2\pi} \int_0^\infty d\omega \cdot J(\omega) e^{-\omega|\tau|} \quad (2.35)$$

where  $J(\omega)$  is spectral density of the oscillator bath, given by:

$$J(\omega) = \frac{\pi}{2} \sum_j \frac{c_j^2}{m_j \omega_j^2} \delta(\omega - \omega_j) \quad (2.36)$$

A correction similar to eq 2.33 was obtained by Dakhnovsky and Ovchinnikov<sup>108</sup> based on analysis of the generalized Kramers theory.

**2.3.1.2. Marcus Theory.** When applied to ET in a condensed phase environment, for example, solvent, such formulation turns into the Marcus theory of electron transport.<sup>109–115</sup> This theory carefully takes into account various contributions to the free energy change along the reaction coordinate. In summary, the Marcus rate equation is given by:

$$k(T) = \kappa A \sigma^2 \exp \left( -\frac{w^r + \frac{\lambda}{4} \left( 1 + \frac{\Delta \tilde{G}^0}{\lambda} \right)^2}{k_B T} \right) \quad (2.37)$$

$$\Delta \tilde{G}^0 = \Delta G^0 + w^p - w^r \quad (2.38)$$

where  $A\sigma^2$  is the collision frequency,  $\sigma$  is the mean separation distance between the centers of the reacting species in a transition state complex,  $\Delta G^0$  is the standard free energy of the reaction in the medium, and  $\Delta \tilde{G}^0$  is the work-corrected free energy of the reaction. The quantities  $w^r$  and  $w^p$  represent the work required to bring the reactant and product particles, respectively, to the separation distance  $\sigma$ . Finally, the quantity  $\lambda$  is the reorganization energy needed to form the transition state complex from the reactant species and the surrounding solvent. This quantity is computed as a sum of contributions coming from the reactant,  $\lambda_r$ , and the solvent,  $\lambda_{sol}$ :

$$\lambda = \lambda_r + \lambda_{sol} \quad (2.39)$$

The reactant and solvent contributions of the reorganization energy are given by:<sup>112,116,117</sup>

$$\lambda_r = \sum_i \frac{f_i^{(r)} f_i^{(p)}}{f_i^{(r)} + f_i^{(p)}} (\Delta q_i)^2 \quad (2.40)$$

$$\lambda_{sol} = (\Delta e)^2 \left( \frac{1}{2R_1} + \frac{1}{2R_2} - \frac{1}{\sigma} \right) \left( \frac{1}{\epsilon_s} - \frac{1}{\epsilon_{op}} \right) \quad (2.41)$$

Here,  $f_i^{(r)}$  and  $f_i^{(p)}$  are the force constants for the  $i$ th normal mode of the reactant and product states, respectively,  $\Delta q_i$  is the change in the  $i$ th normal coordinate,  $\Delta e$  is the amount of charge transferred from reactant to product,  $R_I$ ,  $I = 1, 2$ , are the diameters of reacting species (assumed to be spherical), and  $\epsilon_s$  and  $\epsilon_{op}$  are the static and optical dielectric constants of the solvent, respectively.

It is worth noting that in the simplest formulation, the Marcus theory is based on consideration of two diabatic potential energy surfaces (PES) corresponding to the reactant and product states (Figure 5a). In the adiabatic limit, the reaction coordinate describes motion of the system on the lower adiabatic PES, obtained from the diabatic PES by

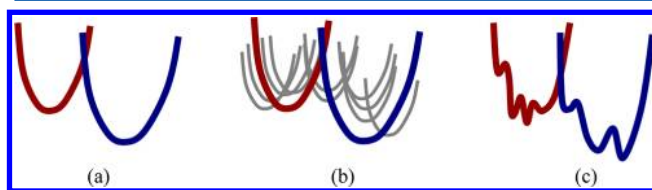


**Figure 5.** Schematic representation of the diabatic energy surfaces for the simplest two-state donor–acceptor Marcus model (a), inclusion of bath modes as a collection of displaced harmonic oscillators (b), and two-state model with intrinsic disorder (e.g., in glasses) where multiple local minima are present (c).

including interaction between the reactant and the product (see also Figure 4a). Because realistic systems are multidimensional objects, coordinates other than the reaction coordinate can play an important role in the system evolution. Because of the complexity of a detailed description of such effects, they are usually treated as a bath of harmonic oscillators coupled to the reaction coordinate (Figure 5b). Finally, the assumption of the Marcus theory that the PESs are approximated by two parabolas (diabatic picture) or as a double-well potential (adiabatic picture) may not always be valid. This is often the case for amorphous materials, such as glasses and biological polymers, where multiple local minima are created because of intrinsic disorder and long-range interactions (Figure 5c). In the following paragraphs, we briefly discuss the ways to take into account the effects of system–bath interactions and intrinsic disorder.

**2.3.1.3. Adiabatic ET in a Dissipative Environment.** Parallel to the TST framework, alternative theories were proposed for the description of reaction rates, including those of adiabatic ET.<sup>118–124</sup> One of the first among them was proposed by Kramers,<sup>125</sup> who investigated escape rates from a metastable state, represented by a double-well potential with a barrier. The elaboration of the problem led Kramers to the “diffusion” model of the reaction dynamics. Similar Markovian-type diffusion models were developed by Zusman,<sup>120,121</sup> Alexandrov,<sup>126</sup> and Calef and Wolynes.<sup>118</sup>

The description was generalized by Grote and Hynes,<sup>106</sup> who used time-correlation functions to describe the dynamics of the reaction mode. Effectively, they considered a non-Markovian dynamics of the classical degrees of freedom with a frequency-dependent friction kernel, which is represented by the generalized Langevin equation (GLE):

$$m\ddot{q} + \frac{dw(q)}{dq} + \int_0^t d\tau \gamma(t-\tau)\dot{q}(\tau) = \xi(t) \quad (2.42)$$

where  $q$  is the reaction coordinate,  $w(q)$  is the potential of mean force along the reaction coordinate, and  $\xi(t)$  is a Gaussian random force, whose correlation function satisfies the fluctuation–dissipation condition,  $\langle \xi(t)\xi(0) \rangle = k_B T \gamma(t)$ . Such formulation was shown<sup>104,127–129</sup> to be equivalent to the dynamics of a classical particle in a bath of harmonic oscillators:

$$H = \frac{p_q^2}{2m} + w(q) + \frac{1}{2} \sum_j \left[ \frac{p_{x_j}^2}{m_j} + m_j \left( \omega_j x_j - \frac{c_j q}{m_j \omega_j} \right)^2 \right] \quad (2.43)$$

where  $x_j$  are nonreactive (bath) modes, represented by harmonic oscillators linearly coupled to the reaction coordinate. The friction kernel  $\gamma$  is related to the parameters of the oscillators by:

$$\gamma(t) = \sum_j \frac{c_j^2}{m_j \omega_j^2} \cos(\omega_j t) \quad (2.44)$$

Thus, instead of directly solving the GLE eq 2.42, one can compute the classical dynamics with the Hamiltonian eq 2.43. Called the spin-boson Hamiltonian, it was studied extensively by many researchers in the context of both adiabatic and nonadiabatic ET in dissipative environment.<sup>130–138</sup> We shall discuss this approach in more detail in section 2.3.2 in the context of nonadiabatic ET. In the above description, the coefficients  $c_j$  are assumed to be constants, thus providing linear

coupling between the reaction coordinate and bath modes. In a more general treatment, such coefficients can depend on the reaction coordinate, making the system–bath coupling nonlinear. It has been shown that nonlinear effects can change reaction rates by orders of magnitude, especially at low temperatures.<sup>139</sup>

The inclusion of the nonreactive, dissipative modes is of paramount importance for an accurate calculation of the reaction rates. For example, as shown by Gertner et al.<sup>140</sup> using direct MD calculations, the Kramers theory significantly underestimates reaction rates. On the contrary, the Grote–Hynes results are in a much better agreement with the direct MD simulations, as well as with the more accurate TST. Thus, the inclusion of dynamical correlation via a non-Markovian memory kernel is essential. Because such kernel arises due to bath modes (solvent, nonreactive vibrations, etc.), proper description of energy dissipation into the bath modes is important.

Applied to reactions involving ET in a polarizable solvent, the friction effects representing the charge–solvent interaction were studied by the Hynes group.<sup>124</sup> They found that the interaction between the charge transfer and the solvent becomes increasingly important as the solvent dynamics slows, and the rate constant becomes very sensitive to the magnitude of such interaction. The significance of the electron–solvent interaction was also discussed by Calef and Wolynes,<sup>118</sup> who analyzed the conditions under which either adiabatic or nonadiabatic description of the dynamics becomes more adequate.

**2.3.1.4. Time-Scale Separation and Nonexponential Kinetics.** In addition to the quantitative effect of bath modes and energy dissipation on the ET reaction rates, the interaction between reactive and nonreactive modes can qualitatively change reaction kinetics, resulting in decay laws that are more complex than a simple exponential. Such effects are especially pronounced when the time-scales of the ET reaction and bath relaxation are comparable. This is often the case in disordered systems or near critical points of phase diagrams. In glass materials,<sup>141,142</sup> intrinsic disorder and the long-range nature of electrostatic interactions lead to large variations in the system Hamiltonian, making it crucial to carefully average over possible configurations. For a two-state system, the kinetic equations read:

$$\begin{aligned} \frac{d\langle P_1(t) \rangle}{dt} &= -\langle \Gamma_1 P_1 \rangle + \langle \Gamma_2 P_2 \rangle \\ \frac{d\langle P_2(t) \rangle}{dt} &= \langle \Gamma_1 P_1 \rangle - \langle \Gamma_2 P_2 \rangle \end{aligned} \quad (2.45)$$

where  $P_i(t)$  is a time-dependent population of state  $i$ , and  $\Gamma_i$  is the decay rate for the corresponding state. Note that the state is not necessarily an electronic state, which would imply the nonadiabatic ET mechanism, but can rather point to the spatial localization of the electron or to a state in the diabatic representation. Depending on the relationship between the time-scales of the ET reaction,  $\Gamma^{-1}$ , and the relaxation of bath modes,  $\tau$ , one may encounter two scenarios:

- (a) The ET is fast in comparison to the bath modes,  $\tau \ll \Gamma^{-1}$ . In this case, during the reaction dynamics, the environment remains in equilibrium corresponding to the reactant state, and one can use the approximation:

$$\langle \Gamma_i P_i \rangle \approx \langle \Gamma_i \rangle \langle P_i \rangle \quad (2.46)$$

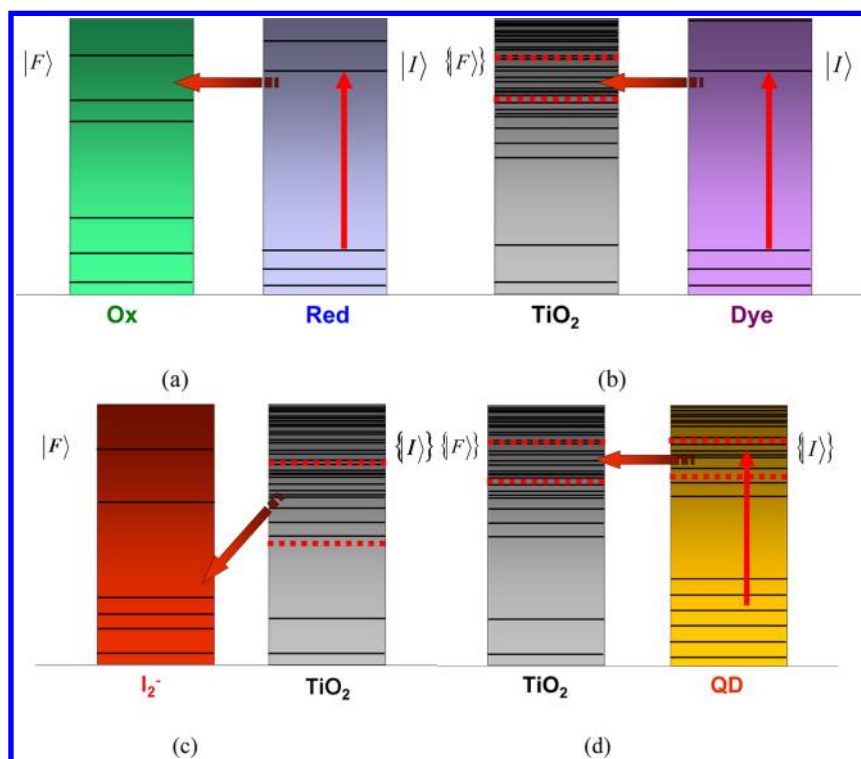


**Figure 6.** Several types of interfacial ET reactions: donor with a discrete spectrum (a,b); donor with a quasi-continuous spectrum (c,d); acceptor with a discrete spectrum (a,c); acceptor with a quasi-continuous spectrum (b,d). The four examples can be found in the following systems: (a) any molecular redox process; (b) electron injection from a photoexcited dye molecule into the conduction band (CB) of a semiconductor, e.g.,  $\text{TiO}_2$ ; (c) electron recombination from the CB of a semiconductor, e.g.,  $\text{TiO}_2$ , to the oxidized form of a dye or electrolyte, e.g.,  $\text{I}_2^-$ ; and (d) ET from the CB of a quantum dot (QD) or graphene to the CB of a semiconductor, e.g.,  $\text{TiO}_2$ .

to arrive at the single exponential kinetics law:

$$\langle P_1(t) \rangle = \frac{\langle \Gamma_2 \rangle + \langle \Gamma_1 \rangle \exp[-(\langle \Gamma_2 \rangle + \langle \Gamma_1 \rangle)t]}{\langle \Gamma_1 \rangle + \langle \Gamma_2 \rangle} \quad (2.47)$$

- (b) The ET is slow while the relaxation of the bath modes is fast,  $\tau \gg \Gamma^{-1}$ . In this case, the environment is not in equilibrium and responds to the changes in the system. Hence, eq 2.46 is no longer valid. Instead, one averages the populations of each state. In combination with the detailed balance condition, this gives nonexponential reaction kinetics:

$$\langle P_1(t) \rangle = \frac{1}{1 + \exp(-\Delta G/k_B T)} \frac{\langle \exp[-\Gamma_1(1 + \exp(\Delta G/k_B T))t] \rangle}{1 + \exp(\Delta G/k_B T)} \quad (2.48)$$

Note that the averaging in the numerator is done outside of the exponent, representing independent relaxation for each of many disordered configurations of a glassy material, and making the kinetics multiexponential.

In the regime of slow bath modes, the reaction rate can take the so-called “false tunneling”<sup>141</sup> form:

$$\langle \Gamma_1 \rangle = \frac{\Delta^2}{\hbar} \sqrt{\frac{\pi}{k_B E_r (T + T_0)}} \exp\left(-\frac{(E_r + \Delta G)^2}{4k_B E_r (T + T_0)}\right) \quad (2.49)$$

Here,  $E_r$  is the reorganization energy of the ordinary polar modes,  $\Delta G$  is the reaction free energy, and  $k_B T_0$  is the reorganization energy parameter representing glass strength:

$$k_B T_0 \approx n E_r \left( \frac{E_d}{E_r} \right)^2 \quad (2.50)$$

where  $E_d$  is the reorganization energy of the polar degrees of freedom of the glass.

As follows from eq 2.49, if  $T_0 \gg T$ , the reaction rate becomes practically independent of temperature, leading to the “false tunneling” regime. The standard Arrhenius law is recovered for  $T_0 \ll T$ .

Nonexponential relaxation kinetics often arises due to the effect of the solvent. The influence of the bath is especially pronounced when the bath modes relax faster than the ET time. This situation may lead to decaying coherent oscillations in the state population,<sup>143</sup>  $P(t) \approx \cos(\Delta \cdot t)/\sqrt{t}$ , where  $\Delta$  is the nonadiabatic coupling in the adiabatic representation or the donor–acceptor coupling in the diabatic representation. Large values of the coupling  $\Delta$  and small energy barriers favor slow oscillation decay. On the contrary, when the coupling is small and the barriers (reorganization energy) are large, the relaxation is fast. We should emphasize that large values of  $\Delta$  result in faster intrinsic relaxation times, but slow the overall reaction rates, including effects of the environment. The asymptotic behavior of the population decay can show power-law dependence,<sup>144</sup> such as  $P(t) \approx t^{-E_{\text{rf}}/E_{\text{rs}}}$ . Here,  $E_{\text{rf}}$  and  $E_{\text{rs}}$  are the reorganization energies for the fast and slow modes, respectively.



**2.3.2. Nonadiabatic ET.** **2.3.2.1. Fermi Golden Rule.** The rate of nonadiabatic ET is described most frequently using the Fermi golden rule, which follows from the first-order time-dependent perturbation theory. According to this treatment, the rate of transition between the initial  $|I\rangle$  and final  $|F\rangle$  states with energies  $E_I$  and  $E_F$ , respectively, is given by:

$$k_{I \rightarrow F} = \frac{2\pi}{\hbar} |\langle F|H'|I\rangle|^2 \delta(E_F - E_I) \quad (2.51)$$

where  $H'$  is the time-dependent perturbation that arises from the interaction with electro-magnetic radiation or nuclear vibrations, for instance.

The states above are defined in a general sense. If ET is faster than nuclear motion, such states can be assumed to be purely electronic:  $|I\rangle = |i\rangle$  and  $|F\rangle = |f\rangle$ . However, if the ET process is slower than the time-scale of nuclear motions (vibrations, rotations), then the corresponding types of states should be introduced explicitly and labeled with additional quantum numbers. For example, if ET happens on a 10 fs to 1 ps time-scale, vibronic (electronic-vibrational) wave functions should be used,  $|I\rangle = |i, \chi_{\text{vib},i}\rangle$  and  $|F\rangle = |f, \chi_{\text{vib},f}\rangle$ , where the symbols  $\chi_{\text{vib},i}$  and  $\chi_{\text{vib},f}$  represent the vibrational quantum numbers associated with the initial and final electronic states, respectively. The vibrational states can be described by a collection of the normal mode quantum numbers:  $\chi_{\text{vib},i} = \{v_{i1}, v_{i2}, v_{i3}, \dots, v_{iN}\}$  and  $\chi_{\text{vib},f} = \{v_{f1}, v_{f2}, v_{f3}, \dots, v_{fN}\}$ . If ET happens on a time-scale of 1 ps to 1 ns, then rotational quantum numbers should be introduced, resulting in  $|I\rangle = |i, \chi_{\text{vib},i}, \chi_{\text{rot},i}\rangle$  and  $|F\rangle = |f, \chi_{\text{vib},f}, \chi_{\text{rot},f}\rangle$ . Because rotational energy levels are separated from each other by energy that is smaller than the thermal energy, their quantization has a negligible effect on ET dynamics. However, rotational states may become relevant at low temperatures and other extreme conditions. In some cases (e.g., with ultrafast ET), vibrational states can be neglected as well. The discussion below uses vibronic states and omits the subscript “vib” in the notation for the nuclear wave function. The ET rates for purely electronic states can then be obtained as a special case.

Vibronic states are often represented as direct products of electronic and nuclear (vibrational) wave functions:  $|i, \chi_i\rangle = |i\rangle | \chi_i \rangle$  and  $|f, \chi_f\rangle = |f\rangle | \chi_f \rangle$ . Here,  $| \chi_i \rangle$  and  $| \chi_f \rangle$  are the nuclear wave functions for the initial and final electronic states  $|i\rangle$  and  $|f\rangle$ , respectively. The vibrational wave functions can further be expressed as products of wave functions associated with normal modes:  $| \chi_i \rangle = \prod_k | \chi_{ik} \rangle$  and  $| \chi_f \rangle = \prod_k | \chi_{fk} \rangle$ .

Interfacial ET can involve dense manifolds of initial  $\{|I\rangle\}$  and final  $\{|F\rangle\}$  states. This fact is reflected in the Fermi golden rule by integrating over the initial and final state energies:

$$k_{\{I\} \rightarrow \{F\}} = \frac{2\pi}{\hbar} \int |\langle F|H'|I\rangle|^2 \delta(E_I - E_F) dE_F dE_I \quad (2.52)$$

The integral is substituted by a summation for systems with discrete energy levels.  $|I\rangle$  and  $|F\rangle$  are vibronic states, and  $E_I$  and  $E_F$  are total electron–nuclear energies. Equation 2.52 is very general and comprises many special cases (Figure 6).

In the simplest case, both the initial  $\{|I\rangle\}$  and the final state  $\{|F\rangle\}$  manifolds include one electronic state (Figure 6a). This case is particularly convenient for explicitly discussing the contributions of nuclear motion in the rate expression. Other cases listed in Figure 6 require more complicated notation. Each of the two electronic states support a manifold of vibrational levels, and the general formula 2.52 turns into:

$$k_{I \rightarrow F} = \frac{2\pi}{\hbar} \int |\langle f, \chi_f | H' | i, \chi_i \rangle|^2 \delta(E_{i,n_i} - E_{f,n_f}) dE_{f,n_f} dE_{i,n_i} \quad (2.53)$$

In discrete notation, this expression has been used by Prezhdo and Rossky:<sup>145</sup>

$$k_{I \rightarrow F} = \frac{2\pi}{\hbar} \sum_{n_i} p(E_{i,n_i}) \sum_{n_f} |\langle f, \chi_f | H' | i, \chi_i \rangle|^2 \delta(E_{i,n_i} - E_{f,n_f}) \quad (2.54)$$

The probability of finding the system in the initial state  $|i, \chi_i\rangle$  is given by the Boltzmann factor:

$$p(E_{i,n_i}) = \frac{e^{-E_{i,n_i}/k_B T}}{\sum_{n_i} e^{-E_{i,n_i}/k_B T}} \quad (2.55)$$

Under the assumption that the perturbation Hamiltonian  $H'$  is independent of the nuclear coordinates, the term  $\langle f, \chi_f | H' | i, \chi_i \rangle$  can be factorized:

$$\langle f, \chi_f | H' | i, \chi_i \rangle = \langle f | H' | i \rangle \langle \chi_f | \chi_i \rangle \quad (2.56)$$

The first term in the above expression is electronic coupling. The overlap of the nuclear wave functions,  $\langle \chi_f | \chi_i \rangle$ , is known as the Franck–Condon factor. However, in general, the perturbation Hamiltonian  $H'$  may depend on nuclear coordinates (e.g., due to electron–vibrational coupling), and the factorization of the Franck–Condon factor becomes less straightforward. A more rigorous treatment of the rate constant includes the coupling between nuclear wave functions,  $\langle \chi_f | \nabla_n | \chi_i \rangle$ . By rearranging the terms in eq 2.54, one can obtain an expression<sup>145</sup> for the rate constant that is similar to that used by Marcus:<sup>110</sup>

$$k_{I \rightarrow F} = \frac{2\pi}{\hbar} \langle f | H' | i \rangle \sum_{n_i, n_f} p(E_{i,n_i}) \langle \chi_f | \chi_i \rangle \delta(E_{i,n_i} - E_{f,n_f}) \quad (2.57)$$

When all vibrational frequencies are small,  $\hbar \nu_i < (1/2)k_B T$ , and remain the same before and after the reaction, the above expression can be simplified further:

$$k_{I \rightarrow F} = \frac{2\pi}{\hbar} \langle f | H' | i \rangle \frac{1}{\sqrt{4\pi\lambda k_B T}} \exp\left(-\frac{(\tilde{E}^0 + \lambda)^2}{4\lambda k_B T}\right) \quad (2.58)$$

Here,  $\tilde{E}^0$  is the reaction enthalpy for the donor–acceptor separation distance  $\sigma$  in the prevailing medium, and  $\lambda$  is reorganization energy, eq 2.39.

Consider other cases of the general eq 2.52. For simplicity, the focus is on electronic states. Nuclear energy levels can be added to the discussion in a manner similar to the case of the one-donor state and one-acceptor state, analyzed in detail above. Now, consider the situation in which the electron donor is still represented by a single electronic state  $|I\rangle$ , while the acceptor contains a dense manifold of electronic states  $\{|F\rangle\}$ . This situation is very common in interfacial ET. As an example, it describes the electron injection from a photoexcited chromophore into the continuum of states in the conduction band (CB) of a semiconductor, such as  $\text{TiO}_2$  (Figure 6b). The general formula eq 2.52 simplifies to:

$$k_{I \rightarrow \{F\}} = \frac{2\pi}{\hbar} \int |\langle F | H' | I \rangle|^2 \delta(E_I - E_F) dE_F \quad (2.59)$$

Assuming that the electronic coupling is constant for a given energy range, the integral can be represented as:

$$k_{i \rightarrow \{f\}} = \frac{2\pi}{\hbar} |\langle f | H' | i \rangle|^2 \int \delta(E_i - E_f) dE_f$$

$$= \frac{2\pi}{\hbar} |\langle f | H' | i \rangle|^2 \rho(E_i) \quad (2.60)$$

where  $\rho(E_i)$  is the density of semiconductor states evaluated at the injection energy  $E_i$ . Troisi and co-workers developed such a model beginning from the Newns–Anderson Hamiltonian and implementing the retarded Green's function approach.<sup>21,146</sup> (Note: To relate the current notation to that used in the above references, substitute  $k_{i \rightarrow \{f\}} = \Gamma(\varepsilon)|_{\varepsilon=E_i}$  and  $V_{if} = \langle f | H' | i \rangle$ .) The molecular orbitals  $|i\rangle$  and  $\{|f\rangle\}$  were expressed in terms of atomic orbitals, and were assumed to be localized on either the dye or the substrate:  $|i\rangle = \sum_a c_{ia} |a\rangle$ , and  $|f\rangle = \sum_b c_{fb} |b\rangle$ . The coupling between the molecular orbitals was expressed in terms of the coupling between the atomic orbitals  $V_{if} = c_{ia}^* c_{fb} V_{ab}$ , and the above rate constant was represented as:

$$k_{i \rightarrow \{f\}} = \frac{2\pi}{\hbar} \sum_{f,a,a',b,b'} c_{ia} c_{fb}^* c_{ia'}^* c_{fb'} V_{ab}^* V_{a'b} \delta(E_i - E_f)$$

$$= \frac{2\pi}{\hbar} \sum_{a,a',b,b'} c_{ia} c_{ia'}^* V_{ab}^* V_{a'b} \sum_f c_{fb}^* c_{fb'} \delta(E_i - E_f) =$$

$$= \frac{2\pi}{\hbar} \sum_{a,a',b,b'} c_{ia} c_{ia'}^* V_{ab}^* V_{a'b} \rho_{bb'}(E_i) \quad (2.61)$$

where the local density of states in the semiconductor was defined as:

$$\rho_{bb'}(E) = \sum_f c_{fb}^* c_{fb'} \delta(E - E_f) \quad (2.62)$$

The advantage of this method is that the local density of states eq 2.62 of the semiconductor surface depends only on the properties of the surface, and hence it can be computed only once for different dye fragments. Normally the surface includes the anchor group of the dye molecule, because it is strongly coupled to the semiconductor, and that anchor group remains the same for different chromophores. In a similar vein, the computation of the atomic orbital coefficients in the expansion of the donor molecular orbital of the chromophore  $\{c_i^*\}$  can be performed once for an isolated chromophore molecule. The chromophore–semiconductor couplings then can be explicitly evaluated for all combinations of dye/semiconductor pairs. This approach allowed for efficient computational testing of a large number of chromophores that were interacting with a given substrate/anchor structure. Such testing would have required significantly longer computations if all of the parts of the system were required to be considered explicitly in each simulation.

A conceptually similar approach was adopted by May and coauthors,<sup>25,147,148</sup> who derived the rate constant using Green's function and linear response approaches. The resulting simple expression is:

$$k_{i \rightarrow \{f\}} = 2\bar{\Gamma} = \frac{2\pi}{\hbar^2} \bar{N} |\bar{V}_e|^2 \quad (2.63)$$

where  $\bar{\Gamma}$  is the absorption line broadening,  $\bar{N} = \langle \rho(\omega) \rangle_\omega$  is the mean (frequency-averaged) density of states, which is related to the mean (energy-averaged) density of states in eq 2.60 via the scaling transformation  $\bar{N} \langle \rho(\omega) \rangle_\omega = \hbar \langle \rho(E) \rangle_E$ , and  $\bar{V}_e$  is the average coupling.

An even simpler expression for the rate constant that describes electron injection from a dye into a semiconductor was used by Labat and co-workers:<sup>23,149</sup>

$$\tau = \frac{658}{\Delta} \quad (2.64)$$

Here,  $\tau$  is the injection time (in fs),  $\Delta$  is broadening of the donor orbital of the dye upon adsorption (in meV), and 658 is a proportionality constant. The expression was also derived on the basis of the Newns–Anderson approach.<sup>150</sup> It has been shown that, typically, such approximation gives transition times that are one-half that of experimentally measured values.<sup>151</sup>

The third case (Figure 6c), which is similar to the previous one, describes the situation in which ET occurs from a manifold of donor states into a single energy level of the acceptor. For example, this situation can be realized in the electron–hole recombination reaction, when an electron, initially injected into the TiO<sub>2</sub> CB, is transferred back to either the oxidized dye fragment or the oxidized form of the electrolyte, such as I<sub>2</sub><sup>−</sup>. In this case, the general expression is simplified to:

$$k_{\{I\} \rightarrow F} = \frac{2\pi}{\hbar} \int |\langle F | H' | I \rangle|^2 \rho(E_I) dE_I \quad (2.65)$$

The approximations discussed above can be applied here as well. In particular, Maggio and Troisi<sup>152,153</sup> used an expression for the nonadiabatic ET rate from the CB of a semiconductor to an acceptor state, describing the recombination process as follows:

$$k_{\text{recombination}} = \int_{E_{\text{CB}} + eV}^{+\infty} d\varepsilon f(\varepsilon, \varepsilon_F) \cdot F(\varepsilon, \Delta E, \lambda) \cdot \Gamma(\varepsilon) \quad (2.66)$$

where  $f(\varepsilon, \varepsilon_F)$  is the Fermi–Dirac distribution function, parametrized by the quasi-Fermi energy  $\varepsilon_F$ ,  $V$  is the bias voltage, and  $F(\varepsilon, \Delta E, \lambda) = \langle \chi_i | \chi_f \rangle_T$  is the thermally averaged Franck–Condon integral between the initial  $|\chi_i\rangle$  and final  $|\chi_f\rangle$  nuclear wave functions. In the high-temperature harmonic approximation limit, the contribution of the nuclear wave functions can be expressed in terms of the energy difference between the initial and final electronic states,  $\Delta E$ , and the reorganization energy,  $\lambda$ :

$$F(\varepsilon, \Delta E, \lambda) = \frac{1}{\sqrt{4\pi\lambda k_B T}} \exp\left(-\frac{(\varepsilon + \Delta E + \lambda)^2}{4\lambda k_B T}\right) \quad (2.67)$$

The above expression is similar to that presented earlier in eq 2.58. The reciprocal electronic half-life  $\Gamma(\varepsilon)$ , encountered in eq 2.66, has been discussed earlier; see eq 2.60. The above approaches use vibronic wave functions, allowing one to incorporate the effects of the nuclear motions of the system, as well as the coupling with solvent vibrational modes. Such treatment is crucial, because it incorporates the exponential dependence of the ET rate on the donor–acceptor energy difference, introduced via the thermally averaged Franck–Condon factor, eq 2.67. This strong exponential dependence accounts for variations in the recombination rates observed experimentally under various conditions, ranging from 1 ps to 20 s, which are presented in later sections.

Finally, the fourth case of ET involves manifolds of both initial  $\{|I\rangle\}$  and final  $\{|F\rangle\}$  states (Figure 6d). An example of this situation is in a QD<sup>154</sup> or graphene<sup>155</sup>-sensitized TiO<sub>2</sub> system. The initial excitation promotes an electron to a range of

donor levels within a given energy window. The injection takes place from any of the closely lying states into the CB of the semiconductor. In this case, one needs to consider the densities of the states of both donor and acceptor moieties, as given in the general expression 2.52. A method for calculating the photocurrent between a QD and a semiconductor under light illumination has been developed by Dahnovsky,<sup>156</sup> who considered a Newns–Anderson-type Hamiltonian and employed nonequilibrium quantum correlation functions (Keldysh functions).

**2.3.2.2. Nonadiabatic ET in a Dissipative Environment: The Spin-Boson Hamiltonian.** As discussed in section 2.3.1, the interaction of the reactive and environmental degrees of freedom plays an important role in the dynamics of the adiabatic ET. It is thus reasonable to expect that interactions with environment are also important in the nonadiabatic ET reactions. As mentioned previously, the spin-boson Hamiltonian provides a useful framework to describe such interactions. The method was introduced by Coalson<sup>133,134</sup> who mapped the condensed matter spin-boson approach (hence the name) to spectroscopic problems. It has later been used by Makri,<sup>130,131</sup> Makarov,<sup>132</sup> Coalson,<sup>135,157</sup> Nitzan,<sup>137</sup> and Mak<sup>138</sup> in various contexts.

In a simple case, the spin-boson model includes two excited-state surfaces,  $V_1(x)$  and  $V_{-1}(x)$ , coupled radiatively to the ground state,  $V_g(x)$ , through the electronic transition dipole moment, representing a photoexcitation. The two excited states are coupled nonradiatively with each other via the nonadiabatic coupling,  $g(x)$ . Normally one state, say  $V_1(x)$ , interacts with the ground state more strongly than the other state. Hence, one can assume that this excited state is populated at the initial time. The main goal is then to track the relaxation dynamics of the populated state subject to coupling with the environmental fluctuations. Thus, the problem reduces to the two-state model with the Hamiltonian:

$$\hat{H}_e = \begin{pmatrix} \hat{h}_1 & \hat{g}(\hat{x}) \\ \hat{g}(\hat{x}) & \hat{h}_{-1} \end{pmatrix} \quad (2.68)$$

The wave function  $|\Psi\rangle$  is given by a two-component vector (spinor):

$$|\Psi\rangle = \begin{pmatrix} |\phi_1(x)\rangle \\ |\phi_{-1}(x)\rangle \end{pmatrix} \quad (2.69)$$

Here,  $\hat{h}_1$  and  $\hat{h}_{-1}$  are the Hamiltonians of the so-called zeroth order Born–Oppenheimer surfaces, defined as:

$$\hat{h}_i = \hat{T} + V_i(\hat{x}) \quad (2.70)$$

where  $\hat{T}$  is the kinetic energy operator.

The Hamiltonian, eq 2.68, and the wave function, eq 2.69, can be written in the equivalent form of the above-mentioned Newns–Anderson type:

$$\hat{H}_e = |1\rangle\hat{h}_1\langle 1| + |-1\rangle\hat{h}_{-1}\langle -1| + |1\rangle\hat{g}(\hat{x})\langle -1| + |-1\rangle\hat{g}(\hat{x})\langle 1| \quad (2.71)$$

with

$$|\Psi\rangle = |1\rangle|\phi_1(x)\rangle + |-1\rangle|\phi_{-1}(x)\rangle \quad (2.72)$$

where  $|\phi_i(x)\rangle$  are the spatial components of the nuclear wavepackets in each excited state,  $|i\rangle$ .

The basis states  $|i\rangle$  in this methodology are not necessarily distinct electronic states. They may represent the same electronic state, but different vibrational or, more generally, rotational–vibrational levels. This will result in a spin-boson model for the adiabatic ET, similar to that given by eq 2.43. The relevant physical picture then is represented by Raman scattering. In fact, this was the meaning of the basis states in the original papers of Coalson, when he developed the model. Because this Review is primarily focused on relaxation of electronic states (e.g., charge injection), it is convenient to associate  $|i\rangle$  with electronic levels.

To map eq 2.68 to the spin-boson Hamiltonian, the coupled PESs are assumed to be of the form of displaced harmonic oscillators. That is:

$$V_1(x) = \frac{1}{2}\omega^2\left(x + \frac{\delta}{2}\right)^2 \quad (2.73a)$$

$$V_{-1}(x) = \frac{1}{2}\omega^2\left(x - \frac{\delta}{2}\right)^2 + V_e \quad (2.73b)$$

where  $\omega$  is the oscillator frequency, which is assumed the same for each oscillator in the simplest case, while  $\delta$  and  $V_e$  are the displacements between the minima of the oscillators along the coordinate and energy axes, respectively. By simple algebraic transformation, the Hamiltonian eq 2.68 then can be cast into the form:

$$\hat{H}_e = \left(\hat{h}_0 + \frac{V_e}{2} + \frac{\omega^2\delta^2}{8}\right)I + \left(\frac{\omega^2\delta}{2}\hat{x} - \frac{V_e}{2}\right)\sigma_z + \hat{g}\cdot\sigma_x \quad (2.74)$$

where  $\hat{h}_0 = \hat{T} + (\omega^2\hat{x}^2/2)$  is the harmonic oscillator Hamiltonian,  $I$  is the identity matrix, and  $\sigma_z$  and  $\sigma_x$  are the Pauli spin matrices:

$$\sigma_z = \begin{pmatrix} 1 & 0 \\ 0 & -1 \end{pmatrix}, \quad \sigma_x = \begin{pmatrix} 0 & 1 \\ 1 & 0 \end{pmatrix} \quad (2.75)$$

The notation for the basis states  $|1\rangle$  and  $|-1\rangle$  introduced above is directly related to these operators, simply because  $\sigma_z|\pm 1\rangle = \pm 1|\pm 1\rangle$ .

Having defined the Hamiltonian operator, one is interested in the relaxation dynamics of the initial state, which for simplicity can be taken in the form  $|\Psi_i\rangle = |i\rangle|\phi_i(x)\rangle$ . One seeks to calculate the probability to find the system in a final state,  $|\Psi_f\rangle = |f\rangle|\phi_f(x)\rangle$ , after the system has evolved for some time  $t$  according to the Hamiltonian eq 2.74:

$$P(t) = \langle\Psi_f|\exp\left(-\frac{i}{\hbar}\hat{H}_e t\right)|\Psi_i\rangle \quad (2.76)$$

For Raman scattering,  $|i\rangle = |f\rangle$ , and eq 2.76 can be written explicitly as given by Coalson:

$$P(t) = \langle\phi_f(x)|\langle 1|\exp\left(-\frac{i}{\hbar}\hat{H}_e t\right)|1\rangle|\phi_i(x)\rangle \quad (2.77)$$

where we set  $|i\rangle = |1\rangle$  for definiteness, and the subscript of the spatial component refers to eigenstates of the harmonic oscillator. Although the solution of eq 2.77 can be obtained by the wave function propagation techniques discussed above, the integral encountered in eq 2.77 can be more efficiently evaluated using the spin-boson path-integral approach. The computational advantage of such formulation becomes more pronounced for higher-dimensional problems and when a



canonical averaging over initial conditions is desired. Below, we briefly outline the path-integral approach to evaluation of eq 2.77.

Equation 2.77 can be viewed as operator  $\langle 1 | \exp(-i/\hbar \hat{H}_e t) | 1 \rangle$  acting on and propagating the initial nuclear wave packet,  $|\varphi_i(x)\rangle$ , in time, with the final wave function projected on a particular eigenstate  $\langle \varphi_f(x) |$  of the harmonic oscillator. Thus, it is necessary to derive the action of the operator  $\langle 1 | \exp(-i/\hbar \hat{H}_e t) | 1 \rangle$ . The starting point is the composition law:

$$\begin{aligned} \langle s_N | \exp\left(-\frac{i}{\hbar} \hat{H}_e t\right) | s_0 \rangle \\ = \sum_{s_1=\pm 1} \dots \sum_{s_{N-1}=\pm 1} \langle s_N | \exp\left(-\frac{i}{\hbar} \hat{H}_e \varepsilon\right) | s_{N-1} \rangle \dots \langle s_1 | \\ \exp\left(-\frac{i}{\hbar} \hat{H}_e \varepsilon\right) | s_0 \rangle \end{aligned} \quad (2.78)$$

where  $|s_i\rangle \in \{|1\rangle, |-1\rangle\}$ ,  $i = 1 \dots N-1$ , and  $\sigma_z |s_i\rangle = s_i |s_i\rangle$ ,  $\varepsilon = (t/N)$ .

After a number of transformations, it can be reduced to the form:

$$\begin{aligned} \langle s_N | \exp\left(-\frac{i}{\hbar} \hat{H}_e t\right) | s_0 \rangle \\ = \exp\left(-\frac{it}{\hbar} \left[ \frac{V_e}{2} + \frac{m\omega^2 \delta^2}{8} \right]\right) \sum_{s_1=\pm 1} \dots \\ \sum_{s_{N-1}=\pm 1} W_C \exp\left(\frac{iV_e \varepsilon}{2\hbar} \sum_{j=0}^{N-1} s_j\right) \hat{U}_C \end{aligned} \quad (2.79)$$

where  $W_C$  is a weight that depends on the spin configuration  $C = (s_0, \dots, s_N)$  and is given by:

$$W_C = \prod_{j=1}^N F_{s_{j-1}, s_j} \quad (2.80)$$

$$F_{s_{j-1}, s_j} = \begin{cases} \cos(\varepsilon g / \hbar), & s_{j-1} = s_j \\ -i \sin(\varepsilon g / \hbar), & s_{j-1} = -s_j \end{cases} \quad (2.81)$$

Along with eqs 2.80 and 2.81, the exponential factor  $\exp((iV_e \varepsilon / 2\hbar) \sum_{j=0}^{N-1} s_j)$  determines the contribution of the spin configuration (path) to the overall time evolution. It depends on the “total spin”  $\sum_{j=0}^{N-1} s_j$ . Finally, the only part of the reduced operator, eq 2.79, affecting the spatial component of the wave function is operator  $\hat{U}_C$ . It has the meaning of the time-evolution operator for the linearly driven harmonic oscillator:

$$V_C(x) = \frac{m\omega^2 x^2}{2} + f(C)x \quad (2.82)$$

The subscript C in eq 2.82 implies that the potential is modulated by instantaneous pulses, as parametrized by the spin path C. An example of the spin path is presented in Figure 7.

The propagation of the wave-packets due to operator  $\hat{U}_C$ , followed by the computation of the overlap  $\langle \varphi_f(x) | \hat{U}_C | \varphi_i(x) \rangle$ , can be accomplished analytically as detailed by Coalson.<sup>134</sup> The full relaxation dynamics (Raman time kernel), eq 2.77, can be computed as

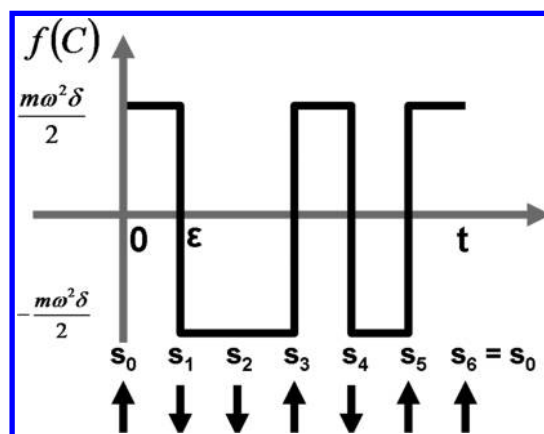


**Figure 7.** Pulse function parametrized by the spin path  $C = \{s_0, s_2, \dots, s_6\}$  of size  $N = 6$ .

$$\begin{aligned} P(t) = \exp\left(-\frac{it}{\hbar} \left[ \frac{V_e}{2} + \frac{m\omega^2 \delta^2}{8} \right]\right) \sum_{s_1=\pm 1} \dots \\ \sum_{s_{N-1}=\pm 1} W_C \exp\left(\frac{iV_e \varepsilon}{2\hbar} \sum_{j=0}^{N-1} s_j\right) \langle \varphi_f(x) | \hat{U}_C | \varphi_i(x) \rangle \end{aligned} \quad (2.83)$$

The spin-boson approach has been extended and widely used by many other authors, for example, Garg et al.<sup>123</sup> One of the important conclusions derived in studying such models is that the bath modes, represented by oscillators, act on the ET subsystem as an external observer, resulting in a so-called “watched pot effect” also known as the quantum Zeno effect.<sup>158,159</sup> The higher is the frequency of the external bath, the higher is the frequency of the observations, which lower the probability of escaping from a given electronic state, resulting in slower ET.

**2.3.2.3. Beyond Fermi’s Golden Rule: Nonequilibrium Green’s Functions (NEGF).** Various methods discussed above are based on Fermi’s golden rule, which originates from the first-order perturbation theory. Only processes that effectively involve one particle (electron, photon, phonon) can be described with such a level of theory reasonably well. However, when a process involves more than one particle, or when electron correlation effects are important, the first-order theory is not valid in general. Such multiparticle processes include multiple exciton generation,<sup>160–162</sup> singlet fission,<sup>18,163–166</sup> photoinduced current in molecular junctions and nanowires,<sup>156,167,168</sup> etc. Luckily, the machinery for accurate treatment of correlation effects and many-body interactions has been developed in the physics community<sup>169</sup> and is known as the nonequilibrium Green’s function (NEGF) technique, or equivalently, many-body perturbation theory (MBPT).

Ideologically, the NEGF approach is equivalent to solving the TD-SE with an arbitrary Hamiltonian, which can include many-body interaction terms. Practically, NEGF is computed using the many-body Green’s function evaluated using one-particle Green’s functions. The approach allows one to make use of advanced techniques, such as Feynman diagrams.

Formally, the NEGF can be defined as a solution of the following equation:

$$\left(\hat{H} - i\hbar \frac{\partial}{\partial t}\right) \hat{G}(r, t, r', t') = -i\hbar \delta(t - t') \delta(r - r') \quad (2.84)$$

with

$$\hat{H}_e = \hat{H}_0 + \hat{H}_{\text{int}} \quad (2.85)$$

In other words, the NEGF has a meaning of the kernel of the time-evolution operator of the TD-SE:

$$|\Psi(r, t)\rangle = \int_0^t dt' \int_{-\infty}^{\infty} dr' \hat{G}(r, t, r', t') |\Psi(r', t')\rangle \quad (2.86)$$

The solution  $\hat{G}(r, t, r', t')$  of eq 2.84 is not unique in general and can be defined in a variety of ways, for example:

$$\hat{G}(r, t, r', t') = -\frac{i}{\hbar} \langle T_t \{ \hat{\psi}_H(r, t) \hat{\psi}_H^\dagger(r', t') \} \rangle \quad (2.87)$$

where  $\langle \cdot \rangle$  denotes averaging over the initial state  $\text{Tr}(\hat{\rho})/\text{Tr}(\hat{\rho})$ ,  $\hat{\psi}_H(r, t)$  and  $\hat{\psi}_H^\dagger(r, t)$  are the field operators (creation and annihilation, respectively) in the Heisenberg representation, and  $T_t$  is the time-ordering operator. Turning from the Heisenberg representation to the interaction picture, the above definition can be expressed as:

$$\hat{G}(r, t, r', t') = -\frac{i}{\hbar} \langle T_t \{ \hat{S} \hat{\psi}_I(r, t) \hat{\psi}_I^\dagger(r', t') \} \rangle \quad (2.88)$$

where  $\hat{S}$  is the operator including the interactions and external perturbations:

$$\hat{S} = \exp\left(-\frac{i}{\hbar} \int dt \hat{H}_{\text{int}} t\right) \quad (2.89)$$

If the interactions are turned off,  $\hat{H}_{\text{int}} = 0$ , eq 2.89 reduces to the definition of the noninteracting Green's function:

$$\hat{G}_0(r, t, r', t') = -\frac{i}{\hbar} \langle T_t \{ \hat{\psi}_I(r, t) \hat{\psi}_I^\dagger(r', t') \} \rangle \quad (2.90)$$

The advantage of Green's function approach over other methods is that the many-body Green's function, eq 2.88, can be expressed in terms of the noninteracting Green's functions, eq 2.90. This way, the many-body interaction terms such as electron–electron, electron–hole, or hole–hole can be accurately taken into account. The importance of taking such correlated dynamics into account was shown by Dakhnovsky's group,<sup>168</sup> using the photoinduced ET in QD solar cells as an example. The QD–substrate system subject to the electric field of light was described by the following Hamiltonian:

$$\begin{aligned} \hat{H} = & \sum_{k \in S} \epsilon_k^S |k\rangle \langle k| + \sum_{k \in \text{QD}} \epsilon_n^{\text{QD}} |n\rangle \langle n| \\ & + \sum_{\substack{k \in S \\ n \in \text{QD}}} V_{kn} |k\rangle \langle n| + V_{nk} |n\rangle \langle k| + \vec{E}(t) \cdot \vec{d}_{nm} \sum_{n \neq m} |n\rangle \langle m| \end{aligned} \quad (2.91)$$

Under such conditions, Green's function evolves according to the Kadanoff–Baym equations for the two-time NEGF. An important feature of such equations is the presence of the non-Markovian term, which accounts for the electron–electron correlation between the QD and the semiconductor substrate. Comparison of solutions of the Kadanoff–Baym equations and their analogues simplified to the Markovian level showed that the injection currents predicted by the more rigorous treatment

were an order of magnitude smaller than those obtained with the Markovian approximation. As a consequence, the approximations, where all processes are considered uncorrelated and described by rate or relaxation constants, significantly overestimate the theoretical efficiency of the solar cell devices. Green's function for the diagonal in time elements of the NEGF (i.e.,  $t_1 = t_2 = t$ ) reduces to the time-dependent density matrix. In the limit when the NEGF is a slowly varying function of both time arguments, the Kadanoff–Baym equations reduce to the master equation for the density matrix. Approaches based on Markovian dynamics of the density matrix, where the correlation effects are neglected, were successfully used by D. Kilin<sup>170,171</sup> and Pimachev.<sup>172</sup>

To conclude this section, we should note that, in addition to Fermi's golden rule and other types of analytical models discussed above, there exist a number of explicit simulation methods that can treat multiple reaction channels simultaneously and on an equal footing. These techniques can properly treat the competition between electron injection, electron–vibrational relaxation, transitions between different spin states (intersystem crossings), electron delocalization into bulk semiconductor, electron–hole recombination, and so on. They employ explicit models for the system Hamiltonian, and solve the TD-SE using either an exact quantum-mechanical treatment or quantum-classical and semiclassical approximations. While these approaches are more expensive than reaction-rate expressions, they are able to provide atomistic details, capture various dynamic regimes (e.g., Gaussian, exponential, and power law), incorporate light–matter interactions and coupling to the environment, include the effect of nuclear motions, etc. Theoretical techniques of this type are reviewed in section 2.4.

**2.3.3. Direct Injection Mechanism.** Direct photoinduced ET was observed experimentally, for instance, in the catechol/TiO<sub>2</sub> system over a decade ago.<sup>173</sup> Recently, such processes were studied more closely experimentally<sup>174</sup> and theoretically<sup>148,174</sup> for catechol-based sensitizers adsorbed on a TiO<sub>2</sub> substrate, as well as experimentally using the antocyanin dye.<sup>175</sup> Recent TD-DFT calculations supported the direct electron-injection mechanism in catechol- and cresol-sensitized TiO<sub>2</sub>.<sup>176</sup> It was found that the injection proceeded via photoactivated electron pumping from the dye-donor state to the TiO<sub>2</sub>-acceptor states. The rate constant for the direct ET was found to be of the second-order with respect to the electric field magnitude. A theoretical description of direct ET requires explicit construction of the system Hamiltonian and solution of the resulting TD-SE, as discussed in section 2.1.

## 2.4. Nonadiabatic Molecular Dynamics

The ET rate constants, derived from the transition state theory and Fermi's golden rule, taken at different levels of approximation, greatly accelerate computations needed for the screening of various materials. Such approaches usually focus on a single process, for example, solely electron injection or electron recombination. In reality, many concurrent processes proceed in parallel and are affected by various external conditions, such as the interaction with a laser field or the environment. A successful description of competing processes requires an explicit solution of the TD-SE. A variety of methods for solving the TD-SE have been developed, including exact techniques, as well as approximations at various levels of accuracy. This section describes some of the most

popular approaches. A more detailed discussion can be found in specialized reviews.<sup>177–183</sup>

The TD-SE is typically solved in two steps after the separation of the electronic and nuclear degrees of freedom. First, a solution of the electronic problem for fixed nuclear coordinates is found, and then the nuclear wave function is propagated on the electronic potential energy. The hierarchies of such approximations and the methodologies for solving the electronic problem have been presented in section 2.1. This section focuses on the methods used to solve the nuclear part of the TD-SE:

$$i\hbar \frac{\partial \tilde{\chi}_i(t, R(t))}{\partial t} = \sum_j \left\{ (T_{\text{nuc}} + E_j(R)) \delta_{ij} - \hbar^2 \frac{d_{ij}^{(1)}}{M} \nabla - \hbar^2 \frac{d_{ij}^{(2)}}{2M} \right\} \tilde{\chi}_j(t, R(t)) \quad (2.92)$$

The nuclear problem is significantly more challenging than the electronic problem for a number of reasons. For one, typically a system contains a variety of nuclei, each with different properties such as mass and speed, while all electrons are identical. Therefore, for instance, one can design a density functional for electrons and apply it to a broad range of systems, while each type of vibration (nucleus) would require its own functional. Because of the universality of the electronic problem, as well as the fact that one needs to solve the electronic problem first to provide a potential energy surface for the nuclear problem, the electronic structure theory is a significantly more advanced field than nuclear quantum dynamics.

The exact solution of the nuclear TD-SE 2.92 can be obtained numerically on a grid, but only for systems with small dimensions. The FFT technique<sup>184</sup> and Trotter factorization of the evolution operator<sup>185,186</sup> are routinely used for this purpose. As the dimensionality of the problem increases, such approaches become impractical, requiring alternative methodologies and approximations. A semiclassical approximation simplifies eq 2.92 to:

$$i\hbar \frac{\partial \tilde{\chi}_i(t, R(t))}{\partial t} = \sum_j \left\{ E_j(R) \delta_{ij} - i\hbar \frac{p}{M} d_{ij}^{(1)} \right\} \tilde{\chi}_j(t, R(t)) \quad (2.93)$$

as shown in section 2.1, for example, eq 2.23.

A more general form of the above equation, including multiple electronic states, can be written as:

$$i\hbar \frac{\partial \tilde{\chi}_i(t, R(t))}{\partial t} = \sum_j H_{ij}(t, R(t)) \tilde{\chi}_j(t, R(t)) \quad (2.94)$$

A Hamiltonian of the Newns–Anderson type:

$$\hat{H} = \sum_{i,j} |\tilde{\chi}_i(t, R(t))\rangle H_{ij}(t, R(t)) \langle \tilde{\chi}_j(t, R(t))| \quad (2.95)$$

leads to the simple expression:

$$i\hbar \frac{\partial \tilde{\chi}(t, R(t))}{\partial t} = \hat{H} \tilde{\chi}(t, R(t)) \quad (2.96)$$

where the nuclear wave functions associated with different electronic states form a vector:

$$|\tilde{\chi}(t, R(t))\rangle = (|\tilde{\chi}_1(t, R(t))\rangle |\tilde{\chi}_2(t, R(t))\rangle \dots)^T \quad (2.97)$$

The time-dependent populations of the electronic energy levels are given by the squares of the nuclear wave functions  $|\tilde{\chi}_i(t, R(t))|^2$ . The matrix elements of the Hamiltonian  $H_{ij}(t, R(t))$  can be expressed either in the diabatic (noninteracting, reactant/product) representation,  $V_{ij}(t, R(t))$ , or in the adiabatic (interacting, electronic eigenstate) representation  $\{E_i(t, R(t)), d_{ij}^{(1)}(t, R(t))\}$  presented above. In addition, the Hamiltonian matrix elements can include the interaction of the system with an external laser or sun-light electromagnetic field,<sup>25,147,148,156,187–189</sup>  $H_{ij} \rightarrow H_{ij} + A(t)\mu_{ij}$ , or describe spin–orbit coupling,<sup>187</sup> allowing electronic transitions between states of different electronic multiplicity  $H_{ij} \rightarrow H_{ij} + H_{ij}^{\text{SO}}$ .

The Hamiltonian can be constructed to facilitate the description of the vibrational degrees of freedom and the system–environment interaction. For example, in the simplest case of two diabatic electronic states,  $|\phi_1\rangle$  and  $|\phi_2\rangle$ , with energies  $V_1$  and  $V_2$  and coupling  $V_{1,2} = V_{2,1}$ , the Hamiltonian can be represented as:<sup>190,191</sup>

$$\hat{H} = |\phi_1\rangle V_1 \langle \phi_1| + |\phi_2\rangle V_2 \langle \phi_2| + |\phi_1\rangle V_{1,2} \langle \phi_2| + |\phi_2\rangle V_{2,1} \langle \phi_1| + \hat{H}_B + \hat{H}_{\text{SB}} \quad (2.98)$$

where the bath (environment) Hamiltonian  $H_B$  is represented by an ensemble of harmonic oscillators, eq 2.99, linearly coupled to the system via  $H_{\text{SB}}$ , eq 2.100:

$$H_B = \frac{1}{2} \sum_j (p_j^2 + \omega_j^2 x_j^2) \quad (2.99)$$

$$H_{\text{SB}} = |\phi_1\rangle \sum_j c_j^1 x_j \langle \phi_1| + |\phi_2\rangle \sum_j c_j^2 x_j \langle \phi_2| \quad (2.100)$$

The positions and momenta (mass-weighted) of bath modes are represented by  $(x_j, p_j)$ , and  $c_j^i$  is the coupling constant between the  $j$ th bath mode and the  $i$ th electronic state. To describe the electronic–vibrational couplings, the diabatic potential energy surfaces  $V_i$  and the couplings  $V_{ij}$  are expanded in nuclear coordinates (normal modes, reaction coordinates, etc.):

$$V_i(\{Q_l\}) = \varepsilon_i + \sum_l k_l^i Q_l + \frac{1}{2} \sum_l \Omega_l^2 Q_l^2 \quad (2.101a)$$

$$V_{i,j}(\{Q_l\}) = \varepsilon_{i,j} + \sum_l k_l^{i,j} Q_l + \sum_{l,k} \gamma_{l,k}^{i,j} Q_l Q_k \quad (2.101b)$$

where  $\varepsilon_i$  is the vertical transition energy for the diabatic state  $|\phi_i\rangle$ .

The Hamiltonian can also include the Coulombic interaction terms, such as those used by Dahnovsky<sup>156</sup> in the description of the QD–semiconductor charge transfer:

$$\hat{H}_{\text{Coul}} = \frac{1}{2} \sum_{n_1, n_2, n_3, n_4} V_{n_1, n_2, n_3, n_4}^{(0)} a_{n_1}^+ a_{n_2}^+ a_{n_3} a_{n_4} \quad (2.102)$$

where  $V_{n_1, n_2, n_3, n_4}^{(0)}$  is the Coulomb integral, and  $a_i^+$  and  $a_i$  are the creation and annihilation operators, respectively.

The harmonic approximation used in the expansions 2.101 is adequate in most cases. Often, it is sufficient to keep only the diagonal quadratic terms in the expansion of the diabatic potential energy surfaces, while the general expansion, including nondiagonal terms, may be more advantageous for



electronic coupling elements. Alternatively, the diabatic coupling matrix elements are assumed to be independent of the nuclear coordinates.

It is straightforward to generalize the model given by eq 2.98 to a larger number of electronic states.<sup>192–194</sup> Consider the generalization needed for modeling electron injection from a dye-excited state into the quasi-continuum of CB states in a semiconductor. In such a case, one electronic wave function in eq 2.98 corresponds to the electron donor,  $|\varphi_1\rangle \rightarrow |\varphi_d\rangle$ , while the other wave function is replaced with a set of acceptor states,  $|\varphi_2\rangle \rightarrow \{|\varphi_{a,k}\rangle\}$ . The parameters of the model Hamiltonian can be related to experimental data, leading to semiempirical Hamiltonians,<sup>195</sup> or obtained by a rigorous quantum-mechanical treatment.<sup>24,196,197</sup>

In semiclassical and mixed quantum-classical approaches, the nuclear wave function in eq 2.94,  $\tilde{\chi}_i(t;R(t))$ , is approximated by a function with several parameters that define the nuclear configuration. These parameters can include classical-like positions and coordinates of the nuclei, as well as quantum variables, such as wavepacket width, phase, etc. The populations of the electronic levels become parametrically dependent on the nuclear configuration. For instance, in a quantum-classical approximation, classical nuclei create an external field that enters the Hamiltonian of quantum electrons. In turn, the electronic evolution may influence the nuclear degrees of freedom. The correct treatment of this influence, known as the quantum back-reaction problem, has been the subject of numerous studies.<sup>145,183,198–201</sup> The following section discusses various approximations for the quantum back-reaction.

**2.4.1. Surface Hopping and Related Quantum-Classical Methods.** Typically, a fully quantum-mechanical description of a system takes advantage of electron–nuclear separation (see section 2.1), and associates an independent nuclear wave function to each electronic state, for example, eq 2.9 or 2.95. The branching of the overall nuclear wave function into wave-packets, correlated with different electronic states, is a quantum-mechanical phenomenon. Surface hopping approaches are used to mimic this branching using a classical trajectory.

**2.4.1.1. Fewest-Switches Surface Hopping.** The fewest-switches surface hopping (FSSH) method is currently the most popular quantum-classical approach to nonadiabatic dynamics. Developed by Tully<sup>75</sup> and later extended and analyzed by a number of authors,<sup>202</sup> FSSH assigns a probability for the transition from the current electronic state  $|i\rangle$  to a new state  $|j\rangle$  during a sufficiently small time-interval  $\Delta t$ :

$$g_{i \rightarrow j}(t) = \max(0, P_{i \rightarrow j}(t)) \quad (2.103)$$

where

$$P_{i \rightarrow j}(t) = 2 \frac{\int_t^{t+\Delta t} \text{Re} \left( c_i^*(t') c_j(t') \frac{\bar{P}}{M} \vec{d}_{ij}(t') \right) dt'}{c_i^*(t) c_i(t)} \\ \approx 2 \frac{\text{Re} \left( c_i^*(t) c_j(t) \frac{\bar{P}}{M} \vec{d}_{ij}(t) \right) \Delta t}{c_i^*(t) c_i(t)} \quad (2.104)$$

The coefficients  $c_i(t)$  are obtained by solving the TD-SE, eq 2.93 or 2.96, with  $c_i(t) \equiv |\tilde{\chi}_i(t;R(t))\rangle$ . The probabilities, eq 2.103, are then compared to a uniformly distributed random number to determine if the system should remain in the current electronic state, or if it should move (hop) to a new state. After

a transition, the nuclear velocities are rescaled to conserve the total electron–nuclear, quantum-classical energy. If such rescaling is not possible, the transition is rejected. More details of the derivation and implementation of the algorithm can be found elsewhere.<sup>75,202,203</sup> It has been shown that the rejected (also called frustrated) hops are particularly important for the correct description of quantum-classical equilibrium.<sup>204,205</sup>

**2.4.1.2. The Classical Path Approximation.** The classical path approximation (CPA) provides a particularly simple solution to the quantum back-reaction problem, that is, the influence of the electronic evolution on the classical nuclei. CPA assumes that the classical trajectory is independent of electronic dynamics, while the electronic dynamics still depends on the classical coordinates. CPA is valid if the energy of the nuclei is sufficiently greater than that of the electrons, such that the electron–nuclear energy exchange does not affect the nuclear evolution appreciably. CPA is also valid if the potential energy surfaces that are associated with different electronic states differ only slightly, as compared to the amplitude of the thermal fluctuations in the nuclear coordinates, for instance.

Used in the context of FSSH, CPA greatly reduces computational expense, while still maintaining quantum-classical equilibrium.<sup>22</sup> Because statistically relevant FSSH calculations require a large number of trajectories, involving different realizations of the stochastic surface hopping process, the calculations are relatively expensive, particularly for large system. However, if electronic state surfaces differ little from each other, which is often the case in large systems, the trajectory of the classical subsystem can be assumed to be known a priori.<sup>206</sup> In this case, the trajectory is precomputed only once, and a large number of stochastic surface hops is obtained along the trajectory, significantly increasing the calculation speed, and thus allowing for the application to be feasible in larger system sizes or for those with longer time-scales.<sup>74,207,208</sup> To represent the hop-rejection of the original FSSH, the transition probabilities  $g_{i \rightarrow j}(t)$ , eq 2.103, are rescaled by the Boltzmann factor, taking into account the detailed balance:

$$g_{i \rightarrow j}(t) \rightarrow g_{i \rightarrow j}(t) b_{i \rightarrow j}(t) \quad (2.105)$$

$$b_{i \rightarrow j}(t) = \begin{cases} \exp\left(-\frac{E_j - E_i}{k_B T}\right), & E_j > E_i \\ 1, & E_j \leq E_i \end{cases} \quad (2.106)$$

**2.4.1.3. The Ehrenfest (Mean-Field) Method.** The Ehrenfest, or mean-field approach, is an alternative formulation of nonadiabatic molecular dynamics, in which the evolution of a quantum-classical system occurs self-consistently on an average potential energy surface.<sup>177,178,183,206,209</sup> In this method, the nuclei move on the average electronic potential energy surface, according to the force:

$$\vec{F}_{\text{mf}} = \sum_i |c_i|^2 \vec{F}_i + \sum_{i,j} c_i^* c_j (E_i - E_j) \vec{d}_{ij}^{(1)} \quad (2.107)$$

which is computed on the basis of the contribution of each state,  $|c_i|^2$ , to the time-dependent electronic wave function. The following expression:

$$\vec{F}_i = -\langle i | \frac{\partial V}{\partial R} | i \rangle \quad (2.108)$$

gives the force corresponding to the adiabatic electronic state  $|i\rangle$ . The nonadiabatic coupling is defined in eq 2.22a. The trajectories generated in the Ehrenfest dynamics are fully deterministic and continuous. There are no stochastic hops between energy surfaces.

The Ehrenfest method can be reformulated by mapping the quantum variables into the fully classical Hamiltonian equations of motion. This equivalency has been shown by McCurdy and Miller,<sup>210</sup> and generalized later by Meyer and Miller<sup>211,212</sup> and by Stock and Thoss.<sup>192,193</sup> The conjugate classical variables, such as positions,  $\{q_i\}$ , and momenta,  $\{n_i\}$ , or, equivalently, the action-angle variables, are related to the electronic state coefficients,  $\{c_i\}$ :

$$c_i(t) = \sqrt{n_i(t)} \exp(-iq_i(t)) \quad (2.109)$$

Representation of the wave function  $|\psi\rangle$  in the diabatic or adiabatic basis  $\{|i\rangle\}$ :

$$|\psi\rangle = \sum_i c_i(t) |i\rangle \quad (2.110)$$

leads to the following expression for the expectation value of the electronic Hamiltonian:

$$\begin{aligned} H_{\text{el}} &= \langle \psi | \hat{H}_{\text{el}} | \psi \rangle = \sum_{i,j} c_i^* c_j H_{ij} \\ &= \sum_{i,j} \sqrt{n_i n_j} \exp(-i[q_i - q_j]) H_{ij} \end{aligned} \quad (2.111)$$

The evolution of the electronic degrees of freedom represented by the conjugate variables  $\{q_i\}$  and  $\{n_i\}$  is obtained from the resulting (mean-field) Hamiltonian function, eq 2.111, using the classical-mechanical Hamiltonian equations of motion:

$$\dot{q}_i = \frac{\partial H_{\text{el}}}{\partial n_i} \quad (2.112)$$

$$\dot{n}_i = -\frac{\partial H_{\text{el}}}{\partial q_i} \quad (2.113)$$

The resulting equations are equivalent to the TD-SE 2.93. The specific choice of the conjugate variables, eq 2.109, used in the original work of Meyer and Miller, is not unique, and the variables may be chosen quite arbitrarily,<sup>186</sup> depending on the representation of the potential.

The Ehrenfest method has been used successfully in many applications,<sup>209,213,214</sup> although it is limited in scope. In particular, the method is only valid in regions where the coupling is relatively strong, so that the weights of different electronic states are comparable to one other. Under such conditions, surface hopping can produce frequent surface hops between coupled potential energy surfaces, and therefore would effectively be similar to the mean-field treatment.

Despite the presence of a convenient continuous and Hamiltonian formulation, the Ehrenfest method has serious limitations,<sup>46</sup> namely, its inability to collapse onto pure states, that is, eigenfunctions of the Hamiltonian.<sup>215</sup> For example, after an interaction event, the wave function continues to exist in a mixture of pure states, even in regions with negligible coupling between states. As a result, the classical trajectory evolves on an unphysical potential energy surface. In addition, it has been shown that Ehrenfest dynamics is unable to achieve thermal equilibrium in mixed quantum-classical systems.<sup>204,205,216,217</sup> In particular, it misrepresents energy flow from the electronic to

the nuclear subsystem, and violates the principle of detailed balance.

**2.4.1.4. Bohmian Quantum-Classical Dynamics.** The Bohmian formulation of quantum mechanics provides an alternative solution to the quantum back-reaction problem. Using the polar representation of the wave function  $|\psi(x)\rangle = (\rho(x))^{1/2} \exp[iS(x)/\hbar]$ , one can express the expectation value of the electronic Hamiltonian in the following form:

$$\begin{aligned} H_{\text{el}} &= \int dx^3 \Psi^*(x) \left[ -\frac{\hbar^2}{2m} \nabla_x^2 + V(x; R) \right] \Psi(x) \\ &= \int dx^3 \rho(x) \left[ \frac{(\nabla_x S(x))^2}{2m} + Q(x) + V(x; R) \right] \end{aligned} \quad (2.114)$$

where  $Q(x)$  is the “quantum potential”:

$$Q(x) = -\frac{\hbar^2}{2m} \frac{\nabla_x^2 \sqrt{\rho(x)}}{\sqrt{\rho(x)}} \quad (2.115)$$

Because  $\rho(x)$  is the quantum-mechanical probability density, the mean-field force, which is expressed as:

$$F_{\text{mf}} = -\nabla_R H_{\text{el}} = -\nabla_R \int dx^3 \rho(x) V(x; R) \quad (2.116)$$

can be interpreted in a statistical sense. In particular, one can sample “Bohmian particles” representing the electron from the probability distribution  $\rho(x)$ , and compute the force on the classical nuclei for each member of the Bohmian ensemble:

$$F_x = -\nabla_R V(x; R) \quad (2.117)$$

Note that in contrast to eqs 2.107 and 2.116, the force given by eq 2.117 depends explicitly on the coordinates of the quantum Bohmian particle,  $x$ . The Bohmian quantum-classical approach can also be derived starting from a fully quantum description, and, neglecting the components of the quantum potential, eq 2.115, be explicitly dependent on the nuclear degrees of freedom.<sup>218</sup> Neglecting the quantum potential for all coordinates results in the Hamilton–Jacobi (hydrodynamic) formulation of classical mechanics.

Similarly to FSSH, the Bohmian quantum-classical approach generates an ensemble of nuclear trajectories for each electronic wave function, thereby providing asymptotically distinct nuclear motions associated with different states of the electron. The Bohmian quantum-classical evolution conserves energy only in the ensemble sense, potentially causing numerical instabilities at the level of individual evolutions.

**2.4.1.5. Combinations of Ehrenfest and Surface Hopping Methods.** The FSSH and Ehrenfest methods constitute the two most basic approaches to nonadiabatic molecular dynamics, each with their own advantages and weaknesses. Ehrenfest quantum-classical dynamics can be rigorously derived and provides a continuous and self-consistent treatment of both electronic and nuclear degrees of freedom. At the same time, it excludes the correlation of nuclear trajectories with individual electronic states, and, in the long-time limit, mistreats energy flow from the classical to the quantum subsystem. FSSH is designed to generate different trajectories for each distinct electronic state and, to a high degree of accuracy, describes the quantum-classical equilibrium and energy exchange. However, FSSH is a model that can be justified but not derived from the basic quantum-mechanical equations.

A number of groups have proposed hybrid approaches, combining the advantageous features of both the FSSH and the Ehrenfest methods. Webster and Rossky developed a stationary phase surface hopping,<sup>219,220</sup> eliminating the instantaneous hop approximation and generating smooth surface switching. The latter was achieved with the method of Pechukas,<sup>221,222</sup> which is analogous to the Ehrenfest method but uses different boundary conditions. Coker<sup>223</sup> showed that in the short-time limit, surface switching according to the Pechukas method reduces to the nuclear velocity rescaling of FSSH.

Motivated by the fact that the Ehrenfest approach can be derived rigorously<sup>198,224–229</sup> and has well-established limits of validity,<sup>226,227</sup> Prezhdo and Rossky<sup>200</sup> proposed a method of carrying out Ehrenfest dynamics in the regions where it is valid, and performing FSSH when the Ehrenfest approximation breaks down. The discontinuities of FSSH were addressed further in Truhlar's continuous surface switching (CSS) method.<sup>178,230</sup> According to this formulation, the effective Ehrenfest Hamiltonian eq 2.111 is replaced with a more general expression:

$$H_{\text{el}}^{\text{MF}} = \sum_{i,j} c_i^* c_j H_{ij} \rightarrow H_{\text{el}}^{\text{CSS}} = \sum_{i,j} w_{ij}(c_i^* c_j) H_{ij} \quad (2.118)$$

where  $w_{ij}(\cdot)$  are smooth functions of the arguments, constructed to obey the asymptotic properties of the interaction model. The approach gives FSSH-type results in regions of weak coupling between the states and behaves similarly to the Ehrenfest method when the coupling is strong. The discontinuous surface hopping is substituted with a continuous surface switching. The method is self-consistent in the trajectory ensemble sense, as opposed to the single trajectory sense of the Ehrenfest method.

A combination of the mean-field (Ehrenfest) and surface hopping methods provides advantages if the system contains both discrete energy levels and quasi-continua of electronic states. This is often the case in interfacial ET (refer, for instance, to parts b and c of Figure 6). As pointed out by Sholl and Tully,<sup>202</sup> having infinitely many states can cause problems for surface hopping, while this situation allows for regular treatment with the mean-field approximation. Hence, one can apply the Ehrenfest method with the quasi-continuum of states and resort to surface hopping between the continuum and the discrete states. Such combination of the FSSH and Ehrenfest approaches was implemented in surface hopping with the excited Ehrenfest potential (SHEEP) method by Li and co-workers.<sup>231</sup> This allowed the authors to accelerate the calculations, while keeping the correct asymptotic behavior.

**2.4.1.6. Decoherence-Induced Surface Hopping.** A classical description of nuclei creates a number of approximations. In particular, the loss of quantum coherence within the electronic subsystem that is induced by the interaction with quantum-mechanical vibrational motions is completely absent in the Ehrenfest approach and is only partially included in FSSH. Loss of coherence is particularly rapid in condensed-phase systems, for instance, in the interfacial ET. The issue was raised by Bittner and Rossky,<sup>232,233</sup> who introduced a decoherence correction to FSSH. Prezhdo pointed out<sup>234</sup> that decoherence constitutes the physical mechanism for stochastic quantum transitions and nuclear trajectory branching that surface hopping was designed to achieve. A number of approaches to nonadiabatic molecular dynamics were followed based on the decoherence ideas.<sup>145,200,235–240</sup> These techniques are closely related to stochastic Schrödinger equations.<sup>200,241,242</sup>

Decoherence-induced surface hopping (DISH) is a particularly simple algorithm of the above type.<sup>243</sup> In DISH, decoherence events are stochastically identified, and trajectory surface hops occur during these events. Specifically, the DISH algorithm involves the following steps:

- (1) The electronic wave function and nuclear wave function are initialized.
- (2) Classical particles are propagated.
- (3) The electronic wave function is propagated using the TD-SE, eq 2.93 or 2.96.
- (4) The coherence interval,  $\tau_{\alpha}$  of each electronic state is evaluated as

$$\frac{1}{\tau_{\alpha}} = \sum_{i \neq \alpha} |c_i|^2 r_{\alpha i} \quad (2.119)$$

where  $|c_i|^2$  is the population of state  $i$ , and the pairwise decoherence rates,  $r_{\alpha i}$  can be evaluated using any number of available approaches, such as optical response theory, which is directly related to experimental observables.

- (5) Determine whether the current time is within the coherence interval for each state. If it is, the simulation returns to step 2; if not, steps 6 and 7 are performed.
- (6) Project out the decohered component of the wave function, and perform a surface hop.
- (7) Rescale the nuclear velocities to conserve the total electron–nuclear energy.

Simultaneously, the DISH algorithm provides an improvement over the Ehrenfest and FSSH methods, eliminates the need for ad hoc surface hopping prescriptions, and incorporated decoherence effects that are critical for condensed phase nonadiabatic dynamics.

**2.4.1.7. Quantum-Classical Liouville Equation.** Quantum and classical degrees of freedom are treated equally with the joint quantum-classical density matrix operator  $\hat{\rho}(t)$ . In quantum mechanics, the density matrix evolves according to the quantum Liouville equation:

$$\frac{\partial \hat{\rho}}{\partial t} = -\frac{i}{\hbar} [\hat{H}, \hat{\rho}] \quad (2.120)$$

As shown explicitly by Kisil and Prezhdo,<sup>199</sup> the  $\hbar \rightarrow 0$  limit taken with respect to the nuclear degrees of freedom produces a quantum-classical bracket, which is a combination of the quantum commutator,  $[\cdot, \cdot]$ , and the classical Poisson bracket,  $\{\cdot, \cdot\}$ :

$$i\hat{L} \cdot = \frac{i}{\hbar} [\hat{H}_W, \cdot] - \frac{1}{2} (\{\hat{H}_W, \cdot\} - \{\cdot, \hat{H}_W\}) \quad (2.121)$$

The resulting quantum-classical Liouville equation:

$$\frac{\partial}{\partial t} \hat{\rho}_W(X, t) = -i\hat{L} \hat{\rho}_W(X, t) \quad (2.122)$$

was extensively explored by Kapral and Ciccotti<sup>244,201,245</sup> in modeling nonadiabatic dynamics. The partial Wigner transform of the density matrix operator is  $\hat{\rho}_W(X, t)$ . This quantity itself is a quantum operator, which depends on the classical degrees of freedom  $X = \begin{pmatrix} R^{3N} \\ P^{3N} \end{pmatrix}$ . The partial Wigner transform of the total Hamiltonian is  $\hat{H}_W$ :



$$\hat{H}_W(R, P) = \frac{P^2}{2M} + \frac{\hat{p}^2}{2m} + \hat{V}_W(\hat{q}, R) = \frac{P^2}{2M} + \hat{h}_W(R) \quad (2.123)$$

Equation 2.78 can be represented on the basis of the adiabatic states,  $\{|i; R\rangle\}$ , which are eigenstates of the quantum component of the total Hamiltonian 2.123:  $\hat{h}_W(R)|i; R\rangle = E_i(R)|i; R\rangle$ . The adiabatic state representation transforms eq 2.122 into

$$\frac{\partial}{\partial t} \rho_W^{ij}(X, t) = \sum_{k,l} -iL_{ijkl} \rho_W^{kl}(X, t) \quad (2.124)$$

where

$$-iL_{ijkl} = \left( -\frac{i}{\hbar} (E_i(R) - E_j(R)) - iL_{ij}^{\text{cl}} \right) \delta_{ik} \delta_{jl} + J_{ijkl} \quad (2.125)$$

$$iL_{ij}^{\text{cl}} = \frac{P}{M} \frac{\partial}{\partial R} + \frac{1}{2} (F_W^i + F_W^j) \frac{\partial}{\partial P} \quad (2.126)$$

$$J_{ijkl} = -\left( \frac{P}{M} d_{ik} + \frac{1}{2} (E_i - E_k) d_{ik} \frac{\partial}{\partial P} \right) \delta_{ik} - \left( \frac{P}{M} d_{jl}^* + \frac{1}{2} (E_j - E_l) d_{jl}^* \frac{\partial}{\partial P} \right) \delta_{jl} \quad (2.127)$$

The action of the operator  $(-i/\hbar)(E_i(R) - E_j(R)) - iL_{ij}^{\text{cl}} \delta_{ik} \delta_{jl}$  is equivalent to the adiabatic propagation of the nuclear (classical) degrees of freedom. The  $J_{ijkl}$  term allows nonadiabatic transitions. This operator is singular. It creates instantaneous jumps between adiabatic states having corresponding momentum rescaling to conserve the total energy of the quantum-classical system. The solution of the quantum-classical Liouville equation can be obtained in terms of the surface-hopping trajectories.<sup>201,245–248</sup> This fact illustrates the close relationship between the quantum-classical Liouville equation and Tully's surface hopping method.

This quantum-classical method has been extensively studied by Kapral and co-workers.<sup>247,249</sup> In particular, they considered a number of model systems, including the spin-boson, for which the quantum-classical Liouville equation gives an exact quantum solution. The technique was extended to account for the dissipation and decoherence of the quantum-classical system that was induced by coupling with the environment (bath).<sup>250,251</sup>

**2.4.2. Wave Function Propagation Methods.** The quantum-classical methods discussed in the previous section focus on the evolution of the electronic states in the presence of an external field that is created by classical nuclei. In some cases, for example, DISH, the quantum properties of the nuclei are introduced in the form of a semiclassical correction. Situations exist in which an explicit quantum-mechanical treatment of nuclei is required. Examples include the calculation of Franck–Condon factors for the optical absorption spectra that is involved in the electron photo-excitation and direct ET mechanism (section 2.2), evaluation of the fully quantum expressions for the ET rates, for example, eq 2.54, and modeling of coherent oscillations observed in the ET signals of ultrafast laser experiments. These goals can be achieved by explicit propagation of the nuclear wave function.

This section discusses the multiconfiguration time-dependent Hartree (MCTDH) method, full multiple spawning (FMS), and quantized Hamiltonian dynamics (QHD). These approaches are closely related to Gaussian wave packet

propagation techniques, which have been proposed and applied to various models and realistic systems to account for quantum effects in nuclear dynamics.<sup>252–266</sup> In addition, we consider a wave packet propagation technique, which appears in the context of the spin-boson Hamiltonian treatment of the system–bath interactions. The propagator is formally equivalent to the exact solution of the TD-SE, although technically its action is evaluated using a perturbation theory expansion, which can be truncated at a desired order.

**2.4.2.1. Multiconfiguration Time-Dependent Hartree Method.** The MCTDH method developed by Meyer and co-workers<sup>180,267,268</sup> is one of the most accurate wave function propagation techniques available. The methodology starts with the general eq 2.92, and uses a time-dependent single-particle expansion for the nuclear wave function:

$$\begin{aligned} |\tilde{\chi}_i(t, R_1, R_2, \dots, R_f)\rangle \\ = \sum_{j_1}^{n_1} \dots \sum_{j_f}^{n_f} A_{j_1 \dots j_f}^1(t) |\chi_{j_1}^1(t, R_1)\rangle \dots |\chi_{j_f}^1(t, R_f)\rangle \end{aligned} \quad (2.128)$$

Application of the variational principle to the TD-SE results in a system of equations for the propagation of both of the amplitudes of each configuration,  $A_{j_1 \dots j_f}^1(t)$ , and the single particle nuclear wave functions,  $\{|\chi_{j_k}^1(t, R_k)\rangle\}$ . The MCTDH approach imposes weak constraints on the form of allowed wave functions that are associated with the discrete value representation of the matrix elements involved in the calculations.

The MCTDH method has been extended to the self-consistent hybrid construction,<sup>190,269</sup> in which part of the system is treated quantum-mechanically, while its surroundings are described at a lower level of theory to accomplish an increased computational speed. The boundary between the high- and low-level subsystems can be adapted to test convergence and to achieve high numerical accuracy in an efficient manner.

MCTDH provides an exact quantum description of nuclear dynamics. For this reason, it is computationally expensive. The complexity of the calculations scales as  $N^f$ , where  $N$  is the number of primitive basis functions per degree of freedom, and  $f$  is the total number of degrees of freedom. The method is limited to systems composed of 20–60 nuclear coordinates.<sup>270,271</sup> The computational limitations of the original MCTDH approach have been improved in the multilayer MCTDH (ML-MCTDH) technique.<sup>272–274</sup> This method considers a smaller number of collective coordinates  $R_k^{\text{coll},1} = \{R_{1,p} \dots R_{d_k,p}\}$ ,  $1 < k < p$ , where  $p$  is the number of collective coordinates, and  $d_k$  is the number of regular coordinates combined in the  $k$ th collective mode:

$$\begin{aligned} |\tilde{\chi}_i(t, R_1, R_2, \dots, R_f)\rangle \\ = \sum_{j_1}^{n_1} \dots \sum_{j_p}^{n_p} A_{j_1 \dots j_p}^1(t) |\chi_{j_1}^1(t, R_1^{\text{coll},1})\rangle \dots |\chi_{j_p}^1(t, R_p^{\text{coll},1})\rangle \end{aligned} \quad (2.129)$$

The dimension of the vector of amplitudes is reduced from  $\prod_{k=1}^f n_k \approx N^f$  to  $\prod_{k=1}^p n_k \approx N'^p$ , at the expense of having to use many-particle basis wave functions,  $\{|\chi_{j_k}^1(t, R_k^{\text{coll},1})\rangle\}$ , instead of the single-particle basis functions,  $\{|\chi_{j_k}^1(t, R_k)\rangle\}$ . The many-

particle functions can be represented in terms of basis functions of smaller dimensionality  $\{|\chi_{j_k}^2(t, R_k^{\text{coll},2})\rangle\}$ :

$$|\chi_i^1(t, R_k^{\text{coll},1})\rangle = \sum_{j_1}^{n_1} \dots \sum_{j_{p'}}^{n_{p'}} A_{j_1 \dots j_{p'}}^2(t) |\chi_{j_1}^2(t, R_k^{\text{coll},2})\rangle \dots |\chi_{j_{p'}}^2(t, R_{p'}^{\text{coll},2})\rangle \quad (2.130)$$

The procedure can be repeated as many times as necessary, resulting in a layered structure of equations of motion. The layered hierarchy of the nuclear wave function decomposition leads to significant improvement in the performance of the algorithm, due to the fact that the exponent in the scaling law is moved down to the base. ML-MCTDH can be applied to systems with several thousands of degrees of freedom.<sup>274,275</sup>

**2.4.2.2. Multiple Spawning.** A somewhat similar methodology, known as full multiple spawning (FMS), has been developed by Ben-Nun and Martinez.<sup>179,276–279</sup> The goal of FMS is to account for the divergence of nuclear wave-packets, eliminating the need to propagate the diverged branches simultaneously. The nuclear wave function is represented as a superposition of the time-dependent multidimensional Gaussian wave-packets:

$$|\tilde{\chi}_i(t, R^f)\rangle = \sum_j A_{ij}(t) |\tilde{\chi}_{ij}(R^f; R_{ij}^f(t), P_{ij}^f(t), \gamma_{ij}(t), \alpha_{ij}^f)\rangle \quad (2.131)$$

Each multidimensional Gaussian is represented as the product of the corresponding one-dimensional Gaussians:

$$|\tilde{\chi}_{ij}(R^f; R_{ij}^f(t), P_{ij}^f(t), \gamma_{ij}(t), \alpha_{ij}^f)\rangle = \exp(i\gamma_{ij}(t)) \prod_{k=1}^f |G(R_k; R_{k,ij}(t), P_{k,ij}(t), \alpha_{k,ij})\rangle \quad (2.132)$$

$$|G(R_k; R_{k,ij}(t), P_{k,ij}(t), \alpha_{k,ij})\rangle = \left(\frac{2\alpha_{k,ij}}{\pi}\right)^{1/4} \exp[-\alpha_{k,ij}(R_k - R_{k,ij}(t))^2 + iP_{k,ij}(t)(R_k - R_{k,ij}(t))] \quad (2.133)$$

Here,  $|\tilde{\chi}_i(t, R_f)\rangle$  is the nuclear function for the  $i$ th electronic state.  $|\tilde{\chi}_{ij}(R^f; R_{ij}^f(t), P_{ij}^f(t), \gamma_{ij}(t), \alpha_{ij}^f)\rangle$  is the  $j$ th nuclear basis function in the expansion of the full nuclear wave function for  $i$ th electronic state. The collection of all  $f$  degrees of freedom is denoted by the  $f$ -dimensional coordinate,  $R^f$ . The  $f$ -dimensional positions, momenta, and widths of the  $j$ th multidimensional basis function for the  $i$ th electronic state are represented by  $R_{ij}^f(t)$ ,  $P_{ij}^f(t)$ , and  $\alpha_{ij}^f$ , respectively; the  $k$ th component of such vectors are  $R_{k,ij}(t)$ ,  $P_{k,ij}(t)$ , and  $\alpha_{k,ij}$ . The nuclear basis functions are made time-dependent through the explicit time-dependence of the parameters  $R_{ij}^f(t)$ ,  $P_{ij}^f(t)$ , and  $\gamma_{ij}(t)$ . The widths,  $\alpha_{ij}^f$ , are time-independent, and the phase factors,  $\gamma_{ij}(t)$ , are assumed to be the same for all nuclear basis functions for a given electronic potential energy surface. In contrast to MCTDH and related methods, which rely entirely on a quantum-mechanical description of the nuclear wave functions, the time evolution of the nuclear wave function in FMS is governed by the classical dynamics of the time-dependent wave function parameters. This description is

semiclassical in nature, as opposed to the exact description adopted in MCTDH.

Adaptive change of the basis size along the nuclear trajectory constitutes one of the most important distinguishing features of FMS. When the parent nuclear wave function traveling on the  $i$ th electronic potential energy surface enters a region of strong nonadiabatic coupling with the  $j$ th potential energy surface, as determined by certain criteria,<sup>276</sup> new basis functions are spawned on the  $j$ th surface. The algorithm accounts for wave function branching and accurately describes scattering probabilities and state populations. The dynamics proceeds until the next coupling event, at which point additional wave functions can be spawned. This process continues until the desired convergence is reached. Recently, this algorithm has been optimized to decrease the number of spawned functions needed to reach the desired accuracy, allowing for more efficient computations.<sup>280</sup>

Propagation of a wave function composed of traveling Gaussian basis functions is the main signature of FMS. The Gaussian wave packet representation of the nuclear wave function is among the most widely used approximations. The Gaussian wave packet was introduced in the chemistry community by Heller, who studied Gaussian dynamics in various potentials.<sup>181,228,281–283</sup> The exact quantum nuclear wave function can be obtained by expansion in the time-dependent Gaussian basis,<sup>283</sup> similarly to the construction used in the FMS and MCTDH methods. Gaussians with time-independent width parameters, used in FMS, are known as frozen Gaussians.<sup>282</sup> An alternative approximation, where the Gaussian width is allowed to vary with time, is known as thawed Gaussians.<sup>181</sup> Thawed Gaussians introduce additional flexibility in the description of the nuclear wave function.

**2.4.2.3. Quantized Hamilton Dynamics.** The parameters of the nuclear basis functions in the FMS, thawed, and frozen Gaussians methods evolve by the classical Hamiltonian equations of motion. Therefore, these methods are classified as semiclassical, and, in principle, cannot fully account for quantum effects. MCTDH and related methods are fully quantum mechanical and do account for all quantum nuclear effects; however, they are significantly more complex and computationally expensive. An alternative way to fully account for quantum effects in nuclear dynamics was introduced by Prezhdo and co-workers,<sup>182,284–286</sup> in the method known as quantized-Hamiltonian dynamics (QHD).

QHD formulation starts with a rigorous quantum-mechanical result, the Heisenberg equations of motion, which describe the time evolution of the expectation values of observables represented by the operators  $\hat{A}$ :

$$i\hbar \frac{d\langle \hat{A} \rangle}{dt} = \langle [\hat{A}, \hat{H}] \rangle \quad (2.134)$$

Once the Hamiltonian describing the system is defined, one can substitute the general operator  $\hat{A}$  with a particular operator of interest, such as position,  $\hat{q}$ , momentum,  $\hat{p}$ , spin, electronic state population, nuclear kinetic energy, quantum force, etc., and obtain an equation of motion for the corresponding expectation value. The quantum mechanical average  $\langle \rangle$  can be represented as a time-dependent superposition of basis states, similar to those used in the methods discussed above. Equation 2.134 can be used to obtain exact results and to derive Gaussian approximations, including frozen and thawed Gaussians.<sup>287,288</sup>

Eliminating the need for propagating a wave function, eq 2.134 provides a starting point for a hierarchy of equations for

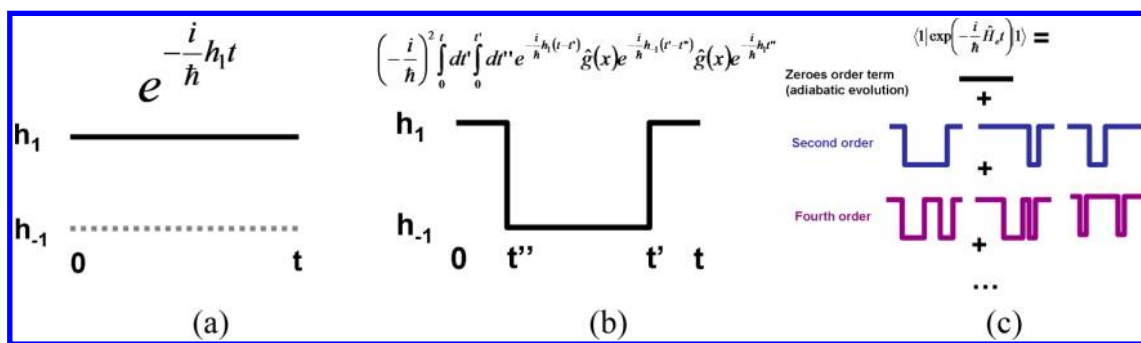


**Figure 8.** Schematic representation of various terms in the PT expansion of operator, eq 2.145: (a) zeroth-order term, corresponding to adiabatic propagation of the system in state  $|1\rangle$ ; (b) second-order term, where two hops are allowed such that the wave packet starts and ends in state  $|1\rangle$ ; and (c) PT expansion of operator, eq 2.145, in terms of the zeroth-, second-, and fourth-order spin paths.

various observables, defined as expectation values of corresponding operators. Approximations are obtained by closures of the hierarchy. The QHD hierarchy for the moments and cumulants of the position and momentum operators,  $\langle \hat{q}_i^n \hat{p}_j^m \rangle$ , can be achieved using a Taylor expansion of the potential energy:<sup>285,287,289,290</sup>

$$V^{(n)}(\hat{q}) = \sum_{k=0}^N \frac{1}{k!} V^{(n+k)}(\langle \hat{q} \rangle) (\hat{q} - \langle \hat{q} \rangle)^k + O((\hat{q} - \langle \hat{q} \rangle)^{k+1}) \quad (2.135)$$

Alternatively, one can use generalized dynamical variables, such as  $\langle V^{(n)} \rangle$  or  $\langle \hat{q}_i^m V^{(n)} \hat{p}_i^k \rangle$ , avoiding approximations introduced by the Taylor series expansion.<sup>288</sup>

The dynamics obtained from the Heisenberg eq 2.134 in lower order QHDs can be mapped to the purely classical formulation<sup>287</sup> with the effective Hamiltonian:

$$H = \frac{p^2}{2m} + \frac{p_s^2}{2m} + \frac{\hbar^2}{8ms_q^2} + V(q) + \frac{1}{2}V^{(2)}(q)s_q^2 + \frac{1}{8}V^{(4)}(q)s_q^4 \quad (2.136)$$

involving the classical-like coordinate and momentum:

$$q = \langle \hat{q} \rangle \quad (2.137)$$

$$p = \langle \hat{p} \rangle \quad (2.138)$$

the width variable:

$$s_q = \sqrt{\langle \hat{q}^2 \rangle - \langle \hat{q} \rangle^2} \quad (2.139)$$

and its conjugate momentum:

$$p_s = \frac{\langle \langle \hat{p} \hat{q} \rangle_s \rangle - \langle \hat{p} \rangle \langle \hat{q} \rangle}{s_q} \quad (2.140)$$

Variables 2.139 and 2.140 capture quantum mechanical zero-point energy. The equations of motion for the mapped variables follow directly from the Hamiltonian equations of motion:

$$\frac{dq}{dt} = \frac{\partial H}{\partial p} = \frac{p}{m} \quad (2.141)$$

$$\frac{dp}{dt} = -\frac{\partial H}{\partial q} = -V^{(1)}(q) - \frac{1}{2}V^{(3)}(q)s_q^2 - \frac{1}{8}V^{(5)}(q)s_q^4 \quad (2.142)$$

$$\frac{ds_q}{dt} = \frac{\partial H}{\partial p_s} = \frac{p_s}{m} \quad (2.143)$$

$$\frac{dp_s}{dt} = -\frac{\partial H}{\partial s_q} = \frac{\hbar^2}{4ms_q^3} - V^{(2)}(q)s_q - \frac{1}{2}V^{(4)}(q)s_q^3 \quad (2.144)$$

Coupling of the QHD description of nuclear motion with the electronic wave function results in the quantized Ehrenfest<sup>291</sup> and related<sup>292,293</sup> approaches.

**2.4.2.4. Perturbation Theory (PT).** In the context of the spin-boson model, solved with the path-integral method, one needs to evaluate the action of the following operator, for example, see eq 2.77:

$$\langle 1 | \exp\left(-\frac{i}{\hbar} \hat{H}_e t\right) | 1 \rangle \quad (2.145)$$

The operator is discussed in the current section, because it acts on nuclear wave functions. Following the original work of Coalson,<sup>133</sup> we outline how perturbation theory (PT) can be used to construct a wave packet propagation technique. The starting point of such an approach is a Hamiltonian factorization:

$$\hat{H}_e = \hat{H}_0 + \hat{H}_{\text{int}} \quad (2.146a)$$

$$\hat{H}_0 = |1\rangle \hat{h}_1 \langle 1| + |-1\rangle \hat{h}_{-1} \langle -1| \quad (2.146b)$$

$$\hat{H}_{\text{int}} = |1\rangle \hat{g}(\hat{x}) \langle -1| + |-1\rangle \hat{g}(\hat{x}) \langle 1| \quad (2.146c)$$

The operator  $\exp(-(i/\hbar)\hat{H}_e t)$  then can be computed in the interaction representation:

$$\hat{H}_I = e^{i/\hbar \hat{H}_0 t} \hat{H}_{\text{int}} e^{-i/\hbar \hat{H}_0 t} \quad (2.147)$$

as

$$\begin{aligned} \exp\left(-\frac{i}{\hbar} \hat{H}_e t\right) &= \exp\left(-\frac{i}{\hbar} \hat{H}_0 t\right) T \left[ \exp\left(-\frac{i}{\hbar} \int_0^t \hat{H}_I dt'\right) \right] \\ &= \exp\left(-\frac{i}{\hbar} \hat{H}_0 t\right) \left[ 1 - \frac{i}{\hbar} \int_0^t \hat{H}_I dt' + \left(-\frac{i}{\hbar}\right)^2 \right. \\ &\quad \left. \int_0^t \hat{H}_I(t') dt' \int_0^{t'} \hat{H}_I(t'') dt'' + \dots \right] \end{aligned} \quad (2.148)$$

where  $T[\cdot]$  is a time-ordering operation.

Using eq 2.146b and the fact that:



$$\exp\left(-\frac{i}{\hbar}\hat{H}_0t\right) = \exp\left(-\frac{i}{\hbar}\hat{h}_1t\right)|1\rangle\langle 1| + \exp\left(-\frac{i}{\hbar}\hat{h}_{-1}t\right)|-1\rangle\langle -1| \quad (2.149)$$

the interaction Hamiltonian eq 2.147 can be written as:

$$\hat{H}_I = e^{i/\hbar h_1 t} \hat{g}(x) e^{-i/\hbar h_{-1} t} |1\rangle\langle -1| + e^{i/\hbar h_{-1} t} \hat{g}(x) e^{-i/\hbar h_1 t} |-1\rangle\langle 1| \quad (2.150)$$

Using eq 2.150 and the perturbation series expansion, eq 2.148, the reduced propagator  $\langle 1|\exp(-i/\hbar\hat{H}_e t)|1\rangle$  can be evaluated:

$$\begin{aligned} \langle 1|\exp\left(-\frac{i}{\hbar}\hat{H}_e t\right)|1\rangle &= e^{-i/\hbar h_1 t} + \left(-\frac{i}{\hbar}\right)^2 \int_0^t dt' \int_0^{t'} dt'' e^{-i/\hbar h_1(t-t')} \hat{g}(x) e^{-i/\hbar h_{-1}(t'-t'')} \hat{g}(x) e^{-i/\hbar h_1 t''} \\ &+ O(g^4) \end{aligned} \quad (2.151)$$

The result, eq 2.151, can be extended to include higher-order terms as well as finite temperatures. However, we want to focus on the physical interpretation of this result, as it directly leads to a prescription for computing excited-state relaxation dynamics (including Raman scattering processes originally targeted by Coalson<sup>33</sup>).

We need to reiterate that eq 2.151 is a reduced operator, propagating the nuclear wave packet,  $|\varphi_i(x)\rangle$ , which depends on spatial coordinates. The propagation is represented schematically in Figure 8. The action of the first term is trivial; it simply evolves the wave packet,  $|\varphi_i(x)\rangle$ , on a single Born–Oppenheimer surface, state  $|1\rangle$ , for the whole duration of time,  $t$  (Figure 8a). The action of the second term can be described as the following sequence of operations (Figure 8b):

- propagation in state  $|1\rangle$  for time  $t''$ ;
- instantaneous jump to surface  $|-1\rangle$ , with multiplication of the wave packet by the nonadiabatic coupling,  $g$ ;
- propagation in state  $|-1\rangle$  for time  $t' - t''$ ;
- jump from surface  $|-1\rangle$  back to surface  $|1\rangle$ , with multiplication by the nonadiabatic coupling,  $g$ ;
- propagation in state  $|1\rangle$  for time  $t - t'$ .

The double integral in the second term implies that the operations (a)–(e) should be performed for all possible combinations of the jump times. This notion directly relates the PT approach to the spin-boson method described in the previous section. In particular, truncating the PT expansion at the second order is equivalent to spin configurations (paths) with only one pulse (two switches between the surfaces, back and forth). Similarly, the fourth-order terms in the PT expansion correspond to spin paths with two pulses (Figure 8c), and so on.

Finally, it is worth relating the PT approach to Tully's FSSH method. The construction of the two methods is remarkably similar; both methods propagate the wave packet (or swarm of trajectories) on multiple surfaces. The difference stems from the treatment of the transitions; FSSH is aimed to minimize the number of the pulses, which corresponds to retaining only the leading terms in the expansion. Moreover, the switches in FSSH are performed stochastically based on the values of the nonadiabatic coupling (as well as coherences and state populations). This can be considered as importance sampling; only including those transitions (spin paths) for which nonadiabatic coupling is relatively large will notably contribute to the PT expansion or spin-boson path-integral terms. On the

contrary, in the direct PT expansion method, all possible spin paths (trajectories) are included even though their weight may be negligible because the nonadiabatic coupling is small. Because in the PT expansion one enumerates only those spin paths that contain a specific number of pulses, the computational complexity of the method can be minimized in comparison to the full, exhaustive enumeration used in the spin-boson PI method.

### 3. COMPOSITION OF THE PHOTOACTIVE MATERIALS

The properties and ultimate efficiency of photovoltaic and photochemical cells are dependent upon many factors, including the molecular structure of the carrier (semiconductor), the sensitizer (dye), the bonding geometry between the two, and the electronic structure of the combined system. The way in which the band levels of each component align with respect to each other and the magnitude of the coupling between the electronic states of the substrate and sensitizer are also critical. Additionally, the presence of solvents, impurities, defects, and dopants on the carrier surface (substrate) can have a significant impact on the overall efficiency of the device. In the current section, we will first focus on the molecular and electronic structure of the carrier (or substrate), as well as the effects of doping. Next, we will examine the molecular and electronic structures of various sensitizers. Finally, the overall properties of the combined sensitizer–substrate complex will be discussed and summarized.

#### 3.1. Molecular and Electronic Structure of the Substrate

Metal oxides are the most commonly used materials for the photoelectrodes in Grätzel-type photovoltaic cells and photocatalytic applications. Titanium dioxide ( $\text{TiO}_2$ ) is particularly popular<sup>1,7,16,294–299</sup> because of its relatively low cost and ease of manufacture.  $\text{TiO}_2$  exists predominantly in one of two major allomorphic forms, rutile (Figure 9a) and anatase (Figure 9b). The rutile form is more energetically stable due to its symmetry. In this crystal structure, each Ti atom has an octahedral O coordination, with each O in a trigonal-planar coordination with 3 neighboring Ti atoms. Other metal oxides, such as  $\text{SnO}_2$ ,  $\text{CrO}_2$ ,  $\text{NbO}_2$ ,  $\text{PbO}_2$ ,  $\text{WO}_2$ ,  $\text{TaO}_2$ , and  $\text{RuO}_2$ ,<sup>300</sup>

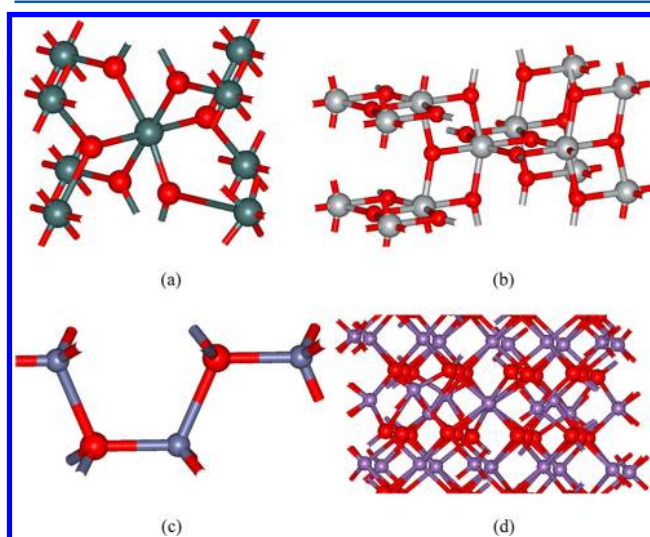


**Figure 9.** Oxide crystal structures: (a) rutile ( $\text{TiO}_2$ ,  $\text{SnO}_2$ ); (b) anatase ( $\text{TiO}_2$ ); (c) wurtzite ( $\text{ZnO}$ ); and (d) bixbyite ( $\text{Mn}_2\text{O}_3$ ,  $\text{In}_2\text{O}_3$ ).



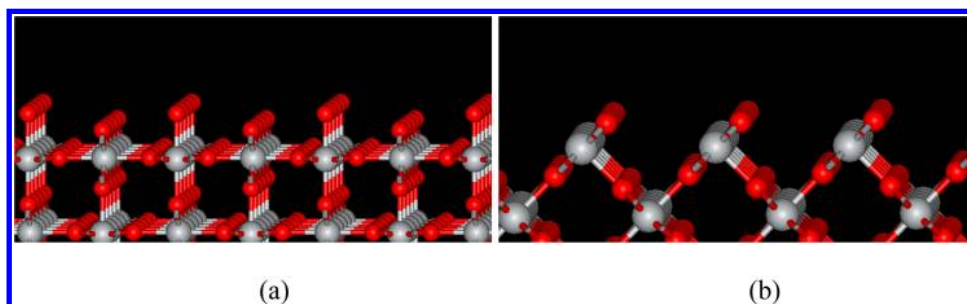


Figure 10. Rutile surfaces: (a) (110); (b) (100).

also adopt this rutile structure. The anatase structure exhibits the same coordination numbers but is less symmetrical.

The surface of a rutile crystal structure can show a variety of cleavage planes.<sup>36,300,301</sup> The most stable among them are the (110), (100), (011), and (001) surfaces, two of which are shown in Figure 10.

DFT calculations<sup>302</sup> indicate that the (110) surface has the smallest number of unpassivated bonds, and is therefore the most stable among all of the crystallographic planes of rutile TiO<sub>2</sub>. The relative energies of the surfaces are summarized in Table 1. The ideal surfaces relax to minimize the number of unsaturated valence bonds, leading to a significant reduction in the surface energy.

Table 1. Energies of Different Rutile TiO<sub>2</sub> Surfaces

surface	Ti surface coordination	O surface coordination	$E_{\text{surf}}$ (unrelaxed), meV/a.u. <sup>2</sup>	$E_{\text{surf}}$ (relaxed), meV/a.u. <sup>2</sup>
(110)	5,6	2,3	30.7	15.6
(100)	5	2	33.8	19.6
(011)	5	2,3	36.9	24.4
(001)	4	2	51.4	28.9

It should be noted that such reconstruction of the idealized surface exists only in ultrahigh vacuum conditions. In realistic systems, the surface of the metal oxide would most likely be saturated with adsorbed molecules such as water that exist naturally in air. When the coverage is small and dangling bonds are present, the adsorption is mostly reactive (chemisorption), leading to chemically modified surfaces<sup>301,303,304</sup> with saturated valences (no dangling bonds). Once most of the reactive sites of the ideal surface are occupied, the subsequent adsorption is relatively weak (physisorption).<sup>301</sup> For example, in recent ab initio MD simulations of water on TiO<sub>2</sub>(110) surfaces, it has been found that ~20% of water molecules dissociate, while the remaining are physisorbed (no dissociation).<sup>305</sup>

The near-surface vibrational modes of the rutile TiO<sub>2</sub>(110) surface have been characterized experimentally.<sup>306</sup> Phonons at 179, 191, 359, 440, 507, 609, and 823 cm<sup>-1</sup> have been attributed to the surface vibrations of the semiconductor.

The second most popular material for photovoltaic applications is ZnO.<sup>1,307–309</sup> Like TiO<sub>2</sub>, it exists in a variety of different crystal forms, with the wurtzite (Figure 9c) structure being the most stable. Each atom (Zn and O) has a tetragonal coordination. Among the binary oxides of the A<sub>2</sub>B<sub>3</sub> type, In<sub>2</sub>O<sub>3</sub> is most commonly used<sup>308–312</sup> due to its relatively small band gap.<sup>313</sup> In<sub>2</sub>O<sub>3</sub> crystallizes in the bixbyite structure, in which each O has tetragonal coordination with In atoms, and each In has octahedral coordination with O atoms (Figure 9d). This crystal structure is remarkable for its large unit cell, which

contains 40 atoms. Other popular binary oxides include SnO<sub>2</sub>,<sup>308,309,314–316</sup> Nb<sub>2</sub>O<sub>5</sub>,<sup>308,309,317</sup> WO<sub>3</sub>,<sup>309</sup> and Ta<sub>2</sub>O<sub>5</sub>.<sup>309</sup>

There are notable ternary phases among the complex oxides proposed for photochemical and photovoltaic applications, including SrTiO<sub>3</sub>,<sup>317</sup> InVO<sub>4</sub>,<sup>318</sup> BiVO<sub>4</sub>,<sup>297,319–322</sup> Pb<sub>3</sub>Nb<sub>4</sub>O<sub>13</sub>,<sup>323</sup> and BiPO<sub>4</sub>.<sup>324</sup> The perovskite structures of type ABB'O<sub>3</sub>, including Pb(Ti<sub>1-x</sub>Ni<sub>x</sub>)O<sub>3</sub>,<sup>325</sup> Pb(Zn<sub>1/3</sub>Nb<sub>2/3</sub>)O<sub>3</sub>, Pb(Mg<sub>1/3</sub>Nb<sub>2/3</sub>)O<sub>3</sub>,<sup>326</sup> Bi(Zn<sub>3/4</sub>W<sub>1/4</sub>)O<sub>3</sub>, and Bi(Zn<sub>3/4</sub>Mo<sub>1/4</sub>)O<sub>3</sub>,<sup>327</sup> have been proposed as potential candidates for optoelectronic and photocatalytic applications. For an extensive discussion of various complex oxide materials, we refer the reader to recent reviews.<sup>6,8</sup>

The oxides used in the photovoltaic applications are wide-band gap semiconductors, having a CB edge–VB edge gap ranging from 2 to 7 eV, as summarized in Table 2. The band

Table 2. Band Gaps of Selected Oxides, Obtained with Different Methods

material	band gap, eV
TiO <sub>2</sub> (rutile)	3.0, experiment <sup>330</sup>
TiO <sub>2</sub> (anatase)	3.2, experiment <sup>330</sup>
TiO <sub>2</sub> (rutile, 110)	1.99, theory <sup>328</sup> 2.6, experiment <sup>329</sup>
ZnO	3.3, theory <sup>331</sup> (more data available in this Review) 3.2, theory <sup>332</sup> 3.59, theory <sup>333</sup> (GW calculation, zinc blend) 3.4, theory <sup>313</sup> ("scissor-corrected" from 0.8)
SnO <sub>2</sub>	3.596, theory <sup>334</sup> 3.7, theory <sup>335</sup> 3.6, theory <sup>313</sup> ("scissor-corrected" from 0.7)
In <sub>2</sub> O <sub>3</sub>	3.7, theory <sup>313</sup> ("scissor-corrected" from 0.9) 1–1.5, theory <sup>336</sup> (LDA)
WO <sub>3</sub>	3.1, theory <sup>337</sup> (B3LYP)
Ta <sub>2</sub> O <sub>5</sub>	4.65, experiment <sup>338</sup>
Al <sub>2</sub> O <sub>3</sub>	6.95, experiment <sup>338</sup> 6.7 ± 0.2, experiment <sup>339</sup>
ZrO <sub>2</sub>	5.5, experiment <sup>338</sup> 5.6 ± 0.2, experiment <sup>339</sup> 5.65, experiment <sup>340</sup>
HfO <sub>2</sub>	5.7, experiment <sup>340</sup>
Y <sub>2</sub> O <sub>3</sub>	6.0 ± 0.05, experiment <sup>341</sup>

gap depends on the crystal structure (allotropy) of the material. For instance, the band gap of bulk rutile TiO<sub>2</sub> is 3.0 eV, while the TiO<sub>2</sub> anatase modification band gap is 3.2 eV (see Table 2). The band gap is usually smaller for surfaces than for bulk material. This can be attributed to two factors: the 3D translational invariance of the crystal structure is broken, which introduces new high-lying VB and low-lying CB surface states;

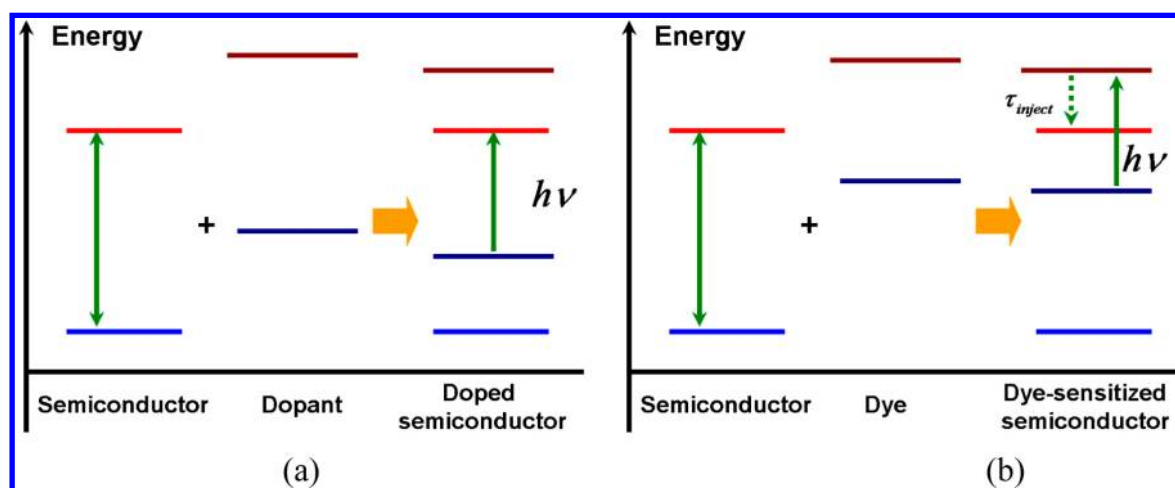


**Figure 11.** Photosensitization of the semiconductor: (a) with doping of the semiconductor material; and (b) by sensitizing the oxide with a chromophore (dye, QD, etc.).

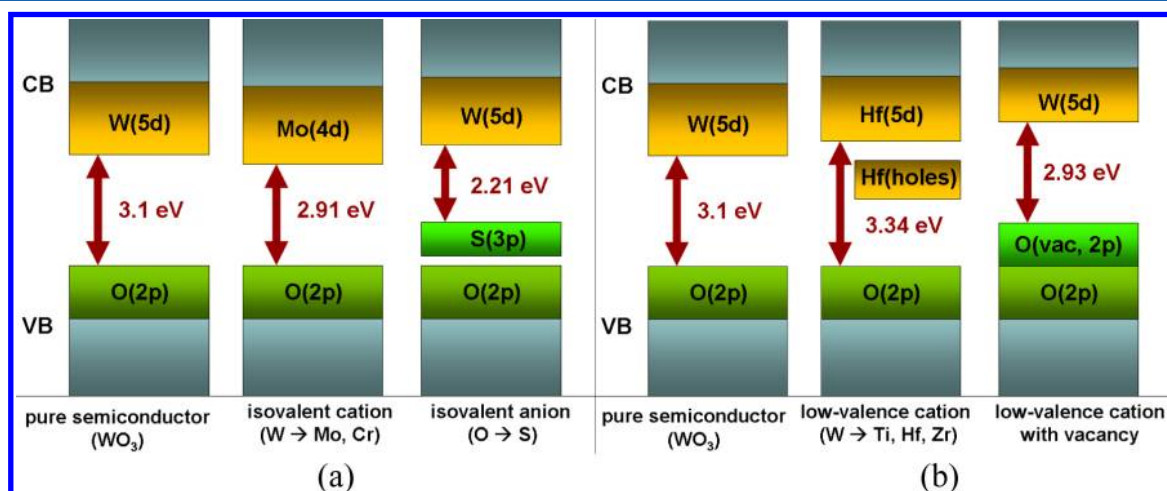


**Figure 12.** Energy diagrams for two cases of doping: (a) isovalent cation/anion substitution; and (b) doping with a low-valence cation, with and without vacancy formation.

second, the surface relaxation leads to different atomic structures, which introduces new states and reduces the overall band gap. For example, the rutile TiO<sub>2</sub>(110) surface band gap displays a range from 1.99 eV<sup>328</sup> to 2.6 eV.<sup>329</sup> Thus, the reported band gap values for the same material can often vary dramatically. The differences encountered in reported experimental results can be attributed to the level of purity of the material, as well as different ratios of the various allomorphic phases contained in the material. The variation between different theoretical results is due to the different levels of theory being used. For example, the band gap obtained with DFT methods is often significantly underestimated as compared to experimental values. This is a well-known limitation of pure DFT functionals originating from an improper description of electron self-interaction. The band gap is significantly larger in case of hybrid functionals or when it is calculated with many-body perturbation theory (GW).

With such wide band gaps the oxides presented in Table 2 are transparent to most of the photons in the visible spectrum. The energy difference between their CB and VB edges (band gap) corresponds to UV photons, which are efficiently absorbed by the ozone shell of the earth, and hence are not major energy carriers. For efficient operation, the material of

the photoelectrode in a photochemical/photovoltaic cell should be able to absorb the photons in the visible part of the solar spectrum. This can be accomplished through two major types of material (oxide) modifications: doping and sensitizing with various chromophores (Figure 11a and b, respectively). In some specific cases, though, an appropriate combination of the metal oxides can be used directly, an emerging area of the all-oxide photovoltaics.<sup>42</sup>

The objective of the two approaches is the same, to make the excitation energy (although not necessarily the band gap) of the resulting material comparable to the energy of visible light photons. The difference between two methods is how this objective is achieved. In the doped semiconductor (Figure 11a), the distance between the CB and the VB edges (HOMO/LUMO) of both the original material (oxide) and the dopant may both be large. However, they are normally shifted with respect to each other, so when the pure components are mixed, the band gap of the resulting material will be smaller than that of each individual component. Alternatively, in a dye (or QD)-sensitized semiconductor, the band gap is defined primarily by the nature of the dye (or QD). During the adsorption of the dye on the semiconductor surface, the orbitals of both components change slightly, but the band gap in the adsorbed

dye normally remains on the same order as it is in the pure molecular system (Figure 11b).

An important difference between these two approaches is the dynamics of the photogenerated electron. With semiconductor doping, an electron is directly promoted (injected) from the VB to CB of the doped semiconductor; no injection between “dye” and semiconductor is required (Figure 11a). In the case of sensitization with a chromophore, the electron is initially localized on the dye group and is later injected into the CB of the semiconductor. Except in rare cases of direct ET, the electron cannot be directly excited from the VB (HOMO) of the dye molecule to the CB of the semiconductor (Figure 11b).

### 3.2. Semiconductor Doping

Band gap engineering<sup>326,327,342</sup> is a promising route toward the production of photoactive semiconductors. This approach primarily uses semiconductor doping with various anion nonmetals (C, H, O, N, S, F, B),<sup>343–351</sup> cation-metals,<sup>337,352–355</sup> and cation-nonmetals (e.g., substitution of Ti with P).<sup>356–360</sup> This semiconductor doping introduces new intermediate states in the original band gap of the semiconductor, resulting in the reduction of the original band gap. Typically, the dopants used are the heavier isovalent cousins to one of the elements in original semiconductor composition. This ensures that the orbitals of the dopant atoms are generally of higher energy than that of analogous orbitals of the atom being substituted, which is important for the creation of new states in the band gap.

The doping can be more complicated than the simple case explained previously. In fact, to predict the particular outcome of a dopant, one needs to use the knowledge of the electronic structure of both the pure (undoped) and the doped materials.<sup>325,337,350,361,362</sup> To illustrate this point, we will use the example of the  $\text{WO}_3$  semiconductor, which has been studied recently with a DFT method.<sup>337</sup> The pure material has a band gap of 3.1 eV. The VB edge states are formed mostly by the 2p states of the O atoms, while the main contribution to the CB edge is from the 5d states of the W atoms. It is convenient to consider two possible cases of doping, substitution of either the cation or the anion with an isovalent ion (Figure 12a) or substitution of the cation with a lower-valence ion, with or without the creation of the nonmetal (oxygen) vacancy (Figure 12b).

In the first case, in which the ions are substituted with an isovalent species, predictions can be made on the basis of the size of the corresponding ions and the orbital energies of the elements involved. For example, to modify the energy of the VB edge, one could partially substitute O with S atoms. By doping  $\text{WO}_3$  with S, states are created in the original band gap because the 3p orbitals of S have a higher energy than the 2p orbitals of O, resulting in a substantially smaller band gap of 2.21 eV (Figure 12a). On the other hand, to modify the energy of the CB edge, one might partially substitute the metal atoms by doping the  $\text{WO}_3$  with Mo atoms. This lowers the energy of the CB edge because the energy of the 4d orbitals of Mo is lower than that of the 5d orbitals of W. This results in a slightly decreased band gap of 2.91 eV.

The size mismatch between native and dopant species has a significant impact on the band gap. For instance, when a W atom is substituted with the similarly sized Mo, the change of the lattice structure is minor. The symmetry of the lattice is not significantly altered, nor is there a creation of a large energy spread. On the contrary, when O atoms are substituted with the

significantly larger S atoms, the lattice structure is changed drastically. Such a large size mismatch breaks the crystal symmetry and creates many distinct states, which are distributed over a large interval of energies. As a result, the band gap decreases significantly, as opposed to the modest decrease in the case of Mo doping. It should be noted that in the case of S-doped ZnO, the band gap decreases because of the effects of the higher energy of S 3p orbitals, as well as the disorder in the lattice structure. In contrast, for the B-doped ZnO nanorods,<sup>363</sup> the decrease of the band gap (from 3.25 to 3.19 eV, measured experimentally) is attributed primarily to disorder effects, because the energy of the B 2p orbital is lower than that of the O 2p orbital. Introducing dopants or vacancies in the perovskite-type oxides ( $\text{ABO}_3$ ) can affect the band gap by relaxing the crystal structure to a geometry with a degree of tetragonality that leads to different metal–oxygen (vacancy) bonding interactions.<sup>325–327</sup>

The disorder induced by the ion-size mismatch has a significant impact on the number of states. The maximum is observed near 50% doping, corresponding to the largest number of states. This fact can be rationalized by statistical considerations. For example, the substitution of O atoms in ZnO with the Se atoms (12% Se) decreases the band gap to 2.05 eV,<sup>364</sup> which is ideal for a water splitting reaction. Raising the content of the Se dopant further facilitates the reduction of the band gap even more, to 1.63 eV (Figure 13).

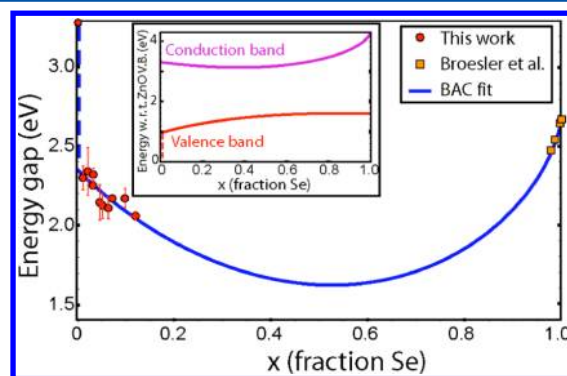


**Figure 13.** Dependence of the band gap of Se-doped ZnO as a function of the Se concentration. Reprinted with permission from ref 364. Copyright 2010 American Institute of Physics.

Considering the second case, in which doping involves substitution of metal ions with lower-valence cations (Figure 12b), the mismatch in the size of the cations plays a particularly important role in increasing the energy of the CB edge. Theoretical calculations<sup>337</sup> have been performed for a hypothetical case in which the doping does not involve the creation of an oxygen vacancy. This resulted in the appearance of hole (unoccupied) states in the metal ions. The band gap was controlled solely by the size of the dopant cation. The holes were compensated by oxygen vacancies, thereby leading to increased energy of the VB edge (Figure 12b) and to a decreased band gap. The special role of the size of cationic dopant with a lower valency than the substituted cation has been demonstrated experimentally in the case of Nd, Fe, and Pt-doped  $\text{TiO}_2$ . As the size-mismatch of the substituted cation grew, the photocatalytic activity of the doped material increased,<sup>352</sup> pointing to a lower band gap of the resulting material.



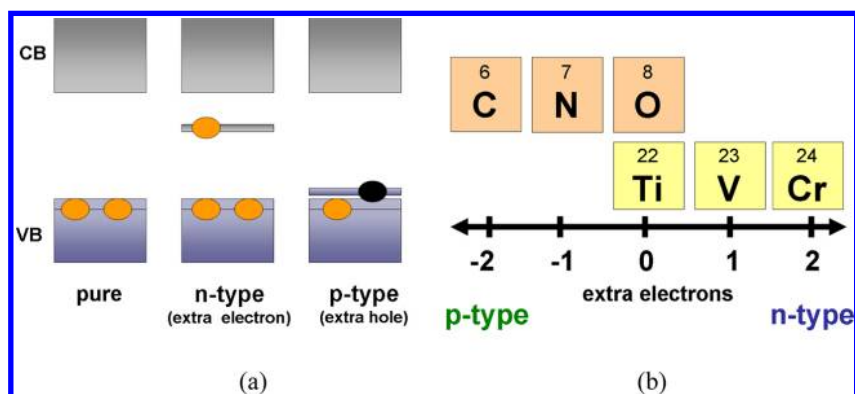


**Figure 14.** Illustration of doping classification. (a) Schematics of a pure semiconductor, a semiconductor that has been doped with an n-type dopant that creates an excess electron in the conduction band, and a semiconductor that has been doped with a p-type dopant that creates an excess hole in the valence band of pristine semiconductor. (b) Schematics demonstrating how codoping in  $\text{TiO}_2$  can be compensated or noncompensated leading to net n- or p-type doping.

In addition to doping semiconductors with heavier isovalent cousins to a native element, there is also p-type and n-type doping. The latter is achieved when a semiconductor is doped with a material that donates excess electrons; doping with a material that accepts excess electrons is an example of p-type doping. An illustration of these principles is given in Figure 14a. Just as with isovalent doping, n- and p-type doping are done to decrease the band gap, therefore reducing the energy threshold for photoactivation.

Substitution of the Ti sites of the  $\text{TiO}_2$  lattice with the metal cations, such as Cr and V, is an example of n-type doping (Figure 14b, positive direction). This process introduces donor levels within the  $\text{TiO}_2$  band gap. The n-type doping allows for the absorption of lower energy photons, extending the photocatalytic activity of  $\text{TiO}_2$  into the visible region of the solar spectrum. Unfortunately, both of the above examples result in localized d-states deep within the band gap of  $\text{TiO}_2$ . These localized states often act as recombination centers for the photoexcited electrons and holes.<sup>337,348,365,366</sup>

Replacement of oxygen atoms with nitrogen or carbon atoms in a  $\text{TiO}_2$  lattice (Figure 14b, negative direction) provides examples of p-type doping.<sup>348,367</sup> The acceptor states, introduced within the  $\text{TiO}_2$  band gap, are supported by p-orbitals of the dopant atoms, similarly to the deep, intrinsic donor levels of the semiconductor. Because of this fact, the newly created dopant states have sufficient overlap with the band states of  $\text{TiO}_2$ , minimizing the problems arising with the localized states in n-type doping. Nitrogen doping has been shown to increase light absorption of  $\text{TiO}_2$  to wavelengths above 500 nm, opening up the possibility of photocatalytic activity with visible light irradiation.<sup>348</sup> However, to increase the efficiency of a particular photocatalyst, it is necessary to do more than simply change the optical absorption. There are fundamental limitations on the thermodynamic solubility in substitutional doping of  $\text{TiO}_2$ . The solubility happens to be very low for most dopants, and it is especially low for p-type doping.<sup>368,369</sup> For example, an isolated interstitial N atom has to overcome a 2.34 eV energy barrier to become a substitutional dopant. Meanwhile, the energy barrier for the reverse process is only 0.51 eV. As a result, the dopants reside at undesirable interstitial sites, compromising the effectiveness of band gap reduction as well as providing recombination centers for the photogenerated electron–hole pair.<sup>369,370</sup>

To avoid the shortcomings of both p- and n-type doping of oxide semiconductors, the concept of n–p codoping has been proposed.<sup>370,371</sup> Coulombic attraction between n- and p-type dopants of opposite charge allows for substantial enhancement of both thermodynamic and kinetic solubilities in substitutional doping. Co-doping can be characterized as compensated and noncompensated. In compensated codoping, the n-type dopant donates as many donor states as the p-type dopant does acceptor states. In noncompensated codoping, the numbers of acceptor or donor states are not balanced, leading to a net n- or p-type doping. Figure 14b provides a demonstration of these scenarios. Zhu et al.<sup>370</sup> investigated doping bulk anatase  $\text{TiO}_2$  with four different n–p pairs: V–C (net p-type), Cr–N (net n-type), Cr–C (compensated), and V–N (compensated). It was found that the noncompensated pairs (V–C and Cr–N) were best at narrowing the intrinsic band gap. Because of strong hybridization, the levels created from noncompensated doping are substantially broader than the localized impurity levels contributed by adding an n- or p-type dopant alone.

Focusing on the noncompensated cases, the formation energies of systems with different configurations of dopants occupying interstitial or substitutional sites were compared. It was found that doping with V and C in substitutional sites was not energetically favorable. However, substitutional doping with Cr and N was favored in O-rich conditions. Furthermore, the final state for Cr–N codoping is about 0.71 eV lower than that for doping with N alone.<sup>370</sup> As a result, this codoping scheme enhances both the thermodynamic and the kinetic solubilities of the dopants in the host semiconductor. Recent theoretical studies have also proposed a “compensating” codoping of  $\text{TiO}_2$  by (C, 2H) and (N, H) as a way of avoiding localized band gap states, while simultaneously decreasing the band gap of the original semiconductor.<sup>366</sup>

An increase in the open-circuit voltage in a dye-sensitized solar cell (DSSC) is made possible by the fact that the energy of the CB edge of the semiconductor can be increased. For example, when the Ti atoms in porphyrin-sensitized  $\text{TiO}_2$  were partially (~5% mol) substituted by Nb, Ge, or Zr,<sup>353</sup> the power conversion efficiency increased by 20% (Ge), with respect to the pure  $\text{TiO}_2$  substrate, although this did not change the lattice structure of the  $\text{TiO}_2$  used in the experiment (anatase). Similar increases in power conversion efficiencies for DSSCs based on doped semiconductors have been reported for a number of other setups.<sup>344,348,372</sup>



To correctly describe the effects of the dopants on the positions of the VB and CB edges and the band gap, the appropriate theoretical methods must be employed. For instance, pure DFT functionals are not able to correctly predict the band gaps, while hybrid functionals are able to do so.<sup>325,337,360,373</sup> Other successful methods include the application of the on-site Coulomb correction to DFT (DFT + U)<sup>325,361,366,374</sup> and many-body perturbation theory (GW).<sup>325</sup>

Semiconductor doping is a powerful tool used to tune the properties of an oxide substrate for various applications, either photovoltaic or photocatalytic. However, as the composition of the altered material becomes more complex (e.g., going from binary oxides to ternary) and as the number of codopants increases, the number of possible combinations grows combinatorially. Recently, an experimental high-throughput screening technique based on inkjet printing was developed in the Parkinson group.<sup>8,375</sup> This approach helped to identify the best compositions for water oxidation in iron oxide Fe<sub>2</sub>O<sub>3</sub> doped with up to three different elements. However, because the number of possible types of dopants and oxides is very large, a similar search in our case would be prohibitively expensive and not feasible. Thus, novel and efficient theoretical methods for the screening and the rational design for these materials is one of the important directions to take in this field.

### 3.3. Molecular and Electronic Structure of Sensitizers

An alternative method to cause a wide band gap semiconductor to absorb light in the visible range of the solar spectrum is through various sensitization techniques. A photon excites an electron in a smaller cap chromophore, which is then injected into the semiconductor material. In contrast to semiconductor doping, where the dopant species are distributed in the crystal structure of the substrate material (via substitution or interstitially), the sensitization is achieved by attaching small-gap chromophores to the semiconductor surface. The working principle of such a construction is illustrated in Figure 11b. The sensitizer (chromophore) groups can be classified into several categories as follows:

- (a) metallo–organic sensitizers
- (b) organic molecular sensitizers
- (c) inorganic sensitizers – quantum dots (QD)
- (d) polymers and nanoscale carbon

In the following sections, we will briefly discuss each of these groups of sensitizers.

**3.3.1. Metallo–Organic Sensitizers.** Metallo–organic sensitizers are typically built with a transition metal center and organic ligands attached to it with N–M, O–M, S–M, and similar types of bonds (as opposed to direct C–M bonds, in case of organo–metallic compounds). A sensitizer of this type was one of the first classes of chromophores successfully used in DSSC applications.

The excited state of the metallo–organic sensitizer can be described as a charge transfer from the d orbitals of the metal atom to the  $\pi$ -system of the organic ligands,<sup>23</sup> also known as metal-to-ligand charge transfer (MLCT),<sup>27</sup> although in some cases the moiety containing d-metal can be a part of the linker between the donor and acceptor fragments.<sup>376</sup> Thus, when the sensitizer absorbs a photon, an electron is promoted to the orbital that is not only higher in energy, which allows charge injection into semiconductor CB thermodynamically, but has a significant overlap with the CB orbitals of the oxide material, and allows electron transfer kinetically.

The most famous metallo–organic sensitizer, the ruthenium-based complex *cis*-Ru(dcbpyH<sub>2</sub>)<sub>2</sub>(NCS)<sub>2</sub> (dcbpy = 4,4′-dicarboxy-2,2′-bipyridine), also known as the N3 dye (Figure 15a), has been used since the pioneering work of Grätzel and

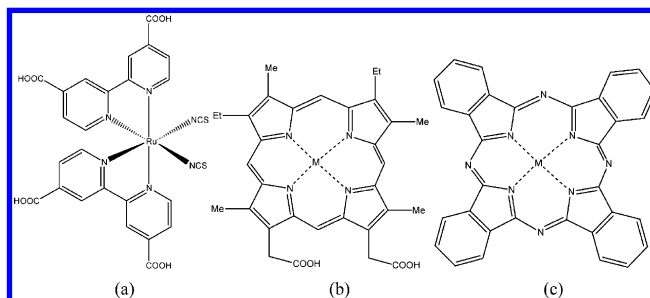


**Figure 15.** Transition metal chromophores: (a) N3 dye; (b) metal protoporphyrin; and (c) metal phthalocyanine.

O'Regan.<sup>29</sup> This sensitizer possesses >80% incident photon-to-current efficiency (IPCE) and has a broad adsorption with a high extinction coefficient (up to  $\sim 10^4$  M<sup>-1</sup>cm<sup>-1</sup>). Both of these features lead to high power conversion efficiency of  $\sim 11\%$ , one of the largest values reported so far. However, the high cost of Ru and its derived compounds makes its use impractical on a large scale, so a lot of focus has been placed on the development of less expensive analogues.<sup>9</sup> Despite the existence of a wide variety of possible metallo–organic dyes, we will only discuss a few of them, porphyrins and phthalocyanines. For a more detailed discussion of other metallo–organic dyes, as well as pure organic dyes, the reader is referred to a recent comprehensive review.<sup>1</sup>

The most natural option for a less expensive metal–organic sensitizer is the metal porphyrins and their derivatives (Figure 15b). This option comes from nature itself, in the photosynthetic complexes, where the porphyrin compounds are the main components of the green pigment chlorophyll. Phthalocyanines (Figure 15c) are structurally similar to porphyrins, and their complexes exhibit similar spectroscopic properties. These chromophores can be synthesized using inexpensive starting materials. Both types of compounds have high absorbance maxima in the visible spectrum, ranging from  $10^5$  to  $10^7$  M<sup>-1</sup>cm<sup>-1</sup>.<sup>377,378</sup> For a detailed discussion of the properties of these types of compounds, we refer the reader to previous reviews.<sup>378,379</sup>

As discussed in a recent review,<sup>9</sup> there are advantages and drawbacks in the use of each of these groups of compounds. For example, the porphyrin derivatives show poor light-harvesting properties relative to the N3 dye. In contrast, the phthalocyanines possess strong absorption maxima, around 300 and 700 nm, and can efficiently harvest solar light. However, they have a greater tendency to aggregate than the porphyrins, leading to weaker coupling with the CB of the semiconductor. The shortcomings of each type of sensitizer can be resolved by tuning the structure of the system, as we will discuss in the following sections.

**3.3.1.1. Size of the  $\pi$ -Conjugated System.** Increasing the size of the  $\pi$ -conjugated system causes broadening and a red-shift of the absorption spectrum, thereby increasing the efficiency of the corresponding dye up to  $\sim 11\%$ ,<sup>380</sup> which is similar to that of the N3 dye. This effect can be understood by treating the 1D or 2D polyenes as a quantum-mechanical

particle-in-a-box of corresponding dimensionality. The energy levels in such a model are given by:

$$E_n = \frac{\pi^2 \hbar^2}{2mL^2} n^2 \quad (3.1)$$

Thus, as the size of the conjugated aromatic system increases (analogous to an increasing  $L$ ), the spacing between levels decreases, resulting in a red-shift of the spectrum.

**3.3.1.2. Asymmetry via Push–Pull Groups.** Breaking the symmetry of the molecule with the help of “push” and “pull” groups aids in the reduction of aggregation and increases the coupling between dye and substrate. Experimentally measured power conversion in the range of 5.1–7.1% and IPCE up to 75% has been reported for the substituted porphyrins.<sup>381</sup> The efficiency of the various compounds has been found to be relatively independent of the nature of the aromatic substituent groups attached to the main porphyrin ring. A similar approach applied to the porphyrins resulted in a total efficiency of 11%,<sup>376</sup> approaching the efficiency of the significantly more expensive N3 dye. Additional discussion on this subject can be found in the following section.

**3.3.2. Organic Molecular Sensitizers.** Purely organic sensitizers have been developed as an inexpensive alternative to metallo–organic complexes such as the N3 dye. The basic principle in the design of such chromophores is a combination of an electron-donating (donor, D) group with an electron-withdrawing group (acceptor, A), Figure 16a. In the ground

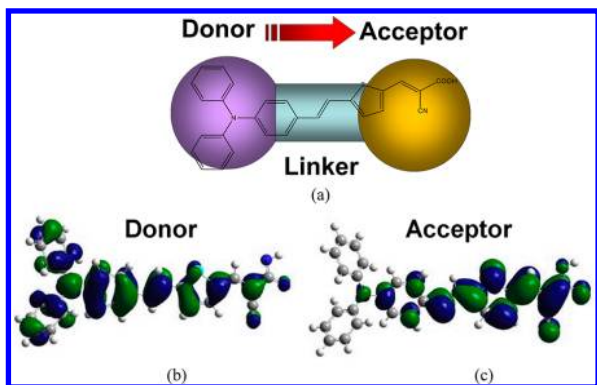


**Figure 16.** An illustration of the push–pull mechanism of electron transfer in organic chromophores. See the text for explanation. Panels b and c are adapted with permission from ref 382. Copyright 2006 The Royal Society of Chemistry.

state, the electron density of the HOMO orbital is mostly localized on the donor group (Figure 16b). When the molecule is photoexcited, an electron is promoted to the LUMO orbital, which is mostly localized on the electron-acceptor group (Figure 16c). The net effect is seen as an electron transfer from donor group D to acceptor group A (Figure 16a). This construction principle for sensitizers is also known as the push–pull mechanism.

Pure organic dyes possess larger molar absorption coefficients than Ru complexes, in the order of  $10^4$ – $10^5$  ( $M^{-1} \text{ cm}^{-1}$ ).<sup>35,382</sup> The diversity of various structural motifs and progress in organic synthesis make the preparation of such dyes relatively straightforward and cost-effective. The push–pull pattern in the construction of such chromophores allows for rational tuning of the HOMO and LUMO levels, which is necessary for each particular system. The huge number of dyes

available has been produced, in part, to fill this need. For an extensive discussion on this topic, we refer the reader to a recent review.<sup>1</sup> In Figure 17, we present a select few dyes, which have been used in theoretical as well as experimental studies of the electron transfer processes in DSSC.

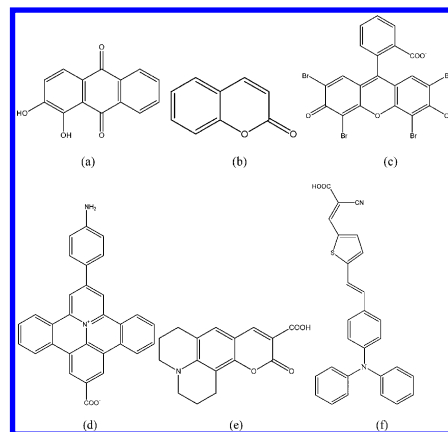


**Figure 17.** Organic chromophores: (a) alizarin; (b) coumarin; (c) eosin Y; (d) P1 dye; (e) coumarin 343; and (f) D5 dye.

Many of the principles discussed for the metallo–organic dyes also apply to pure organic chromophores. For example, increasing the length of the conjugated-linker leads to a red-shift<sup>383–386</sup> of the absorption spectra of the corresponding dyes and makes the oxidation potential  $E_{D/D^+}$  less positive (see eq 3.1). Such structural changes can increase the HOMO level (and hence  $V_{oc}$ ),<sup>383</sup> although that is not always the case.<sup>384</sup>

**3.3.3. Inorganic Sensitizers – Quantum Dots (QD).** Another alternative to conventional metallo–organic and pure organic chromophores is quantum dots, which can be considered as an inorganic type of sensitizer. Such materials achieve high light-harvesting efficiency at low cost.<sup>10,387</sup> Most often QDs are prepared from the low band gap chalcogenides and V-group binary compounds, such as CdS,<sup>388–391</sup> PbS,<sup>390,392–395</sup> Bi<sub>2</sub>S<sub>3</sub>,<sup>390,396,397</sup> CdSe,<sup>398–401</sup> InP,<sup>402</sup> or by using a core–shell structure CdSe/ZnS,<sup>403–405</sup> which can absorb photons in the visible range of the solar spectrum. Such inorganic chromophores can sensitize various wide-band gap nanostructured materials, such as colloid TiO<sub>2</sub>, in the form of nanoparticles, thin films,<sup>396,398</sup> or even nanotubes.<sup>399,406</sup> In addition, depending on the preparation conditions and techniques, various types of QD-sensitized TiO<sub>2</sub> phases can be produced.<sup>407</sup> For example, at low temperatures, 8 nm CdSe nanocrystals spaced 1–2 nm apart are formed. At higher temperatures, the CdSe phase is embedded in the TiO<sub>2</sub> phase.

Among the advantages of QDs as potential sensitizers for photovoltaic and photochemical applications are:

- the possibility of tuning the band gap via the size and shape of the QD;<sup>10,406</sup>
- high absorbance for efficient harvesting of solar light;
- the possibility of suppressing charge recombination and facilitating the charge injection processes with large dipole moments created in QD and quantum rods (QR) during electron–hole creation and separation;<sup>391</sup>
- the ability to generate multiple excitons (charge carriers) per single photon absorbed, a phenomenon known as multiple-exciton generation (MEG; refs 11, 160–162, 394, 395, and 408–416), may be used to boost the light-

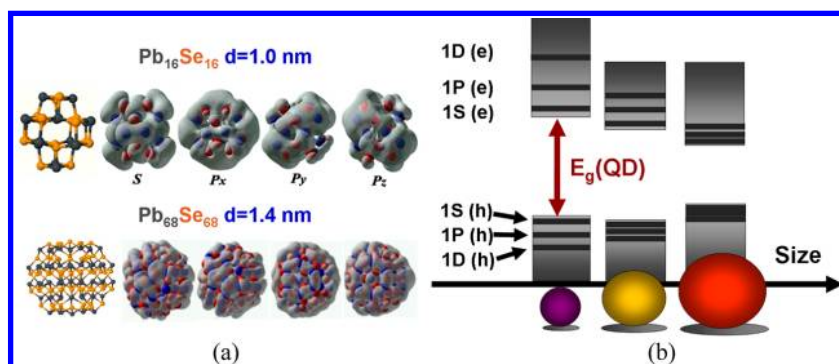


**Figure 18.** (a) Hydrogen-like orbitals of a QD. Adapted with permission from refs 417, 419. Copyright 2007, 2009 American Chemical Society. (b) Energy levels of electrons and holes in a QD.

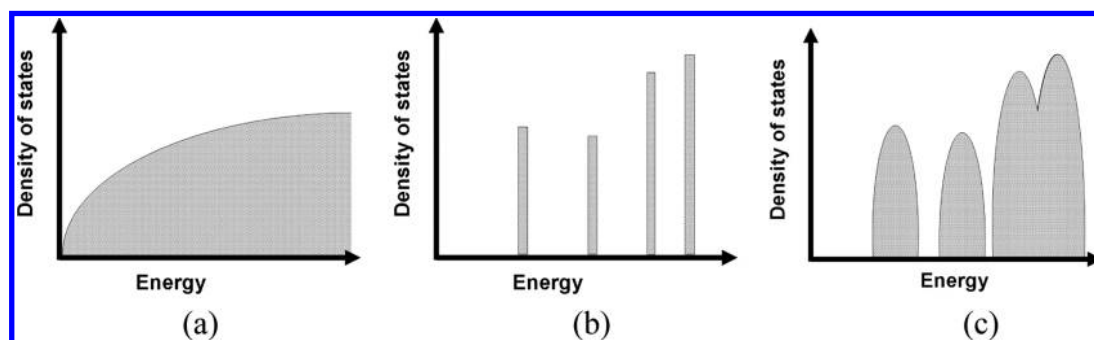


**Figure 19.** Energy levels in: (a) bulk material, quasi-continuous DOS; (b) ideal QD, discrete energy levels; and (c) realistic QD, broadened energy levels.

to-energy conversion efficiency of QD-sensitized solar cells.

Below, we will briefly discuss some of these properties of QDs.

**3.3.3.1. Quantum Confinement Effects.** On a nanometer scale, the electronic structure of the semiconductor material is strongly dependent on the size and shape of the system. This phenomenon, known as quantum confinement, has become one of the main considerations in tuning the properties of the QD or QR. A simple quantum-mechanical description of QD orbitals can be obtained with a particle-in-a-sphere model, leading to hydrogen-like wave functions. Thus, the states of QDs are named according to hydrogen atom terminology (S, P, D, etc.). The orbitals of small QDs indeed resemble the orbitals of hydrogen-like atoms<sup>417</sup> (Figure 18a, top), although this similarity becomes less obvious for larger QDs (Figure 18a, bottom).<sup>418,419</sup>

Unlike in the hydrogen atom, an electron (or hole) in a QD moves in the field of the crystal lattice. The energy levels of the QD can be obtained using the effective-mass theory (EMT), which is an advanced version of the particle-in-a-sphere model:

$$E_{n,e} = E_{CB} + \frac{\pi^2 \hbar^2}{2m_e^* L^2} n^2 \quad (3.2)$$

$$E_{n,h} = E_{VB} - \frac{\pi^2 \hbar^2}{2m_h^* L^2} n^2 \quad (3.3)$$

Here,  $E_{CB}$ ,  $E_{VB}$  denote the conduction and valence band edges, respectively, and  $m_e^*$ ,  $m_h^*$  are the effective masses of electrons and holes. Equations 3.2 and 3.3 predict that the spacing between the energy levels and, consequently, the band gap will decrease with a larger  $L$ , for larger QDs (Figure 18b). This

relationship explains why tuning the band gap of the QD is possible by varying its size.<sup>10,387,406,420,421</sup> The actual dependence of the band gap on the QD diameter  $d$  can be more complex. For example, for the ZnO QD, the following relationship has been found:<sup>420</sup>

$$E_g(d) = 3.30 + \frac{0.293}{d} + \frac{3.94}{d^2} \quad (3.4)$$

The effective masses of the electrons and holes often differ by several orders of magnitude ( $m_e^* \ll m_h^*$ ). This is reflected in the hole energy levels near the VB edge being much closer to each other than the corresponding energy levels of the electron states near CB edge, as shown in Figure 18b. Although an ideal QD would display discrete energy levels, a break in the degeneracies caused by imperfections in shape, defects, thermal fluctuations, etc. (similar to those found in molecular systems), would create a distribution of states that is more appropriately described with a density of states similar to bulk materials (Figure 19). Despite this, the QD DOS, and particularly the optical spectra, still have pronounced peaks, corresponding to the hydrogen-like levels predicted by the EMT.

The presence of the imperfections in QDs has an important implication to the phenomenon known as the electron–phonon relaxation “bottleneck”. It was originally hypothesized that because of the large spacing between the energy levels obtained using an ideal model of a QD, phonon modes having significantly smaller energy would be unable to induce the electronic transitions between such levels. As a consequence, it was expected that the electron–phonon relaxation would be slow. However, because of the QD imperfections, the energy spacing between the electronic states is significantly smaller than it would be in the ideal case. With notable exceptions,<sup>422</sup>



this allows efficient and relatively fast electronic relaxation to proceed without the phonon bottleneck.<sup>417–419</sup>

**3.3.3.2. Surface Modifications of the QD.** Because the QD is a very small object, the surface-to-volume ratio is relatively large. Therefore, modifications to the QD surface have a significant impact on its electronic properties. This surface modification may be employed in one of two ways: (a) changes of surface dipoles, creating shifts in the energy levels;<sup>10</sup> and (b) introduction of surface and band gap states.<sup>423</sup>

The effect of surface dipoles on the positions of the CB and VB edges is illustrated in Figure 20a. The position of the VB

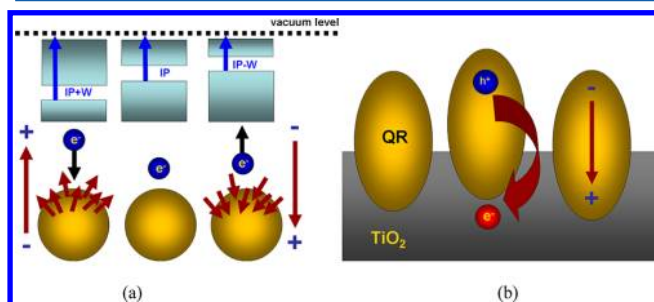


**Figure 20.** (a) Effect of dipoles on the semiconductor surface (e.g., QD or  $\text{TiO}_2$ ) on the energy levels; and (b) QR on  $\text{TiO}_2$ , illustrating dipole-enhanced electron–hole stabilization.

edge is related to the ionization potential, defined as the energy needed to remove an electron from the system out to infinity (Figure 20a, middle). However, if the surface of the semiconductor is covered with an array of dipoles directed away from the surface (Figure 20a, left), the position of the CB and VB will shift to lower energies. The positive direction of the dipole is the direction of force acting on a positively charge particle. Thus, when the electron removal process leading to ionization occurs, the surface dipoles attract the electron, thereby increasing the energy needed to remove the electron by the work ( $W$ ) performed to overcome the dipole forces:

$$W \approx q \cdot \mu \quad (3.5)$$

In this relationship,  $\mu$  is the dipole moment, and  $q$  is the charge transferred. As a consequence, the ionization energy will be larger for a system that has its surface dipoles directed away from the surface. The net effect can be seen as a downshift of the CB and VB (Figure 20a, left). The opposite effect occurs when the surface dipoles are directed toward the surface (Figure 20a, right). Equation 3.5 implies a linear relationship between the dipole moment of the adsorbed species and the magnitude of the CB or VB level shift. Indeed, this has been found experimentally for a dye-sensitized  $\text{TiO}_2$  system<sup>424</sup> and a CdSe QD.<sup>425</sup>

The principle of the dipole-induced energy level shifts is applicable to any semiconductor, including  $\text{TiO}_2$  substrates. The effect of surface dipoles on the energy level alignment in dye- and QD-sensitized solar cells has been discussed in detail elsewhere.<sup>10</sup> QRs can also produce dipoles on  $\text{TiO}_2$  surfaces. Because of the QR elongation, a significant dipole moment is created when electron–hole separation occurs (Figure 20b), leading to an upward shift of the  $\text{TiO}_2$  CB edge. The electric field generated by the QR dipole accelerates electron injection and slows electron–hole recombination, increasing the efficiency of such photovoltaic devices.<sup>391</sup>

The energy levels created on the QD surface by defects and ligands act as electron and hole traps, and generate additional states inside the band gap. It is believed that traps are responsible for QD blinking,<sup>426–429</sup> lower MEG yields,<sup>416</sup> acceleration of electron–phonon energy relaxation,<sup>430</sup> and, generally, significantly altering the idealized QD behavior. Therefore, significant experimental and theoretical efforts are dedicated to understanding and controlling the conditions of the QD surfaces.<sup>10,425,431–435</sup>

**3.3.4. Hybrid Structures, Nanoscale Carbon, and Polymers.** In addition to the sensitizer types discussed above, including the metallo–organic or organic dyes, QDs, and QRs, a number of alternative routes to sensitization on wide band gap semiconductors have been developed. Such approaches are often conceived as extensions or combinations of the standard techniques, or exploit ideas that are not applicable to the use of standard types of chromophores.

**3.3.4.1. Cosensitization (Diads, Panchromatic Sensitization).** Cosensitization, leading to panchromatic solar cells, is one of the most logical extensions of the standard methods. The limitations of the photovoltaic devices based on a single dye arise because the dye absorbs photons in a limited range of the solar spectrum. Photons with higher or lower energies are simply transmitted or lost as heat, and thus their energy is not converted to electric power. The idea behind cosensitization is to use a combination of dyes having absorbances at complementary wavelengths (Figure 21a).

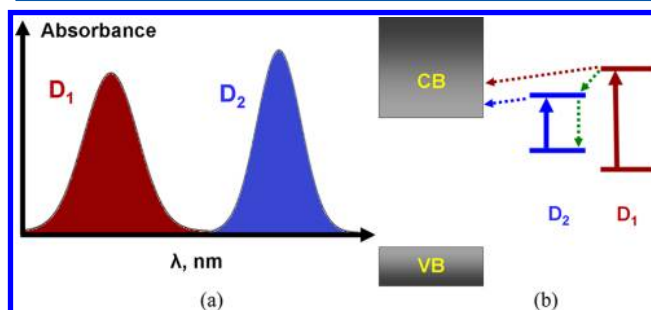


**Figure 21.** Working principle of cosensitization: (a) enhanced absorption; and (b) electron transfer from each dye to CB of semiconductor.

Such an approach allows one to efficiently maximize the overlap of the DSSC spectrum with the solar spectrum and use photons of different energy. For example, using a mixture of black dye with D131, it was possible to achieve an 11%<sup>436</sup> power conversion efficiency. In another study, a step-by-step procedure using black dye and NK3705 dye was developed, leading to an efficiency of 9.16%.<sup>437</sup> Cosensitization of Zn porphyrin (LD12) and spirally configured dye (CD5) achieved an efficiency of 9%, superior to that of each of the components individually, 7.5% and 5.7%, respectively.<sup>438</sup> There are also reports of successful applications of cosensitization methods in solid-state solar cells<sup>439</sup> and in other solid-state heterojunctions.<sup>377</sup> Among the possible cosensitization schemes is one in which one of the sensitizers is a QD, while the other is a metal–organic or organic dye,<sup>316,440,441</sup> or a polymer.<sup>442</sup> For a more detailed discussion of various cosensitization methods, we refer the reader to recent reviews.<sup>379,443</sup>

One of the problems with the cosensitization approach is that because the number of binding sites on the semiconductor surface remains constant, the gain in efficiency due to the



adsorption of one dye can be dampened by the reduced efficiency of the other dyes.<sup>443</sup> The overall effect is a relatively minor increase in the efficiency of the mixture of dyes relative to that of each individual dye alone. This is demonstrated in the example of a blend of Zr- and Hf-porphyrine complexes.<sup>444</sup> In addition to the mass-effect related problem, the presence of two chromophores next to each other may complicate the charge transfer mechanisms, leading to chromophore–chromophore CT and relaxation (Figure 21b, green path) instead of electron injection into the CB of the semiconductor (Figure 21b, blue and red paths).<sup>445</sup>

**3.3.4.2. Nanoscale Carbon Materials and Polymers.** Polymers<sup>446–448</sup> and nanoscale carbon systems, such as fullerenes,<sup>449–451</sup> graphenes,<sup>452–454</sup> carbon nanotubes,<sup>455,456</sup> and derivatives such as graphene oxide,<sup>457</sup> are often used as components of photoelectrodes. These materials can be combined with other sensitizers, such as QDs<sup>452</sup> or polymers,<sup>447,458</sup> resulting in improved power conversion efficiency for solar cells. Polymers have been deposited on a TiO<sub>2</sub> surface for photovoltaic and hydrogen production applications.<sup>459</sup> Conjugated polymers provide an alternative to small molecular chromophores, because they are capable of simultaneously absorbing light and conducting charges, and they are inexpensive and easy to process. A new type of nanoscale carbon material, graphene QD, has emerged as a sensitizer for photovoltaic applications in combination with ZnO nanowires<sup>460</sup> and on SnO<sub>2</sub><sup>461</sup> or TiO<sub>2</sub> nanoparticles.<sup>462</sup> As with inorganic QDs and conjugated aromatic dyes, it is possible to tune the band gap in graphene QDs by changes in its size and shape. In this case, quantum-confinement effects are described by a two-dimensional particle-in-a-box problem.

Because of the transparency and high electron conductivity<sup>454</sup> of graphene, which is a very thin metal, it can be used in multifunctional hybrid materials composed of a sensitizer (e.g., QDs or dye-sensitized TiO<sub>2</sub>), a graphene connector, and an electron collector (e.g., Pt),<sup>463–468</sup> as shown in Figure 22. In

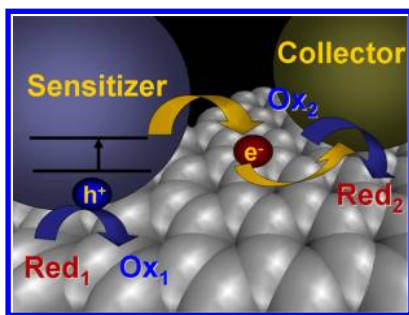


**Figure 22.** Working principle of a sensitizer/graphene/collector hybrid structure.

such a structure, the centers where oxidation and reduction take place are spatially separated, thus allowing one to selectively produce the desired chemical species at different sites. The photoexcited electron can transfer from the sensitizer through the graphene conducting layer to the electron collector, where it can be used for a reduction reaction like hydrogen production. Simultaneously, on the other end, the hole created on the sensitizer can be used for an oxidation reaction, such as oxygen production. Graphene itself can be used as a sensitizer, provided that the electrons are extracted from graphene on a time-scale that is faster than the electron–phonon energy losses.<sup>155</sup>

### 3.4. Molecular and Electronic Structure of Sensitizer–Substrate Complexes

When a sensitizer is deposited on the surface of a substrate, such as a metal oxide, it can interact either by chemisorption, resulting in the breaking of some chemical bonds and the formation of new ones, or it may simply involve physisorption, due to relatively weak van der Waals dispersion interactions. In the latter case, no chemical bonds are broken or created. For practical use, the sensitizer/substrate complexes should be stable for a relatively long time, so the preferred mode of dye–semiconductor binding is chemisorption. This is achieved by adding chemically reactive groups, known as anchors, to the dye molecules to form strong bonds with the surface. Among the most commonly used anchor groups are carboxylic acid (–COOH), phosphoric acid (–OP(=O)(OH)<sub>2</sub>), and hydroxyl (–OH) groups (Figure 23a–c). More than one anchor

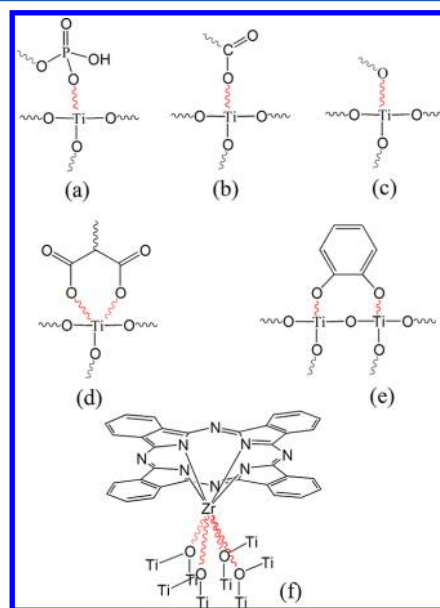


**Figure 23.** Various modes of binding of chromophores to oxide surfaces.

group, or groups with several binding centers (e.g., malonate –CH(COOH)<sub>2</sub>), are often used, leading to chelating and polydentate adsorption (Figure 23d,e). In the chelating case, two or more anchors bind to the same site (Figure 23d), while in the polydentate case, each anchor binds to a distinct site on the oxide substrate (Figure 23e). When a metal phthalocyanine or porphyrin dye is used for sensitization, a special binding mode can be achieved, in which the chromophore can bind directly to the surface via a metal atom in the central ring, leading to a parallel orientation of the phthalocyanine and porphyrin rings with respect to the oxide surface (Figure 23f).

The binding geometry and electronic structure of the adsorbate can significantly depend on its coverage. For example, relatively flat sensitizers, such as zinc phthalocyanine on ZnO(10 $\bar{1}$ 0)<sup>469</sup> and zinc protoporphyrin (ZnPP) on rutile TiO<sub>2</sub>(110),<sup>470</sup> prefer to align themselves parallel or with a slight tilt<sup>471</sup> to the surfaces at submonolayer coverages. However, at a higher coverages, their orientation is nearly perpendicular to the substrate surface, due to the stabilization caused by strong lateral interactions.<sup>470,472</sup> Similar coverage dependency on orientation was found for triphenylamine-cyanoarylic acid dye adsorption on a TiO<sub>2</sub>(110) surface.<sup>473</sup>

At low coverages, when the porphyrins and phthalocyanines are parallel to the surface, the orbitals of the dye molecule strongly overlap with those of the CB of semiconductor, leading to strong donor–acceptor couplings, thus providing the basis for fast and efficient injection of the photoexcited electron from the excited sensitizer group into the substrate.<sup>469</sup> It has been shown experimentally<sup>470</sup> that the interaction of a ZnPP metal atom and a rutile  $\text{TiO}_2$  (110) surface at submonolayer coverage is so strong that the metal atom is pulled out from the metallo–organic complex, thus diminishing the light-harvesting properties of the latter. In the physisorption mode, the metal atom of the sensitizer remains in the complex, thus preserving its optical properties. However, spatial separation between the dye and the semiconductor decreases their coupling, leading to an overall reduction of DSSC efficiency. Therefore, is it not always possible to take advantage of both planar coordination and chemical functionality of such dye molecules.

Using particular substituents in the porphyrin and phthalocyanine rings, one can favor specific binding modes (parallel or perpendicular to the surface) on the semiconductor surfaces and prevent aggregation.<sup>443,474–477</sup> For example, the presence of four carboxylic groups in the substituents of the porphyrin ring resulted in spider-like coordination<sup>474,476</sup> of the sensitizer on the oxide surface, with the ring parallel to the substrate surface (Figure 24, left). On the contrary, if only one

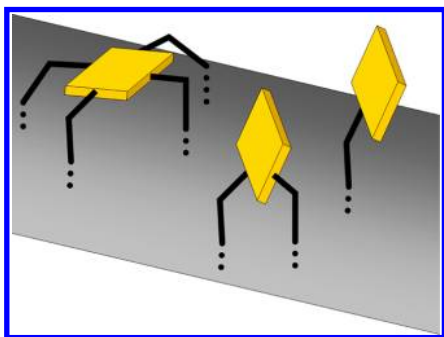


**Figure 24.** Binding modes of porphyrins and phthalocyanines, depending on the number and type of substituents.

or two carboxylic anchors are available, the resulting binding mode is perpendicular (Figure 24, middle, right) so the coupling between the aromatic ring and the surface is minimized and mediated only by the  $\pi$ -system of the carboxylate anchor. In the parallel coordination case, the direct coupling between the aromatic porphyrin ring and the CB of the semiconductor can be realized, leading to a more efficient charge transfer and a higher efficiency of the DSSC.

Wrapping porphyrins in long alkoxy and alkyl chains helps prevent face-to-face aggregation ( $\pi$ -stacking), and increases the CB edge energy, thus resulting in higher voltage.<sup>478</sup> In addition, bulky alkyl or alkoxy chains help to prevent charge recombination between the dye and the electrolyte species by protecting porphyrin rings via formation of a hydrophobic layer (see Figure 25). These innovations have resulted in increased energy conversion efficiency for such sensitizers, up to almost 11%.<sup>478</sup>

### 3.5. Donor and Acceptor States

An understanding of the properties of donor and acceptor states is necessary to accurately describe the electron injection process from a dye molecule to a semiconductor substrate. Depending on the nature of the chromophore, the substrate,

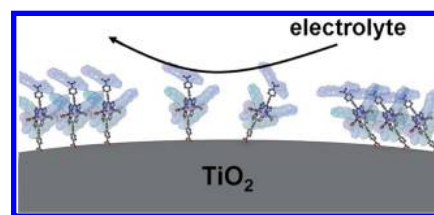


**Figure 25.** Hydrophobic alkyl/alkoxy chains help to prevent electron recombination to electrolyte. Adapted with permission from ref 478. Copyright 2012 The Royal Society of Chemistry.

and their interactions, it is possible to classify the states into two types, weakly and strongly mixed.

**3.5.1. Weak Mixing.** If the donor and acceptor fragments are connected by a bridge, the coupling is weak, and the initial and final states of the ET process are well localized on the corresponding fragments. This is particularly true for donors that have discrete energy levels. Examples include molecular sensitizers, such as alizarin, coumarin, N3, and small QDs (Figure 26). After photoexcitation occurs, the donor orbitals

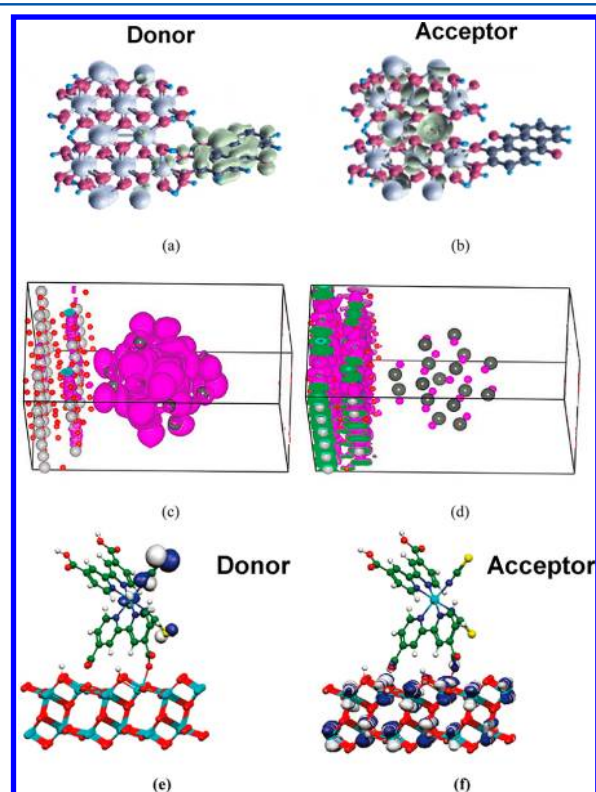


**Figure 26.** Electron donor and acceptor states in  $\text{TiO}_2$  sensitized with molecular and QD chromophores. (a,b) Alizarin/ $\text{TiO}_2$  donor and acceptor states; (c,d) QD- $\text{TiO}_2$  donor and acceptor states. Adapted with permission from ref 154. Copyright 2011 American Chemical Society. (e,f) N3/ $\text{TiO}_2$  donor and acceptor states. Adapted with permission from ref 149. Copyright 2009 American Chemical Society.

are almost completely localized on the sensitizer group, while the acceptor orbitals are localized on the substrate. Increasing the length of the chromophore–semiconductor bridge accentuates state localization on the donor and acceptor fragments. In an idealized case, in which the donor and acceptor states are degenerate, the eigenstates of the electronic Hamiltonian (i.e., adiabatic states) are spread over both fragments, even with weak donor–acceptor coupling. However,

the states localize as soon as the degeneracy is lifted even slightly.

**3.5.2. Strong Mixing.** If the donor and acceptor fragments interact directly, as in the case of TiO<sub>2</sub> interacting with graphene and wet electrons, the coupling is strong, and the states involved in the ET are delocalized over both fragments (Figure 27). The delocalization is enhanced in the presence of

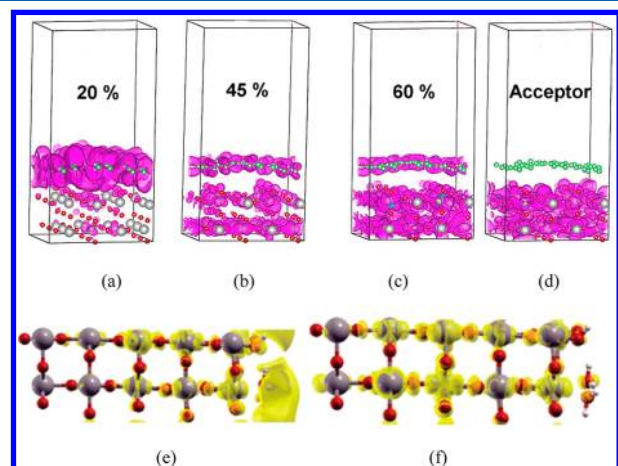


**Figure 27.** Illustration of strong mixing between donor and acceptor states. (a)–(c) Different excited donor states in the graphene/TiO<sub>2</sub> system; (d) the acceptor state in the graphene/TiO<sub>2</sub> system with complete localization on TiO<sub>2</sub>; (e) the donor state of the wet electron/TiO<sub>2</sub> system with significant delocalization into TiO<sub>2</sub>; and (f) the acceptor state of the wet electron/TiO<sub>2</sub> system with some electron density in the water layer. Pictures a–d are adapted with permission from ref 155. Copyright 2012 American Chemical Society. Pictures e,f are adapted with permission from ref 481. Copyright 2009 American Chemical Society.

multiple donor and acceptor states, because the states are more likely to become (quasi-)degenerate. The strong coupling regime is also observed for some molecular dyes, such as catechol,<sup>173,174,176,479</sup> cresol,<sup>176</sup> antocyanine,<sup>175</sup> and polyene-diphenylaniline DSL2A1.<sup>480</sup> Because of the strong coupling, the initial state of the ET process extends onto the acceptor subsystem. The electron injection from the adsorbate to the substrate is very fast, and the direct ET mechanism noticeably contributes to the overall ET process.

## 4. INTERFACIAL CHARGE TRANSFER IN PHOTOVOLTAIC CELLS

This section will focus on the mechanisms of various ET processes that happen on the oxide interfaces in photovoltaic cells. The emphasis will be on the kinetics of the steps involved in the processes shown in Figure 2a in section 1. By combining experimental findings with results obtained using theoretical methods discussed in section 2, a thorough insight into the ET dynamics on oxide interfaces can be attained.

### 4.1. Kinetics of Electron Injection from Sensitizers to Oxide Substrates

The electron injection step is the most studied of all of the processes that take place in a functioning DSSC. This is where the photoexcited electron of the chromophore transfers to the substrate material. The nature of the donor and acceptor states has been discussed in the previous section.

The kinetics of the ET from an excited chromophore donor into the semiconductor has been studied extensively during the

past decade, both experimentally and theoretically. Table 3 summarizes the injection times, computed and measured for different dye/semiconductor pairs by various research groups. The rates are strongly affected by the mechanism of the underlying process, as well as by the nature of the semiconductor and dye, and the environment, including the solvent, additives, and electrolyte. In this section, we will discuss the various factors affecting the dynamics of ET from sensitizers into semiconductors.

**4.1.1. Electronic Structure of the Semiconductor and Chromophore.** **4.1.1.1. Density of States in the Semiconductor and Injection Energy of the Sensitizer.** The general theoretical results discussed in section 2 suggest that the ET rate depends on the following factors: the coupling between the substrate and the dye orbitals, the density of states of the substrate material, and the injection energy, which is determined by the energy of the excited state of the sensitizer (see, for example, eq 2.59). The density of states near the CB edge can be approximated by:

$$\rho(E_i; E_{CB}) = \frac{(2m^*)^{3/2}}{2\pi^2\hbar^2} \sqrt{E_i - E_{CB}} \quad (4.1)$$

where  $E_i$  is the injection energy,  $E_{CB}$  is the energy of CB edge, and  $m^*$  is the effective mass of the electron in a given semiconductor (determined by the semiconductor properties). It follows from eq 4.1 that the density of states increases as the difference between the injection energy and CB edge-energy of the semiconductor increases. As a consequence, the injection rate increases as well, as illustrated in Figure 28a.

The nature of both the oxide and the dye was systematically studied by the Lian group as a factor that determines the rates of ET processes (Figure 28b).<sup>487</sup> They measured ET rates for various combinations of dyes and oxides, keeping the properties of one dye or oxide fixed while varying the properties of the other. For instance, in one such study, the role of the substrate was examined for various rhodamine B (RhB)-sensitized oxides: In<sub>2</sub>O<sub>3</sub>, SnO<sub>2</sub>, and ZnO (Figure 28c).<sup>497</sup> The different time-scales observed for electron injection in these materials can be explained on the basis of the general theory (Figure 28a). The position of the CB edge of ZnO is significantly higher (−0.4 V vs a saturated calomel electrode (SCE), pH = 0) than that of In<sub>2</sub>O<sub>3</sub> (−0.01 V vs SCE, pH = 0) or SnO<sub>2</sub> (0.07 V vs SCE, pH = 0). Thus, the density of states in ZnO at the excited-state oxidation potential for RhB (−0.94 V vs SCE) is significantly smaller than that for In<sub>2</sub>O<sub>3</sub> and SnO<sub>2</sub>. This results in a significantly slower ET into ZnO (7 ps) as compared to the other oxides (~1.2 ps), as illustrated in Figure 28c. Qualitatively similar results were found for the structurally and electronically different N3 dye on the surfaces of the metal oxides mentioned above,<sup>493–495</sup> as well as for coumarin 343 (C343) on TiO<sub>2</sub>, SnO<sub>2</sub>, and ZnO surfaces.<sup>15</sup> These results point to a significant role of the substrate and its density of states on the rate of ET.

The effect of the dye-excited state energy on the electron-injection process has been systematically studied by studying Ru-dyes adsorbed on In<sub>2</sub>O<sub>3</sub>,<sup>494</sup> Nb<sub>2</sub>O<sub>5</sub>,<sup>496</sup> and SnO<sub>2</sub>.<sup>493</sup> surfaces. For each surface, a series of dyes were used, each with a different excited-state position. As the energy of the excited state of the dye decreased, the ET rates significantly decreased (Figure 28d), in agreement with theoretical predictions.

Similar conclusions have been drawn by Jones and Troisi,<sup>146</sup> and later by Martsinovich and Troisi,<sup>500</sup> who performed a



Table 3. Electron Injection Times for Different Dye/Semiconductor Pairs<sup>a</sup>

dye/semiconductor pair	theoretical injection time, fs	experimental injection time, fs
C343/TiO <sub>2</sub> (anatase)	~20, ref 195 13, ref 196	~200, ref 482 <100, ref 483 <150, ref 15
C343/SnO <sub>2</sub>		multiexponential: 450 fs (81%), 3 ps (19%), ref 15
C343/ZnO		multiexponential: 1.8 ps (55%), 24.7 ps (45%), ref 15
alizarin/TiO <sub>2</sub>	5–10, ref 24 7.1–13, ref 207 4.3–11.8, ref 484	6, ref 485
EY/ZnO	8, refs 23,149	
EY/TiO <sub>2</sub>		multiexponential: 160 ± 50 fs (58%), 960 ± 190 fs (42%), ref 486
EY/ZrO <sub>2</sub>		multiexponential: 800 ± 70 fs (52%), 210 ± 20 fs (48%), ref 486
EY/Al <sub>2</sub> O <sub>3</sub>		490 ± 40 fs (77%), ref 486
N3/TiO <sub>2</sub>	22, refs 23,149	~50 ± 25, ref 487,488 3–100, ref 489 <20, ref 490 multiexponential: <150 fs (50%), 1.2 ± 0.2 ps (50%) <sup>491</sup> multiexponential: 28 ± 3 fs (50%), 1 ± 0.1 ps (11%), 9.5 ± 1 ps (12%), 50 ± 5 ps (7%), ref 492
N3/SnO <sub>2</sub>		~ 4 ps, ref 487 multiexponential: <100 fs (8.9%), 2.5 ps (29.3%), 15.8 ps (33.7%), 212 ps (28.1%), ref 493
N3/In <sub>2</sub> O <sub>3</sub>		~5.1 ± 0.8 ps, multiexponential: 2.0 ps (26%), 13 ps (57%), 64 ps (17%), ref 494
N3/ZnO		~100 ps, ref 487 multiexponential: <1 ps (18%), 42 ps (46%), 450 ps (36%), ref 495
N3/Nb <sub>2</sub> O <sub>3</sub>		multiexponential: <100 fs (37%), 30 ps (15%), 438 ps (48%), ref 496
Rh B/SnO <sub>2</sub>		1.19 ps, ref 497
Rh B/In <sub>2</sub> O <sub>3</sub>		1.20 ps, ref 497
Rh B/ZnO		multiexponential: 2.6 ps (62%), 14.2 (38%), ref 497
BINA/TiO <sub>2</sub>	2, refs 23,149	<3, ref 498
perylene derivatives/ TiO <sub>2</sub>	10–57, ref 147	
PbSe(QD)/TiO <sub>2</sub>	9.7 (8.6 fs, adiabatic –80%; 57 fs, nonadiabatic –20%), ref 154	<50, ref 499

<sup>a</sup>Dye abbreviations: Coumarin C343 (C343), eosin Y (EY), rhodamine B (Rh B).

systematic screening of various chromophores (Figure 29) using *ab initio* calculations, combined with nonadiabatic ET theory (outlined in section 2). Their results show that, in general, as the energy of the excited state of the dye (injection energy) increases, the rate of the ET process also increases (summarized in Table 4). However, exceptions to this correlation do exist; for instance, chromophores (a) and (c) do not follow this general trend, which can be explained by the localization of donor orbitals, and subsequent changes in the coupling strength between donor and acceptor states, as will be discussed in section 4.1.4.

Complementing the screening approaches, an alternative method exists called the inverse design method, developed by Batista and co-workers, to search for optimal chromophores with suitable photoabsorption properties for DSSC applications.<sup>26</sup> In this method, the core structure of a chromophore is fixed, while a number of substituents are varied. The substituent groups are then associated with a set of continuous variables (parameters) in the electronic structure calculations. Subsequent optimization of the target quantity (e.g., IPCE, CB-edge position, etc.) with respect to these continuous variables leads to a set of optimal variables, which are then mapped onto discrete parameters, defining the chemical nature of the substituent groups.

Simultaneous variation of both the semiconductor and the dye across different experiments shows that the relative position of the excited state of the dye with respect to the CB edge of the semiconductor can be a rate-determining factor. This conclusion can apply to other experimental and theoretical systems as well. However, the intrinsic properties of the pure materials that can vary depending on the system should be taken into account to obtain accurate quantitative predictions, such as the effective electron mass of the semiconductor, as well as the properties of the interface, for example, chromophore–semiconductor couplings.

**4.1.1.2. Symmetry of the Donor State Wave Function.** In theoretical studies of ET from catechol to TiO<sub>2</sub> by Batista and co-workers, it was found that the symmetry of the dyes' excited state relative to the orbitals of the substrate has an influence on the ET rates.<sup>501</sup> The initial ET injection time from catechol-LUMO was found to take approximately 6 fs, while it was twice as fast for catechol-LUMO+1, at 3 fs. Because the energy levels of these excited states are very close to each other, the difference in the ET kinetics arises because of the symmetry of the wave functions, which determines the charge density and the donor–acceptor coupling. The LUMO weakly couples with the d-orbitals of Ti atoms, and ET happens slowly through the empty space between the dye and substrate. On the contrary, the coupling between LUMO+1 and the d-orbitals of Ti atoms



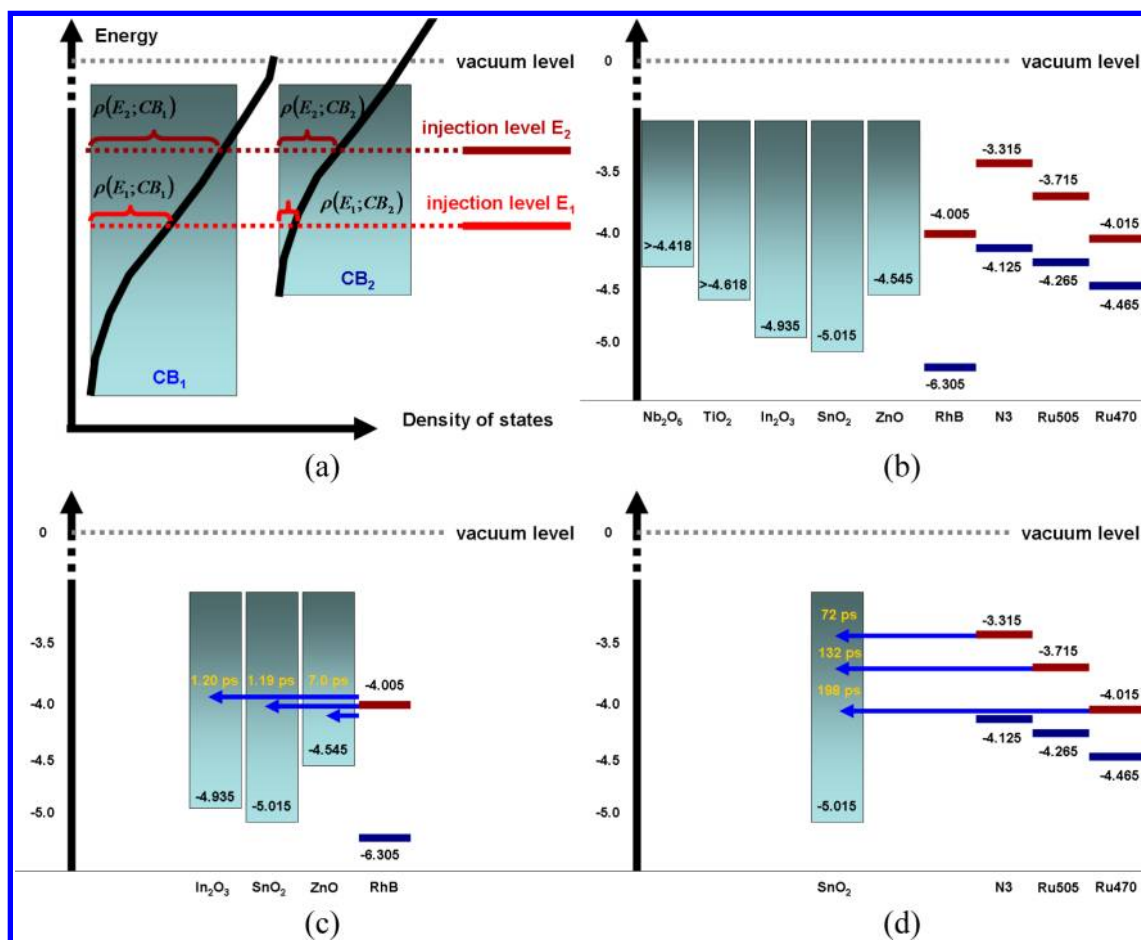


**Figure 28.** The ET injection rates as a function of the position of the CB edge of the semiconductor and the excited-state energy of the dye (injection energy). (a) Illustration of the general principle for the determination of ET rates. (b) Energy levels of various oxides and dyes. (c) Injection from the same dye into different oxides. (d) Injection from different dyes into the same oxide.

is strong, and ET happens through-bond, resulting in faster electron injection. Similar explanations based on the symmetry of the wave function have been extended to a  $TiO_2$  slab to account for the significant anisotropy of charge-diffusion along different crystallographic directions of the  $TiO_2$  substrate, as observed in calculations.

**4.1.1.3. Correlation of ET Rates with Sensitizer Size.** As a general rule, the smaller is the sensitizer, the larger are the ET rates. This can be rationalized by the fact that smaller systems have a larger percentage of their total charge density localized near the substrate surface. To illustrate this fact, we will discuss the system of pyridine (Py) and perylene (Pe) dyes attached to  $TiO_2$  via similar anchor groups, phosphate (P) and carboxylate (C).<sup>197</sup> For the smaller Py chromophores, a greater fraction of the electron density is located near the  $TiO_2$  surface, resulting in faster ET rates (1.9 fs for PyC and 11.3 fs for PyP), as compared to analogous systems using the perylene chromophore (16.2 fs for PeC and 41.7 fs for PeP). Additionally, as we will discuss in later sections, an increase in the linker size usually results in a decrease in the ET rates.<sup>502–504</sup> This effect can be partially attributed to a decrease in the fraction of the electron density that is localized near the substrate surface. ET from a QD provides an additional example that illustrates the correlation between the size of the sensitizer and the rates for the electron injection process. Typically, the injection time from a QD is much longer (tens of hundreds of fs) than that from molecular adsorbates (few fs to tens of fs), although there

are exceptions, due to other factors, which will be discussed further in this Review.

**4.1.1.4. Injection from QDs.** Although we have primarily focused on dye-sensitized oxide systems, the conclusions and theoretical framework described thus far are equally applicable to QD-sensitized metal oxides. A systematic study of the effects of the properties of both QDs and metal oxides on ET rates was recently performed in the Kamat group.<sup>12</sup> As with Lian's studies on molecular sensitizers, they used a series of oxides ( $SnO_2$ ,  $TiO_2$ ,  $ZnO$ ), but, in addition, they also used CdSe QDs of various sizes. In general, their results show that as the difference between the excitation energy of QDs and the CB-edge energy of the oxides increases, the ET rates increase. In contrast to molecular sensitizers, the variation of the rates observed in the QD/ $TiO_2$  system as a function of the metal oxide composition is rather weak (2–4 times). This effect was explained by the cooling of initially prepared “hot” QD excited states, which occurred on the  $\sim 0.77$  eV/ps time-scale. Electron transfer from the QDs to metal oxides was found to proceed on a much longer time-scale of 2–50 ps. The slower ET rates can be explained by the fact that the injection from the QD to the metal oxide occurs from the CB edge of the QD.

The ratio of the electronic cooling rate to the ET rate in QD-sensitized metal oxides strongly depends on the nature of the QD material. In contrast to CdSe QDs, ET transfer from PbSe to  $TiO_2$  can proceed much faster, on a sub-50 fs time-scale.<sup>394,499,505</sup> Thus, ET can successfully compete with the

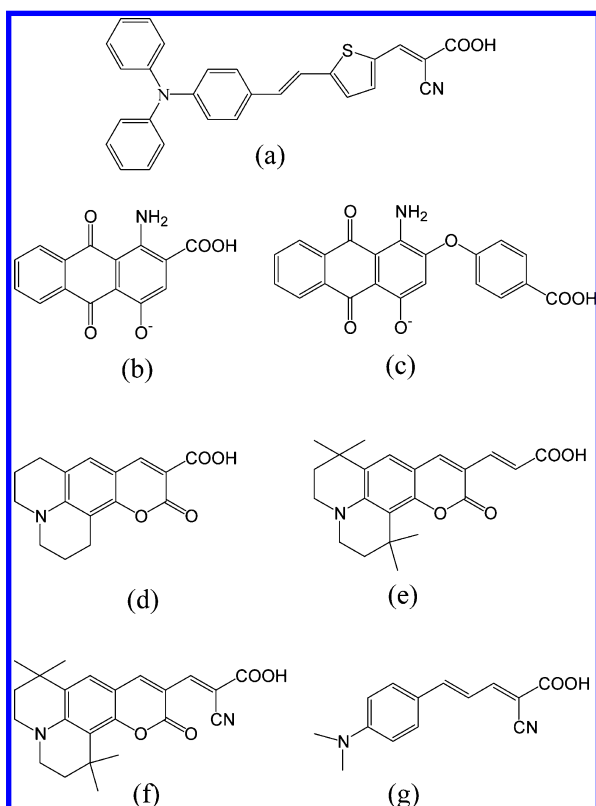


**Figure 29.** Sensitizers used in the systematic theoretical screening of dyes.

**Table 4.** ET Rates as a Function of Injection Energy (Dye LUMO)

$E_{inj}$ , eV	injection time, rutile (110), fs	injection time, anatase (101), fs	chromophore (see Figure 2)
−1.87	1.35	1.57	(d)
−2.02	1.51	2.56	(e)
−2.34	0.82	2.88	(g)
−2.46	2.18	4.06	(f)
−2.72	21.05	4.32	(a)
−2.73	1584.2	73.16	(c)
−3.09	656.24	16.30	(b)

cooling, provided that one can achieve strong QD–oxide coupling, by using, for instance, short QD ligands, or by eliminating the ligands altogether. The injection of “hot” electrons can be utilized to increase the voltage of the photovoltaic cell.

Long and Prezhdo studied ET from a PbSe QD to a  $\text{TiO}_2$  substrate theoretically and found that the calculated ET time for this system ( $\sim 10$  fs) was in good agreement with experimental values.<sup>154</sup> They found that the overall ET proceeded simultaneously via both adiabatic and nonadiabatic mechanisms, as indicated by the 8.6 and 57 fs times, respectively. The adiabatic pathway was found to be dominant (80%) because of the strong coupling between the donor and acceptor states. The transfer was driven by high-frequency polaron modes of QD/ $\text{TiO}_2$ . These vibrations polarize the QD–substrate interface and couple the donor and the acceptor states to each other via electrostatic interactions.

**4.1.1.5. Molecular versus QD Sensitizers.** It is informative to explicitly compare the ET kinetics between QD semiconductors and molecular sensitizers. In general, QD semi-

conductors are representative of typical nanoscale-inorganic materials, including carbon nanotubes, metallic nanoparticles, etc. Molecular chromophores are small and soft organic materials, as are conjugated polymers and electrolyte molecules. QDs and molecules have different electronic structures; the former exhibit a quasi-continuous density of states, while the latter have discrete energy levels. The dense manifold of states in QDs at higher energies contributes to the fast cooling of “hot” electrons, while the discrete spectrum of molecular adsorbates leads to faster electron injection and avoids phonon-induced energy losses. Electron–phonon coupling in a QD is related to its large intrinsic dipole moment, so vibrations that cause small changes in the geometry of the system can lead to large changes in the electrostatic potential and result in a notable redistribution of the electron density. Long-range electrostatic electron–vibrational interactions are at the heart of adiabatic ET, which the atomistic calculations show is the dominant ET mechanism.<sup>154</sup>

Another notable difference between the two types of sensitizers is that QDs are much larger than molecular dyes. Furthermore, QDs have a uniform chemical composition, while molecular chromophores, with their multiple types of atoms and functional groups, do not. As a result, the QD wave function is delocalized over the material, and only a small fraction of the charge density extends onto the QD/substrate interface. On the other hand, the complex electrostatic potential generated in molecular dyes caused by the rapidly changing pattern of atoms produces substantially more localized wave functions. With an appropriate choice in the composition of the dye fragment, it is possible to favor the localization of the donor state to reside primarily on the dye/substrate interface. Thus, molecular chromophores provide significantly more possibilities to fine-tune the donor–acceptor interactions and to control various ET and relaxation processes that occur at oxide interfaces.

**4.1.2. Modulation of the Conduction-Band Edge of the Semiconductor.** As discussed in the previous subsection, the position of the CB edge of the semiconductor is one of the rate-determining factors for the ET process. Significant fluctuations in the CB band edge can arise from changes in the pH level or from the addition of coadsorbates.

Modification of the metal oxide with coadsorbates affects the CB edge in two ways. For one, it generates dipole moments on the substrate surface; these surface dipoles change the amount of energy that is required to remove an electron from the material, thereby affecting the position of the CB edge relative to the vacuum level, as discussed in section 3.3.3 (Figure 20). Second, the hybridization of the substrate and adsorbate orbitals changes the electronic structure of the metal oxide surface itself and, therefore, the energies of the CB orbitals. Modifications to the surface properties by a change in the pH level can be thought of as a special case of modification by coadsorbate, and the two CB effects apply. In aqueous solutions, pH is controlled by  $\text{H}_3\text{O}^+$  ions, while in organic electrolytes it is adjusted by molecules such as  $\text{RR}'\text{R}''\text{NH}^+$ . In general, it is difficult to separate the influences of the introduction of surface dipoles from the hybridization of the substrate and adsorbate orbitals on the overall change in the CB edge position.

**4.1.2.1. Effect of pH.** The position of the CB edge of the semiconductor depends on the pH level, as described by the Nernst equation:<sup>506,507</sup>

$$E_{\text{CB}}(\text{pH}) = E_{\text{CB}}(\text{pH} = 0) + 0.059 \cdot \text{pH} \quad (4.2)$$

where  $E_{\text{CB}}(\text{pH})$  is the energy of the CB edge at a given pH value and  $E_{\text{CB}}(\text{pH} = 0)$  is the energy at pH = 0. Note that this definition uses a plus sign in front of the pH term, because we are interested in the CB-edge energy (physical interpretation) rather than the electrochemical potential. Thus, the higher is the pH, the higher is the CB edge energy. For example, it follows from eq 4.2 that the variation in the pH level by 7 units (e.g., from 0 to 7), which is realistic in aqueous solutions, raises the CB energy by as much as 0.413 eV. This is comparable to the difference between the CB edges of ZnO and  $\text{In}_2\text{O}_3$  under the same conditions.

The effect of pH on the interfacial ET rate has been studied systematically for a wide variety of oxide surfaces by the Lian group.<sup>495,497,508</sup> One of their general findings was that the higher is the pH, the slower is the injection. This result is in agreement with the theoretical predictions obtained from eq 4.2, and it also confirms the role of the CB-edge energy discussed in section 4.1.1.

**4.1.2.2. Effects of Coadsorbates: Solvent, Electrolyte, and Additives.** The position of the CB edge depends on the chemical composition of the semiconductor surface. The molecules of the solvent, additives, and electrolyte used in a DSSC can coadsorb on the substrate along with the sensitizer groups. In many cases, this causes a positive shift of the CB edge of the metal oxide.<sup>35,509–513</sup> This change is correlated with the acidic or basic nature of the adsorbed molecules. The donor number (DN) index, defined as the negative enthalpy in a reaction between one molecule of a substance with  $\text{SbCl}_5$ , quantitatively characterizes the acid/base properties of a substance. The higher is the DN, the more basic is a solvent.

As explained in Figure 2a, the open circuit voltage of a solar cell,  $V_{\text{oc}}$ , depends on the quasi-Fermi level of the semiconductor with the photoinjected electron,  $\varepsilon_{\text{F}}$ , and on the chemical potential of the electrolyte redox pair,  $\mu(\text{I}_3^-/\text{I}^-)$ . Specifically, we use the iodide/tri-iodide pair, which is the most commonly used electrolyte in DSSCs. In the equation:

$$eV_{\text{oc}} = \varepsilon_{\text{F}} - \mu(\text{I}_3^-/\text{I}^-) \quad (4.3)$$

$e$  is the charge of an electron. The quasi-Fermi level of the semiconductor is determined by the density of electrons in the CB,  $n_{\text{CB}}$ , the density of states at the CB edge,  $N_{\text{CB}}$ , temperature,  $T$ , and the position of the CB edge,  $E_{\text{CB}}$ :

$$\varepsilon_{\text{F}} = E_{\text{CB}} + k_{\text{B}}T \ln \frac{n_{\text{CB}}}{N_{\text{CB}}} \quad (4.4)$$

The chemical potential of the redox pair is related to the Nernst potential,  $E_{\text{N}}(\text{I}_3^-/\text{I}^-)$ :

$$\mu(\text{I}_3^-/\text{I}^-) = eE_{\text{N}}(\text{I}_3^-/\text{I}^-) = eE^0(\text{I}_3^-/\text{I}^-) + \frac{2.303RT}{2F} \ln \left( \frac{a_{\text{I}_3^-}}{a_{\text{I}^-}^3} \right) \quad (4.5)$$

where  $E^0(\text{I}_3^-/\text{I}^-)$  is the standard electrochemical potential of the corresponding redox pair,  $a_{\text{I}_3^-}$ ,  $a_{\text{I}^-}$  are the activities of the corresponding ions,  $R$  is the universal gas constant, and  $F$  is the Faraday constant. When eqs 4.3 and 4.4 are applied, it is evident that shifting  $E_{\text{CB}}$  toward the vacuum level, the open circuit voltage,  $V_{\text{oc}}$ , and ultimately the efficiency of the DSSC (see eq 1.1), can dramatically increase. Coadsorption of a solvent or an additive with a large DN will shift the  $E_{\text{CB}}$  and can thereby be used to increase the DSSC efficiency.

The solvent effect in a DSSC based on ZnO was determined in a recent study that combined theoretical and experimental approaches.<sup>514</sup> Several solvents spanning a large range of DN indexes were used, including nitromethane (NM), acetonitrile (MeCN), and dimethylformamid (DMF), as well as a combination of MeCN with the addition of *p*-tert-butylpyridine (TBP). It was found that as the DN of the solvent increased, the open circuit voltage and the efficiency of the corresponding solar cell device increased (Table 5). This increase in voltage

**Table 5. Effect of Basic Properties (Quantified by Donor Number, DN) of the Solvent on the CB-Edge Energy of the Semiconductor,  $E_{\text{CB}}$ , Open Circuit Voltage,  $V_{\text{oc}}$ , and Power Conversion Efficiency,  $\eta$ , of a DSSC**

	NM	MeCN	DMF	MeCN+TBP
DN <sup>516</sup>	2.5	14.1	26.6	33.1 (pyridine)
$E^0(\text{I}_3^-/\text{I}^-)$ vs NHE, V, experiment	0.367	0.307	0.558	0.338
D149/ZnO <sup>514</sup>				
$E_{\text{CB}}$ , eV, theory	−1.95	−1.85	−1.66	−1.44
$V_{\text{oc}}$ , eV, experiment	0.50	0.59	0.67	0.64
$\eta$ , %, experiment	0.9	2.9	2.4	3.1
Mercurochrome/ $\text{TiO}_2$ <sup>515</sup>				
$V_{\text{oc}}$ , eV, experiment	0.45	0.52	0.82	
$\eta$ , %, experiment	0.69	1.23	1.32	
N719/ $\text{TiO}_2$ <sup>512</sup>				
$V_{\text{oc}}$ , eV, experiment		0.603	0.744	
$\eta$ , %, experiment		7.5	5.47	
N3/ $\text{TiO}_2$ <sup>513</sup>				
$V_{\text{oc}}$ , eV, experiment		0.657	0.751	
$\eta$ , %, experiment		7.73	4.22	
Triphenylamine-CH-rhodamine-3-acetate/ $\text{TiO}_2$ <sup>35</sup>				
$V_{\text{oc}}$ , eV, experiment		0.5		0.61
$\eta$ , %, experiment		2.7		1.3

can be explained by a positive shift of the CB-edge energy,  $E_{\text{CB}}$ , as previously demonstrated via direct quantum calculations for the D149/ZnO system.<sup>514</sup> A similar correlation has been found by other authors for a  $\text{TiO}_2$ -based DSSC using the same solvents.<sup>512,513,515</sup>

Unlike the open circuit voltage  $V_{\text{oc}}$ , the photocurrent  $J_{\text{sc}}$  usually decreases as the DN of the electrolyte increases.<sup>512,513,515</sup> Therefore, the power conversion efficiency of a DSSC,  $\eta$ , is a nonmonotonic function of the DN of the solvent.

The trend of a decreasing photocurrent with an increasing DN can be explained by several factors. As the DN of the solvent increases, the molecules act as stronger Lewis bases and therefore interact more strongly with the oxide surface. As a consequence, the solvent molecules begin to replace the sensitizer,<sup>517</sup> decreasing its surface density. Even in cases where this replacement does not occur, steric interference can pull the sensitizer groups away from the surface. This decreases the electronic coupling between the donor states that are localized on the sensitizer and the acceptor states, which are localized on the semiconductor. As a result, the rates for electron injection decrease, and the photocurrent  $J_{\text{sc}}$  is reduced. However, it has also been proposed that in some cases the additive/solvent only act to substitute weakly bound sensitizer molecules. Yet because those molecules already possessed weak coupling between donor and acceptor states, there is little change in the overall photocurrent.<sup>517</sup>



In addition to the DN being the measure of the solvent polarity, it is also correlated with the viscosity of the solvent: the larger is the polarity, the higher is the viscosity. A higher viscosity has the effect of decreasing the diffusion rates of the electrolyte species, which is necessary for regenerating the ground state of the sensitizer, and thus for producing electrical current.

Finally, as was discussed in the previous subsections, when the CB edge shifts up in energy, injection rates decrease because of the lower density of states in the semiconductor at the injection energy (Figure 30). This also explains why the

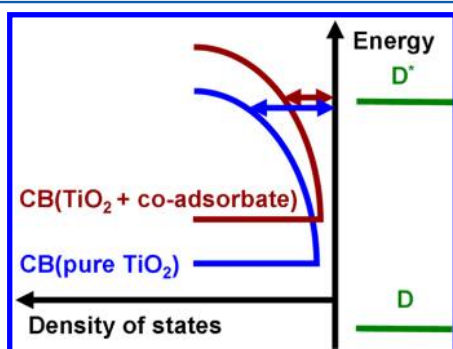


**Figure 30.** The effect of coadsorbates, such as solvent, electrolyte, and additives, on the position of the CB edge of the semiconductor.

photocurrent is smaller for more basic solvents and additives with higher DN. For example, the addition of 4-*tert*-butylpyridine to dye-sensitized  $\text{TiO}_2$  has been found to reduce electron-injection rates and decrease the overall efficiency of charge transfer from the photoexcited dye to the CB of the semiconductor.<sup>35</sup>

The shift of the CB edge position that occurs when molecules on the oxide surface are adsorbed also depends on the properties of the surface itself. For example, in recent theoretical studies, Martinsovich and Troisi showed that the adsorption of benzoic acid on an anatase (101) surface does not change its electronic structure significantly, while the adsorption on a rutile (110) surface increased the energy of the  $\text{TiO}_2$  CB by  $\sim 1.0$  eV.<sup>518</sup> This difference can be attributed to the effects of the different surface dipoles (see Figure 20 of

section 3.3.3): the anatase (101) surface is less polar than the rutile (110) surface. The adsorbed benzoic acid in effect becomes a compensating capping ligand, which decreases the large polarity of the surface. Because the original dipole of the rutile (110) surface is so large, such compensation in the surface dipole has a major effect, leading to a notable shift of the CB edge. On the other hand, the original polarity of the anatase (101) surface is small, and benzoic acid does not introduce a new dipole. Thus, the change in the overall surface dipole is rather small, leading to a negligible change in the electronic structure of the adsorbate/substrate system. The differences in polarity of the rutile (110) and anatase (101) surfaces are indirectly manifested by the presence of the oscillation of the band gap computed for rutile (110) as a function of the slab thickness, which is absent in the case of the less polar anatase (101) surface.

**4.1.3. Multiexponential Kinetics.** The dynamics of the charge transfer from metallo–organic dyes (Ru-complexes, in particular) to various metal oxides has been found to be multiexponential.<sup>491–493,496,519,520</sup> The fast component is typically 20–100 fs, while the slow component ranges from 1 to 100 ps. This phenomenon has been explained by assuming that the initially prepared excited singlet state of a dye can relax to the lower energy triplet states. The injection to the CB of the semiconductor can then proceed simultaneously from the singlet and triplet states, producing fast and slow injection components, respectively, and resulting in multiexponential (multiphasic) kinetics (Figure 31a).<sup>492,493,496,519</sup>

Tachibana and co-workers described a nonuniform distribution of surface protonation sites of a substrate that lead to different local electrochemical potentials and therefore to different injection rates.<sup>522</sup> A model proposed by McNeil and co-workers has resulted in a power distribution of injection rates.<sup>523</sup> They argued that the dispersive kinetics of ET is related to the kinetics of charge transport in the semiconductor, which is affected by the trap states due to defects, vacancies, etc. The increase of the concentration of  $\text{Li}^+$  or  $\text{H}^+$  cations in the electrolyte results in an increase in the possible number of local defect states, leading to a wider distribution of defect-state energies. This distribution is reflected in more dispersive kinetics of the interfacial ET.

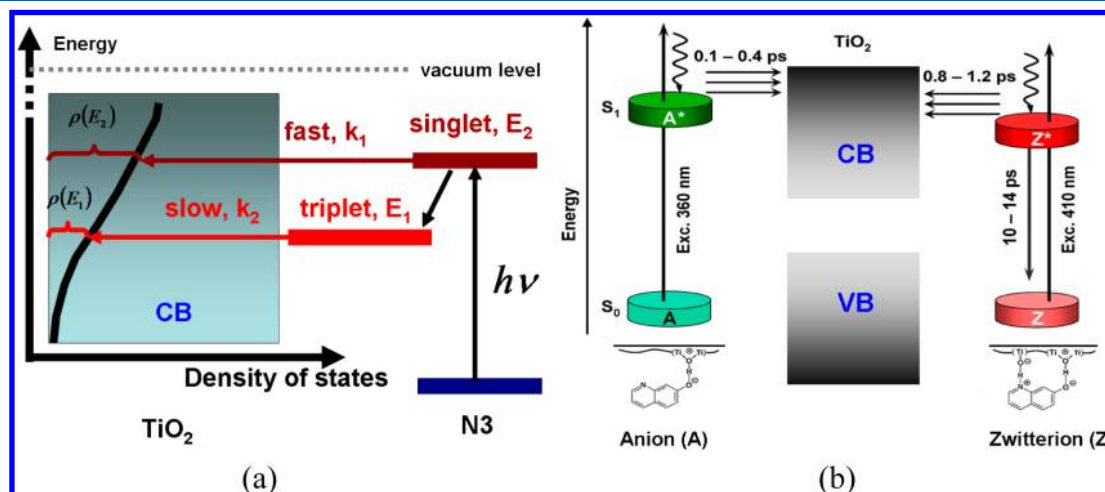


**Figure 31.** Rationalization of multiexponential kinetics: (a) relaxation of the excited singlet state to lower-lying triplet states; and (b) different binding modes of a dye molecule. Adapted with permission from ref 521. Copyright 2012 American Chemical Society.



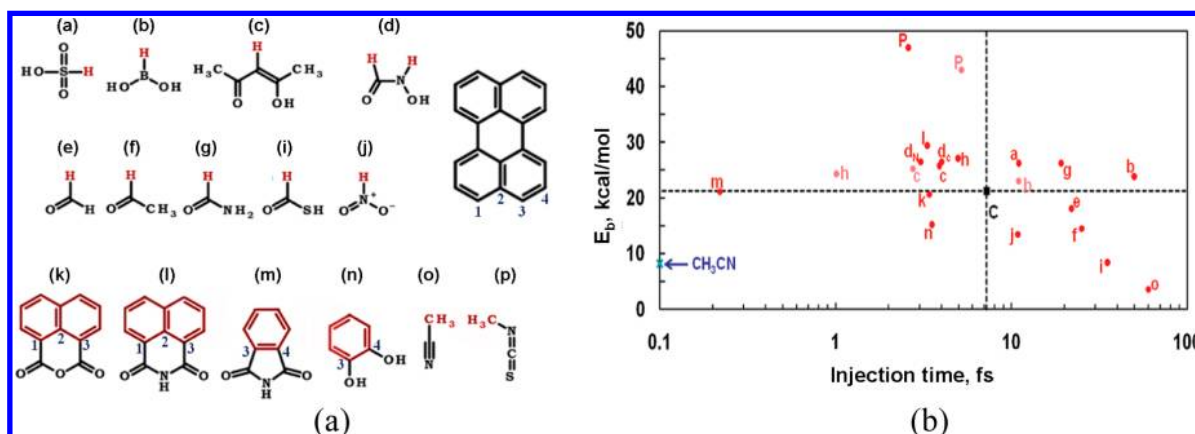


**Figure 32.** Anchor group screening: (a) structure of the anchor groups used in study; and (b) the classification of the anchor groups, based on their binding strength and on the injection rate. Adapted with permission from ref 525. Copyright 2012 American Chemical Society.

Multiexponential kinetics can also arise because of loosely attached molecules and the aggregation of dye molecules. By changing the conditions to prevent dye aggregation and improve adsorption, Moser and co-workers have been able to obtain single-exponential injection kinetics with a fast component of only <20 fs.<sup>490</sup> The heterogeneity in ET rates was observed in recent kinetic studies of the ET from 7-hydroxyquinoline in mesoporous titania.<sup>521</sup> The differences in the ultrafast injection times were explained by the presence of different forms of the dye molecule (anionic, zwitterionic) and different binding modes (Figure 31b).

In recent theoretical studies, Labat and co-workers showed that the binding mode of the N3 dye may have significant implications on the injection time.<sup>489</sup> Depending on dye coordination, the position of the LUMO of the dye with respect to the CB edge of the semiconductor can change from 0.42 to 1.40 eV. This leads to an injection time variation in the range of 3–100 fs, in accordance with the general scheme presented in (Figure 1a). Similar conclusions can be drawn from the computational studies performed in the Troisi group.<sup>524,525</sup> Depending on the binding mode (rutile or anatase) and properties of the surface (crystallographic plane), the calculated ET rates varied by up to 2 orders of magnitude. Such computational studies further support the idea that multiexponential kinetics depend on the heterogeneity of the binding modes of the dye. These studies do not exclude the possibility of the involvement of triplet states in the ET dynamics, contributing additional time-scales to the multiexponential kinetics.

**4.1.4. Role of the Anchor Group.** It follows from the theory of nonadiabatic processes (see section 2) that ET rates strongly depend on the coupling between donor and acceptor states. This coupling can be affected by the chemical composition and structure of the anchor group. The role of the anchoring group on the interfacial electron-transfer process has been extensively studied by the Troisi group.<sup>524,525</sup> They performed a systematic investigation of the effects of the anchoring group on the electron injection rates in a perylene dye. Figure 32a shows several of the anchoring fragments they studied connected to perylene dye.

The various anchor groups are classified in Figure 32b based on their adsorption energy and injection time-scale. The carboxylate group is one of the most frequently used anchoring groups in DSSC; as such, it can serve as a standard for comparison of the other groups used in the study, allowing one

to categorize the anchors into four groups. Figure 32b focuses on the sensitization of the anatase (101) surface. Only the anchor groups that are found in the upper left quadrant can be considered as efficient anchors, because they provide strong binding between the dye and the substrate, and allow for fast electron injection. For the rutile (110) surface, the diagram changes, because the number of oxygen atoms available for coordination increases. Thus, some anchors, which coordinate in a monodentate way on the anatase (101) surface, can form bidentate and chelate coordinations on the rutile (110) surface. Adsorption via a chelate with bidentate coordination increases the coupling between the dye and the semiconductor, increasing the binding energy. In particular, this is the case for the carboxylate group itself. Hence, the reference point, defined by the intersection of the dashed lines in Figure 32b, moves to the upper left portion of the diagram, thus showing a smaller number of efficient linker groups on the rutile (110) surface in comparison to those available for anatase (101). The role of the anchor binding mode was also studied theoretically by Jakubikova and co-workers.<sup>526</sup> They found that the bidentate coordination of a phosphonate anchor increases the injection rate by 1 order of magnitude, as compared to the monodentate coordination.

The chemistry of the interaction between the anchoring group and the substrate is not the only factor that determines the ET rate. The fraction of the electron density of the sensitizer excited state localized on the group is what quantitatively characterizes the electron injection rates discussed in the previous paragraph. This idea has been validated in later studies by the Troisi group, which examined the injection times for perylene with carboxylate anchoring groups in different positions.<sup>146,500</sup> Although the anchoring group was the same in each case (–COOH), the fraction of the LUMO localized on it varied for different isomers (Figure 33).

To eliminate the effects of the injection energy levels for the different isomers, the theoreticians artificially fixed it to the value of one of the chromophores. Thus, only the effects of orbital localization were under investigation. The calculated injection rates changed by an order of magnitude, correlating with the fraction of the LUMO localized on the anchor group (Table 6). The experimental results for injection energies of each chromophore are in agreement with these predictions. Table 6 also shows the comparison of the injection times for other dyes having energies of the excited states similar to those previously discussed. The ET rates for these dyes vary by 2

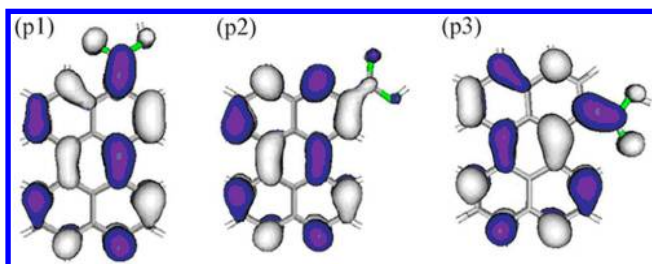


**Figure 33.** Charge density of the excited perylene chromophore with different positions of the carboxylate anchoring group. The fraction of the excited electron density on the ( $-\text{COO}^-$ ) group is significant in isomers p1 and p3, and negligible for p2. Adapted with permission from ref 146. Copyright 2010 PCCP Owner Societies.

**Table 6.** Effect of the Fraction of the LUMO, Localized on the Anchor Group, and the Injection Energy on the ET Rate<sup>a</sup>

chromophore	injection energy, eV	injection time, rutile (110), fs	injection time, anatase (101), fs	% of LUMO, localized on anchor
P2, shifted	-2.32	17.94		2.89%
P3, shifted	-2.32	4.75		9.44%
P1	-2.32	5.31	2.71	11.1%
P2	-2.12	21.24	5.29	2.89%
P3	-2.27	5.14	1.93	9.44%
P1	-2.32	5.31	2.71	11.1%
(a)	-2.72	21.05	4.32	7.8%
(c)	-2.73	1584.2	73.16	0.22%

<sup>a</sup>See Figure 29 for the structure of dyes (a) and (c), and Figure 33 for the structure of dyes P1, P2, and P3.

orders of magnitude, in agreement with the fraction of the LUMO localized on the anchor group of the corresponding dyes.

An experimental study on two structurally similar dyes differing only in anchor composition, cyanoacrylic acid (Figure 34a, DSL2A1) and rhodamine-3-acetic acid (Figure 34a, DSL2A3), showed how electron density distribution can change ET dynamics.<sup>480</sup> In both cases, electron injection occurred on a sub-200 fs time-scale. However, the electron recombination with the oxidized dye for the DSL2A3 dye was faster than that for the DSL2A1 dye, resulting in different photovoltaic efficiencies: 6% for DSL2A1 and 1.7% for DSL2A3. Because only the anchor composition was varied, the different rates of electron recombination can be attributed to qualitative differences in the anchors. The electron that is

injected from the DSL2A3 dye is localized primarily near the interface and can be captured in surface states, facilitating recombination with the oxidized dye (Figure 34b, bottom). On the other hand, the injected electron for the DSL2A1 dye is significantly delocalized toward the bulk of semiconductor, slowing its recombination with the oxidized chromophore, as illustrated in Figure 34b, top.

The electronic and geometric structures of the DSL2A1 and DSL2A3 dyes have been studied theoretically by Peng et al.<sup>527</sup> Their results suggest that the DSL2A1 dye adsorbs in a conformation that is aligned with the surface normal, and that it has a large dipole moment that is perpendicular to the surface (Figure 34c, left). In contrast, the DSL2A3 dye adsorbs in a bent conformation, with the dipole moment forming a 25° angle with the surface plane (Figure 34c, right). Thus, the DSL2A3 dye has a significantly smaller component of the dipole moment normal to the surface. The difference in binding modes, and hence in the normal component of the dipole moments, leads to different CB-edge shifts toward the vacuum energy level, as discussed in detail in section 3.3.3 (Figure 20). The different recombination rates observed in the experiment can also be attributed to differences in the normal component of the dipole moments of the dyes.<sup>480</sup> Because the DSL2A1 dye has a larger component of its dipole moment normal to the oxide surface, Coulomb repulsion between the dye and electron in the  $\text{TiO}_2$  substrate is significant enough to inhibit recombination. This repulsion is weaker in the DSL2A3 dye because of a smaller normal component of its dipole moment; consequently, the recombination of the injected electron with the DSL2A3 dye is faster.

Several experimental and theoretical groups have studied the effect of the anchor group on the rates of interfacial ET for perylene-sensitized  $\text{TiO}_2$ .<sup>147,151,197,524,528,529</sup> Some representative results are shown in Table 7. Because the injection rate is defined primarily by the coupling between donor and acceptor states, it is sensitive to factors that determine this coupling. To illustrate this, consider the excited state of perylene containing a carboxylate group,  $-\text{COOH}$ : it is strongly coupled to the CB states of  $\text{TiO}_2$  via delocalized  $\pi$ -orbitals of the  $-\text{C}=\text{O}$  fragment, while perylene with a phosphate group,  $-\text{P}(\text{O})(\text{OH})_2$ , is weakly coupled to the semiconductor, because the connection is achieved via  $\sigma$ -orbitals of the  $-\text{P}-\text{OH}$  group. This weaker coupling leads to slower electron injection.

**4.1.5. Role of the Linker Group – Sensitizer–Substrate Spatial Separation.** In theoretical and experimental studies, May and co-workers investigated the effect of the length and chemical structure of the linker on the electron

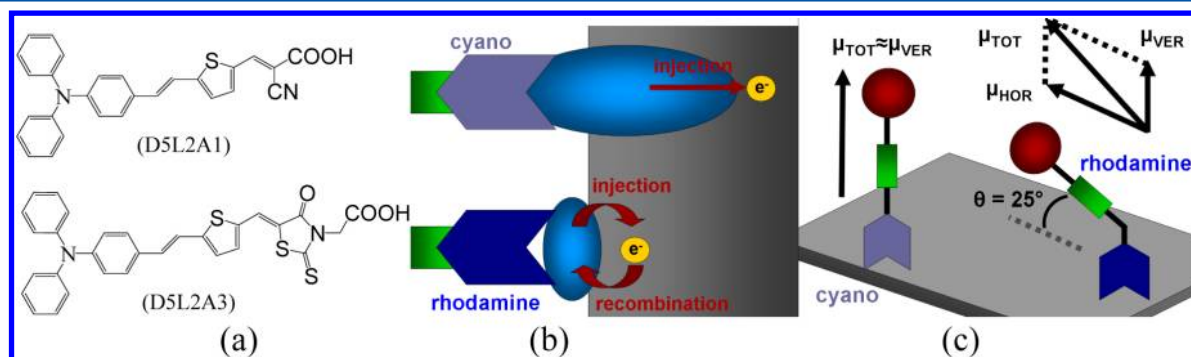


**Figure 34.** Dyes with various anchor groups: (a) chemical structure; (b) schematic of electron density near the anchor and its relationship to the ET processes; and (c) binding geometry of the dyes.

**Table 7. Electron Transfer Times from Perylene into TiO<sub>2</sub> for Different Anchor and Linker Groups**

dye-linker-anchor / substrate	injection time, fs, experimental	injection time, fs, theoretical
DTB-Pe-COOH/TiO <sub>2</sub>	13, refs 147,529	5, ref 147
Pe-COOH/TiO <sub>2</sub>	13, ref 151	5.8, ref 528 5–10, ref 151 2.1–10.8, ref 500 16.2, ref 197
DTB-Pe-(CH) <sub>2</sub> -COOH/TiO <sub>2</sub>	10, ref 147	6, ref 147
Pe-(CH) <sub>2</sub> -COOH/TiO <sub>2</sub>	10, ref 151	6.4, ref 528 6, ref 151 3.4–6.6, ref 500
DTB-Pe-P(O)(OH) <sub>2</sub> /TiO <sub>2</sub>	28, refs 147,529	9, ref 147
Pe-P(O)(OH) <sub>2</sub> /TiO <sub>2</sub>		2.6–14.8, ref 524 41.7, ref 197
DTB-Pe-(CH <sub>2</sub> ) <sub>2</sub> -COOH/TiO <sub>2</sub>	57, ref 147	16, ref 147
Pe-(CH <sub>2</sub> ) <sub>2</sub> -COOH/TiO <sub>2</sub>	57, ref 151	47.4, ref 528 33, ref 151 507–1601, ref 147

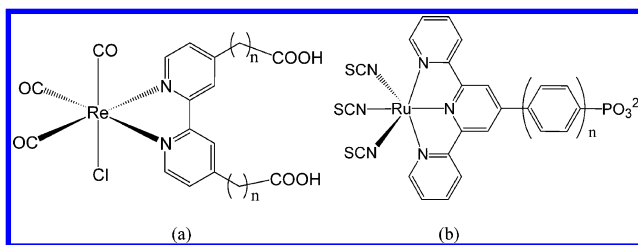
injection rate (Table 7).<sup>147</sup> Similar studies have been performed theoretically by Thoss and co-workers<sup>528</sup> and by Persson and co-workers,<sup>151</sup> also summarized in Table 7. It was found that the addition of a =CH– linker group increases the spatial separation between the dye moiety and the semiconductor surface. Because =CH– is a  $\pi$ -conjugated system, the electron density in the excited state of the dye is delocalized onto the =CH– fragment. Thus, the coupling between the donor and acceptor states is still strong, despite the increased spatial separation between the dye and the semiconductor. As a consequence, the injection time is comparable to that of the system without the linker.

Alternatively, when  $\pi$ -conjugation is not present (for instance, in –CH<sub>2</sub>– linkers), the coupling between the donor and acceptor states rapidly (exponentially) decays as their spatial separation increases. This is reflected in the longer injection times observed with the –(CH<sub>2</sub>)<sub>2</sub>– linker, Table 7.

The Lian group used a methylene-bridged Re(CO)<sub>3</sub>Cl-(dcbpy) dye on an SnO<sub>2</sub> substrate to systematically investigate how injection times depend on the length of the linker between substrate and dye.<sup>504</sup> As expected from ET theory, an increase in the dye–substrate length decreased the coupling and led to slower injection rates. An exponential dependence on the injection rate for sufficiently long ( $n = 3$ –5) linker chains was observed, while for shorter chains ( $n = 1$ –2), the rate was independent of the size of the linker.

$$k(n) = \begin{cases} k(0) \exp(-\beta n), & 3 \leq n \leq 5 \\ \text{const}, & n = 1, 2 \end{cases} \quad (4.6)$$

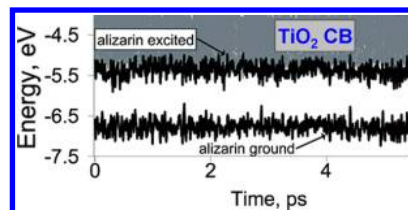
An exponential scaling relationship was obtained experimentally by Moser and co-workers as well, who used a series of conjugated aromatic dyes containing a *p*-oligophenylene linker group (Figure 35b).<sup>502,503</sup> The exponential dependence of the ET rate arises from the fact that the electronic coupling strength is exponentially dependent on distance. Exponential dependence can be interpreted as a decay law in the overlap of the orbitals of the donor and acceptor species that are separated by a given distance, while the ET process can be viewed as

**Figure 35.** Dyes used to study the effect of the dye–substrate separation distance on electron-injection kinetics.

tunneling across the barrier, whose width is determined by the linker length.

The effect of the separation distance between dye and substrate was also studied by Gratzel and co-workers, who found that electron injection from eosin Y (EY) to TiO<sub>2</sub> was several orders of magnitude smaller in the presence of polyvinyl alcohol (PVA).<sup>486</sup> PVA adsorbs on the TiO<sub>2</sub> surface and decreases the interaction between TiO<sub>2</sub> particles, preventing their coagulation. However, the weaker interaction between TiO<sub>2</sub> particles also prevents the EY molecules from adsorbing in close proximity on the TiO<sub>2</sub> surface and decreases the dye–substrate coupling. As a consequence, the observed injection rate is significantly slower than it is in the same system not containing PVA. The fastest ET components in the two cases are  $1.1 \pm 0.3$  ps and  $160 \pm 50$  fs, respectively.

**4.1.6. Role of Vibrational Modes – Thermal Fluctuations.** Thermal fluctuations can have important implications in the electron injection process, particularly when the energy of the excited state of the chromophore is comparable to or lower than the energy of the CB edge of the substrate. For example, consider the alizarin molecule: when the LUMO level is below the CB of TiO<sub>2</sub> at 0 K, ET from alizarin to the semiconductor is prevented. However, the energy difference between the LUMO level of the alizarin molecule and the CB of TiO<sub>2</sub> is relatively small and comparable to the thermal energy. Thus, at ambient temperatures, thermal fluctuations result in energy level crossings between the orbitals of the dye and semiconductor CB (Figure 36). This allows for successful electron injection into the semiconductor on a femtosecond time-scale.<sup>207,484,530</sup>

**Figure 36.** Effects of thermal nuclear motions on the energy of the alizarin excited state. Adapted with permission from ref 530. Copyright 2007 American Chemical Society.

Batista and co-workers investigated catechol-sensitized TiO<sub>2</sub> systems to determine the role of thermal fluctuations on the rates of ET.<sup>531</sup> In their low-temperature studies, they found a significant anisotropy in the charge delocalization along different crystallographic directions.<sup>501</sup> At low temperatures, the orientation of the dye remains fixed at all times, leading to different overlaps between the orbitals that are localized on the dye (donor) or substrate (acceptor) groups. This defines different couplings along different directions, thus resulting in anisotropic charge diffusion. In contrast, at room temperature,



anisotropy becomes significantly less pronounced.<sup>531</sup> This is because at higher temperatures, the orientation of the chromophore molecules is averaged over all directions, leading to isotropic ET.

In addition, at low temperatures, ET in the catechol/TiO<sub>2</sub> system occurs in two steps, initial fast interfacial charge transfer ( $\sim 3$ – $6$  fs), followed by slow charge diffusion in the TiO<sub>2</sub> substrate ( $\sim 38$  fs).<sup>501,531</sup> Thus, the kinetics can be described by a two-exponential law. In contrast, at room temperature, the overall charge transfer process can be described by a single-exponential kinetics law with a decay time of  $\sim 2.5$  fs for injections from the LUMO or LUMO+1. The charge is almost completely transferred within 10 fs.

Ramakrishna and co-workers used model systems to study the coupling of vibrational modes with electronic states.<sup>532–535</sup> One of their major conclusions was that nuclear vibrations become less important in the case of zero reorganization energy, provided that the electronic couplings and the density of acceptor states vary slowly as a function of nuclear coordinates. When these conditions are met, nuclear motion does not affect the electronic wave functions, and hence the thermal fluctuations do not have a significant effect on the ET rates. Inversely, thermal fluctuations will affect ET rates if the reorganization energy associated with any of the vibrational modes is large, or if the electronic coupling varies strongly with nuclear coordinates. In such cases, neglecting vibrational modes will result in overestimated ET rates.

Another important effect of thermal vibrations is that they significantly change the coherences of the electronic states involved in ET reactions. Kondov and Thoss explicitly studied the role of electron–vibration coupling in coumarin-343 on a TiO<sub>2</sub> surface.<sup>195,196</sup> They found that if only electronic couplings are used and electron–vibrational interactions are ignored, quantum interference effects become significant; the population of the donor state oscillates in time (Figure 37). When the

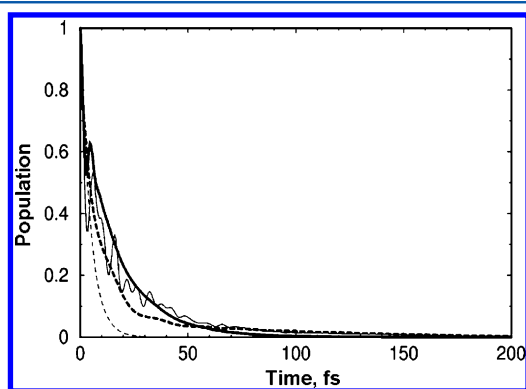


**Figure 37.** Population of the donor state, obtained using *ab initio* (solid lines) and semiempirical (dashed lines) models. Results obtained with fully vibronic and purely electronic descriptions of ET dynamics are represented by the thick and thin lines, respectively. Adapted with permission from ref 196. Copyright 2007 American Chemical Society.

coupling to nuclear motions is present, the coherence of the electronic states is quenched rapidly. By quenching electronic coherence, nuclear modes generally slow ET. This conclusion represents an example of the so-called quantum Zeno effect, which states that quantum transitions slow and even stop altogether if interactions with the environment induce coherence loss.<sup>159,536</sup>

Numerous studies have reported oscillations in the population of the donor state, either when a purely electronic description was employed or when full vibronic wave functions were used with specific parameters. These oscillations were quenched when coupling to vibrational modes was introduced, or when other parameter values were chosen with the vibronic states.<sup>501,531–535,537</sup> The quenching of the quantum oscillations by the thermal motion of the nuclei illustrates the fact that vibrational modes are the physical origin for the decoherence of quantum states. The coupling to vibrational modes becomes more important as the intrinsic time-scale for ET increases. When electron injection happens on a time-scale of a few femtoseconds, only high-frequency modes are involved. However, as the overall rate of ET decreases, the role of lower-frequency vibrations becomes more pronounced.

**4.1.7. Interaction with a Field.** In most studies of injection dynamics on an interface, it is assumed that the excited state has been prepared with a quantitative yield. However, an explicit description of the light–matter interaction that occurs during the photoexcitation step may be crucial for a more accurate description of the photoinduced ET and estimation of the power conversion efficiency in photovoltaic cells. An explicit modeling of the interaction of a dye with a laser field has been performed by the May group.<sup>25,147,148</sup> These simulations revealed that the laser pulse might only result in a partial population of the excited state. The quantum yield in such cases is less than 100%, and a significant fraction of dye molecules remains in the ground state after photoexcitation. In particular, for perylene derivatives attached to a TiO<sub>2</sub> surface (Figure 38), nearly 30–40% of the population remains in the ground state after the laser pulse excitation. This fraction is larger for systems with smaller donor–acceptor coupling.

The strength of the electronic coupling between donor and acceptor states can define different mechanisms for the injection of photoexcited electrons. In the case of strong coupling (Figure 38a), the laser pulse will populate the charge transfer state almost instantaneously, leading to one-step charge separation. On the contrary, if the coupling is relatively weak, the laser pulse initially populates the excited state, which later decays to the charge-separated state (Figure 38b). The entire process involves two elementary reactions: the creation of an exciton localized on the chromophore, followed by its dissociation and ET into the semiconductor.

In numerous theoretical studies of interfacial ET, the initial state of the system is assumed to be prepared with the excitation localized on the chromophore (refs 146, 154, 484, 501, 518, 524, 526, and 530). This assumption breaks down when ET proceeds through a direct-injection mechanism. To accurately describe this mechanism, the interaction with the electromagnetic field of a laser during the excitation stage should be explicitly accounted for. As discussed in section 3.3.2, when the light–matter interaction is considered explicitly, the initial state of the system corresponds to its ground electronic state. Once the interaction with a field has occurred, the system evolves into an excited state (which can be localized on the chromophore, leading to a two-step ET) or on the semiconductor, resulting in direct electron injection.

**4.1.8. Direct and Sequential Electron Injection.** To thoroughly study the direct-injection mechanism and to distinguish it from the two-step sequential mechanism, the Sanchez group performed TD-DFTB calculations that explicitly included the field–matter interaction on the initial photo-



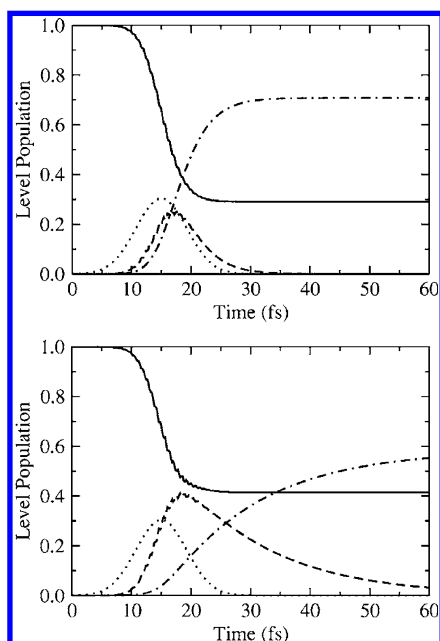


**Figure 38.** Population of the ground, excited, and charge transfer states, solid, dashed, and dashed–dotted lines, respectively, during the photoexcitation process. The dotted line represents the envelope of the laser pulse envelope. Upper panel: strong donor–acceptor coupling. Lower panel: weak donor–acceptor coupling. Reprinted with permission from ref 25. Copyright 2006 American Institute of Physics.

excitation stage.<sup>176,538</sup> They identified the qualitative differences between the direct and indirect mechanisms using theoretical simulations (Table 8). The fundamental differences between

**Table 8. Signatures of Direct and Indirect Interfacial ET Mechanisms from Time-Dependent Simulations**

parameter	direct injection	sequential injection
absorption spectrum	appearance of new bands (peaks)	no new bands (peaks)
dependence of interfacial current on field strength $E$	$\sim E^2$	$\sim E^3$
population of states (e.g., LUMO) as a function of time	complex, population transfer between states	monotonic decay (rise)

systems proceeding through direct or indirect mechanisms of ET were found to be attributed to the degree of change of the dye electronic structure upon its adsorption on the  $\text{TiO}_2$  surface.

Sanchez-de-Armas and co-workers performed systematic TD-DFT studies on interfacial ET for a number of dyes.<sup>539</sup> These dyes varied in their ability to support ET through either the direct or the indirect mechanism. To highlight one example from their study, if a catechol molecule is used as a sensitizer, ET occurs by the direct injection mechanism; if the NKX-2311 dye is used, ET proceeds via the sequential mechanism (Figure 39,  $x$ -axis). Intermediate situations are also possible, which involve different ratios of direct and sequential ET contributions. Rocca and co-workers also used TD-DFT and found the squarane molecule to be an intermediate case.<sup>540</sup>

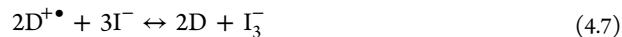
The fundamental factor that determines which ET mechanism will occur is the degree to which the electronic structure of the dye changes upon adsorption on the substrate.

This effect partially correlates with the size of the dye. For instance, consider the case of a small catechol molecule adsorbing on an oxide surface. Its orbital energy levels shift due to the interaction; the energy of the LUMO level of the free dye molecule (Figure 39a, leftmost) goes up, corresponding to the energy of the LUMO+43 level of the dye–semiconductor system (Figure 39b, leftmost). The photoexcited state of catechol is deep in the CB of the semiconductor. Strong donor–acceptor coupling results in hybridization and shifts in its orbital energies. Inversely, these shifts provide an indication of strong donor–acceptor coupling, which facilitates the direct ET channel, in which the electron is photoexcited from the catechol HOMO into the  $\text{TiO}_2$  CB edge. The optical transition corresponding to the direct ET mechanism creates a new band in the optical absorption spectrum (see Table 8).

In contrast, for larger sensitizers, the change in the electronic structure upon adsorption is smaller. This results in the energy of the free photoexcited dye (Figure 39a, right side) to reside near the energy of the excited state of the adsorbed dye (Figure 39b, right side). Thus, the LUMO of the photoexcited dye– $\text{TiO}_2$  system will be very similar to the LUMO of the free-dye, and will therefore be localized primarily on the dye. The fact that changes in the electronic structure of larger sensitizers are small upon adsorption is due mainly because of weaker donor–acceptor coupling, which arises from the larger spatial separation of the donor and acceptor electronic states. In addition, larger sensitizers have smaller excitation energies. Their LUMOs are lower in energy and correspond to a lower density of states in the  $\text{TiO}_2$  CB, decreasing the possibility for donor and acceptor state mixing. The overall effect can be described as the preparation of a photoexcited state on the dye fragment, followed by a separate ET step, resulting in the two-step sequential ET.

## 4.2. Kinetics of Electron Transfer from Substrate to Electrolyte

**4.2.1. Electrolyte Equilibria.** For a DSSC to operate, a photo-oxidized dye molecule must be reduced so that the next photon can be absorbed, and the cycle can then be repeated. To achieve this, a counter-electrode and photoelectrode are connected by an electrolyte medium. The molecules of the electrolyte are reduced on the counter-electrode and diffuse to the photoexcited dye, where they are oxidized by the dye molecule, reducing the dye and allowing the next cycle of operation to proceed. The most common electrolyte used in Gratzel-type cells is the iodide–triiodide pair  $\text{I}^-/\text{I}_3^-$ , although other electrolyte types are frequently used, such as butyronitrile-based,<sup>541</sup> disulfide/thiolate,<sup>542</sup> or metallo–organic.<sup>543,544</sup> The electrode half-reactions for the iodide–triiodide pair can be written as:



Other than  $\text{I}^-$  and  $\text{I}_3^-$ , a number of intermediate species, such as  $\text{I}_2^-$  and  $\text{I}_2$ , are present in the system, although their concentration is negligibly small because of a large association constant:

$$\text{I}_2 + \text{I}^- \leftrightarrow \text{I}_3^-, \quad K_s = \frac{a_{\text{I}_3^-}}{a_{\text{I}_2} a_{\text{I}^-}} \quad (4.9)$$

However, intermediate species do play important roles during the ET processes at the metal oxide interface. The constant  $K_s$

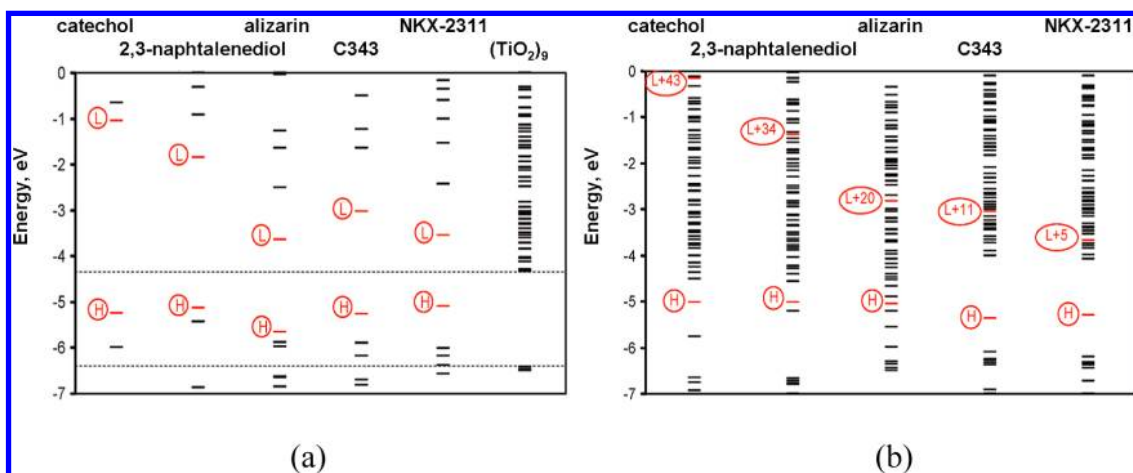


**Figure 39.** Explanation of the origin of the direct and indirect ET mechanisms. (a) Electronic structure of free dyes and a  $\text{TiO}_2$  cluster; and (b) electronic structure of the dye– $\text{TiO}_2$  system. The LUMO (L) and HOMO (H) energy levels of the free dye (a) correspond to the orbitals of the combined system marked in color in panel (b). Adapted with permission from ref 539. Copyright 2011 American Chemical Society.

is  $\sim 10^3 \text{ M}^{-1545}$  in water and  $\sim 10^7$  in acetonitrile.<sup>546</sup> The  $\text{I}_2^-$  species is formed from  $\text{I}_2$  by accepting an electron, eq 4.10.  $\text{I}_2^-$  can be reduced to iodide anions, as shown in eq 4.11, or dismutate to produce iodide and triiodide species, eq 4.12:



The electrons in eqs 4.7–4.11 come from either the counter-electrode or the photoelectrode; in the latter case, the process is called back electron transfer (back-ET). Similar to the case in which the photoinjected electron recombines with the oxidized dye, back-ET constitutes one of the main sources of energy loss in photovoltaic cells. Thus, one of the main objectives in the design of efficient solar cells is to understand the mechanisms of back-ET and to modify the setup to reduce its effect.

**4.2.2. Electron Loss to Electrolytes.** **4.2.2.1. Preventing Electrolyte–Oxide Interaction.** To reduce back-ET from the semiconductor to the electrolyte, special additives, such as pyridine derivatives<sup>511,547,548</sup> and guanidinium thiocyanate, are used.<sup>549</sup> When the additive molecule is adsorbed on the surface, it forms a protective layer between the metal oxide and the electrolyte. Thus, a large increase in the power conversion is available with an appropriately chosen solvent.<sup>514</sup> For example, the adsorption of acetonitrile and pyridine on a  $\text{TiO}_2$  surface was shown to be able to compete with the adsorption of the electrolyte and, therefore, potentially reduce the losses due to back-ET.<sup>546</sup>

A similar effect can be achieved for sensitizers with hydrophobic side-chains, as discussed in section 3.3 (e.g., see Figure 25). On the contrary, dyes, which specifically bind to the electrolyte species and thereby bring them closer to the semiconductor surface for a longer duration, can increase recombination rates.<sup>550,551</sup> A structural change as small as two atoms can lead to a notable increase in the recombination rates between the electrolyte and the dye. For example, substitution of only two oxygen (hard) atoms with sulfur (soft) atoms in a side ligand of a dye increases its interaction with the triiodide (soft) molecules, thus reducing the average distance and facilitating the electronic coupling between the surface and the electrolyte.

The recombination that occurs in QD-sensitized semiconductors can be significantly different from similar processes in dye-sensitized analogues, as discussed by Hod and co-workers.<sup>423</sup> This difference originates from the fact that the surface of a semiconductor sensitized with organic or metallo-organic dyes is more accessible to the electrolyte species. The electrolyte species is then able to easily migrate to the surface of the semiconductor and accept the photoinjected electrons. In contrast, when the QD adsorbs on the substrate, the substrate becomes inaccessible to the electrolyte, and direct back-ET from the semiconductor to the electrolyte is impossible. Instead, an electron, injected into the oxide, can migrate back to the oxidized QD, where it can be transferred to the electrolyte particles. Coating the QD with ligands can reduce the rate of this process and increase the efficiency of the device. This procedure is fairly similar to the use of additives in the DSSC.

Although the qualitative conclusions regarding the role of the solvent or additives in reducing back-ET (as well as the quantitative measurements of the solar cell parameters, such as open-circuit voltage and the photocurrents) have been made, a detailed description of the processes involved in back-ET is still not available. Studies of electron recombination from the surface to the electrolyte are significantly less numerous than studies of electron injection that were discussed in section 4.1. This can partially be attributed to the qualitative difference in the types of processes and systems involved in back-ET as compared to dye–semiconductor ET. For example, a dye molecule is typically bound to a semiconductor surface via covalent bonds, providing strong coupling between the donor and acceptor states and resulting in fast injection times. In addition, such a process usually does not involve significant conformational changes of the system. On the other hand, electrolyte molecules, such as  $\text{I}^-$  and  $\text{I}_2^-$ , are bound to the surface via electrostatic interactions, and can move freely near the surface. In such a case, the coupling can fluctuate significantly and is generally slight because of the larger distance between the electrolyte species and the surface. The coupling in back-ET takes place through-space rather than through a directional bond. The large fluctuations in the position of the electrolyte species will induce significant reorganization effects on the solvent. These effects result in very slow back-ET rates, in the range of nanosecond to

millisecond time-scales. Thus, a direct theoretical simulation of these processes is only possible for a limited number of systems, in which the time-scales are sufficiently small.

**4.2.2.2. Direct Dynamics Simulation of ET Involving Electrolytes Adsorbed on the Oxide Surface.** The dynamics of charge recombination from the surface of  $\text{TiO}_2$  to the  $\text{I}^-/\text{I}_2^-$  electrolyte has been simulated directly using nonadiabatic molecular dynamics by Duncan and Prezhdo.<sup>530</sup> The simulations were performed for a pure electrolyte–substrate system, as well as for systems with adsorbed dye molecules. The calculations assumed that all involved species have diffused to the surface of the oxide and that the solvent does not have significant effect. Although this description is approximate, it allows for insight into the details of the electron transfer process.

The adsorption of the electrolyte  $\text{I}_2^-$  molecules on the semiconductor surface shifts the positions of the LUMO of the dye toward the vacuum level (positive energy), in comparison with the system in which only the dye is adsorbed. Together with thermal fluctuations, this allows for efficient charge injection from the photoexcited dye into the  $\text{TiO}_2$  CB (Figure 40).

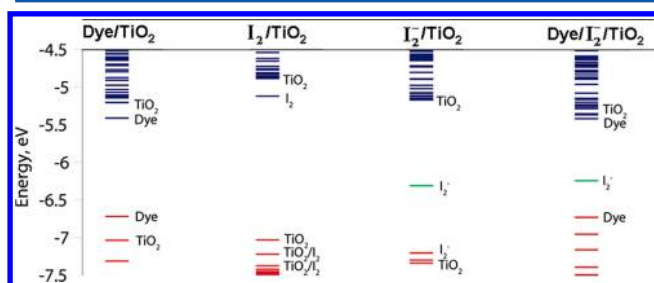


**Figure 40.** Energy diagram for dye/ $\text{TiO}_2$ ,  $\text{I}_2^-/\text{TiO}_2$ ,  $\text{I}_2^-/\text{TiO}_2$ , and dye/ $\text{I}_2^-/\text{TiO}_2$  systems. Adapted with permission from ref 530. Copyright 2007 American Chemical Society.

In the absence of the  $\text{I}_2^-$  species, the electron injected into  $\text{TiO}_2$  relaxes to the CB and reaches a quasi-thermal equilibrium at the CB edge states (Figure 41b). This process occurs on the time-scale of  $\sim 100$ – $200$  fs, independent of the initial injection

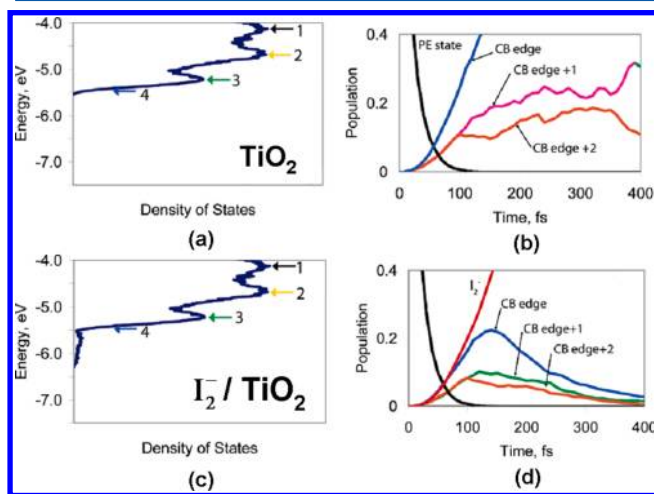


**Figure 41.** Electron injection energies in the  $\text{TiO}_2$  (a) and  $\text{I}_2^-/\text{TiO}_2$  (c) systems. Population of different states as a function of time in the  $\text{TiO}_2$  (b) and  $\text{I}_2^-/\text{TiO}_2$  (d) systems. Adapted with permission from ref 530. Copyright 2007 American Chemical Society.

level (Figure 41b). The presence of the coadsorbed electrolyte significantly changes the dynamics of electron relaxation in the CB of  $\text{TiO}_2$ . Because the energy level of the  $\text{I}_2^-$  LUMO is lower than the CB edge of pure  $\text{TiO}_2$  (Figure 41c), the  $\text{I}_2^-$  species becomes the final electron acceptor. The CB edge states show a transient population, because these states have intermediate relaxation rates (Figure 41d). At the initial stages, the rise of the  $\text{I}_2^-$  population occurs simultaneously with the rise of the population of the CB edge states. Thus, the relaxation of the CB edge will populate the  $\text{I}_2^-$  state only at longer times, starting at 100–150 fs from the initial injection. Therefore, in the initial stages, a direct transition from higher energy states of the  $\text{TiO}_2$  CB to the LUMO of  $\text{I}_2^-$  is a major source of back-ET. In all cases, the relaxation rates are reported to be independent of the initial energy of the excited state.<sup>530</sup> The time-scales for electron transfer to the electrolyte adsorbed on the  $\text{TiO}_2$  surface are in the range of 200–300 fs.

Although the LUMO of the electrolyte  $\text{I}_2^-$  and the HOMO of the dye are relatively close in energy (see Figure 40), ET between these states is slower (Figure 42a) than, for instance, ET between  $\text{TiO}_2$  and an oxidized chromophore (Figure 42b). This can be attributed to the fact that the coupling between the electrolyte and chromophore states is significantly smaller than the chromophore– $\text{TiO}_2$  coupling. Although the positively charged dye group and negatively charged  $\text{I}_2^-$  molecule are attracted electrostatically, the electrolyte remains relatively mobile, because it does not form chemical bonds with the dye. This leads to weak coupling and slow ET between these species. It is also possible for ET to take place indirectly through the mutual coupling of both the dye and the electrolyte molecules to the states delocalized in  $\text{TiO}_2$ . However, because the indirect transfer involves many intermediate surface states, it is also relatively slow and proceeds on a time-scale of  $\sim 1$  ps (Figure 42a). In comparison, the charge transfer between  $\text{TiO}_2$  surface states and the oxidized chromophore proceeds on a time-scale of  $\sim 660$  fs (Figure 42b).

In their simulations, Duncan and Prezhdo found that the electron recombination from  $\text{TiO}_2$  back to the oxidized dye is slightly faster in the presence of the  $\text{I}_2^-$  species (Figure 42c) than in the pure dye/ $\text{TiO}_2$  system (Figure 42b).<sup>530</sup> This slight acceleration happens for several reasons. First, additional relaxation channels, not present in the pure dye/ $\text{TiO}_2$  system, appear via intermediate  $\text{I}_2^-$  states. Second, the adsorption of the  $\text{I}_2^-$  particles changes the electronic structure of the  $\text{TiO}_2$  and the dye, bringing CB edge states of  $\text{TiO}_2$  closer to the dye LUMO (Figure 40). Because of the close energy proximity of the  $\text{TiO}_2$  states and dye-excited state, the orbitals are more likely to mix (hybridize). This leads to stronger nonadiabatic coupling between the  $\text{TiO}_2$  CB states, which now contain an admixture of the dye LUMO, and the dye HOMO, and, therefore, to faster back-ET to the chromophore ground state. One of the manifestations of the orbital mixing is a significant delocalization of the LUMO into the  $\text{TiO}_2$  slab in the combined system, containing  $\text{I}_2^-$  coadsorbed particles (Figure 43b), in contrast to the system composed of only dye and oxide (Figure 43a).

**4.2.2.3. Molecular Dynamics of the Oxide–Electrolyte Interaction.** The charge transfer from  $\text{TiO}_2$  to the electrolyte considered by Duncan and Prezhdo was studied under the assumption that the electrolyte species was already adsorbed on the surface. In addition, they assumed that the electrolyte substitutes for one of the surface –OH groups. However, the migration of the iodine-containing particles to the surface requires a significant solvent shell distortion and is therefore



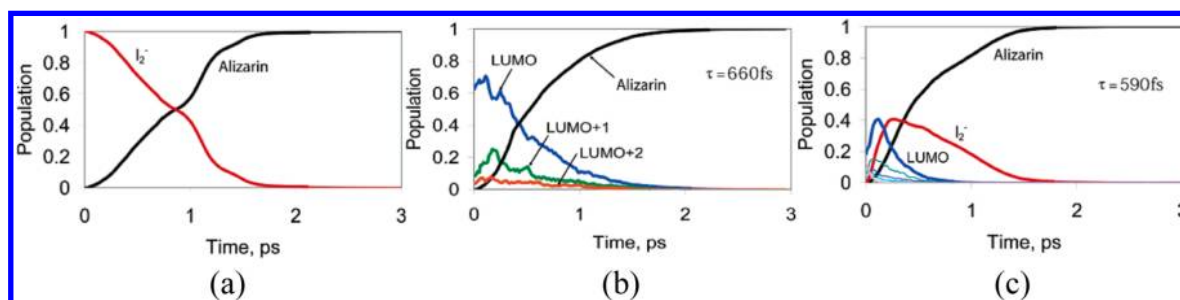


**Figure 42.** Dynamics of ET (a) from  $I_2^-$  to alizarin dye; (b) from  $TiO_2$  to alizarin; and (c) same as (b) but in the presence of  $I_2^-$  ions. Adapted with permission from ref 530. Copyright 2007 American Chemical Society.

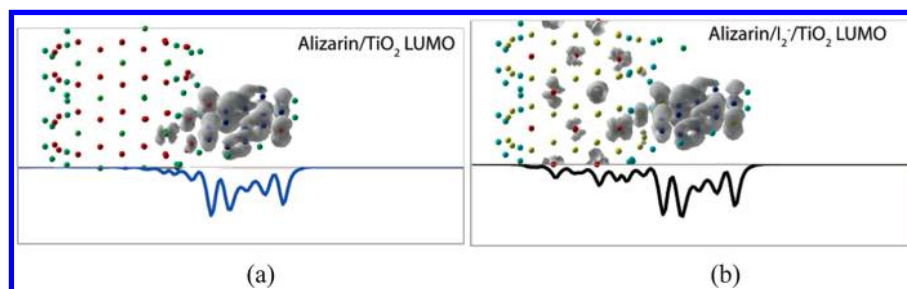


**Figure 43.** Localization of the electron density of the LUMO of alizarin/ $TiO_2$  system (a) and combined alizarin/ $I_2^-$ / $TiO_2$  system (b). The profile of the integrated charge density along the surface normal is shown in the bottom. Adapted with permission from ref 530. Copyright 2007 American Chemical Society.

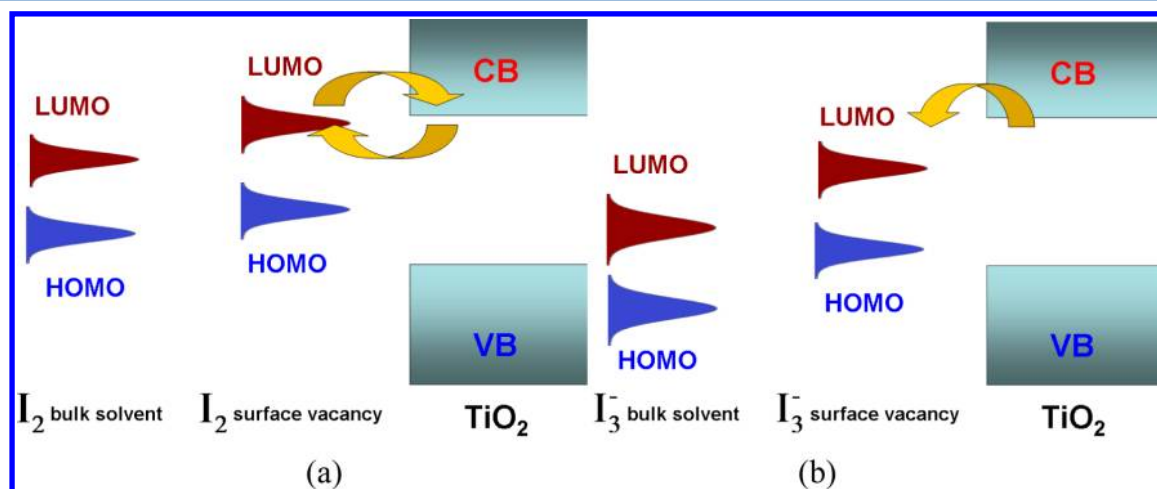


**Figure 44.** Charge transfer mechanisms for electrolyte species  $I_2$  (a) and  $I_3^-$  (b) on the  $TiO_2$  surface.

very slow. A detailed atomistic calculation of these rates and the associated energy changes were performed by da Silva and co-workers.<sup>546</sup> Using molecular dynamics simulations with ab initio parametrization, they have found that the barriers for entering the first layer of solvent molecules on the semiconductor surface are  $\sim 17$ , 20, 32 kcal/mol for the  $I_3^-$ ,  $I_2^-$ , and  $I^-$  particles, respectively. The energies for leaving this first layer are slightly higher:  $\sim 23$  for the  $I_3^-$  and  $I_2^-$  species and  $\sim 35$  kcal/mol for  $I^-$ . The potential energy barriers for adsorption of these species are very small or nonexistent. The barriers reported correspond to free energy, and hence reflect entropic and solvation effects, which are particularly important in polar solvents such as acetonitrile and water.

The free energy barriers correlate with the hardness of the ions; for instance, the barriers are largest for  $I^-$ . As the size of ions with the same charge increases, the hardness drops, and the electrostatic interaction with the polar environment

decreases. This is particularly true of the larger  $I_3^-$  and  $I_2^-$  ions, in which the charge is significantly delocalized over 3 and 2 iodine atoms, respectively. The free-energy barrier is very small: 1–2 kcal/mol for the electroneutral  $I_2$  species. However, the concentration of this species is also small, because of the large equilibrium constant for the formation of the triiodide ion, as shown in eq 4.9.

Assuming the diffusion constant of the ionic species is equal to  $D \approx 1.3 \times 10^{-5} \text{ cm}^2/\text{s}$ ,<sup>552</sup> the calculated rate constants for delivery of  $I_3^-$  and  $I_2^-$  to the semiconductor surface are estimated to be  $k_d(I_3^-) \approx 4 \times 10^{-2} \text{ s}^{-1}$  and  $k_d(I_2^-) \approx 3 \times 10^{-4} \text{ s}^{-1}$ , respectively.<sup>546</sup> Therefore, even though the back-ET from the semiconductor is relatively fast, the removal and intake of the reduced and oxidized electrolyte species, respectively, is the rate-limiting factor for the overall process and can have a significant impact on the performance of the DSSC. Decreasing the polarity of the solvent can decrease the free-energy barriers

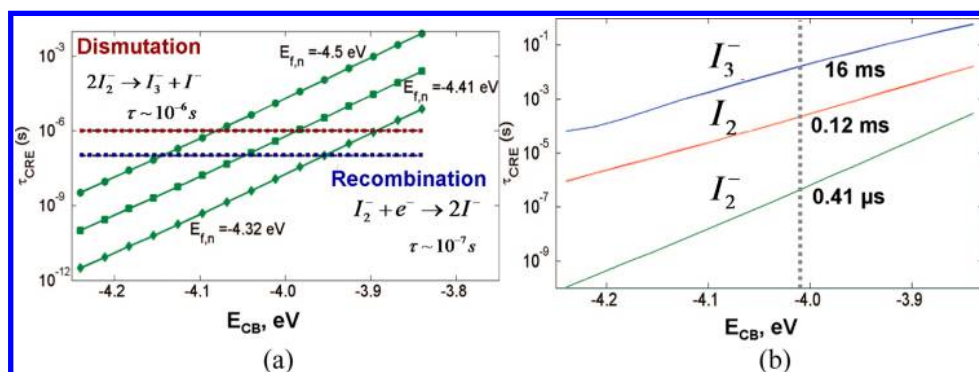


**Figure 45.** Charge recombination (CRE) times obtained in the modeling of back-ET from the oxide surface to the electrolyte species. (a) Overall back-ET times as functions of the CB edge energy. The three values of the quasi-Fermi energies,  $E_{F,m}$ , correspond to different concentrations of electrons in the photoelectrode, depending on illumination. The horizontal lines represent experimental time-scales of the dismutation and recombination reactions. (b) Computed back-ET times involving different electrolyte species under illumination as functions of the CB edge energy. Adapted with permission from ref 152. Copyright 2012 American Institute of Physics.

related to solvation effects, and hence increase the exchange rates of the electrolyte species near the surface of semiconductor.

Electronic structure calculations, performed by the same authors, da Silva et al., indicated that it is possible for the back-ET mechanisms for the  $I_2$  and  $I_3^-$  particles to be qualitatively different.<sup>546</sup> When the particles cross the solvation free-energy barriers and reach the surface of the semiconductor, their orbital energies are shifted toward the vacuum level (Figure 44), with the extent of the shift depending on the particle. Upon adsorption of the  $I_2$  molecule on a vacancy defect site of the  $TiO_2$  surface, its LUMO level is pushed up and almost reaches the CB edge of the semiconductor (Figure 44a). Thermal fluctuations may cause the energy levels to cross, resulting in charge transfer and the dissociation of  $I_2^-$ , eq 4.10, followed by the second ET step, eq 4.11. This mechanism has been proposed by Liu and co-workers<sup>553</sup> and experimentally supported by Green and co-workers.<sup>554</sup> In contrast, the LUMO of adsorbed  $I_3^-$  stays significantly below the CB edge of the semiconductor (Figure 44b). Thus, the back-ET to the  $I_3^-$  particle will be significantly slower than the transfer to the  $I_2$  particle.

**4.2.2.4. Multiscale Modeling of the Back-ET Process.** The discussed theoretical methodologies by Duncan and Prezhd, as well as by da Silva and co-workers, considered two complementary phases of interfacial ET between the semiconductor surface and the electrolyte dissolved in a liquid phase. Both approaches consider the processes on different time-scales. A combined theoretical–experimental approach for the description of the back-ET process from the anatase surface to the iodide/triiodide electrolyte shuttle, covering a large range of the time-scales using the same basic foundation, has been developed recently in the Troisi group.<sup>152,153</sup> The description of the ET processes is based on nonadiabatic formalism (discussed in section 2, eqs 2.66, 2.67, for example), although some of the parameters in the model are obtained from available experimental data.

Some parameters entering the model, such as the reorganization energy,  $\lambda$ , the reciprocal electron half-time,  $\Gamma(E)$ , and the energy difference between the initial (oxidized) and final (reduced) states of the electrolyte can be obtained from ab initio calculations. They can also be derived from available experimental data or from a combination of both methods. The other two parameters of the model, the CB edge

energy of semiconductor,  $E_{CB}$ , and the quasi-Fermi energy level,  $\epsilon_F$ , can be derived by purely theoretical means.<sup>153</sup> However, as discussed in section 4.1, it is possible that the position of the CB edge could change significantly upon the adsorption of solvent molecules and additives, or from modifications of pH, temperature, and ionic strength. If  $E_{CB}$  is obtained from ab initio calculations, it can depend significantly on the level of theory used.

The quasi-Fermi energy,  $\epsilon_F$ , is prone to uncertainties from experimental conditions. It depends strongly on whether the system is in the working mode under light illumination or in the standby (dark) mode. Under illumination, electrons are injected from the sensitizer into the semiconductor, so the concentration of charge carriers increases. On the other hand, a higher concentration of electrons in the CB of the semiconductor will accelerate electron recombination. Under illumination, a quasi-equilibrium, steady-state charge density is reached, and determines the quasi-Fermi level according to eq 4.4.

To minimize the uncertainties and to reflect possible variations in operational conditions, both  $E_{CB}$  and  $\epsilon_F$  were allowed to vary within a given range, and their values were determined on the basis of experimental data. Such data included the following observations:

- Back-ET to  $I_2$  is approximately 2 orders of magnitude faster than that for  $I_3^-$ .<sup>554,555</sup>
- Under dark conditions, the absolute rate of back-ET is on the order of 0.01–1 s.<sup>556</sup>
- Under illumination, back-ET is significantly faster<sup>39</sup> ( $\sim 100$  ns<sup>557</sup>) than under dark conditions (0.5 s).<sup>558</sup>

The ratio of the recombination rates to  $I_2$  and  $I_3^-$  mentioned in point (a) above, as well as the absolute recombination rate under dark conditions described in point (b) above, have been reproduced with the value of  $E_{CB} = -4.24$  eV.<sup>152</sup> A similar value for the CB edge was found experimentally for a  $TiO_2$ /water interface.<sup>330</sup> However, to match the experimental data obtained under illumination, mentioned in point (c) above, with the rate constant for the dismutation reaction, eq 4.12, the  $E_{CB}$  value should be within the relatively narrow interval of  $-4.07$  to  $-3.95$  eV (Figure 45a), which is significantly higher than the value for the dark conditions. The recombination rates were calculated for different electrolyte species (Figure 45b). In particular, using the above value for  $E_{CB}$  gives the recombination times of 16 ms, 0.12 ms, and 0.41  $\mu$ s for  $I_3^-$ ,

$I_2$ , and  $I_2^-$ , respectively. The computed ratio of the recombination rates to  $I_2$  and  $I_3^-$  is also close to the experimentally observed ratio stated in point (a) above.

## 5. PHOTOCATALYTIC PROCESSES

From the time of Fujishima and Honda's observation of photocatalytic water splitting<sup>32,559</sup> and carbon dioxide reduction in colloidal  $\text{TiO}_2$ ,<sup>560</sup> research in this area has grown exponentially. As reported by Kubacka, over 1000 publications per year from 2000 to the present can be found using the search tags "photocat\*" and "oxide/semiconductor".<sup>6</sup> Progress in the field of photocatalysis has been reviewed several times over,<sup>4,6,7,27,40,299,561–564</sup> and while a large pool of experimental knowledge has been amassed, a relatively small number of studies have been dedicated to the theoretical description of the processes that occur in photocatalytic systems. In this section, we will focus on the progress in theoretical studies that tie in to the experimental observations. This integration of information will allow us to construct a framework for a more detailed and thorough understanding of the factors that affect the performance of photochemical cells.

The operation of the simplest photocatalytic cell is quite similar to that of the photovoltaic cell and is schematically shown in Figure 46. Initial photoexcitation in the photocatalytic

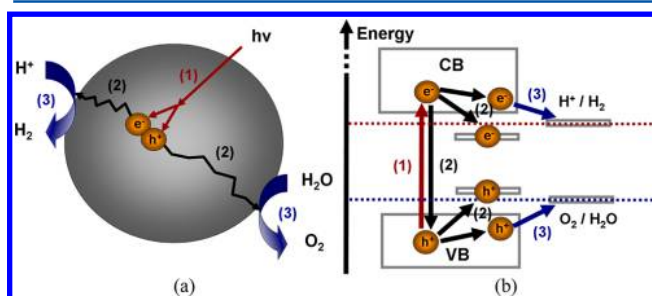


**Figure 46.** The general operation scheme of a photocatalyst: (a) in physical space; and (b) in the energy domain. Processes are denoted as follows: (1) photoexcitation, (2) charge carrier transport and recombination, and (3) chemical reactions.

material creates an electron–hole pair (step 1). Particles that are created can then diffuse to the reaction sites on the surface of the semiconductor or they can undergo recombination (step 2). During a charge carrier diffusion to the surface, the particles can either recombine with one another (radiatively or nonradiatively) or they can be caught in trap states (i.e., vacancies and defects), which reside below the original semiconductor CB edge. Because these states are energetically lower than the reactant states, the process of escaping from such trap states is very slow, and therefore the photocatalytic cell's efficiency is decreased. Finally, when the electrons and holes reach the surface, they can drive the chemical transformations of reduction or oxidation, respectively (step 3). In the following subsections, we will discuss each of these steps in greater detail.

### 5.1. Photoexcitation

The primary photocatalytic cell design consideration in regards to photoexcitation is in choosing materials that have the proper positioning of the VB and CB edges in the semiconductor. For a photoreduction (i.e., a reaction involving the photoexcited electron) reaction to be thermodynamically possible, the CB edge of the semiconductor must have a higher energy than the

LUMO energy of the oxidizer (e.g., Figure 46b, top). On the basis of the electrochemical scale, defined with respect to the NHE potential, the energy of the CB edge should be more negative than the energy of the LUMO. Also, according to the convention used in physics, zero-point energy of the vacuum level, the CB edge would be more positive. Similar conditions apply for the photooxidation reaction involving holes; it is important to note that the energy of the hole is opposite that of the electronic energy level it occupies (Figure 46b, bottom). Physically, this situation corresponds to electron flow from the HOMO of the reduced species to the VB of the semiconductor, where the hole is located.

A diagram indicating the positions of the VB and CB of some of the commonly used oxides is presented in Figure 47. It is

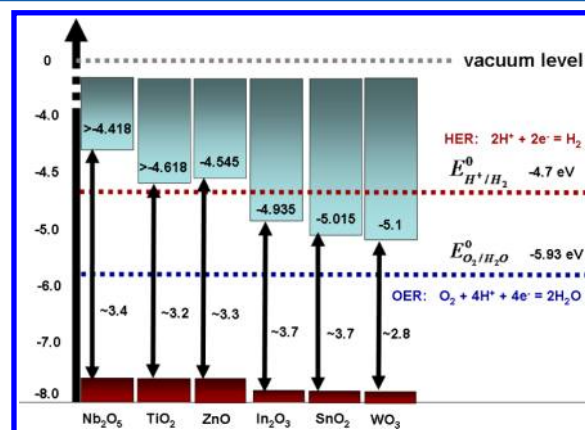


**Figure 47.** Energy of the VB and CB edges for various oxides, with respect to the electrochemical potentials for hydrogen and oxygen reduction.

evident from the diagram that both  $\text{TiO}_2$  and  $\text{ZnO}$  have CB edges that are higher than the electrochemical potential of hydrogen reduction, although not significantly. Niobium oxide ( $\text{Nb}_2\text{O}_5$ ) has an even higher CB edge position, exceeding the NHE potential by  $\sim 0.3$  V. Thus, for all three oxides, it is expected that the hydrogen evolution reaction (HER) will take place upon photoexcitation; indeed, photocatalytic water splitting has been experimentally observed for all three.<sup>32,561,565</sup> As we will discuss later, the electro- and photoelectrochemical reactions on the semiconductor surface often require energy beyond simply that which arises from the energy difference between the CB edge and the electrochemical potential of the corresponding redox process. This difference in energy, above what is expected thermodynamically to drive a reaction, is known as the overpotential. In this view, the larger driving force and the higher CB edge position of  $\text{Nb}_2\text{O}_5$  as compared to that of  $\text{TiO}_2$  or  $\text{ZnO}$  can provide the additional thermodynamic factor that is needed to overcome the overpotential. For the other three oxides ( $\text{In}_2\text{O}_3$ ,  $\text{SnO}_2$ ,  $\text{WO}_3$ ), the CB edge is lower than the HER potential. Thus, photocatalytic hydrogen reduction is not thermodynamically allowed in these instances.

Although not every oxide presented in Figure 47 can catalyze a HER, they can all drive the oxygen evolution reaction (OER), because the VB edge energy is lower than the energy associated with the OER. To drive water oxidation reactions in such materials, one simply needs to remove the photoexcited electrons from the CB. This can be achieved by using a sacrificial electron scavenger, with an electrochemical potential



that is lower than the CB edge of the oxide. Among the most popular electron scavengers are  $\text{O}_2$ ,<sup>566,567,568</sup>  $\text{S}^{2-}$ ,<sup>569</sup>  $\text{Ce}^{4+}$ ,<sup>570</sup>  $\text{Ag}^+$ ,<sup>571</sup>  $\text{IO}_4^-$ ,<sup>568</sup> and  $\text{H}_2\text{O}_2$ .<sup>568</sup> They can be combined in solution or be reduced in a separate counterelectrode as electrons are removed from the photocatalyst via a conducting material. In the latter case, the setup can be regarded as a photogalvanic device. Although the use of sacrificial electrons and hole scavengers provides a convenient way to test a material's ability to drive oxidation and reduction half-reactions, a practical photocatalytic cell should thermodynamically allow for both processes to occur.

In addition to the requirement that the CB and VB edges are in the proper positions, the band gap of the material must also be aligned to allow for the absorption of photons in the visible range of solar the spectrum. As shown in Figure 47, the band gap of most materials is relatively large and is only suitable for the absorption of UV photons. The smallest band gap among the presented oxides is 2.8 eV for  $\text{WO}_3$ ; however, the position of its CB edge makes it thermodynamically incapable of hydrogen reduction.

Fortunately, as discussed in section 3, the band gap of a material, as well as the positions of its VB and CB edges, can be efficiently modified through a variety of methods. Among the most popular methods for photocatalytic applications is the use of dopants and solid solutions. It has been predicted theoretically that doping  $\text{WO}_3$  with a low valence ion such as Hf shifts the CB to energies high enough to drive HER.<sup>337</sup> Solid solutions have been studied in many groups,<sup>572,573</sup> as an example of a result of one such study, the Domen group found that  $\text{ZnO}:\text{GaN}$  solid solutions were able to absorb solar light in the visible range. Although the band gaps for  $\text{ZnO}$  and  $\text{GaN}$  are large (3.3 and 3.4 eV, respectively), in a solid solution the orbitals of each component are shifted with respect to each other, leading to a smaller band gap of 2.29 eV.<sup>572–574</sup> The large number of ternary<sup>319–322,575–580</sup> and more complex<sup>3,581–584</sup> oxides, oxinitrides,<sup>332,571,585</sup> and solid solutions with energy level alignment and band gaps appropriate for photocatalytic water splitting have been found and tested. For a detailed discussion, we refer the reader to recent reviews.<sup>4,20,40,586</sup>

In addition to the factors discussed above and in section 3, which include surface dipoles, pH, etc., the electronic structure of the photocatalyst can also be affected by structural effects, such as the morphology of nanoparticles<sup>6,587</sup> or distortions of crystal structures.<sup>6,20</sup> In contrast to photovoltaic devices, the morphology (e.g., the size and shape of the nanoparticles) in a photocatalyst is especially important. In photovoltaic systems, the surface of the semiconductor is covered with sensitizers; thus the number of undercoordinated atoms is a slow-varying function of the surface structure, regardless of surface type. On the contrary, in the photocatalytic system, the structure of the surface strongly affects the rates for the surface reactions, because it directly determines the structure of interfacial transition states, and governs the adsorption/desorption rates and binding strength of the adsorbed species. In addition, the morphology of the nanoparticles determines the number of defect sites, for example, undercoordinated surface atoms, which carry significant implications for charge trapping and, therefore, reaction yields. For a comprehensive discussion of the effects of morphology on the operation of various oxide photocatalysts, we refer the reader to a recent review by Kubacka and co-workers.<sup>6</sup>

Tantalates of alkali metals with the perovskite chemical composition  $\text{ABO}_3$  ( $\text{A} = \text{Li, Na, K}$ ;  $\text{B} = \text{Ta}$ ) provide a representative illustration of the effects of crystal structure distortions. The crystal structure of such materials is composed of the octahedral  $\text{TaO}_6$  fragments with the alkali metals residing in the cages between the octahedra (Figure 48a). The extent of

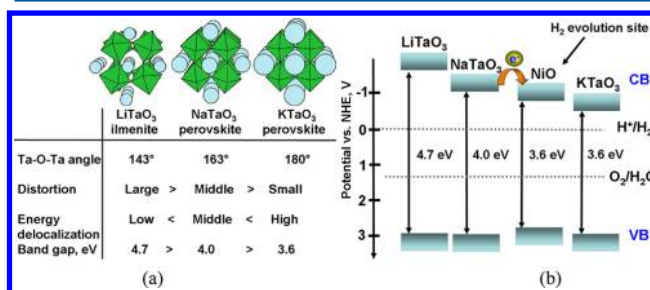


**Figure 48.** Effect of the crystal structure distortion on the CB edge. (a) Crystal structure distortion in alkali metal tantalates; and (b) band energy diagram. Adapted with permission from ref 40. Copyright 2009 The Royal Society of Chemistry.

the structural distortion depends on the size mismatch between the alkali metal ions and the  $\text{TaO}_3$  fragments. This distortion directly affects the position of the CB edge energy (Figure 48b), and hence the driving force for the reduction reaction.

A popular alternative approach to water splitting is based on composite systems, known as Z-schemes,<sup>588–592</sup> in which two photocatalytic materials, A and B, are combined (Figure 49a). A

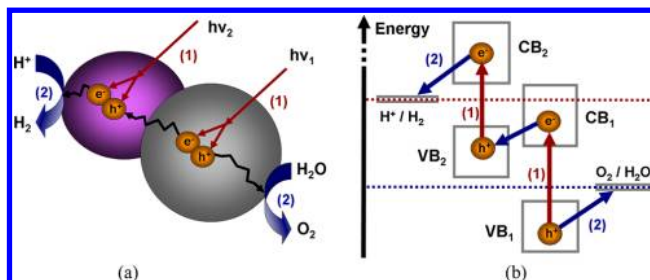


**Figure 49.** Schematic of the Z-scheme principle: (a) in physical space; and (b) in the energy domain. The diffusion, trapping, and recombination of the charge carriers (step 2 in Figure 46 is not shown for clarity).

and B each, individually, is capable of driving one of the half-reactions, but not both, because of the CB and VB edge alignments (Figure 49b). The relative displacement of the A and B energy levels allows them to act as a narrow-gap semiconductor and therefore absorb visible light. It is important to emphasize that two photons are required for the operation of such a system. However, because the photon energies can reside in different parts of the visible spectrum, the absorption of a larger fraction of incident solar energy can occur. This premise is similar to the cosensitization approach used in photovoltaic systems. The transfer of an electron from the CB of one component to the VB of the other (Figure 49b, blue arrow in the middle) can be realized either via direct contact, sometimes involving a solid-state mediator,<sup>590–592</sup> or via a redox pair.<sup>588,589</sup> The latter process is similar to the electron transfer from the counter electrode to the oxidized dye in photovoltaic systems.

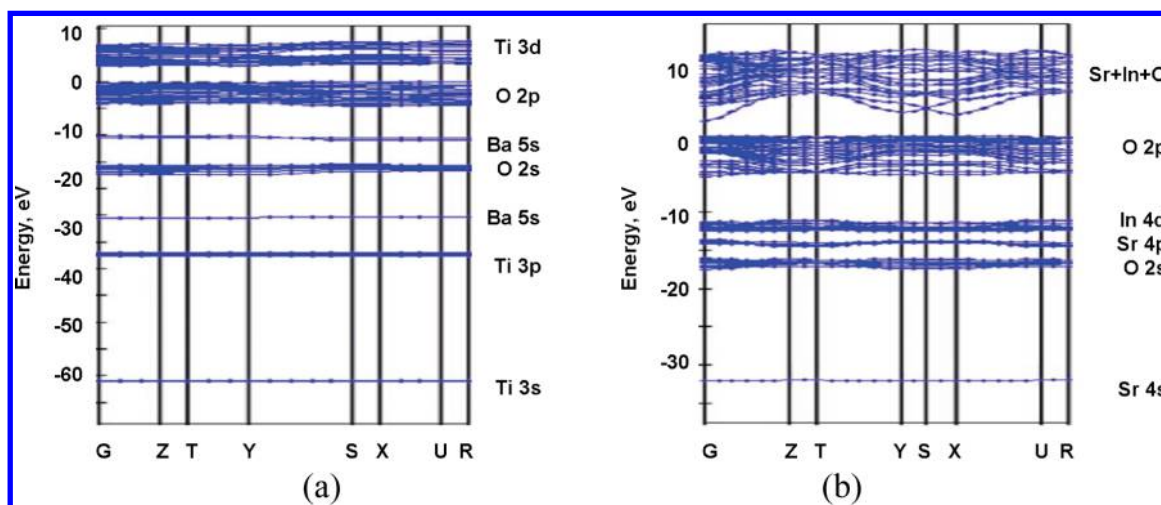


**Figure 50.** Band structure and density of states for selected oxides containing  $d^0$ - and  $d^{10}$ -metals. (a)  $\text{BaTi}_4\text{O}_9$ ,  $d^0$ -metal; (b)  $\text{SrIn}_2\text{O}_4$ ,  $d^{10}$ -metal. Adapted with permission from ref 20. Copyright 2009 The Royal Society of Chemistry.

## 5.2. Charge Separation and Recombination

To a large extent, charge separation determines the efficiency of a photocatalytic cell. If a photogenerated electron rapidly recombines with a photogenerated hole, the solar energy is lost as heat or radiation, and a chemical reaction cannot occur. On the basis of kinetics studies<sup>593,594</sup> and complementary numerical modeling,<sup>595</sup> Domen and co-workers discovered that the majority of photoexcited charge carriers are lost to recombination in photocatalytic nanoparticles. They also found that the kinetic isotope effect (KIE) was significantly smaller for the photocatalytic water splitting, as compared to water electrolysis. Because deuteration only has an effect on surface reactions, they concluded that the rate-limiting step in photocatalysis is not associated with surface reactions, but rather with substrate reactions. This conclusion was also supported by their measurements of the apparent activation energies, which were significantly smaller for the photocatalytic processes when compared to the electrolysis processes. The use of different cocatalysts resulted in the modulation of the apparent activation energy. This effect was attributed to the formation of an energy barrier on the photocatalyst/cocatalyst interface, rather than from a change in the processes taking place on the surface. These experimental observations suggest that the recombination of holes and electrons is much faster than the diffusion of the charge carriers to the surface-reacting sites. Thus, it is important to focus on both charge carrier diffusion and charge carrier recombination.

**5.2.1. Charge Carrier Diffusion.** An expression for the charge carrier mobility,  $w$ , in semiconductors was derived by Fröhlich in 1939:

$$w = \frac{e\bar{l}}{\sqrt{3k_B T}} m^{-3/2} \quad (5.1)$$

where  $m$  is the effective mass of the charge carrier. The mean-free-path of the particle,  $\bar{l}$ , averaged over energy levels is given by:

$$\bar{l} = \frac{6a_0}{\sqrt{\pi}} \frac{(\epsilon - \epsilon_0 + 1)}{\epsilon - \epsilon_0} \left( \frac{T}{\Theta} \right)^{1/2} (e^{T/\Theta} - 1), \quad T < \Theta \quad (5.2)$$

where  $T$  is temperature,  $\Theta = (\hbar\nu_l/k_B)$  is the Debye temperature of the crystal, related to the frequency of its longitudinal mode  $\nu_l$ , and  $a_0 = (\hbar^2/me^2)$  is the Bohr radius. Using eqs 5.1 and 5.2, along with the experimentally measured effective masses of the electron and the hole in anatase  $\text{TiO}_2$ ,  $m_e^* \approx 10m_e$  and  $m_h^* \approx (0.8 \pm 0.2)m_e$ , respectively, Enright and Fitzmaurice estimated the diffusion coefficients:<sup>596</sup>

$$D = \frac{wk_B T}{e} \quad (5.3)$$

The calculated diffusion coefficients for the electron and hole in anatase  $\text{TiO}_2$  were  $1 \times 10^{-6}$  and  $4 \times 10^{-5} \text{ m}^2/\text{s}$ , respectively. These values suggest that in an 8 nm diameter  $\text{TiO}_2$  nanoparticle, the charge carriers will reach the surface on a time-scale of:

$$\tau = \frac{R^2}{D\pi^2} \quad (5.4)$$

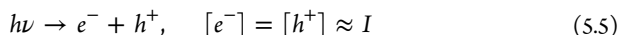
which corresponds to 2 ps and 400 fs for electrons and holes, respectively. Similar time-scales for charge carrier diffusion, in the absence of trap states, were also obtained in other studies.<sup>597,598</sup> In contrast to the relatively high mobility of the charge carriers under ideal conditions, their diffusion is significantly altered by the presence of the trap states in realistic systems.<sup>6,33</sup> As a result, the effective diffusion time-scales range from nanoseconds to hundreds of microseconds, thus leading to only modest gains in efficiencies for modern photocatalytic cells.

Although the Fröhlich theory has been successful at providing a quantitative description of charge carrier mobility in semiconductors, it has its limitations. It requires input parameters, such as effective mass of the carriers, which hinders its applicability as a tool for establishing qualitative relationships between the molecular and electronic structures of the semiconductor and the mobility of the charged particles. In addition, the Fröhlich construction is only valid at low temperatures with respect to the Debye temperature of the crystal. With the development of modern computational techniques, direct ab initio calculations of the electronic band structure of solid-state complex oxides have become possible. For instance, the mobility of electrons and holes can now be

estimated on the basis of the dispersion of the conduction and valence bands, respectively.

Systematic DFT calculations have been performed in the Inoue group for a number of complex oxides.<sup>20,576,577</sup> These calculations made it possible for a number of general relationships between the oxide composition and the charge carrier mobility to be derived. For example, oxides based on d<sup>0</sup>-metals, such as BaTi<sub>4</sub>O<sub>9</sub>, exhibit a relatively small dispersion for both the CB and the VB in k-space (Figure S0a), which explains the small mobility of both electrons and holes in these materials, as well as their low performance in photocatalytic systems. On the contrary, for the oxides based on d<sup>10</sup>-metals, such as SrIn<sub>2</sub>O<sub>4</sub>, the dispersion of the CB and VB is significantly larger (Figure S0b), implying a higher mobility of charge carriers and smaller losses due to recombination. This results in a higher photocatalytic efficiency for such materials.

**5.2.2. Charge Carrier Recombination.** It is expected that recombination rates will increase with the number of defects, because defect sites act as recombination centers, but the rates also increase as the concentration of photoexcited electrons and holes increases. The creation of an electron–hole pair is a first-order kinetics process with respect to light intensity, eq 5.5, and is faster under more intense solar radiation.



Hisatomi and co-workers constructed a kinetic model describing the electron–hole creation, recombination, diffusion, and participation in chemical reactions on the surface.<sup>594</sup> Possible intermediates and transformations are presented in Figure S1.

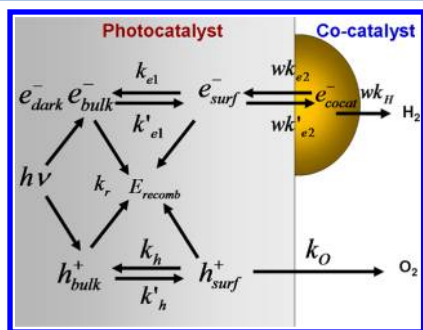
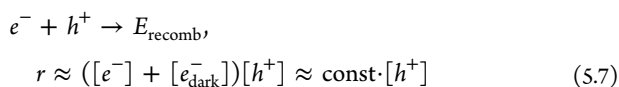
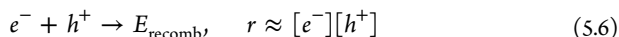


**Figure S1.** Kinetic model of the electron–hole creation, recombination, diffusion, and participation in chemical transformations.

The recombination of the photogenerated electron and hole inside the semiconductor is a second-order process, eq 5.6. However, the intrinsic electron concentration is much higher than that of the photogenerated electron,  $[e^-_{\text{dark}}] \gg [e^-]$ ; thus the kinetics becomes a quasi-first-order process in the concentration of holes, eq 5.7.



Equations 5.5 and 5.7 lead to the following solution to the kinetic model shown in Figure S1:

$$r_{\text{react}} = \frac{wk_{e1}k_{e2}k_H(k_O + k_r[e^-_{\text{dark}}])(\sqrt{1+b}-1)}{2\{k'_{e1}(k'_{e2} + k_H) + wk_{e2}k_H\}k_r} \quad (5.8)$$

$$b = \frac{4\{k'_{e1}(k'_{e2} + k_H) + wk_{e2}k_H\}k_r k_O \alpha I}{wk_{e1}k_{e2}k_H(k_O + k_r[e^-_{\text{dark}}])^2} \quad (5.9)$$

This general expression can be simplified in the limits of small ( $b \rightarrow 0$ ) and high ( $b \rightarrow \infty$ ) light intensities:

$$r_{\text{react}} = \sqrt{\frac{wk_{e1}k_{e2}k_H k_O \alpha I}{k_r}}, \quad b \gg 1 \quad (5.10)$$

$$r_{\text{react}} = \frac{k_O}{k_r[e^-_{\text{dark}}]} \alpha I, \quad b \ll 1 \quad (5.11)$$

where  $K_{e1} = (k_{e1}/K'_{e1})$  and  $K_{e2} = (k_{e2}/K'_{e2})$  are the equilibrium constants for electron exchange between the bulk photocatalyst and its surface, and between the surface of the photocatalyst and the bulk/surface of the cocatalyst.

Equations 5.10 and 5.11 have provided important insights into the potential strategies of improving the efficiency of photocatalytic systems. For one, there exist two asymptotic regimes, depending on the light intensity. For high intensities, the reaction rate is proportional to the square root of the light intensity,  $I^{1/2}$ , while at lower intensities it is linear in  $I$ . These limits have been observed in experimental studies.<sup>593,594</sup> Also, the photocatalytic reaction rate can be significantly enhanced in the linear regime by lowering the intrinsic electron concentration in the photocatalyst. This can be achieved by doping the material with lower-valence cations. The effect has been observed experimentally by Takata and Domen, who doped SrTiO<sub>3</sub> with lower-valence Ga<sup>3+</sup> cations and obtained an order of magnitude improvement in photocatalytic performance.<sup>599</sup>

Alternative methods to increase the lifetime of the electron–hole pair have been developed recently. He and co-workers discussed three possible ways of achieving this via: (1) composite materials; (2) highly dispersed nanoparticles; and (3) nanotubes.<sup>600</sup> The basic premise of the use of composite materials is to direct the flow of electrons to the component with the lower CB edge energy (electron sink), and to deliver holes to the component with the higher VB edge energy (hole sink).<sup>332,601–606</sup> Most often, noble metals such as Rh, Au, Ir, Pt,<sup>601–604</sup> and oxides such as NiO<sub>x</sub>, Rh<sub>2–y</sub>Cr<sub>y</sub>O<sub>3</sub>, RuO<sub>2</sub>,<sup>332,579,605</sup> are used as electron sinks, while oxides such as SnO<sub>2</sub>, WO<sub>3</sub>, IrO<sub>2</sub><sup>571,606</sup> are used as hole sinks. The overall result is an enhanced separation of positively and negatively charged (quasi)particles. The approach is illustrated in Figure S2. It is somewhat similar to the Z-scheme, but in this case only one photon is required for the operation of the composite system.

Electrons and holes are always close to the surface of highly dispersed semiconductor nanoparticles.<sup>601,607,608</sup> Nanoparticles

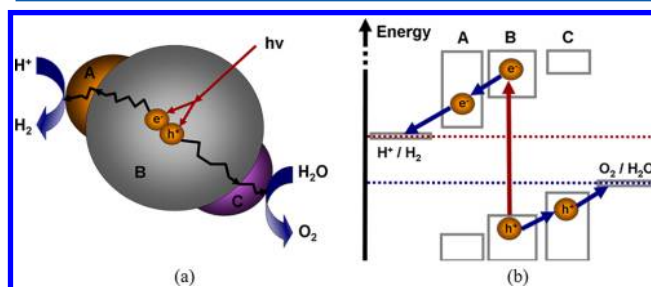


**Figure S2.** A composite material scheme for enhanced charge separation: (a) in physical space; and (b) in the energy domain.



maximize the probability of electron and hole involvement in a chemical reaction, as opposed to their involvement in the recombination process. A smaller nanoparticle has a large surface-to-volume ratio, which speeds the reactive channel due to the mass law. An increased number of surface defects is the primary drawback of highly dispersed nanoparticles, as compared to larger particles. In addition, quantum confinement effects can facilitate recombination processes, although it has been shown that the effects are significant only for very small particles ( $d < 2$  nm).<sup>587</sup>

Finally, the creation of an electron–hole pair in the nanotube architecture<sup>609–611</sup> leads to a significant dipole moment due to nonsymmetric charge distribution. This dipole moment inhibits the recombination reaction and changes the positions of the CB and the VB, in a fashion similar to the nanorods, as discussed in section 3. The overall effect of the nanotube architecture is a significantly increased ( $>200$  nm) mean collision (recombination) length for the electrons, favoring their diffusion to the collecting electrode, and hence facilitating electron–hole separation. In contrast, the charge diffusion length is significantly smaller in nanoparticle arrays, leading to larger recombination probabilities.

It has recently been found that a new class of porous TiO<sub>2</sub> material can be obtained, when oriented TiO<sub>2</sub> nanocrystals are used as building blocks for TiO<sub>2</sub> mesocrystals.<sup>612–614</sup> The open pores between nanocrystals allow for diffusion of the reactants, as well as the penetration of light into the photocatalyst.<sup>614</sup> It has been proposed that ordering nanocrystalline structures considerably improves the performance of photocatalysts and photovoltaic cells by changing the charge transport and recombination properties.<sup>615,616</sup>

Bain et al. performed experiments on a single particle assembly of nanoplate anatase TiO<sub>2</sub> mesocrystals with highly exposed {001} facets.<sup>617,618</sup> They found that the ordered superstructures produced a high yield of photogenerated charges and had high photoconductivity. These properties are usually difficult to achieve in systems consisting of crystalline nanoparticles, due to the high probability of charge recombinations at the interface.<sup>616</sup>

It was determined that the highly enhanced photocatalytic activity of mesocrystalline TiO<sub>2</sub> could be attributed to three factors: (1) the large increase in the efficiency of charge separation, which produces long-lived reactive charges; (2) the large specific surface area, which provides ample reaction sites for photocatalytic activity; and (3) the highly efficient transportation of reactants and products due to system's porous structure.<sup>618</sup>

### 5.3. Photochemical Reactions on the Surface

Currently, oxide photocatalysts are used to catalyze an extensive range of reactions, including CO<sub>2</sub> reduction,<sup>560,619–621</sup> CO oxidation,<sup>622</sup> oxygen reduction,<sup>623</sup> oxidation of organic surfactants<sup>298</sup> and other small organic molecules,<sup>566,624,625</sup> water reduction and oxidation (splitting),<sup>295,296,320,626,627</sup> along with many others. Water splitting is particularly important and has been studied the most extensively. For that reason, we use water splitting studies as a specific example in this section to highlight the basic principles of reactions taking place on the surface of a photocatalyst. First, we discuss the mechanisms behind such transformations, along with the main conclusions obtained from these studies. We then consider the parameters and processes affecting the thermodynamics and kinetics of surface reactions, with

particular emphasis placed on the physical origins of the overpotential.

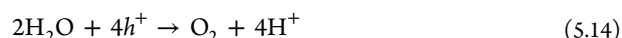
**5.3.1. Reaction Mechanisms.** The photochemical water splitting reaction:



can be considered a combination of two half-reactions taking place on different catalytic sites, for example, Pt and IrO<sub>2</sub> nanoparticles deposited on a TiO<sub>2</sub> substrate. These reactions are an example of the so-called hydrogen evolution reaction (HER):



and the oxygen evolution reaction (OER):

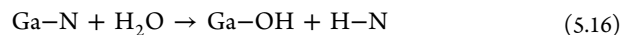


The photogenerated electron and hole on the surface of the photocatalysts are denoted by  $e^-$  and  $h^+$ . The reaction stoichiometry is given by eqs 5.13 and 5.14, but the elementary steps that take place during the transformation are not reflected in these equations. Before discussing the mechanisms of the HER and OER, it is important to understand the particular types of species that become adsorbed on the photocatalyst material.

The adsorption of water has been studied extensively upon a variety of interfaces, including oxides,<sup>2,628–632</sup> oxidized metal surfaces,<sup>633</sup> polyoxometalates,<sup>634</sup> as well as on the surfaces of photoactive materials, such as GaN.<sup>635,636</sup> The activation energy for the dissociation of water is sufficiently small that it is possible for it to dissociate upon adsorption, depending on the surface.<sup>635–637</sup> If water molecules dissociate, they hydroxylate the surface; –OH groups adsorb on metal atoms, as is the case for TiO<sub>2</sub>:

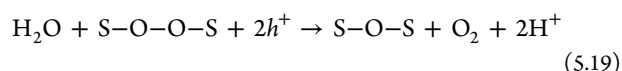
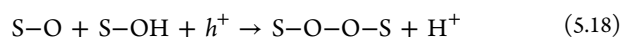
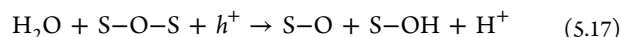


For materials such as GaN, water dissociation can hydrogenate surface atoms:

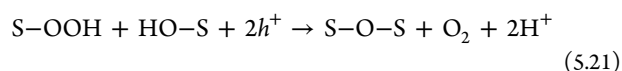
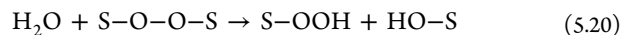


The symbols Ti, Ga, and N in eqs 5.15 and 5.16 represent coordinatively unsaturated centers on the substrate surface. In the following equations, we will use the symbol S to represent a generic unsaturated atom.

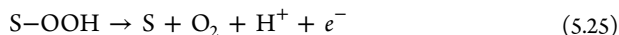
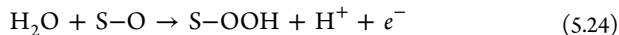
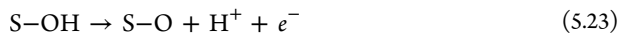
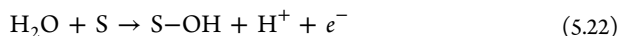
Equations 5.15 and 5.16 represent a simple nucleophilic attack of a water molecule on a given surface bond. Nakamura, Nakato, and coauthors proposed a mechanism of nucleophilic attack combined with oxidation that is intermediated by holes, followed by the coupling of –OH groups adsorbed on the surface.<sup>638,639</sup> They proposed the following reaction mechanism on the basis of their experimental data:



As an alternative to step 5.19, they also considered the following two steps:



The OER has been extensively studied theoretically by the Norskov group.<sup>2,629–631,640</sup> The proposed mechanism for the electrochemical OER consisted of four proton-coupled electron transfer (PCET) steps:



As introduced earlier, S represents a generic coordinatively unsaturated center on the substrate surface.

The Norskov group studied the thermodynamics of the OER by computing the free energy change,  $\Delta G_i$ , of the products and reactants in each step; a typical free energy diagram is presented in Figure 53a. Each step represented in eqs 5.22–5.25 is

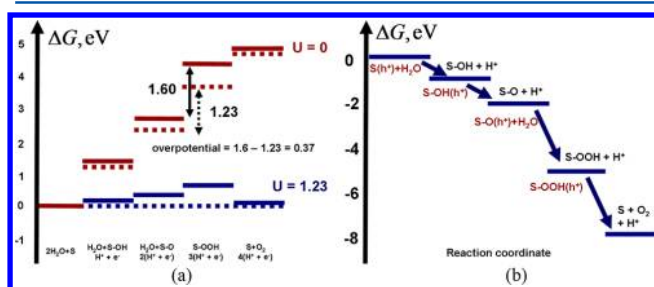


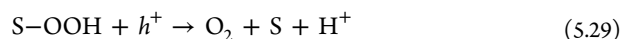
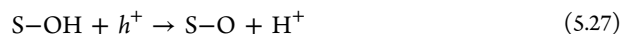
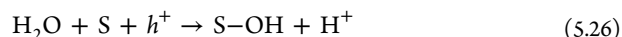
**Figure 53.** Reaction free energy diagram for the OER on TiO<sub>2</sub> calculated with (a) an electrochemical scheme; and (b) a photoelectrochemical scheme.

energetically favorable, implying that the OER stores electrical or photochemical energy in the form of chemical energy in the products. This also indicates that to drive the process, each step must be supplied with a sufficient amount of energy; in Norskov's calculations, this external energy comes from the electrode. This process was modeled empirically by including the energy term  $qU$ , coming from the increased energy of the electrons, shown on the right-hand side of eqs 5.22–5.25; this term arises from the applied voltage. As shown in Figure 53a, at a particular value of an applied voltage bias, it is possible to produce all OER steps so that they are energetically downhill, and therefore will be thermodynamically favorable. The application of a voltage is a necessary but not sufficient condition for driving the OER, because it is possible that the reaction involves kinetic barriers, which are associated with each step and omitted in the reaction free energy calculations.

The chemical steps shown in eqs 5.22–5.25 describe electrolysis. These reactions can be related to the processes taking place during a photocatalytic cycle if an additional term is included in the calculations, associated with the electrochemical potential of the photogenerated hole. Such an approach has been used to study the photooxidation of water on TiO<sub>2</sub><sup>629,631</sup> and WO<sub>3</sub><sup>630</sup> surfaces using periodic DFT calculations on neutral systems. An alternative approach is also available to model the photoinduced water oxidation on TiO<sub>2</sub>, based on finite-size cluster calculations.<sup>641</sup> Cluster methodology has been also used in studies of the water oxidation mechanism of a GaN surface by Shen and co-workers.<sup>642</sup>

In the cluster calculations, the reactant is represented by a positively charged system, which mimics the hole transferred to the reactive site. A neutral system and a proton, which accepts

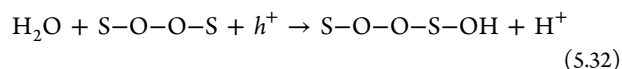
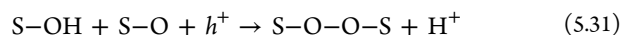
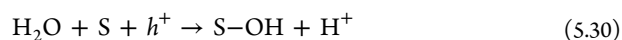
the positive charge of the hole, represent the product state. The OER in this approach is written as:

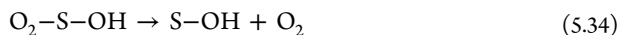
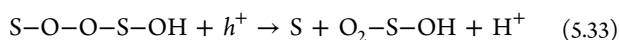


where S is a coordinatively unsaturated center on a given substrate surface. This mechanism has a simpler interpretation, as compared to eqs 5.22–5.25, as the reaction is induced by the hole. The overall process consists of the dissociation of the reactant along with release of an electron and a proton. An energy bias correction is not needed when calculating  $\Delta G_i$  for the reactions described by eqs 5.26–5.29, simplifying the calculations. Cluster models allow for the explicit introduction of a charge, which avoid the artifacts associated with the interaction of the charge with its images in periodic calculations. An example of an energy profile calculated using the cluster method is presented in Figure 53b. All of the elementary steps are energetically downhill, suggesting that the electrochemical potential of the hole is thermodynamically sufficient to drive the water oxidation.

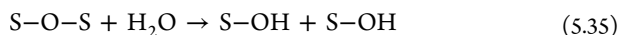
Because kinetic barriers typically increase for reactions with a large  $\Delta G_i$ ,<sup>643</sup> calculated  $\Delta G_i$  values were used to determine the rate-determining steps. The calculations show that the rate-determining step may vary depending on chemical conditions, calculation methodology, and the nature of the substrate. For example, the oxidation rate on rutile TiO<sub>2</sub>(110),<sup>629</sup> as well as on GaN(10 $\bar{1}$ 0),<sup>642</sup> was found to be limited by the first deprotonation step, eq 5.26. In contrast, Valdés et al. found the second deprotonation step, eq 5.27, to be rate-limiting for water oxidation on rutile TiO<sub>2</sub>(110).<sup>631</sup> However, the  $\Delta G_i$  of this reaction was very close to the value of one for the first deprotonation step. Thus, definitive conclusions require more accurate calculations, including calculations of kinetic barriers. It is possible that both steps simultaneously determine the overall rate of water oxidation on rutile TiO<sub>2</sub>(110). The water oxidation rate on various facets of WO<sub>3</sub> was found to be controlled by the second deprotonation step, eq 5.27.<sup>630</sup>

The above calculations use a phenomenological research approach, utilizing the addition of a constant energy term in the calculated  $\Delta G_i$ . However, the electrostatic potential of the system, modulated by the electrode voltage, may have a significant effect on the electronic structure of the system, which can affect the free energy for each intermediate step in the OER, and thereby change the identity of the rate-determining steps. The effect of the electrode voltage has been explicitly included in the computational model developed in the Liu group.<sup>587,623,637,644,645</sup> They studied the mechanisms of the OERs on various surfaces of TiO<sub>2</sub> and found that water adsorbs nondissociatively on the anatase (101) surface and undergoes a chemical transformation only upon arrival of a hole:<sup>637</sup>

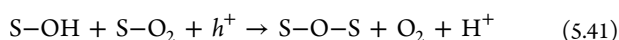
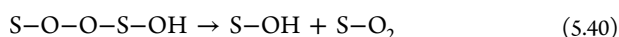
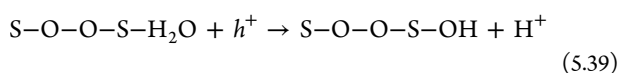
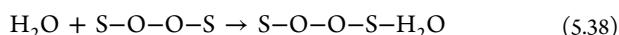
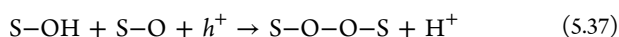
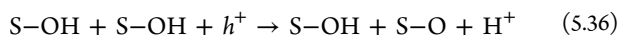




In contrast, water dissociates on anatase (001), covering the substrate surface with hydroxyl groups:



The remaining photocatalytic cycle involves the following elementary steps:



It is worth noting that the Liu mechanism involves the peroxide intermediates S-O-O-S. Liu and co-workers also argue that hydroperoxide, S-OOH, and even hydroxyl terminal groups, S-OH, cannot be major intermediates in the OER, because these hydrogenated species are unstable at high overpotential conditions. Although their mechanisms involve intermediate species different from those found in the studies of Norskov and Shen, the first deprotonation step, eq 5.30, is still the rate-limiting step. It should be emphasized that, in contrast to Norskov's calculations, who estimated energy barriers for transition in approximate way, the approach of Liu and co-workers is based on accurate calculations of the transition states between all of the intermediate pairs. The agreement in the approaches using  $\Delta G_i$  indicates that the correlation between the kinetic barriers and reaction free energies,  $\Delta G_r$ , is an acceptable approximation. Even though the predicted mechanism for the OER can change significantly depending on the computational procedure used, the results obtained from the different methods often are in good agreement.

**5.3.2. Overpotential.** Both the HER and the OER require a supply of external energy; if the source of the consumed energy is solar radiation, it is transformed into an electric current involving electrons and holes. This ultimately leads to the accumulation of chemical energy, for example, in the form of gaseous hydrogen and oxygen. In an electrochemical cell, the external energy is represented by the electrode potential,  $U$ , which lowers the free energy barrier and results in thermodynamic and kinetic transformations. The standard electrochemical potential for water oxidation  $E_{\text{O}_2/\text{H}_2\text{O}}^0$  is 1.23 eV vs NHE. This value corresponds to the ideal free energy diagram for a 4-electron oxidation process, denoted by the red dashed lines in Figure 53a. In this idealistic case, each of the four consecutive steps proceeds with a constant free energy change equal to the standard electrochemical potential,  $E_{\text{O}_2/\text{H}_2\text{O}}^0$ . In real systems, the various steps of the OER, given by eqs 5.22–5.25, have different free energy change values (solid red lines). These deviations originate from the conformational and electronic variations of the reacting subsystem, as well as from the extent to which such reactions change the environment, for example, the solvent and substrate. The maximal  $\Delta G_i$  along the reaction coordinate of the entire process is 1.60 eV. Thus,

applying the ideal electrode potential of 1.23 eV is insufficient to allow the oxidation process to proceed thermodynamically, because there are steps for which the  $\Delta G_i$  will be positive, as shown in Figure 53a (solid blue line). On the other hand, for an ideal system, an external voltage of 1.23 V flattens out the energy diagram (Figure 53a, dashed blue line) and allows all steps to be thermodynamically possible. In a real system, the minimal voltage applied to the electrode must be equal to the largest  $\Delta G_i$  along the reaction pathway, that is, 1.60 V. This value is 0.37 V larger ( $1.60 \text{ V} - 1.23 \text{ V} = 0.37 \text{ V}$ ) than the voltage required for the ideal process. This extra voltage is called the overpotential,  $\eta$ ; it is the deviation of the realistic system from the ideal situation. The theoretically calculated values of the overpotential for  $\text{TiO}_2$  range from  $\sim 0.7^{637}$  to 0.78 V,<sup>629</sup> which is in good agreement with the experimental estimates of 0.9–1.1 V.<sup>646</sup>

Understanding the fundamental origins of the overpotential is important for the rational engineering of photocatalytic materials. Recently, the Liu group has attempted to explain the origin of this phenomenon theoretically based on electronic structure calculations.<sup>637</sup> They established that the significant overpotential for water oxidation, about 0.7 V, was related to the large kinetic barrier for the first proton removal, eq 5.30. The large barrier arises because of the destabilization of the semiconductor surface upon absorption of the –OH groups. This destabilization is caused by a large electron density flow from the substrate to the –OH group (Figure 54, right), leading to a strong polarization at the interface and over-oxidation of the surface.

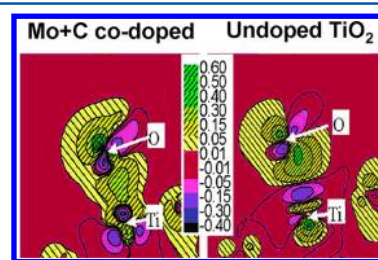


**Figure 54.** Electronic charge density difference before and after –OH adsorption, projected on the plane containing the Ti–O–H fragment. Two conditions are shown, undoped  $\text{TiO}_2$  (right) and Mo+C-codoped  $\text{TiO}_2$  (left). Adapted with permission from ref 637. Copyright 2010 American Chemical Society.

The free energy barrier for the first deprotonation step can be lowered by stabilizing the intermediate, where –OH is adsorbed on the surface. This can be achieved via Mo+C codoping (Figure 54, left). In the doped system, adsorption of the –OH group leads to a somewhat smaller polarization at the interface and a larger bonding character of the orbitals. As shown in Table 9, the overpotential of the codoped system is significantly lower than that of pure  $\text{TiO}_2$ , due to a decreased  $\Delta G_i$  of the first proton removal. However, the stabilization of the Ti–O–H intermediate through codoping results in an increased  $\Delta G_i$  for the second proton removal. This increase has little effect on the overall efficiency of OER, unless it is so significant as to make the second proton removal the rate-determining step.

On the basis of the experimental studies, it has been found that the overpotential follows the phenomenological method known as the Tafel relation:



**Table 9. Effect of Codoping on  $\Delta G_i$  of the Initial Steps in the OER Process**

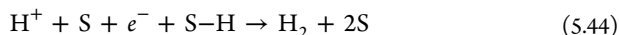
$\Delta G_i$	system	
	pure TiO <sub>2</sub>	Mo+C codoped TiO <sub>2</sub>
Anatase (101)		
$\Delta G_1$ , eV	0.69	0.08
$\Delta G_2$ , eV	−0.96	−0.39
Anatase (001)		
$\Delta G_1$ , eV	0.61	0.2
$\Delta G_2$ , eV	−1.20	−0.82

$$\eta = b \lg \left( \frac{j}{j_0} \right) \quad (5.42)$$

where  $\eta$  is the overpotential,  $j$  is the observed electrochemical current,  $j_0$  is the so-called exchange current, which is the current generated in the ideal case with no overpotential, and  $b$  is the Tafel slope. Although eq 5.42 itself explicitly indicates nothing regarding the physical origins of the overpotential, the dependence of the Tafel slope  $b$  and the exchange current on the nature of the substrate surface provides a fundamental understanding of the overpotential phenomenon.

**5.3.2.1. Exchange Current.** In early experimental measurements, Trasatti found a characteristic volcano shape correlation between the energy of the M–H or M–O bonds (M represents a metal) and the exchange current for the HER or OERs (Figure 55).<sup>647</sup> By performing DFT calculations on a large number of systems, Norskov and co-workers were able to devise an explanation for this correlation.<sup>648,649</sup>

To illustrate the origin for the volcano plot, consider the following sequence of HER steps:



Recall that S represents the binding center on the substrate surface. The exchange current  $j_0$  in the Tafel equation that describes the interfacial electron transfer rate in eq 5.43 at equilibrium is:

$$j_0 = -er_{\text{red}} \quad (5.46)$$

The reduction rate is given by interfacial kinetics:

$$r_{\text{red}} = k_{\text{red}}(1 - \theta)c_{\text{H}^+} \quad (5.47)$$

$$\theta = \frac{n_{\text{occ}}}{n_{\text{tot}}} \quad (5.48)$$

where  $k_{\text{red}}$  is the rate constant, and  $\theta$  is the surface coverage at steady-state, which is defined by the ratio of the number of occupied reaction sites,  $n_{\text{occ}}$ , over the total number of the sites on the surface,  $n_{\text{tot}}$ . The equilibrium coverage is given by the adsorption–desorption equilibrium constant:

$$K = \frac{n_{\text{occ}}}{n_{\text{free}}} = \frac{n_{\text{occ}}}{n_{\text{tot}} - n_{\text{occ}}} = \frac{\theta}{1 - \theta} \Leftrightarrow \theta = \frac{K}{1 + K} \quad (5.49)$$

The equilibrium constant can also be computed using the change in the free energy,  $\Delta G$ , for the adsorption–desorption reaction:

$$K = \exp \left( -\frac{\Delta G}{k_{\text{B}}T} \right) \quad (5.50)$$

Thus, the exchange current can be computed according to:

$$j_0 = -ec_{\text{H}^+} \frac{k_{\text{red}}}{1 + \exp \left( -\frac{\Delta G}{k_{\text{B}}T} \right)} \quad (5.51)$$

Consider two limiting cases, which depend on the interaction strength between the H atoms and the surface binding centers:

- (a) Exothermic reaction,  $\Delta G < 0$ . In this case, the migration of  $\text{H}^+$  ions and electrons to the surface is spontaneous and barrierless. The rate constant  $k_{\text{red}}$  can be assumed to be independent of  $\Delta G$ :

$$k_{\text{red}} = k_0 \quad (5.52)$$

This situation gives rise to the left side of the volcano plot (Figure 55).

- (b) Endothermic reaction,  $\Delta G > 0$ . Here, the system needs to consume energy to retrieve  $\text{H}^+$  ions from the solution and electrons from the oxide to bring them to the semiconductor–liquid interface. The process is thermally activated, and the rate constant can be approximated by:

$$k_{\text{red}} = k_0 \exp \left( -\frac{\Delta G}{k_{\text{B}}T} \right) \quad (5.53)$$

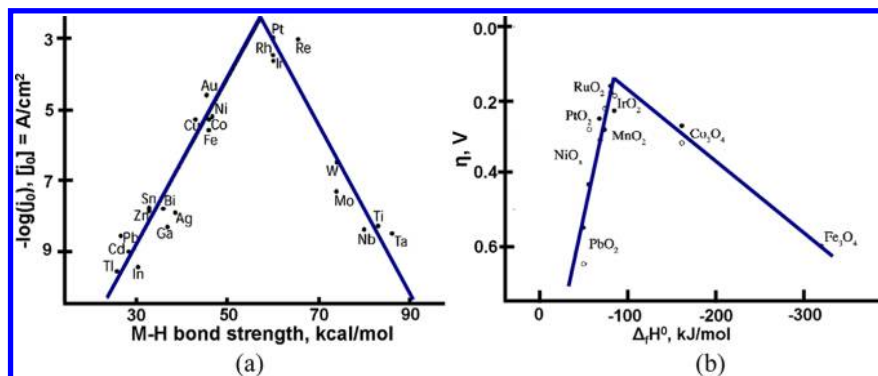


**Figure 55.** Volcano shape correlation between the logarithm of the exchange current, characterizing the overpotential, and the M–X bond strength for (a) hydrides M–H; and (b) oxides M–O. Adapted with permission from ref 4. Copyright 2010 American Chemical Society.

This situation gives rise to the right side of the volcano plot (Figure 55).

A kinetic model describing the entire volcano plot in a unified picture, extending beyond the special cases considered above, has been developed by Parsons.<sup>650</sup> The resulting formula is:

$$j_0 = e^{\frac{k_B T}{h}} (a_{H^+})^{1-\alpha} \theta^\alpha (1-\theta)^{1-\alpha} \exp\left(-\frac{\Delta G^\#}{k_B T}\right) \quad (5.54)$$

The maximal rate is achieved at  $\alpha = \theta = (1/2)$ , which corresponds to an intermediate M–H bond energy. The bond should not be too strong to preclude desorption of the product, but not so weak as to prevent successful interaction between the reactant and the electrons. The effective free energy barrier,  $\Delta G^\#$ , is determined by the free energy barriers for the forward,  $\Delta G_f$ , and backward,  $\Delta G_b$ , reactions (Figure 56):

$$\Delta G^\# = (1 - \alpha)\Delta G_f + \alpha\Delta G_b \quad (5.55)$$

The  $\Delta G^\#$  quantity becomes a free energy barrier in the standard sense when the free energies of the product and the reactant are equal.

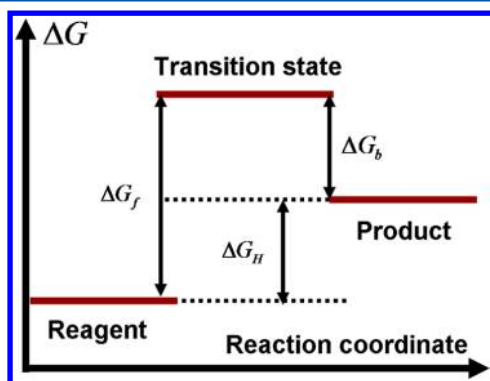


**Figure 56.** Free energy diagram for a chemical transformation, denoting the free energy barriers for the forward,  $\Delta G_f$ , and backward,  $\Delta G_b$ , reactions as well as the value used by Norskov,  $\Delta G_H$ .

The volcano plot for the water oxidation reaction was corroborated by DFT calculations performed in the Norskov group. These studies established a linear relationship for the  $\Delta G$  of each elementary step of the OER and the energy of oxygen binding on the  $\text{RuO}_2(110)$  surface.<sup>640</sup> The slope was found to be positive for the reactions given by eqs 5.22 and 5.23:

$$\Delta G_1 = 0.61\Delta E_O - 0.55 - qU \quad (5.56)$$

$$\Delta G_2 = 0.39\Delta E_O + 0.6 - qU \quad (5.57)$$

The slope was negative for the reactions represented by eqs 5.24 and 5.25:

$$\Delta G_3 = -0.36\Delta E_O + 2.38 - qU \quad (5.58)$$

$$\Delta G_4 = -0.64\Delta E_O + 2.49 - qU \quad (5.59)$$

This situation maximizes the chemical activity for systems with intermediate oxygen–metal binding strengths. In turn, the strength of the M–H or M–O bonds depends more on the fundamental properties of the system. For example, Hammer and co-workers found that the bond strength correlates with the d-orbital energies, in particular, with their position with

respect to the Fermi energy of the material.<sup>651</sup> In addition, using DFT calculations, Greeley and co-workers found a correlation between bond strength and the position of the center of the d-bands.<sup>652</sup>

Recently, Suntivich observed a volcano shape correlation between the chemical activity and the occupation of the  $e_g$  symmetry d-orbitals of the metal in the oxide substrate.<sup>3</sup> This correlation allowed the authors to rationally design an inexpensive complex oxide catalyst,  $\text{Ba}_{0.5}\text{Sr}_{0.5}\text{Co}_{0.8}\text{Fe}_{0.2}\text{O}_{3-\delta}$ , that performed an order of magnitude better than the best known catalyst to date,  $\text{IrO}_2$ . Vojvodic and Norskov rationalized how the d-orbitals with  $e_g$  symmetry could provide a useful correlation parameter for estimating oxide activity.<sup>19</sup> They found that the adsorption energy of the oxygen adatom, that is, the M–O bond strength, correlated with the occupation of the d-orbitals with  $t_{2g}$  symmetry (Figure 57). The

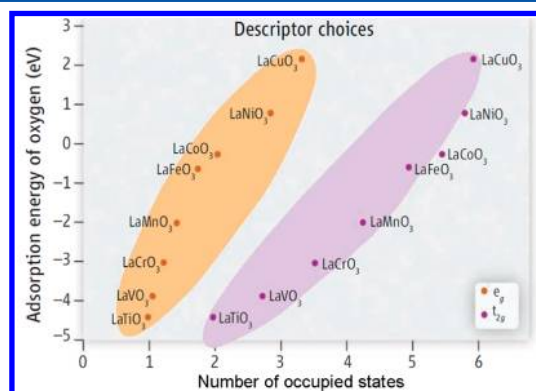


**Figure 57.** Correlation between the occupation number of d-orbitals of the metal and the M–O bond strength. Reprinted with permission from ref 19. Copyright 2011 AAAS.

occupations of both  $t_{2g}$  and  $e_g$  orbitals contain contributions from occupied VB and CB states, with the contributions of the CB states being stronger. When the metal d-orbitals hybridize with the 2p orbitals of the O atoms in an oxide material, a new set of bonding and antibonding orbitals is formed. The occupation of the antibonding hybridized orbital depends on the occupation of CB states in the metal atoms, which in turn is strongly correlated with the occupation of  $e_g$  and  $t_{2g}$  states. The overall effect is that the adsorption energy and the exchange rates correlate with the occupation of the  $e_g$  or  $t_{2g}$  states of the metal atom in the oxide.

**5.3.2.2. Tafel Slope.** The dependence of the Tafel slope on various parameters of the photocatalytic or electrochemical system provides additional information about the fundamental origins of the overpotential. For example, it has been found experimentally that the Tafel slope varies depending on the electrode potential, thus pointing to the possibility of several regimes of electrochemical water oxidation.<sup>653,654</sup> Trasatti suggested that such appearance of particular regimes is defined by the rate-limiting step, which depends on the reaction conditions. A deeper understanding of the processes defining the Tafel slope at different values of the overpotential, or equivalently, the electro-chemical potential, has been achieved in the work of Fang and Liu.<sup>644</sup> Unlike other approaches, they explicitly studied the transition states (TS) for each elementary reaction. Consideration of the TS properties and their dependence on the operation conditions, for example, solvent, potential, etc., was found to be one of the crucial factors in

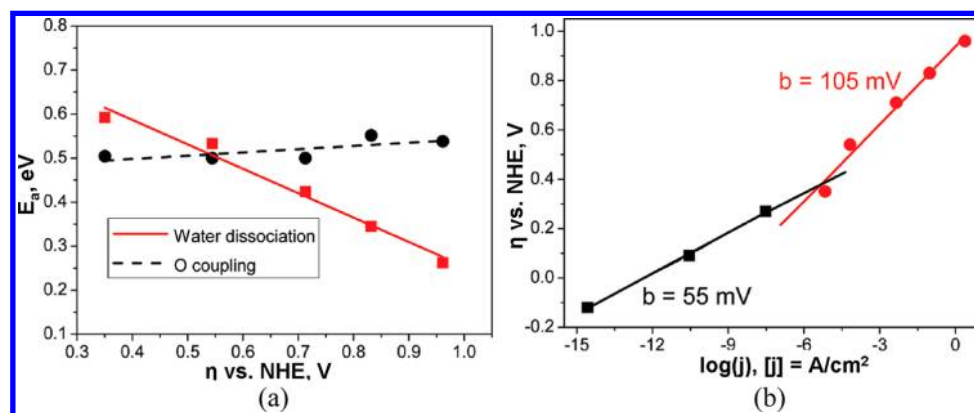


**Figure 58.** The two regimes of the Tafel slope. (a) Activation energy versus overpotential. (b) Overpotential versus logarithm of the exchange current. Adapted with permission from ref 644. Copyright 2010 American Chemical Society.

explaining the dependence of the Tafel slopes on the overpotential.

It should be noted that under the electrolytic conditions ( $U > 1.58 \text{ V}$ ), the surface of  $\text{RuO}_2$  consists primarily of O-terminal sites. Even if some  $-\text{OH}$  sites are present at lower potentials, these groups will dissociate if  $U > 1.58 \text{ V}$ , leading to an exclusively O-terminated surface. Fang and Liu considered two possible mechanisms of water oxidation, water dissociation and oxygen coupling.<sup>644</sup>

In the first mechanism, the water molecule begins in the liquid phase and initially forms a TS with the  $-\text{O}$  sites on the surface. This mechanism is similar to the Eley–Rideal mechanism.<sup>644</sup> The formation of the TS-complex was found to be a rate-limiting step. Because the TS is significantly polarized, the presence of a surface charge, induced by the electrode voltage, can significantly alter the TS energy, and therefore affect the reaction rates and electro-chemical current. Thus, the exchange current depends strongly on the overpotential for such a reaction.

In the alternative mechanism, the oxygen atom on the  $\text{RuO}_2$  surface combines with the neighboring oxygen atom to form oxygen gas. The reaction takes place on the surface and does not involve reactants in the liquid phase, corresponding to the Langmuir–Hinshelwood mechanism.<sup>644</sup> The TS is nonpolar, and the solvent structure remains relatively intact; as a consequence, the activation-energy barrier is only weakly dependent on the surface potential, that is, the overpotential. The rate of the entire reaction is independent of the electrode voltage.

The two operation regimes can be combined in a single diagram, as shown in Figure 58. At a low overpotential, the activation energy for the oxygen coupling mechanism (black lines) is smaller than that for the dissociation mechanism (red lines). The reaction is weakly dependent on the overpotential. Because the TS in the water dissociation mechanism is stabilized at higher potentials, at some point the activation energies for the two mechanisms will coincide. With even larger applied voltages, the activation energy for the water dissociation mechanism will be smaller than that for the oxygen coupling mechanism. The process will proceed through the dissociation mechanism, and the dependence on the overpotential will be stronger than it would be for the coupling mechanism, leading to larger Tafel slopes (Figure 58, red).

To summarize, in this section we have considered some of the most important factors that determine the reactivity of photocatalytic materials, as well as their ability to efficiently

transform the electrochemical and solar energy into the chemical energy of the products. The operation of photochemical devices involves many processes, including photoexcitation, electron–hole pair separation, charge diffusion, recombination, and trapping. Charge carriers that arrive at the surface can be transferred to a cocatalyst or participate directly in the redox processes, with the molecules adsorbing on the surface. These processes occur simultaneously, competing with or reinforcing each other and spanning a large range of time-scales, as represented in Figure 59.<sup>33</sup> Although a partial

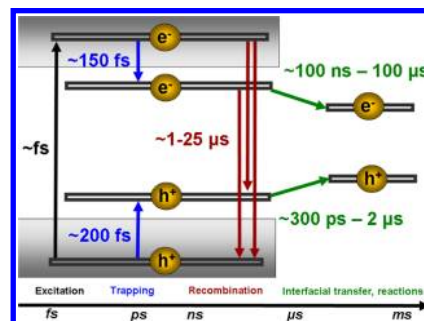


**Figure 59.** Time-scales of the processes taking place in a photocatalytic device.

elucidation of each of the individual processes has been achieved, we do not yet have a complete, unified picture of the operation of photocatalytic materials under various conditions. This can be partially attributed to the complex multidimensional nature of the entire process. Further progress in the elucidation of the operational principles of photochemical devices can possibly be achieved with multiscale approaches.

There is presently a large amount of experimental findings that has been amassed. The theoretical interpretation of this information, supported by computational studies (including *ab initio*, chemical kinetics, and thermodynamics analyses), has made it possible to increase our understanding of the nature of the fundamental chemical and physical processes underlying photochemical catalysis. In general, theory provides valuable insights into the experimental methods suitable for improving the properties of currently available materials, as well as novel approaches for the practical pursuit of new materials. A comprehensive and systematic theoretical analysis, including multiscale approaches, is necessary for constructing a clear picture of photocatalytic and photoelectrochemical processes,



which may then bring us closer to the theoretical limit of photocatalytic efficiency.

## 6. CONCLUSIONS AND OUTLOOK

This Review has described select theoretical and experimental studies of ET at metal oxide interfaces. Particular focus has been placed on the processes that are essential for the operation of photovoltaic and photocatalytic cells, which provide useful illustrations of the practical use of metal oxides in the situation where interfacial ET plays a particularly important role. It is crucial to acquire a complete understanding of ET phenomena to improve the performance of photovoltaic and photocatalytic cells. We have presented experimental results within the framework of electronic and molecular structure theory, along with the theory of nonadiabatic and adiabatic ET kinetics.

Numerous studies of various types of systems that convert the energy of sunlight into useful chemical and electrical work have formed the foundation for the development of novel strategies for their improvement; some examples are technologies such as band gap engineering techniques and solar cell composition schemes. Band gap engineering can be achieved by doping the system with metal or nonmetal elements, or sensitizing the system with organic, metallo-organic, or QD chromophores; this allows for the device to be tuned to absorb solar photons within a specific energy range. Various composite schemes, such as cosensitization and Z-schemes, allow for an increased range of the solar radiation to be converted into useful energy. Techniques based on doping, coadsorbates, the inclusion of specific solvents, and composite schemes make it possible to tune the excitation energy of the material, as well as to shift the positions of the conduction and valence bands of the oxides. This flexibility is particularly important in photocatalytic applications, allowing one to carry out specific reactions under the desired specific working conditions. Overall, significant progress has been achieved in the design of new materials for solar energy conversion.

Despite the enormous amount of studies that have been performed, the best achievable light-to-energy conversion efficiency for photovoltaic applications is only within the range of 11–15%, which is much lower than the theoretically predicted achievable efficiency of 33% for single-junction compositions.<sup>655</sup> Currently, the best photocatalytic cells are able to reach efficiencies of around 6%. Incremental modifications to solar cells, such as tuning the band gaps and the positions of the CB and VB edges, altering the morphology of the nanoparticles, using different solvents, and varying the type of the sensitizer, allow one to systematically change the performance within a relatively narrow range of only a few percent in most cases. This indicates that the understanding of some key aspects of the practical implementation of solar energy conversion is lacking.

Most of the currently available studies focus on the optimization of specific steps in the photovoltaic and photocatalytic cells (Figure 2). The electron injection from a photoexcited sensitizer into a semiconductor substrate is a particularly well-studied process, both experimentally and theoretically. Although the completion of this initial step is crucial for the operation of the device, in most cases it is performed with nearly 100% yield and on an ultrafast time-scale. Thus, it is very unlikely that this step is relevant for predicting the efficiency of photon energy conversion.

However, there are many other processes that are very likely to be efficiency-determining steps; these include back-ET from

the substrate to the electrolyte or oxidized dye, electron and hole trapping within the semiconductor or at the interface, charge separation, and electrolyte or reactant diffusion in the liquid phase. For example, DSSC efficiency can be dramatically increased by reducing the amount of back-ET from the metal oxide surface to the electrolyte with the assistance of coadsorbates. Such an improvement is often larger than the effect on the DSSC efficiency that results from the structural changes of the dye that are induced by the coadsorbate. Yet, if a structural change of the sensitizer decreases back-ET to the chromophore, reducing electron–hole recombination, the observed increase in DSSC efficiency can also be large. As discussed in section 5, the main factors affecting the efficiency of photocatalysts are electron–hole separation and trapping. Although interfacial ET processes are key events in photocatalysis, they do not significantly affect the efficiency of current generation in photocatalytic devices.

The above-mentioned processes that cause electron and energy losses and limit solar cell efficiencies have received significantly less attention than methods that are suitable for tuning the substrate and sensitizer properties. This may be attributed to limitations in the current tools available, as well as to the complexity of the phenomena itself. Because these processes happen on very diverse time-scales, a single tool designed to work within a limited temporal or spatial range cannot account for the full complexity of the system. For example, theoretical modeling of interfacial ET using *ab initio* nonadiabatic MD can be performed only with relatively small systems, involving up to 1000 atoms, and on the time-scale of tens of picoseconds, depending on the approximation used. Smaller systems and those with shorter time-scales can be studied with the highly accurate ML-MCTDH method, while larger systems and those with longer time-scales can be approached with semiempirical electronic structure theory and simplified versions of nonadiabatic MD, such as the classical path approximation, although the results will be less accurate. The processes occurring over long time-scales in real systems can be studied using experimental techniques, albeit with inherent limitations, such as limited resolution and the inability to systematically control all of the parameters that affect the electronic and molecular structure of the system. In some cases, it is possible to incorporate some of the available experimental data and observations into a theoretical framework to construct a model, which spans a large range of time-scales. An example of one such approach has been provided by the back-ET studies from the Troisi group, as discussed in section 4. However, such approaches are in need of further development. An alternative strategy would be to build a corresponding multiscale theoretical model, based on various levels of theory applied to different parts of the system or different processes. Such methodologies have yet to be developed and applied to solar energy conversion problems.

It is crucial that ET processes are examined within a realistic composite system that involves all of the participating components. For example, in some theoretical studies of electron injection from a chromophore to a substrate, typically, only the two parts of the chromophore and substrate are considered. Although such a setup provides a reasonable approximation of ET, the synergetic effects that arise from other parts of the system may be overlooked. The simultaneous consideration of the many other components of a system can lead to system dynamics, which cannot always be understood by a simple superposition of the dynamics arising from the

individual components. An illustration of this effect is the situation where a solvent, electrolyte, or both are present, together with the sensitizer adsorbed on the semiconductor surface, leading to stabilization, destabilization, or a change in the geometry of the sensitizer–metal oxide complex. The new electronic states introduced by the coadsorbed species and the modified electronic states of the original components alter the coupling between the donor and acceptor states, inducing quantitative or even qualitative changes to the dynamics. The dynamics of a multicomponent model can be represented by a kinetic scheme similar to those presented in Figures S1 and S9 in section S. Solving the kinetic model can lead to an expression that defines the overall efficiency of the photoconverting device. This expression can be used to establish relationships between the system parameters, which can be tuned to optimize the energy conversion performance of the solar cell.

The example of a multicomponent approach outlined above can include both the material components, such as reactants, sensitizers, and substrates, as well as light radiation. For example, as discussed in section 3, an explicit description of photon absorption shows that the photoexcited electron can be transferred only partially, lowering the efficiency of the device. The conditions of a working electrode are very different under the steady irradiation of solar light than they are in the dark, for instance, because of the higher density of electrons and differing electrostatic potential between the two conditions. Depending on the energy of incident photons and the properties of the materials used, multiple charge carriers can be generated by the absorption of only one photon. This can cause the kinetic scheme to become more complex, possibly changing the conditions of optimal performance. The description of light–matter interaction may be especially important in composite systems, for example, those involving chromophore diads and Z-schemes, where the adsorption of a photon by a given part of the system may affect the adsorption of a photon of a different energy in another part of the system. As a result, inhibition or reinforcement effects can be achieved, leading to novel design principles.

In summary, significant progress has been achieved in developing photovoltaic and photocatalytic cells for the purpose of converting light into electrical and chemical energy. Many design principles are already in place. At the same time, the significant gap between the current gold standard of these devices and the maximal theoretical efficiency that can be achieved cannot be overlooked. New theoretical frameworks and tools must be developed and qualitatively different design principles need to be established if we are to reach maximal efficiency of these devices. Focusing on the overlooked aspects of the ET processes at metal oxide interfaces, such as light–matter interactions as well as multiscale and multicomponent paradigms, is a promising future research direction.

## AUTHOR INFORMATION

### Corresponding Author

\*E-mail: oleg.prezhdo@rochester.edu.

### Notes

The authors declare no competing financial interest.

## Biographies



Alexey V. Akimov was born in Bryansk oblast, Russia. He received his Diploma in Chemistry in 2007 from M. V. Lomonosov Moscow State University, Moscow, Russia, under joint supervision of Prof. Alexander Nemukhin (MSU, Russia) and Prof. Anatoly Kolomeisky (Rice University, U.S.). He obtained his Ph.D. in Chemistry under Prof. Anatoly Kolomeisky at Rice University in 2011. In 2012 he started working in Prof. Oleg Prezhdo's group at the University of Rochester, and later in 2012 he joined a collaborative project with Dr. James Muckerman at the Department of Chemistry at Brookhaven National Laboratory. Dr. Akimov's research interests include developing new simulation methods based on fundamental physical principles and applying them to a broad range of systems; theoretical photochemistry and photophysics; nanoscience, in particular molecular machines and rotors; surface phenomena; and electron and charge transfer in condensed phase and on interfaces.



Amanda J. Neukirch received her B.S. degree in physics and mathematics from University of Nebraska–Lincoln in 2007. She is currently working toward her Ph.D. in physics under the supervision of Oleg Prezhdo at the University of Rochester. Her research is focused on excitation dynamics in nanoscale systems.



Oleg V. Prezhdo obtained a Diploma in Theoretical Chemistry in 1991 from Kharkiv National University, Ukraine, under Anatoly Luzanov. He completed his Ph.D. with Peter Rossky at the University of Texas, Austin. After a postdoctoral fellowship with John Tully at Yale University, he joined the chemistry department at the University of Washington in 1998, achieving Associate and Full Professor in 2002 and 2005. In 2008, he was elected Fellow of the American Physical Society and in 2010 was offered Senior Professorship at the University of Rochester. Since 2008, he has served as editor for the *Journal of Physical Chemistry*, and, since 2011, as editor for the *Journal of Physical Chemistry Letters*, and, since 2013, as editor for *Surface Science Reports*. Recipient of multiple national and international awards, he held invited professorships in France, Germany, and Japan. His current research interests range from fundamental aspects of semiclassical physics, to excitation dynamics in nanoscale and biological systems.

## ACKNOWLEDGMENTS

The authors thank Julia DeBaecke for comments on the manuscript. O.V.P. and A.J.N. acknowledge financial support from the National Science Foundation, grant CHE-1300118, and U.S. Department of Energy, grant DE-SC0006527. A.V.A. was funded at Brookhaven National Laboratory under contract DE-AC02-98CH10886 with the U.S. Department of Energy.

## REFERENCES

- (1) Hagfeldt, A.; Boschloo, G.; Sun, L.; Kloo, L.; Pettersson, H. *Chem. Rev.* **2010**, *110*, 6595.
- (2) Valdés, Á.; Brillet, J.; Grätzel, M.; Gudmundsdóttir, H.; Hansen, H. A.; Jónsson, H.; Klüpfel, P.; Kroes, G.-J.; Le Formal, F.; Man, I. C.; Martins, R. S.; Nørskov, J. K.; Rossmeisl, J.; Sivula, K.; Vojvodic, A.; Zäch, M. *Phys. Chem. Chem. Phys.* **2012**, *14*, 49.
- (3) Suntivich, J.; May, K. J.; Gasteiger, H. A.; Goodenough, J. B.; Shao-Horn, Y. *Science* **2011**, *334*, 1383.
- (4) Walter, M. G.; Warren, E. L.; McKone, J. R.; Boettcher, S. W.; Mi, Q.; Santori, E. A.; Lewis, N. S. *Chem. Rev.* **2010**, *110*, 6446.
- (5) Maeda, K.; Domen, K. *J. Phys. Chem. Lett.* **2010**, *1*, 2655.
- (6) Kubacka, A.; Fernández-García, M.; Colón, G. *Chem. Rev.* **2012**, *112*, 1555.
- (7) Osgood, R. *Chem. Rev.* **2006**, *106*, 4379.
- (8) Woodhouse, M.; Parkinson, B. A. *Chem. Soc. Rev.* **2009**, *38*, 197.
- (9) Imahori, H.; Umeyama, T.; Ito, S. *Acc. Chem. Res.* **2009**, *42*, 1809.
- (10) Rühle, S.; Shalom, M.; Zaban, A. *ChemPhysChem* **2010**, *11*, 2290.
- (11) Nozik, A. J.; Beard, M. C.; Luther, J. M.; Law, M.; Ellingson, R. J.; Johnson, J. C. *Chem. Rev.* **2010**, *110*, 6873.
- (12) Tvrdy, K.; Frantsuzov, P. A.; Kamat, P. V. *Proc. Natl. Acad. Sci. U.S.A.* **2011**, *108*, 29.
- (13) He, G. S.; Tan, L.-S.; Zheng, Q.; Prasad, P. N. *Chem. Rev.* **2008**, *108*, 1245.
- (14) Anderson, N. A.; Lian, T. *Annu. Rev. Phys. Chem.* **2005**, *56*, 491.
- (15) Stockwell, D.; Yang, Y.; Huang, J.; Anfuso, C.; Huang, Z.; Lian, T. *J. Phys. Chem. C* **2010**, *114*, 6560.
- (16) Linsebigler, A. L.; Lu, G.; Yates, J. T., Jr. *Chem. Rev.* **1995**, *95*, 735.
- (17) Coropceanu, V.; Cornil, J.; Filho, D. A.; da, S.; Olivier, Y.; Silbey, R.; Bredas, J.-L. *Chem. Rev.* **2007**, *107*, 926.
- (18) Smith, M. B.; Michl, J. *Chem. Rev.* **2010**, *110*, 6891.
- (19) Vojvodic, A.; Nørskov, J. K. *Science* **2011**, *334*, 1355.
- (20) Inoue, Y. *Energy Environ. Sci.* **2009**, *2*, 364.
- (21) Martsinovich, N.; Troisi, A. *Energy Environ. Sci.* **2011**, *4*, 4473.
- (22) Prezhdo, O. V.; Duncan, W. R.; Prezhdo, V. V. *Prog. Surf. Sci.* **2009**, *84*, 30.
- (23) Labat, F.; Le Bahers, T.; Ciofini, I.; Adamo, C. *Acc. Chem. Res.* **2012**, *45*, 1268.
- (24) Li, J.; Kondov, I.; Wang, H.; Thoss, M. *J. Phys. Chem. C* **2010**, *114*, 18481.
- (25) Wang, L.; Willig, F.; May, V. *J. Chem. Phys.* **2006**, *124*, 014712.
- (26) Xiao, D.; Martini, L. A.; Snoberger, R. C.; Crabtree, R. H.; Batista, V. S. *J. Am. Chem. Soc.* **2011**, *133*, 9014.
- (27) Ardo, S.; Meyer, G. J. *Chem. Soc. Rev.* **2009**, *38*, 115.
- (28) Hammes-Schiffer, S.; Stuchebrukhov, A. A. *Chem. Rev.* **2010**, *110*, 6939.
- (29) O'Regan, B.; Grätzel, M. *Nature* **1991**, *353*, 737.
- (30) Willig, F.; Eichberger, R.; Sundaresan, N. S.; Parkinson, B. A. *J. Am. Chem. Soc.* **1990**, *112*, 2702.
- (31) Grätzel, M.; Moser, J. *Proc. Natl. Acad. Sci. U.S.A.* **1983**, *80*, 3129.
- (32) Fujishima, A.; Honda, K. *Nature* **1972**, *238*, 37.
- (33) Fujishima, A.; Zhang, X.; Tryk, D. *Surf. Sci. Rep.* **2008**, *63*, 515.
- (34) Grätzel, M. *Acc. Chem. Res.* **2009**, *42*, 1788.
- (35) Marinado, T.; Hagberg, D. P.; Hedlund, M.; Edvinsson, T.; Johansson, E. M. J.; Boschloo, G.; Rensmo, H.; Brinck, T.; Sun, L.; Hagfeldt, A. *Phys. Chem. Chem. Phys.* **2009**, *11*, 133.
- (36) Henrich, V. E. *Prog. Surf. Sci.* **1995**, *50*, 77.
- (37) Duncan, W. R.; Prezhdo, O. V. *Annu. Rev. Phys. Chem.* **2007**, *58*, 143.
- (38) Watson, D. F.; Meyer, G. J. *Annu. Rev. Phys. Chem.* **2005**, *56*, 119.
- (39) O'Regan, B. C.; Durrant, J. R. *Acc. Chem. Res.* **2009**, *42*, 1799.
- (40) Kudo, A.; Miseki, Y. *Chem. Soc. Rev.* **2009**, *38*, 253.
- (41) Kavarnos, G. J.; Turro, N. J. *Chem. Rev.* **1986**, *86*, 401.
- (42) Rühle, S.; Anderson, A. Y.; Barad, H.-N.; Kupfer, B.; Bouhadana, Y.; Rosh-Hodesh, E.; Zaban, A. *J. Phys. Chem. Lett.* **2012**, *3*, 3755.
- (43) Hammes-Schiffer, S.; Tully, J. C. *J. Chem. Phys.* **1994**, *101*, 4657.
- (44) Bornemann, F. A.; Nettesheim, P.; Schütte, C. *J. Chem. Phys.* **1996**, *105*, 1074.
- (45) Gerber, R. B. *J. Chem. Phys.* **1982**, *77*, 3022.
- (46) Gerber, R. B.; Ratner, M. A. *J. Comput. Chem.* **1988**, *92*, 3252.
- (47) Nettesheim, P.; Bornemann, F. A.; Schmidt, B.; Schütte, C. *Chem. Phys. Lett.* **1996**, *256*, 581.
- (48) DasGupta, A.; Huzinaga, S. *Theor. Chim. Acta* **1974**, *35*, 329.
- (49) Dewar, M. J.; Storch, D. M. *J. Am. Chem. Soc.* **1985**, *107*, 3898.
- (50) Řezáč, J.; Fanfrlík, J.; Salahub, D.; Hobza, P. *J. Chem. Theory Comput.* **2009**, *5*, 1749.
- (51) Pyykkö, P.; Laaksonen, L. *J. Phys. Chem.* **1984**, *88*, 4892.
- (52) Simonetta, M.; Gavezzotti, A. *J. Mol. Struct.* **1984**, *107*, 75.
- (53) Hohenberg, P.; Kohn, W. *Phys. Rev.* **1964**, *136*, B864.
- (54) Kohn, W.; Sham, L. J. *Phys. Rev.* **1965**, *140*, 1133.
- (55) Scuseria, G. E. *J. Chem. Phys.* **1992**, *97*, 7528.
- (56) Becke, A. D. *Phys. Rev. A* **1988**, *38*, 3098.
- (57) Becke, A. D. *J. Chem. Phys.* **1992**, *96*, 2155.
- (58) Becke, A. D. *J. Chem. Phys.* **1993**, *98*, 5648.
- (59) Burke, K. *J. Chem. Phys.* **2012**, *136*, 150901.
- (60) Elliott, P.; Lee, D.; Cangi, A.; Burke, K. *Phys. Rev. Lett.* **2008**, *100*, 256406.
- (61) Burke, K.; Perdew, J. P.; Ernzerhof, M. *Int. J. Quantum Chem.* **1997**, *61*, 287.
- (62) Pople, J. A.; Seeger, R.; Krishnan, R. *Int. J. Quantum Chem.* **1977**, *12*, 149.



- (63) Krishnan, R.; Schlegel, H. B.; Pople, J. A. *J. Chem. Phys.* **1980**, *72*, 4654.
- (64) Raghavachari, K.; Pople, J. A. *Int. J. Quantum Chem.* **1981**, *20*, 1067.
- (65) Pople, J. A.; Krishnan, R.; Schlegel, H. B.; Binkley, J. S. *Int. J. Quantum Chem.* **1978**, *14*, 545.
- (66) Bartlett, R. J.; Purvis, G. D. *Int. J. Quantum Chem.* **1978**, *14*, 561.
- (67) Purvis, G. D., III; Bartlett, R. J. *J. Chem. Phys.* **1982**, *76*, 1910.
- (68) Scuseria, G. E.; Janssen, C. L.; Schaefer, H. F. *J. Chem. Phys.* **1988**, *89*, 7382.
- (69) Scuseria, G. E.; Schaefer, H. F. *J. Chem. Phys.* **1989**, *90*, 3700.
- (70) Eade, R. H. A.; Robb, M. A. *Chem. Phys. Lett.* **1981**, *83*, 362.
- (71) Schlegel, H. B.; Robb, M. A. *Chem. Phys. Lett.* **1982**, *93*, 43.
- (72) Frisch, M.; Ragazos, I. N.; Robb, M. A.; Bernhard Schlegel, H. *Chem. Phys. Lett.* **1992**, *189*, 524.
- (73) Yamamoto, N.; Vreven, T.; Robb, M. A.; Frisch, M. J.; Schlegel, H. B. *Chem. Phys. Lett.* **1996**, *250*, 373.
- (74) Craig, C.; Duncan, W.; Prezhdo, O. *Phys. Rev. Lett.* **2005**, *95*, 163001.
- (75) Tully, J. C. *J. Chem. Phys.* **1990**, *93*, 1061.
- (76) Bao, H.; Habenicht, B.; Prezhdo, O.; Ruan, X. *Phys. Rev. B* **2009**, *79*, 235306.
- (77) Chen, L.; Bao, H.; Tan, T.; Prezhdo, O. V.; Ruan, X. *J. Phys. Chem. C* **2011**, *115*, 11400.
- (78) Bixon, M.; Jortner, J.; Cortes, J.; Heitele, H.; Michel-Beyerle, M. E. *J. Chem. Phys.* **1994**, *98*, 7289.
- (79) Engelman, R.; Jortner, J. *Mol. Phys.* **1970**, *18*, 145.
- (80) Nitzan, A. *J. Chem. Phys.* **1975**, *63*, 200.
- (81) Ando, K. *J. Chem. Phys.* **1997**, *106*, 116.
- (82) Lin, S. H. *J. Chem. Phys.* **1970**, *53*, 3766.
- (83) Weber, M.; Lynn, K.; Barbiellini, B.; Sterne, P.; Denison, A. *Phys. Rev. B* **2002**, *66*, 041305(R).
- (84) Tachiya, M.; Barzykin, A. V. *Chem. Phys.* **2005**, *319*, 222.
- (85) Tachiya, M.; Seki, K. *J. Phys. Chem. A* **2007**, *111*, 9553.
- (86) Mataga, N.; Taniguchi, S.; Chosrowjan, H.; Osuka, A.; Kurotobi, K. *Chem. Phys. Lett.* **2005**, *403*, 163.
- (87) Eyring, H. *J. Chem. Phys.* **1935**, *3*, 107.
- (88) Wigner, E. *J. Chem. Phys.* **1937**, *5*, 720.
- (89) Miller, W. H. *Acc. Chem. Res.* **1976**, *9*, 306.
- (90) Pechukas, P. *Annu. Rev. Phys. Chem.* **1981**, *32*, 159.
- (91) Truhlar, D. G.; Hase, W. L.; Hynes, J. T. *J. Phys. Chem.* **1983**, *87*, 2664.
- (92) Vanden-Eijnden, E.; Tal, F. A. *J. Chem. Phys.* **2005**, *123*, 184103.
- (93) Schenter, G. K.; Garrett, B. C.; Truhlar, D. G. *J. Chem. Phys.* **2003**, *119*, 5828.
- (94) Voth, G. A.; Chandler, D.; Miller, W. H. *J. Chem. Phys.* **1989**, *91*, 7749.
- (95) Bartsch, T.; Uzer, T.; Moix, J. M.; Hernandez, R. *J. Phys. Chem. B* **2008**, *112*, 206.
- (96) Miller, W. H. *J. Phys. Chem.* **1983**, *87*, 2731.
- (97) Hele, T. J. H.; Althorpe, S. C. *J. Chem. Phys.* **2013**, *138*, 084108.
- (98) Kawai, S.; Bandrauk, A. D.; Jaffé, C.; Bartsch, T.; Palacián, J.; Uzer, T. *J. Chem. Phys.* **2007**, *126*, 164306.
- (99) Gridelet, E.; Lorquet, J. C.; Leyh, B. *J. Chem. Phys.* **2005**, *122*, 094106.
- (100) Cheney, B. G.; Andersen, H. C. *J. Chem. Phys.* **2003**, *118*, 9542.
- (101) Miller, W. H.; Schwartz, S. D.; Tromp, J. W. *J. Chem. Phys.* **1983**, *79*, 4889.
- (102) Voth, G. A.; Chandler, D.; Miller, W. H. *J. Phys. Chem.* **1989**, *93*, 7009.
- (103) Straus, J. B.; Voth, G. A. *J. Chem. Phys.* **1992**, *96*, 5460.
- (104) Pollak, E. *J. Chem. Phys.* **1991**, *95*, 533.
- (105) Pollak, E. *Chem. Phys. Lett.* **1986**, *127*, 178.
- (106) Grote, R. F.; Hynes, J. T. *J. Chem. Phys.* **1980**, *73*, 2715.
- (107) Wolynes, P. G. *Phys. Rev. Lett.* **1981**, *47*, 968.
- (108) Dakhnovskii, Y. I.; Ovchinnikov, A. A. *Phys. Lett. A* **1985**, *113*, 147.
- (109) Marcus, R. A. *Annu. Rev. Phys. Chem.* **1964**, *15*, 155.
- (110) Marcus, R. A.; Sutin, N. *Biochim. Biophys. Acta, Rev. Bioenerg.* **1985**, *811*, 265.
- (111) Marcus, R. A. *J. Chem. Phys.* **1956**, *24*, 979.
- (112) Marcus, R. A. *J. Chem. Phys.* **1956**, *24*, 966.
- (113) Marcus, R. A. *J. Chem. Phys.* **1957**, *26*, 867.
- (114) Marcus, R. A. *J. Chem. Phys.* **1957**, *26*, 872.
- (115) Marcus, R. A. *J. Phys. Chem.* **1963**, *67*, 853.
- (116) Marcus, R. A. *J. Chem. Phys.* **1965**, *43*, 679.
- (117) Marcus, R. A. *Faraday Discuss. Chem. Soc.* **1982**, *74*, 7.
- (118) Calef, D. F.; Wolynes, P. G. *J. Phys. Chem.* **1983**, *87*, 3387.
- (119) Dakhnovskii, Y. I.; Ovchinnikov, A. A. *Chem. Phys.* **1983**, *80*, 17.
- (120) Zusman, L. D. *Chem. Phys.* **1980**, *49*, 295.
- (121) Zusman, L. D. *Chem. Phys.* **1988**, *119*, 51.
- (122) Rips, I.; Jortner, J. *J. Chem. Phys.* **1987**, *87*, 2090.
- (123) Garg, A.; Onuchic, J. N.; Ambegaokar, V. *J. Chem. Phys.* **1985**, *83*, 4491.
- (124) Van der Zwan, G.; Hynes, J. T. *J. Chem. Phys.* **1982**, *76*, 2993.
- (125) Kramers, H. A. *Physica* **1940**, *7*, 284.
- (126) Alexandrov, I. V. *Chem. Phys.* **1980**, *51*, 449.
- (127) Zwanzig, R. *J. Stat. Phys.* **1973**, *9*, 215.
- (128) Caldeira, A. O.; Leggett, A. J. *Ann. Phys.* **1983**, *149*, 374.
- (129) Pollak, E.; Tucker, S. C.; Berne, B. J. *Phys. Rev. Lett.* **1990**, *65*, 1399.
- (130) Sim, E.; Makri, N. *J. Phys. Chem. B* **1997**, *101*, 5446.
- (131) Makri, N.; Sim, E.; Makarov, D. E.; Topaler, M. *Proc. Natl. Acad. Sci. U.S.A.* **1996**, *93*, 3926.
- (132) Makri, N.; Makarov, D. E. *J. Chem. Phys.* **1995**, *102*, 4600.
- (133) Coalson, R. D.; Kinsey, J. L. *J. Chem. Phys.* **1986**, *85*, 4322.
- (134) Coalson, R. D. *J. Chem. Phys.* **1987**, *86*, 995.
- (135) Coalson, R. D. *Phys. Rev. B* **1989**, *39*, 12052.
- (136) Coalson, R. D.; Evans, D. G.; Nitzan, A. *J. Chem. Phys.* **1994**, *101*, 436.
- (137) Evans, D. G.; Nitzan, A.; Ratner, M. A. *J. Chem. Phys.* **1998**, *108*, 6387.
- (138) Egger, R.; Mak, C. H. *J. Phys. Chem.* **1994**, *98*, 9903.
- (139) Haynes, G. R.; Voth, G. A. *Phys. Rev. A* **1992**, *46*, 2143.
- (140) Gertner, B. J.; Wilson, K. R.; Hynes, J. T. *J. Chem. Phys.* **1989**, *90*, 3537.
- (141) Dakhnovskii, Y.; Lubchenko, V.; Wolynes, P. *J. Chem. Phys.* **1996**, *104*, 1875.
- (142) Onuchic, J. N.; Wolynes, P. G. *J. Chem. Phys.* **1993**, *98*, 2218.
- (143) Hornbach, M. J.; Dakhnovskii, Y. *J. Chem. Phys.* **1999**, *111*, 5073.
- (144) Dakhnovskii, Y. *J. Chem. Phys.* **1999**, *111*, 5418.
- (145) Prezhdo, O. V.; Rossky, P. J. *J. Chem. Phys.* **1997**, *107*, 5863.
- (146) Jones, D. R.; Troisi, A. *Phys. Chem. Chem. Phys.* **2010**, *12*, 4625.
- (147) Wang, L.; Ernstorfer, R.; Willig, F.; May, V. *J. Phys. Chem. B* **2005**, *109*, 9589.
- (148) Wang, L.; Willig, F.; May, V. *J. Chem. Phys.* **2007**, *126*, 134110.
- (149) Labat, F.; Ciofini, I.; Hratchian, H. P.; Frisch, M.; Raghavachari, K.; Adamo, C. *J. Am. Chem. Soc.* **2009**, *131*, 14290.
- (150) Newns, D. M. *Phys. Rev.* **1969**, *178*, 1123.
- (151) Persson, P.; Lundqvist, M. J.; Ernstorfer, R.; Goddard, W. A.; Willig, F. *J. Chem. Theory Comput.* **2006**, *2*, 441.
- (152) Maggio, E.; Martsinovich, N.; Troisi, A. *J. Chem. Phys.* **2012**, *137*, 22A508.
- (153) Maggio, E.; Martsinovich, N.; Troisi, A. *J. Phys. Chem. C* **2012**, *116*, 7638.
- (154) Long, R.; Prezhdo, O. V. *J. Am. Chem. Soc.* **2011**, *133*, 19240.
- (155) Long, R.; English, N. J.; Prezhdo, O. V. *J. Am. Chem. Soc.* **2012**, *134*, 14238.
- (156) Dahnovsky, Y. *Phys. Rev. B* **2011**, *83*, 165306.
- (157) Coalson, R. D. *J. Chem. Phys.* **1990**, *92*, 4993.
- (158) Prezhdo, O. V. *Phys. Rev. Lett.* **2000**, *85*, 4413.
- (159) Prezhdo, O. V.; Rossky, P. J. *Phys. Rev. Lett.* **1998**, *81*, 5294.
- (160) Nozik, A. J. *Chem. Phys. Lett.* **2008**, *457*, 3.
- (161) Beard, M. C.; Midgett, A. G.; Law, M.; Semonin, O. E.; Ellingson, R. J.; Nozik, A. J. *Nano Lett.* **2009**, *9*, 836.

- (162) Ellingson, R. J.; Beard, M. C.; Johnson, J. C.; Yu, P.; Micic, O. I.; Nozik, A. J.; Shabaev, A.; Efros, A. L. *Nano Lett.* **2005**, *5*, 865.
- (163) Muntwiler, M.; Yang, Q.; Tisdale, W.; Zhu, X.-Y. *Phys. Rev. Lett.* **2008**, *101*, 196403.
- (164) Zimmerman, P. M.; Zhang, Z.; Musgrave, C. B. *Nature* **2010**, *2*, 648.
- (165) Zimmerman, P. M.; Bell, F.; Casanova, D.; Head-Gordon, M. J. *Am. Chem. Soc.* **2011**, *133*, 19944.
- (166) Yi, Y.; Coropceanu, V.; Brédas, J.-L. *J. Am. Chem. Soc.* **2009**, *131*, 15777.
- (167) Von Barth, U.; Dahlen, N.; Van Leeuwen, R.; Stefanucci, G. *Phys. Rev. B* **2005**, *72*, 235109.
- (168) Kolesov, G.; Dahnovsky, Y. *Phys. Rev. B* **2012**, *85*, 241309(R).
- (169) Danielewicz, P. *Ann. Phys.* **1984**, *152*, 239.
- (170) Kilin, D. S.; Micha, D. A. *J. Phys. Chem. C* **2011**, *115*, 770.
- (171) Kilin, D. S.; Micha, D. A. *J. Phys. Chem. C* **2009**, *113*, 3530.
- (172) Pimachev, A.; Kolesov, G.; Chen, J.; Wang, W.; Dahnovsky, Y. *J. Chem. Phys.* **2012**, *137*, 244704.
- (173) Rodriguez, R.; Blesa, M. A.; Regazzoni, A. E. *J. Colloid Interface Sci.* **1996**, *177*, 122.
- (174) Gundlach, L.; Ernstorfer, R.; Willig, F. *Phys. Rev. B* **2006**, *74*, 035324.
- (175) Cherepy, N. J.; Smestad, G. P.; Grätzel, M.; Zhang, J. Z. *J. Phys. Chem. B* **1997**, *101*, 9342.
- (176) Negre, C. F. A.; Fuertes, V. C.; Oviedo, M. B.; Oliva, F. Y.; Sánchez, C. G. *J. Phys. Chem. C* **2012**, *116*, 14748.
- (177) Drukker, K. *J. Comput. Phys.* **1999**, *153*, 225.
- (178) Hack, M. D.; Truhlar, D. G. *J. Phys. Chem. A* **2000**, *104*, 7917.
- (179) Hack, M. D.; Wensmann, A. M.; Truhlar, D. G.; Ben-Nun, M.; Martínez, T. J. *J. Chem. Phys.* **2001**, *115*, 1172.
- (180) Beck, M. H.; Jackle, A.; Worth, G. A.; Meyer, H.-D. *Phys. Rep.* **2000**, *324*, 1.
- (181) Heller, E. J. *Acc. Chem. Res.* **2006**, *39*, 127.
- (182) Prezhdo, O. V. *Theor. Chim. Acta* **2006**, *116*, 206.
- (183) Tully, J. C. *Faraday Discuss.* **1998**, *110*, 407.
- (184) Kosloff, D.; Kosloff, R. *J. Comput. Phys.* **1983**, *52*, 35.
- (185) Van Dijk, W.; Toyama, F. *Phys. Rev. E* **2007**, *75*, 036707.
- (186) Gray, S. K.; Manolopoulos, D. E. *J. Chem. Phys.* **1996**, *104*, 7099.
- (187) Marquetand, P.; Richter, M.; González-Vázquez, J.; Sola, I.; González, L. *Faraday Discuss.* **2011**, *153*, 261.
- (188) Ramakrishna, S.; Willig, F.; May, V.; Knorr, A. *J. Phys. Chem. B* **2003**, *107*, 607.
- (189) Schlegel, H. B.; Smith, S. M.; Li, X. *J. Chem. Phys.* **2007**, *126*, 244110.
- (190) Thoss, M.; Domcke, W.; Wang, H. *Chem. Phys.* **2004**, *296*, 217.
- (191) Wang, H.; Thoss, M. *J. Phys. Chem. A* **2007**, *111*, 10369.
- (192) Stock, G.; Thoss, M. *Phys. Rev. Lett.* **1997**, *78*, 578.
- (193) Thoss, M.; Stock, G. *Phys. Rev. A* **1999**, *59*, 64.
- (194) Härtle, R.; Butzin, M.; Rubio-Pons, O.; Thoss, M. *Phys. Rev. Lett.* **2011**, *107*, 046802.
- (195) Kondov, I.; Thoss, M.; Wang, H. *J. Phys. Chem. A* **2006**, *110*, 1364.
- (196) Kondov, I.; Cizek, M.; Benesch, C.; Wang, H.; Thoss, M. *J. Phys. Chem. C* **2007**, *111*, 11970.
- (197) Li, J.; Nilsing, M.; Kondov, I.; Wang, H.; Persson, P.; Lunell, S.; Thoss, M. *J. Phys. Chem. C* **2008**, *112*, 12326.
- (198) Anderson, A. *Phys. Rev. Lett.* **1995**, *74*, 621.
- (199) Prezhdo, O. V.; Kisil, V. V. *Phys. Rev. A* **1997**, *56*, 162.
- (200) Prezhdo, O. V.; Rossky, P. J. *J. Chem. Phys.* **1997**, *107*, 825.
- (201) Kapral, R.; Ciccotti, G. *J. Chem. Phys.* **1999**, *110*, 8919.
- (202) Sholl, D. S.; Tully, J. C. *J. Chem. Phys.* **1998**, *109*, 7702.
- (203) Fabiano, E.; Keal, T. W.; Thiel, W. *Chem. Phys.* **2008**, *349*, 334.
- (204) Parandekar, P. V.; Tully, J. C. *J. Chem. Phys.* **2005**, *122*, 094102.
- (205) Parandekar, P. V.; Tully, J. C. *J. Chem. Theory Comput.* **2006**, *2*, 229.
- (206) Sawada, S. I.; Nitzan, A.; Metiu, H. *Phys. Rev. B* **1985**, *32*, 851.
- (207) Duncan, W. R.; Stier, W. M.; Prezhdo, O. V. *J. Am. Chem. Soc.* **2005**, *127*, 7941.
- (208) Fischer, S. A.; Habenicht, B. F.; Madrid, A. B.; Duncan, W. R.; Prezhdo, O. V. *J. Chem. Phys.* **2011**, *134*, 24102.
- (209) Kirson, Z.; Gerber, R. B.; Nitzan, A.; Ratner, M. A. *Surf. Sci.* **1984**, *137*, S27.
- (210) McCurdy, C. W.; Meyer, H. D.; Miller, W. H. *J. Chem. Phys.* **1979**, *70*, 3177.
- (211) Meyer, H.-D.; Miller, W. H. *J. Chem. Phys.* **1979**, *70*, 3214.
- (212) Meyer, H.-D.; Miller, W. H. *J. Chem. Phys.* **1980**, *72*, 2272.
- (213) Isborn, C. M.; Li, X.; Tully, J. C. *J. Chem. Phys.* **2007**, *126*, 134307.
- (214) Li, X.; Tully, J. C.; Schlegel, H. B.; Frisch, M. J. *J. Chem. Phys.* **2005**, *123*, 084106.
- (215) Fang, J.-Y.; Hammes-Schiffer, S. *J. Chem. Phys.* **1999**, *110*, 11166.
- (216) Käß, G. *Phys. Rev. E* **2002**, *66*, 046117.
- (217) Käß, G. *J. Phys. Chem. A* **2004**, *108*, 8866.
- (218) Gindensperger, E.; Meier, C.; Beswick, J. A. *J. Chem. Phys.* **2000**, *113*, 9369.
- (219) Webster, F. J.; Schnitker, J.; Friedrichs, M. S.; Friesner, R. A.; Rossky, P. J. *Phys. Rev. Lett.* **1991**, *66*, 3172.
- (220) Webster, F.; Rossky, P. J.; Friesner, R. A. *Comput. Phys. Commun.* **1991**, *63*, 494.
- (221) Pechukas, P. *Phys. Rev.* **1969**, *181*, 166.
- (222) Pechukas, P. *Phys. Rev.* **1969**, *181*, 174.
- (223) Coker, D. F.; Xiao, L. *J. Chem. Phys.* **1995**, *102*, 496.
- (224) Ehrenfest, P. *Z. Phys.* **1927**, *45*, 455.
- (225) Shalashilin, D. V.; Michtchenko, A. V.; Lara, F. *Chem. Phys. Lett.* **1993**, *207*, 250.
- (226) Delos, J. B.; Thorson, W. R.; Knudson, S. K. *Phys. Rev. A* **1972**, *6*, 709.
- (227) Delos, J. B.; Thorson, W. R. *Phys. Rev. A* **1972**, *6*, 720.
- (228) Heller, E. J. *J. Chem. Phys.* **1976**, *64*, 63.
- (229) Stock, G. *J. Chem. Phys.* **1995**, *103*, 2888.
- (230) Volobuev, Y. L.; Hack, M. D.; Topaler, M. S.; Truhlar, D. G. *J. Chem. Phys.* **2000**, *112*, 9716.
- (231) Fischer, S. A.; Chapman, C. T.; Li, X. *J. Chem. Phys.* **2011**, *135*, 144102.
- (232) Bittner, E. R.; Rossky, P. J. *J. Chem. Phys.* **1995**, *103*, 8130.
- (233) Bittner, E. R.; Rossky, P. J. *J. Chem. Phys.* **1997**, *107*, 8611.
- (234) Prezhdo, O. V. *J. Chem. Phys.* **1999**, *111*, 8366.
- (235) Bedard-Hearn, M. J.; Larsen, R. E.; Schwartz, B. J. *J. Chem. Phys.* **2005**, *123*, 234106.
- (236) Larsen, R. E.; Bedard-Hearn, M. J.; Schwartz, B. J. *J. Phys. Chem. B* **2006**, *110*, 20055.
- (237) Wong, K. F.; Rossky, P. J. *J. Chem. Phys.* **2002**, *116*, 8418.
- (238) Wong, K. F.; Rossky, P. J. *J. Chem. Phys.* **2002**, *116*, 8429.
- (239) Subotnik, J. E. *J. Chem. Phys.* **2010**, *132*, 134112.
- (240) Granucci, G.; Persico, M.; Zocante, A. *J. Chem. Phys.* **2010**, *133*, 134111.
- (241) Kondov, I.; Kleinekathöfer, U.; Schreiber, M. *J. Chem. Phys.* **2003**, *119*, 6635.
- (242) Schröder, M.; Kleinekathöfer, U. *Phys. Status Solidi* **2004**, *241*, 2157.
- (243) Jaeger, H. M.; Fischer, S.; Prezhdo, O. V. *J. Chem. Phys.* **2012**, *137*, 22A545.
- (244) Kelly, A.; Van Zon, R.; Schofield, J.; Kapral, R. *J. Chem. Phys.* **2012**, *136*, 084101.
- (245) Nielsen, S.; Kapral, R.; Ciccotti, G. *J. Stat. Phys.* **2000**, *101*, 225.
- (246) Mac Kernan, D.; Ciccotti, G.; Kapral, R. *J. Chem. Phys.* **2002**, *116*, 2346.
- (247) Mac Kernan, D.; Ciccotti, G.; Kapral, R. *J. Phys. Chem. B* **2008**, *112*, 424.
- (248) Nielsen, S.; Kapral, R.; Ciccotti, G. *J. Chem. Phys.* **2000**, *112*, 6543.
- (249) Bonella, S.; Ciccotti, G.; Kapral, R. *Chem. Phys. Lett.* **2010**, *484*, 399.
- (250) Kapral, R. *J. Phys. Chem. A* **2001**, *105*, 2885.
- (251) Rank, J. P.; Kapral, R. *J. Chem. Phys.* **2010**, *132*, 074106.

- (252) Sielk, J.; Von Horsten, H. F.; Krüger, F.; Schneider, R.; Hartke, B. *Phys. Chem. Chem. Phys.* **2009**, *11*, 463.
- (253) Morelli, J.; Hammes-Schiffer, S. *Chem. Phys. Lett.* **1997**, *269*, 161.
- (254) Hyeon-Deuk, K.; Ando, K. *J. Chem. Phys.* **2010**, *132*, 164507.
- (255) Hyeon-Deuk, K.; Ando, K. *J. Chem. Phys.* **2009**, *131*, 064501.
- (256) Garraway, B. M. *J. Phys. B: At. Mol. Opt. Phys.* **2000**, *33*, 4447.
- (257) Grad, J.; Yan, Y. J.; Haque, A.; Mukamel, S. *J. Chem. Phys.* **1987**, *86*, 3441.
- (258) García-Vela, A.; Gerber, R. B.; Imre, D. G. *J. Chem. Phys.* **1992**, *97*, 7242.
- (259) Frantsuzov, P. A.; Mandelshtam, V. A. *J. Chem. Phys.* **2004**, *121*, 9247.
- (260) Frantsuzov, P. A.; Mandelshtam, V. A. *J. Chem. Phys.* **2008**, *128*, 094304.
- (261) Billing, G. D. *J. Chem. Phys.* **1999**, *110*, 5526.
- (262) Ando, K. *Bull. Chem. Soc. Jpn.* **2009**, *82*, 975.
- (263) Ando, K. *Chem. Phys. Lett.* **2003**, *376*, 532.
- (264) Arickx, F.; Broeckhove, J.; Coene, W.; Van Leuven, P. *Int. J. Quantum Chem.* **1986**, *30*, 471.
- (265) Chapman, C. T.; Cina, J. A. *J. Chem. Phys.* **2007**, *127*, 114502.
- (266) Chapman, C. T.; Cheng, X.; Cina, J. A. *J. Phys. Chem. A* **2011**, *115*, 3980.
- (267) Manthe, U.; Meyer, H.-D.; Cederbaum, L. S. *J. Chem. Phys.* **1992**, *97*, 3199.
- (268) Meyer, H. D.; Manthe, U.; Cederbaum, L. S. *Chem. Phys. Lett.* **1990**, *165*, 73.
- (269) Wang, H.; Thoss, M.; Miller, W. H. *J. Chem. Phys.* **2001**, *115*, 2979.
- (270) Wang, H. *J. Chem. Phys.* **2000**, *113*, 9948.
- (271) Nest, M.; Meyer, H.-D. *J. Chem. Phys.* **2003**, *119*, 24.
- (272) Manthe, U. *J. Chem. Phys.* **2008**, *128*, 164116.
- (273) Wang, H.; Thoss, M. *J. Chem. Phys.* **2009**, *131*, 024114.
- (274) Wang, H.; Thoss, M. *J. Chem. Phys.* **2003**, *119*, 1289.
- (275) Vendrell, O.; Meyer, H. D. *J. Chem. Phys.* **2011**, *134*, 044135.
- (276) Ben-Nun, M.; Martínez, T. J. *J. Chem. Phys.* **1998**, *108*, 7244.
- (277) Ben-Nun, M.; Quenneville, J.; Martínez, T. J. *J. Phys. Chem. A* **2000**, *104*, 5161.
- (278) Martínez, T. J.; Ben-Nun, M.; Levine, R. D. *J. Phys. Chem.* **1996**, *100*, 7884.
- (279) Martínez, T. J.; Ben-Nun, M.; Ashkenazi, G. *J. Chem. Phys.* **1996**, *104*, 2847.
- (280) Yang, S.; Coe, J. D.; Kaduk, B.; Martínez, T. J. *J. Chem. Phys.* **2009**, *130*, 134113.
- (281) Heller, E. J. *J. Chem. Phys.* **1975**, *62*, 1544.
- (282) Heller, E. J. *J. Chem. Phys.* **1981**, *75*, 2923.
- (283) Lee, S.-Y.; Heller, E. J. *J. Chem. Phys.* **1982**, *76*, 3035.
- (284) Prezhdo, O. V.; Pereverzev, Y. V. *J. Chem. Phys.* **2000**, *113*, 6557.
- (285) Prezhdo, O. V.; Pereverzev, Y. V. *J. Chem. Phys.* **2002**, *116*, 4450.
- (286) Pahl, E.; Prezhdo, O. V. *J. Chem. Phys.* **2002**, *116*, 8704.
- (287) Prezhdo, O. V. *J. Chem. Phys.* **2002**, *117*, 2995.
- (288) Akimov, A. V.; Prezhdo, O. V. *J. Chem. Phys.* **2012**, *137*, 224115.
- (289) Heatwole, E. M.; Prezhdo, O. V. *J. Chem. Phys.* **2005**, *122*, 234109.
- (290) Heatwole, E. M.; Prezhdo, O. V. *J. Phys. Soc. Jpn.* **2008**, *77*, 044001.
- (291) Brooksby, C.; Prezhdo, O. V. *Chem. Phys. Lett.* **2003**, *378*, 533.
- (292) Horsfield, A. P.; Bowler, D. R.; Fisher, A. J.; Todorov, T. N.; Sánchez, C. G. *J. Phys.: Condens. Matter* **2004**, *16*, 8251.
- (293) Bowler, D. R.; Horsfield, A. P.; Sánchez, C. G.; Todorov, T. N. *J. Phys. (Paris)* **2005**, *17*, 3985.
- (294) Kumar, S. G.; Devi, L. G. *J. Phys. Chem. A* **2011**, *115*, 13211.
- (295) Wrighton, M. S.; Ginley, D. S.; Wolczanski, P. T.; Ellis, A. B.; Morse, D. L.; Linz, A. *Proc. Natl. Acad. Sci. U.S.A.* **1975**, *72*, 1518.
- (296) Weston, M.; Reade, T. J.; Britton, A. J.; Handrup, K.; Champness, N. R.; O'Shea, J. N. *J. Chem. Phys.* **2011**, *135*, 114703.
- (297) Teoh, W. Y.; Scott, J. A.; Amal, R. *J. Phys. Chem. Lett.* **2012**, *3*, 629.
- (298) Tada, H.; Kubo, Y.; Akazawa, M.; Ito, S. *Langmuir* **1998**, *14*, 2936.
- (299) Chen, X.; Mao, S. S. *Chem. Rev.* **2007**, *107*, 2891.
- (300) Bonnell, D. A. *Prog. Surf. Sci.* **1998**, *57*, 187.
- (301) Diebold, U. *Surf. Sci. Rep.* **2003**, *48*, 53.
- (302) Ramamoorthy, M.; Vanderbilt, D.; King-Smith, R. D. *Phys. Rev. B* **1994**, *49*, 16721.
- (303) Shapovalov, V.; Wang, Y.; Truong, T. N. *Chem. Phys. Lett.* **2003**, *375*, 321.
- (304) Zhang, Z.; Fenter, P.; Cheng, L.; Sturchio, N. C.; Bedzyk, M. J.; Předota, M.; Bandura, A.; Kubicki, J. D.; Lvov, S. N.; Cummings, P. T.; Chialvo, A. A.; Ridley, M. K.; Bénézeth, P.; Anovitz, L.; Palmer, D. A.; Machesky, M. L.; Wesolowski, D. J. *Langmuir* **2004**, *20*, 4954.
- (305) Zhang, W.; Yang, J.; Luo, Y.; Monti, S.; Carravetta, V. *J. Chem. Phys.* **2008**, *129*, 064703.
- (306) Nomoto, T.; Sasahara, A.; Onishi, H. *J. Chem. Phys.* **2009**, *131*, 084703.
- (307) Anta, J. A.; Guillén, E.; Tena-Zaera, R. *J. Phys. Chem. C* **2012**, *116*, 11413.
- (308) Hara, K.; Horiguchi, T.; Kinoshita, T.; Sayama, K.; Sugihara, H.; Arakawa, H. *Sol. Energy Mater. Sol. Cells* **2000**, *64*, 115.
- (309) Sayama, K.; Sugihara, H.; Arakawa, H. *Chem. Mater.* **1998**, *10*, 3825.
- (310) Reyes-Gil, K. R.; Reyes-Garcia, E. A.; Raftery, D. *J. Phys. Chem. C* **2007**, *111*, 14579.
- (311) Mu, J.; Chen, B.; Zhang, M.; Guo, Z.; Zhang, P.; Zhang, Z.; Sun, Y.; Shao, C.; Liu, Y. *ACS Appl. Mater. Interfaces* **2012**, *4*, 424.
- (312) Mori, S.; Asano, A. *J. Phys. Chem. C* **2010**, *114*, 13113.
- (313) Mi, Y.; Odaka, H.; Iwata, S. *Jpn. J. Appl. Phys.* **1999**, *38*, 3453.
- (314) Bedja, I.; Hotchandani, S.; Kamat, P. V. *J. Phys. Chem. C* **1994**, *98*, 4133.
- (315) Ferrere, S.; Zaban, A.; Gregg, B. A. *J. Phys. Chem. B* **1997**, *101*, 4490.
- (316) Shinde, D. V.; Lim, I.; Kim, C. S.; Lee, J. K.; Mane, R. S.; Han, S.-H. *Chem. Phys. Lett.* **2012**, *542*, 66.
- (317) Lenzmann, F.; Krueger, J.; Burnside, S.; Brooks, K.; Grätzel, M.; Gal, D.; Rühle, S.; Cahen, D. *J. Phys. Chem. B* **2001**, *105*, 6347.
- (318) Enache, C. S.; Lloyd, D.; Damen, M. R.; Schoonman, J.; Van de Krol, R. *J. Phys. Chem. C* **2009**, *113*, 19351.
- (319) Fan, H.; Jiang, T.; Li, H.; Wang, D.; Wang, L.; Zhai, J.; He, D.; Wang, P.; Xie, T. *J. Phys. Chem. C* **2012**, *116*, 2425.
- (320) Ng, Y. H.; Iwase, A.; Kudo, A.; Amal, R. *J. Phys. Chem. Lett.* **2010**, *1*, 2607.
- (321) Liang, Y.; Tsubota, T.; Mooij, L. P. A.; Van de Krol, R. *J. Phys. Chem. C* **2011**, *115*, 17594.
- (322) Wetchakun, N.; Chaiwichain, S.; Inceesungvorn, B.; Pingmuang, K.; Phanichphant, S.; Minett, A. I.; Chen, J. *ACS Appl. Mater. Interfaces* **2012**, *4*, 3718.
- (323) Merka, O.; Yarovyi, V.; Bahnmann, D. W.; Wark, M. *J. Phys. Chem. C* **2011**, *115*, 8014.
- (324) Pan, C.; Zhu, Y. *Environ. Sci. Technol.* **2010**, *44*, 5570.
- (325) Gou, G.; Bennett, J.; Takenaka, H.; Rappe, A. *Phys. Rev. B* **2011**, *83*, 205115.
- (326) Qi, T.; Curnan, M.; Kim, S.; Bennett, J.; Grinberg, I.; Rappe, A. *Phys. Rev. B* **2011**, *84*, 245206.
- (327) Qi, T.; Grinberg, I.; Rappe, A. *Phys. Rev. B* **2011**, *83*, 224108.
- (328) Vogtenhuber, D.; Podloucky, R.; Neckel, A.; Steinemann, S. G.; Freeman, A. J. *Phys. Rev. B* **1994**, *49*, 2099.
- (329) Kurtz, R. L.; Stock-Bauer, R.; Msdey, T. E.; Román, E.; De Segovia, J. L. *Surf. Sci.* **1989**, *218*, 178.
- (330) Kavan, L.; Grätzel, M.; Gilbert, S. E.; Klemenz, C.; Scheel, H. J. *J. Am. Chem. Soc.* **1996**, *118*, 6716.
- (331) McCluskey, M. D.; Jokela, S. J. *J. Appl. Phys.* **2009**, *106*, 071101.
- (332) Maeda, K.; Takata, T.; Hara, M.; Saito, N.; Inoue, Y.; Kobayashi, H.; Domen, K. *J. Am. Chem. Soc.* **2005**, *127*, 8286.
- (333) Oshikiri, M.; Aryasetiawan, F. *Phys. Rev. B* **1999**, *60*, 10754.



- (334) Robertson, J. J. *Phys. C* **1979**, *12*, 4767.
- (335) Mishra, K. C.; Johnson, K. H.; Schmidt, P. C. *Phys. Rev. B* **1995**, *51*, 13972.
- (336) Mryasov, O.; Freeman, A. *Phys. Rev. B* **2001**, *64*, 233111.
- (337) Wang, F.; Di Valentin, C.; Pacchioni, G. *J. Phys. Chem. C* **2012**, *116*, 8901.
- (338) Miyazaki, S. *J. Vac. Sci. Technol., B* **2001**, *19*, 2212.
- (339) Nohira, H.; Tsai, W.; Besling, W.; Young, E.; Petry, J.; Conard, T.; Vandervorst, W.; De Gendt, S.; Heyns, M.; Maes, J.; Tuominen, M. *J. Non-Cryst. Solids* **2002**, *303*, 83.
- (340) Puthenkovilakam, R.; Chang, J. P. *J. Appl. Phys.* **2004**, *96*, 2701.
- (341) Ohta, A.; Yamaoka, M.; Miyazaki, S. *Microelectron. Eng.* **2004**, *72*, 154.
- (342) Mayer, M. A.; Yu, K. M.; Speaks, D. T.; Denlinger, J. D.; Reichertz, L. A.; Beeman, J. W.; Haller, E. E.; Walukiewicz, W. *J. Phys. Chem. C* **2012**, *116*, 15281.
- (343) Park, J. H.; Kim, S.; Bard, A. J. *Nano Lett.* **2006**, *6*, 24.
- (344) Ma, T.; Akiyama, M.; Abe, E.; Imai, I. *Nano Lett.* **2005**, *5*, 2543.
- (345) Livraghi, S.; Paganini, M. C.; Giamello, E.; Selloni, A.; Di Valentin, C.; Pacchioni, G. *J. Am. Chem. Soc.* **2006**, *128*, 15666.
- (346) Gopal, N. O.; Lo, H.-H.; Ke, S.-C. *J. Am. Chem. Soc.* **2008**, *130*, 2760.
- (347) In, S.; Orlov, A.; Berg, R.; García, F.; Pedrosa-Jimenez, S.; Tikhov, M. S.; Wright, D. S.; Lambert, R. M. *J. Am. Chem. Soc.* **2007**, *129*, 13790.
- (348) Asahi, R. *Science* **2001**, *293*, 269.
- (349) Barolo, G.; Livraghi, S.; Chiesa, M.; Paganini, M. C.; Giamello, E. *J. Phys. Chem. C* **2012**, *116*, 20887.
- (350) Sun, H.; Fan, W.; Li, Y.; Cheng, X.; Li, P.; Zhao, X. *J. Phys. Chem. C* **2010**, *114*, 3028.
- (351) Sun, X.; Long, R.; Cheng, X.; Zhao, X.; Dai, Y.; Huang, B. *J. Phys. Chem. C* **2008**, *112*, 9861.
- (352) Shah, S. I.; Li, W.; Huang, C. P.; Jung, O.; Ni, C. *Proc. Natl. Acad. Sci. U.S.A.* **2002**, *99*, 6482.
- (353) Imahori, H.; Hayashi, S.; Umeyama, T.; Eu, S.; Oguro, A.; Kang, S.; Matano, Y.; Shishido, T.; Ngamsinlapasathian, S.; Yoshikawa, S. *Langmuir* **2006**, *22*, 11405.
- (354) Long, R.; Dai, Y.; Huang, B. *J. Phys. Chem. C* **2009**, *113*, 650.
- (355) Márquez, A. M.; Plata, J. J.; Ortega, Y.; Fdez Sanz, J. *J. Phys. Chem. C* **2011**, *115*, 16970.
- (356) Gopal, N. O.; Lo, H.-H.; Ke, T.-F.; Lee, C.-H.; Chou, C.-C.; Wu, J.-D.; Sheu, S.-C.; Ke, S.-C. *J. Phys. Chem. C* **2012**, *116*, 16191.
- (357) Hong, X.; Wang, Z.; Cai, W.; Lu, F.; Zhang, J.; Yang, Y.; Ma, N.; Liu, Y. *Chem. Mater.* **2005**, *17*, 1548.
- (358) Körösi, L.; Papp, S.; Bertóti, I.; Dékány, I. *Chem. Mater.* **2007**, *19*, 4811.
- (359) Zhao, D.; Chen, C.; Wang, Y.; Ji, H.; Ma, W.; Zang, L.; Zhao, J. *J. Phys. Chem. C* **2008**, *112*, 5993.
- (360) Su, W.; Zhang, Y.; Li, Z.; Wu, L.; Wang, X.; Li, J.; Fu, X. *Langmuir* **2008**, *24*, 3422.
- (361) Spadavecchia, F.; Cappelletti, G.; Ardizzone, S.; Ceotto, M.; Falcicola, L. *J. Phys. Chem. C* **2011**, *115*, 6381.
- (362) Long, R.; English, N. J. *J. Phys. Chem. C* **2010**, *114*, 13942.
- (363) Yu, Q.; Li, J.; Li, H.; Wang, Q.; Cheng, S.; Li, L. *Chem. Phys. Lett.* **2012**, *539–540*, 74.
- (364) Mayer, M. A.; Speaks, D. T.; Yu, K. M.; Mao, S. S.; Haller, E. E.; Walukiewicz, W. *Appl. Phys. Lett.* **2010**, *97*, 022104.
- (365) Borgarello, E.; Kiwi, J.; Graetzel, M.; Pelizzetti, E.; Visca, M. *J. Am. Chem. Soc.* **1982**, *104*, 2996.
- (366) Li, M.; Zhang, J.; Guo, D.; Zhang, Y. *Chem. Phys. Lett.* **2012**, *539–540*, 175.
- (367) Khan, S. U. M. *Science* **2002**, *297*, 2243.
- (368) Zhang, S. B. *J. Phys.: Condens. Matter* **2002**, *14*, R881.
- (369) Di Valentin, C.; Finazzi, E.; Pacchioni, G.; Selloni, A.; Livraghi, S.; Paganini, M. C.; Giamello, E. *Chem. Phys.* **2007**, *339*, 44.
- (370) Zhu, W.; Qiu, X.; Iancu, V.; Chen, X.-Q.; Pan, H.; Wang, W.; Dimitrijevic, N.; Rajh, T.; Meyer, H.; Paranthaman, M.; Stocks, G.; Weitering, H.; Gu, B.; Eres, G.; Zhang, Z. *Phys. Rev. Lett.* **2009**, *103*, 226401.
- (371) Liu, L.; Chen, S.; Sun, W.; Xin, J. *J. Mol. Struct.* **2011**, *1001*, 23.
- (372) Qi, L.; Li, C.; Chen, Y. *Chem. Phys. Lett.* **2012**, *539–540*, 128.
- (373) Mikulas, T.; Fang, Z.; Gole, J. L.; White, M. G.; Dixon, D. A. *Chem. Phys. Lett.* **2012**, *539–540*, 58.
- (374) Li, P.; Deng, S.; Liu, G.; Hou, K. *Chem. Phys. Lett.* **2012**, *543*, 92.
- (375) He, J.; Parkinson, B. A. *ACS Comb. Sci.* **2011**, *13*, 399.
- (376) Bessho, T.; Zakeeruddin, S. M.; Yeh, C.-Y.; Diau, E. W.-G.; Grätzel, M. *Angew. Chem., Int. Ed.* **2010**, *49*, 6646.
- (377) Varotto, A.; Nam, C.-Y.; Radivojevic, I.; P. C. Tomé, J.; Cavaleiro, J. A. S.; Black, C. T.; Drain, C. M. *J. Am. Chem. Soc.* **2010**, *132*, 2552.
- (378) Darwent, J. R.; Douglas, P.; Harriman, A.; Porter, G.; Richoux, M. C. *Coord. Chem. Rev.* **2005**, *44*, 83.
- (379) Drain, C. M.; Varotto, A.; Radivojevic, I. *Chem. Rev.* **2009**, *109*, 1630.
- (380) Wang, C.-L.; Chang, Y.-C.; Lan, C.-M.; Lo, C.-F.; Wei-Guang Diau, E.; Lin, C.-Y. *Energy Environ. Sci.* **2011**, *4*, 1788.
- (381) Campbell, W. M.; Jolley, K. W.; Wagner, P.; Wagner, K.; Walsh, P. J.; Gordon, K. C.; Schmidt-Mende, L.; Nazeeruddin, M. K.; Wang, Q.; Grätzel, M.; Officer, D. L. *J. Phys. Chem. C* **2007**, *111*, 11760.
- (382) Hagberg, D. P.; Edvinsson, T.; Marinado, T.; Boschloo, G.; Hagfeldt, A.; Sun, L. *Chem. Commun.* **2006**, 2245.
- (383) Xu, W.; Peng, B.; Chen, J.; Liang, M.; Cai, F. *J. Phys. Chem. C* **2008**, *112*, 874.
- (384) Liang, M.; Xu, W.; Cai, F.; Chen, P.; Peng, B.; Chen, J.; Li, Z. *J. Phys. Chem. C* **2007**, *111*, 4465.
- (385) Kitamura, T.; Ikeda, M.; Shigaki, K.; Inoue, T.; Anderson, N. A.; Ai, X.; Lian, T.; Yanagida, S. *Chem. Mater.* **2004**, *16*, 1806.
- (386) Ince, M.; Cardinali, F.; Yum, J.-H.; Martínez-Díaz, M. V.; Nazeeruddin, M. K.; Grätzel, M.; Torres, T. *Chem.-Eur. J.* **2012**, *18*, 6343.
- (387) Kamat, P. V. *J. Phys. Chem. C* **2008**, *112*, 18737.
- (388) Vogel, R.; Pohl, K.; Weller, H. *Chem. Phys. Lett.* **1990**, *174*, 241.
- (389) Kohtani, S.; Kudo, A.; Sakata, T. *Chem. Phys. Lett.* **1993**, *206*, 166.
- (390) Vogel, R.; Hoyer, P.; Weller, H. *J. Phys. Chem.* **1994**, *98*, 3183.
- (391) Salant, A.; Shalom, M.; Tachan, Z.; Buhbut, S.; Zaban, A.; Banin, U. *Nano Lett.* **2012**, *12*, 2095.
- (392) Plass, R.; Pelet, S.; Krueger, J.; Grätzel, M.; Bach, U. *J. Phys. Chem.* **2002**, *106*, 7578.
- (393) Bubenhofer, S. B.; Schumacher, C. M.; Koehler, F. M.; Luechinger, N. A.; Grass, R. N.; Stark, W. J. *J. Phys. Chem. C* **2012**, *116*, 16264.
- (394) Sambur, J. B.; Novet, T.; Parkinson, B. A. *Science* **2010**, *330*, 63.
- (395) Shen, Q.; Katayama, K.; Sawada, T.; Hachiya, S.; Toyoda, T. *Chem. Phys. Lett.* **2012**, *542*, 89.
- (396) Suarez, R.; Nair, P. K.; Kamat, P. V. *Langmuir* **1998**, *14*, 3236.
- (397) Peter, L. M.; Wijayantha, K. G. U.; Riley, D. J.; Waggett, J. P. *J. Phys. Chem. B* **2003**, *107*, 8378.
- (398) Poulouse, A. C.; Veerananarayanan, S.; Varghese, S. H.; Yoshida, Y.; Maekawa, T.; Sakthi Kumar, D. *Chem. Phys. Lett.* **2012**, *539–540*, 197.
- (399) Mukherjee, B.; Smith, Y. R.; Subramanian, V. R. *J. Phys. Chem. C* **2012**, *116*, 15175.
- (400) Liu, D.; Kamat, P. V. *J. Phys. Chem.* **1993**, *97*, 10769.
- (401) Shalom, M.; Buhbut, S.; Tirosh, S.; Zaban, A. *J. Phys. Chem. Lett.* **2012**, *3*, 2436.
- (402) Zaban, A.; Micic, O. I.; Gregg, B. A.; Nozik, A. J. *Langmuir* **1998**, *14*, 3153.
- (403) Sambur, J. B.; Parkinson, B. A. *J. Am. Chem. Soc.* **2010**, *132*, 2130.
- (404) Shen, Q.; Kobayashi, J.; Diguna, L. J.; Toyoda, T. *J. Appl. Phys.* **2008**, *103*, 084304.
- (405) Mora-Seró, I.; Giménez, S.; Fabregat-Santiago, F.; Gómez, R.; Shen, Q.; Toyoda, T.; Bisquert, J. *Acc. Chem. Res.* **2009**, *42*, 1848.

- (406) Kongkanand, A.; Tvrđy, K.; Takechi, K.; Kuno, M.; Kamat, P. V. *J. Am. Chem. Soc.* **2008**, *130*, 4007.
- (407) Kim, J.; Choi, S.; Noh, J.; Yoon, S.; Lee, S.; Noh, T.; Frank, A. J.; Hong, K. *Langmuir* **2009**, *25*, 5348.
- (408) Schaller, R.; Klimov, V. *Phys. Rev. Lett.* **2004**, *92*, 186601.
- (409) Efros, A. L.; Kharchenko, V. A.; Rosen, M. *Solid State Commun.* **1995**, *93*, 281.
- (410) Nozik, A. J. *Inorg. Chem.* **2005**, *44*, 6893.
- (411) Nozik, A. J. *Annu. Rev. Phys. Chem.* **2001**, *52*, 193.
- (412) Shabaev, A.; Efros, A. L.; Nozik, A. J. *Nano Lett.* **2006**, *6*, 2856.
- (413) Schaller, R. D.; Pietryga, J. M.; Goupalov, S. V.; Petruska, M. A.; Ivanov, S. A.; Klimov, V. I. *Phys. Rev. Lett.* **2005**, *95*, 196401.
- (414) Hyeon-Deuk, K.; Prezhdo, O. V. *ACS Nano* **2012**, *6*, 1239.
- (415) Hyeon-Deuk, K.; Prezhdo, O. V. *Nano Lett.* **2011**, *11*, 1845.
- (416) Prezhdo, O. V. *Acc. Chem. Res.* **2009**, *42*, 2005.
- (417) Kilina, S. V.; Craig, C. F.; Kilin, D. S.; Prezhdo, O. V. *J. Phys. Chem. C* **2007**, *111*, 4871.
- (418) Isborn, C. M.; Kilina, S. V.; Li, X.; Prezhdo, O. V. *J. Phys. Chem. C* **2008**, *112*, 18291.
- (419) Kilina, S. V.; Kilin, D. S.; Prezhdo, O. V. *ACS Nano* **2009**, *3*, 93.
- (420) Jacobsson, T. J.; Edvinsson, T. *J. Phys. Chem. C* **2012**, *116*, 15692.
- (421) Layek, A.; Manna, B.; Chowdhury, A. *Chem. Phys. Lett.* **2012**, *539–540*, 133.
- (422) Pandey, A.; Guyot-Sionnest, P. *Science* **2008**, *322*, 929.
- (423) Hod, I.; González-Pedro, V.; Tachan, Z.; Fabregat-Santiago, F.; Mora-Seró, I.; Bisquert, J.; Zaban, A. *J. Phys. Chem. Lett.* **2011**, *2*, 3032.
- (424) Rühle, S.; Greenshtein, M.; Chen, S.-G.; Merson, A.; Pizem, H.; Sukenik, C. S.; Cahen, D.; Zaban, A. *J. Phys. Chem. B* **2005**, *109*, 18907.
- (425) Shalom, M.; Rühle, S.; Hod, I.; Yahav, S.; Zaban, A. *J. Am. Chem. Soc.* **2009**, *131*, 9876.
- (426) Ye, M.; Searson, P. *Phys. Rev. B* **2011**, *84*, 125317.
- (427) Bharadwaj, P.; Novotny, L. *Nano Lett.* **2011**, *11*, 2137.
- (428) Jin, S.; Song, N.; Lian, T. *ACS Nano* **2010**, *4*, 1545.
- (429) Jin, S.; Hsiang, J.-C.; Zhu, H.; Song, N.; Dickson, R. M.; Lian, T. *Chem. Sci.* **2010**, *1*, 519.
- (430) Wei, H. H.-Y.; Evans, C. M.; Swartz, B. D.; Neukirch, A. J.; Young, J.; Prezhdo, O. V.; Krauss, T. D. *Nano Lett.* **2012**, *12*, 4465.
- (431) Morris-Cohen, A. J.; Aruda, K. O.; Rasmussen, A. M.; Canzi, G.; Seideman, T.; Kubiak, C. P.; Weiss, E. A. *Phys. Chem. Chem. Phys.* **2012**, *14*, 13794.
- (432) Tagliazucchi, M.; Tice, D. B.; Sweeney, C. M.; Morris-Cohen, A. J.; Weiss, E. A. *ACS Nano* **2011**, *5*, 9907.
- (433) Morris-Cohen, A. J.; Frederick, M. T.; Cass, L. C.; Weiss, E. A. *J. Am. Chem. Soc.* **2011**, *133*, 10146.
- (434) Knowles, K. E.; Tice, D. B.; McArthur, E. A.; Solomon, G. C.; Weiss, E. A. *J. Am. Chem. Soc.* **2010**, *132*, 1041.
- (435) Barea, E. M.; Shalom, M.; Giménez, S.; Hod, I.; Mora-Seró, I.; Zaban, A.; Bisquert, J. *J. Am. Chem. Soc.* **2010**, *132*, 6834.
- (436) Ogura, R. Y.; Nakane, S.; Morooka, M.; Orihashi, M.; Suzuki, Y.; Noda, K. *Appl. Phys. Lett.* **2009**, *94*, 073308.
- (437) Inakazu, F.; Noma, Y.; Ogomi, Y.; Hayase, S. *Appl. Phys. Lett.* **2008**, *93*, 093304.
- (438) Lan, C.-M.; Wu, H.-P.; Pan, T.-Y.; Chang, C.-W.; Chao, W.-S.; Chen, C.-T.; Wang, C.-L.; Lin, C.-Y.; Diau, E. W.-G. *Energy Environ. Sci.* **2012**, *5*, 6460.
- (439) Yum, J.-H.; Hardin, B.; Moon, S.-J.; Baranoff, E.; Nuesch, F.; McGehee, M.; Grätzel, M.; Nazeeruddin, M. *Angew. Chem., Int. Ed.* **2009**, *48*, 9277.
- (440) Sarkar, S.; Makhali, A.; Lakshman, K.; Bora, T.; Dutta, J.; Kumar Pal, S. *J. Phys. Chem. C* **2012**, *116*, 14248.
- (441) Shen, H.; Lin, H.; Liu, Y.; Li, J.; Oron, D. *J. Phys. Chem. C* **2012**, *116*, 15185.
- (442) Wang, J.; Zhang, T.; Wang, D.; Pan, R.; Wang, Q.; Xia, H. *Chem. Phys. Lett.* **2012**, *541*, 105.
- (443) Clifford, J. N.; Martínez-Ferrero, E.; Viterisi, A.; Palomares, E. *Chem. Soc. Rev.* **2011**, *40*, 1635.
- (444) Radivojevic, I.; Bazzan, G.; Burton-Pye, B. P.; Ithiuphalap, K.; Saleh, R.; Durstock, M. F.; Francesconi, L. C.; Drain, C. M. *J. Phys. Chem. C* **2012**, *116*, 15867.
- (445) Lazarides, T.; McCormick, T. M.; Wilson, K. C.; Lee, S.; McCamant, D. W.; Eisenberg, R. *J. Am. Chem. Soc.* **2011**, *133*, 350.
- (446) Guo, J.; She, C.; Lian, T. *J. Phys. Chem. C* **2008**, *112*, 4761.
- (447) Ai, X.; Anderson, N.; Guo, J.; Kowalik, J.; Tolbert, L. M.; Lian, T. *J. Phys. Chem. B* **2006**, *110*, 25496.
- (448) Friend, R. H.; Phillips, M.; Rao, A.; Wilson, M. W. B.; Li, Z.; McNeill, C. R. *Faraday Discuss.* **2012**, *155*, 339.
- (449) Segura, J. L.; Martin, R. W.; Guldi, D. M. *Chem. Soc. Rev.* **2005**, *34*, 31.
- (450) Scharber, M. C.; Mühlbacher, D.; Koppe, M.; Denk, P.; Waldauf, C.; Heeger, A. J.; Brabec, C. J. *Adv. Mater.* **2006**, *18*, 789.
- (451) Kamat, P. V. *J. Am. Chem. Soc.* **1991**, *113*, 9705.
- (452) Kaniyankandy, S.; Rawalekar, S.; Ghosh, H. N. *J. Phys. Chem. C* **2012**, *116*, 16271.
- (453) Wu, J.; Pisula, W.; Müllen, K. *Chem. Rev.* **2007**, *107*, 718.
- (454) Wang, X.; Zhi, L.; Müllen, K. *Nano Lett.* **2008**, *8*, 323.
- (455) Chen, J.; Li, B.; Zheng, J.; Zhao, J.; Zhu, Z. *J. Phys. Chem. C* **2012**, *116*, 14848.
- (456) Jia, Y.; Wei, J.; Wang, K.; Cao, A.; Shu, Q.; Gui, X.; Zhu, Y.; Zhuang, D.; Zhang, G.; Ma, B.; Wang, L.; Liu, W.; Wang, Z.; Luo, J.; Wu, D. *Adv. Mater.* **2008**, *20*, 4594.
- (457) Chen, C.; Cai, W.; Long, M.; Zhou, B.; Wu, Y.; Wu, D.; Feng, Y. *ACS Nano* **2010**, *4*, 6425.
- (458) Park, S.-Y.; Seo, H. O.; Kim, K.-D.; Shim, W. H.; Heo, J.; Cho, S.; Kim, Y. D.; Lee, K. H.; Lim, D. C. *J. Phys. Chem. C* **2012**, *116*, 15348.
- (459) Park, H.; Choi, W. *Langmuir* **2006**, *22*, 2906.
- (460) Dutta, M.; Sarkar, S.; Ghosh, T.; Basak, D. *J. Phys. Chem. C* **2012**, *116*, 20127.
- (461) Kavan, L.; Yum, J.-H.; Grätzel, M. *Nano Lett.* **2011**, *11*, 5501.
- (462) Yan, X.; Cui, X.; Li, B.; Li, L. *Nano Lett.* **2010**, *10*, 1869.
- (463) Kamat, P. V. *J. Phys. Chem. Lett.* **2012**, *3*, 663.
- (464) Kamat, P. V. *J. Phys. Chem. C* **2012**, *116*, 11849.
- (465) Ng, Y. H.; Lightcap, I. V.; Goodwin, K.; Matsumura, M.; Kamat, P. V. *J. Phys. Chem. Lett.* **2010**, *1*, 2222.
- (466) Wang, W.-S.; Wang, D.-H.; Qu, W.-G.; Lu, L.-Q.; Xu, A.-W. *J. Phys. Chem. C* **2012**, *116*, 19893.
- (467) Lightcap, I. V.; Kosel, T. H.; Kamat, P. V. *Nano Lett.* **2010**, *10*, 577.
- (468) Lightcap, I. V.; Murphy, S.; Schumer, T.; Kamat, P. V. *J. Phys. Chem. Lett.* **2012**, *3*, 1453.
- (469) Mattioli, G.; Melis, C.; Mallocci, G.; Filippone, F.; Alippi, P.; Giannozzi, P.; Mattoni, A.; Amore Bonapasta, A. *J. Phys. Chem. C* **2012**, *116*, 15439.
- (470) Rienzo, A.; Mayor, L. C.; Magnano, G.; Satterley, C. J.; Ataman, E.; Schnadt, J.; Schulte, K.; O'Shea, J. N. *J. Chem. Phys.* **2010**, *132*, 084703.
- (471) Yu, S.; Ahmadi, S.; Sun, C.; Adibi, P. T. Z.; Chow, W.; Pietzsch, A.; Göthelid, M. *J. Chem. Phys.* **2012**, *136*, 154703.
- (472) Cherian, S.; Wamser, C. C. *J. Phys. Chem. B* **2000**, *104*, 3624.
- (473) Yu, S.; Ahmadi, S.; Zuleta, M.; Tian, H.; Schulte, K.; Pietzsch, A.; Hennies, F.; Weissenrieder, J.; Yang, X.; Göthelid, M. *J. Chem. Phys.* **2010**, *133*, 224704.
- (474) De Tacconi, N. R.; Chanmanee, W.; Rajeshwar, K.; Rochford, J.; Galoppini, E. *J. Phys. Chem. C* **2009**, *113*, 2996.
- (475) Werner, F.; Gnichwitz, J.-F.; Marczak, R.; Palomares, E.; Peukert, W.; Hirsch, A.; Guldi, D. M. *J. Phys. Chem. B* **2010**, *114*, 14671.
- (476) Rochford, J.; Chu, D.; Hagfeldt, A.; Galoppini, E. *J. Am. Chem. Soc.* **2007**, *129*, 4655.
- (477) Rochford, J.; Galoppini, E. *Langmuir* **2008**, *24*, 5366.
- (478) Wang, C.-L.; Lan, C.-M.; Hong, S.-H.; Wang, Y.-F.; Pan, T.-Y.; Chang, C.-W.; Kuo, H.-H.; Kuo, M.-Y.; Diau, E. W.-G.; Lin, C.-Y. *Energy Environ. Sci.* **2012**, *5*, 6933.
- (479) Miller, S. A.; West, B. A.; Curtis, A. C.; Papanikolas, J. M.; Moran, A. M. *J. Chem. Phys.* **2011**, *135*, 081101.

- (480) Wiberg, J.; Marinado, T.; Hagberg, D. P.; Sun, L.; Hagfeldt, A.; Albinsson, B. *J. Phys. Chem. C* **2009**, *113*, 3881.
- (481) Fischer, S. A.; Duncan, W. R.; Prezhdo, O. V. *J. Am. Chem. Soc.* **2009**, *131*, 15483.
- (482) Rehm, J. M.; McLendon, G. L.; Nagasawa, Y.; Yoshihara, K.; Moser, J.; Grätzel, M. *J. Phys. Chem.* **1996**, *100*, 9577.
- (483) Wachtveitl, J.; Huber, R.; Spörlein, S.; Moser, J. E.; Grätzel, M. *Int. J. Photoenergy* **1999**, *1*, 153.
- (484) Stier, W.; Duncan, W. R.; Prezhdo, O. V. *Adv. Mater.* **2004**, *16*, 240.
- (485) Huber, R.; Moser, J.-E.; Grätzel, M.; Wachtveitl, J. *J. Phys. Chem. B* **2002**, *106*, 6494.
- (486) Pelet, S.; Grätzel, M.; Moser, J.-E. *J. Phys. Chem. B* **2003**, *107*, 3215.
- (487) Asbury, J. B.; Hao, E.; Wang, Y.; Ghosh, H. N.; Lian, T. *J. Phys. Chem. B* **2001**, *105*, 4545.
- (488) Asbury, J. B.; Ellingson, R. J.; Ghosh, H. N.; Ferrere, S.; Nozik, A. J.; Lian, T. *J. Phys. Chem. B* **1999**, *103*, 3110.
- (489) Labat, F.; Ciofini, I.; Adamo, C. *J. Mater. Chem.* **2012**, *22*, 12205.
- (490) Wenger, B.; Grätzel, M.; Moser, J.-E. *J. Am. Chem. Soc.* **2005**, *127*, 12150.
- (491) Tachibana, Y.; Moser, J. E.; Grätzel, M.; Klug, D. R.; Durrant, J. R. *J. Phys. Chem.* **1996**, *100*, 20056.
- (492) Benkö, G.; Kallioinen, J.; Korppi-Tommola, J. E. I.; Yartsev, A. P.; Sundström, V. *J. Am. Chem. Soc.* **2002**, *124*, 489.
- (493) Ai, X.; Anderson, N. A.; Guo, J.; Lian, T. *J. Phys. Chem. B* **2005**, *109*, 7088.
- (494) Guo, J.; Stockwell, D.; Ai, X.; She, C.; Anderson, N. A.; Lian, T. *J. Phys. Chem. B* **2006**, *110*, 5238.
- (495) Asbury, J. B.; Wang, Y.; Lian, T. *J. Phys. Chem. B* **1999**, *103*, 6643.
- (496) Ai, X.; Guo, J.; Anderson, N. A.; Lian, T. *J. Phys. Chem. B* **2004**, *108*, 12795.
- (497) Huang, J.; Stockwell, D.; Boulesbaa, A.; Guo, J.; Lian, T. *J. Phys. Chem. C* **2008**, *112*, 5203.
- (498) Schnadt, J.; Bruhwiler, P. A.; Patthey, L.; O'Shea, J. N.; Sodergren, S.; Odelius, M.; Ahuja, R.; Karis, O.; Bassler, M.; Persson, P.; Siegbahn, H.; Lunell, S.; Martensson, N. *Nature* **2002**, *418*, 620.
- (499) Tisdale, W. A.; Williams, K. J.; Timp, B. A.; Norris, D. J.; Aydil, E. S.; Zhu, X.-Y. *Science* **2010**, *328*, 1543.
- (500) Martsinovich, N.; Troisi, A. *J. Phys. Chem. C* **2011**, *115*, 11781.
- (501) Rego, L. G. C.; Batista, V. S. *J. Am. Chem. Soc.* **2003**, *125*, 7989.
- (502) Wenger, B.; Bauer, C.; Nazeeruddin, M. K.; Comte, P.; Zakeeruddin, S. M.; Grätzel, M.; Moser, J.-E. *Proc. SPIE* **2006**, *6325*, 63250V 1.
- (503) Bauer, C.; Teuscher, J.; Pelet, S.; Wenger, B.; Bonhote, P.; Nazeeruddin, M. K.; Zakeeruddin, S. M.; Comte, P.; Grätzel, M.; Moser, J. E. *Curr. Sci.* **2010**, *99*, 343.
- (504) Anderson, N. A.; Ai, X.; Chen, D.; Mohler, D. L.; Lian, T. *J. Phys. Chem. B* **2003**, *107*, 14231.
- (505) Tisdale, W. A.; Zhu, X.-Y. *Proc. Natl. Acad. Sci. U.S.A.* **2010**, *108*, 965.
- (506) Lyon, L. A.; Hupp, J. T. *J. Phys. Chem. B* **1999**, *103*, 4623.
- (507) Enright, B.; Redmond, G.; Fitzmaurice, D. *J. Phys. Chem.* **1994**, *98*, 6195.
- (508) She, C.; Anderson, N. A.; Guo, J.; Liu, F.; Goh, W.-H.; Chen, D.-T.; Mohler, D. L.; Tian, Z.-Q.; Hupp, J. T.; Lian, T. *J. Phys. Chem. B* **2005**, *109*, 19345.
- (509) Zhang, Z.; Zakeeruddin, S. M.; O'Regan, B. C.; Humphry-Baker, R.; Grätzel, M. *J. Phys. Chem. B* **2005**, *109*, 21818.
- (510) Kopidakis, N.; Neale, N. R.; Frank, A. J. *J. Phys. Chem. B* **2006**, *110*, 12485.
- (511) Hara, K.; Dan-oh, Y.; Kasada, C.; Ohga, Y.; Shinpo, A.; Suga, S.; Sayama, K.; Arakawa, H. *Langmuir* **2004**, *20*, 4205.
- (512) Fukui, A.; Komiya, R.; Yamanaka, R.; Islam, A.; Han, L. *Sol. Energy Mater. Sol. Cells* **2006**, *90*, 649.
- (513) Lee, K.-M.; Suryanarayanan, V.; Ho, K.-C. *J. Power Sources* **2009**, *188*, 635.
- (514) Le Bahers, T.; Labat, F.; Pauporté, T.; Ciofini, I. *Phys. Chem. Chem. Phys.* **2010**, *12*, 14710.
- (515) Hara, K.; Horiguchi, T.; Kinoshita, T.; Sayama, K.; Arakawa, H. *Sol. Energy Mater. Sol. Cells* **2001**, *70*, 151.
- (516) Gutmann, V. *Coord. Chem. Rev.* **1976**, *18*, 225.
- (517) Neale, N. R.; Kopidakis, N.; Van de Lagemaat, J.; Grätzel, M.; Frank, A. J. *J. Phys. Chem. B* **2005**, *109*, 23183.
- (518) Martsinovich, N.; Jones, D. R.; Troisi, A. *J. Phys. Chem. C* **2010**, *114*, 22659.
- (519) Kallioinen, J.; Benkö, G.; Sundström, V.; Korppi-Tommola, J. E. I.; Yartsev, A. P. *J. Phys. Chem. B* **2002**, *106*, 4396.
- (520) Fessenden, R. W.; Kamat, P. V. *J. Phys. Chem.* **1995**, *99*, 12902.
- (521) Gil, M.; Organero, J. A.; Navarro, M. T.; Corma, A.; Douhal, A. *J. Phys. Chem. C* **2012**, *116*, 15385.
- (522) Tachibana, Y.; Nazeeruddin, M. K.; Grätzel, M.; Klug, D. R.; Durrant, J. R. *Chem. Phys.* **2002**, *285*, 127.
- (523) McNeil, I. J.; Ashford, D. L.; Luo, H.; Fecko, C. J. *J. Phys. Chem. C* **2012**, *116*, 15888.
- (524) Ambrosio, F.; Martsinovich, N.; Troisi, A. *J. Phys. Chem. C* **2012**, *116*, 2622.
- (525) Ambrosio, F.; Martsinovich, N.; Troisi, A. *J. Phys. Chem. Lett.* **2012**, *3*, 1531.
- (526) Jakubikova, E.; Snoberger, R. C., III; Batista, V. S.; Martin, R. L.; Batista, E. R. *J. Phys. Chem. A* **2009**, *113*, 12532.
- (527) Peng, B.; Yang, S.; Li, L.; Cheng, F.; Chen, J. *J. Chem. Phys.* **2010**, *132*, 034305.
- (528) Li, J.; Wang, H.; Persson, P.; Thoss, M. *J. Chem. Phys.* **2012**, *137*, 22A529.
- (529) Ernstorfer, R.; Gundlach, L.; Felber, S.; Storck, W.; Eichberger, R.; Willig, F. *J. Phys. Chem. B* **2006**, *110*, 25383.
- (530) Duncan, W. R.; Craig, C. F.; Prezhdo, O. V. *J. Am. Chem. Soc.* **2007**, *129*, 8528.
- (531) Abuabara, S. G.; Rego, L. G. C.; Batista, V. S. *J. Am. Chem. Soc.* **2005**, *127*, 18234.
- (532) Ramakrishna, S.; Willig, F.; May, V. *Phys. Rev. B* **2000**, *62*, R16330.
- (533) Ramakrishna, S.; Willig, F. *J. Phys. Chem. B* **2000**, *104*, 68.
- (534) Ramakrishna, S.; Willig, F.; May, V. *J. Chem. Phys.* **2001**, *115*, 2743.
- (535) Ramakrishna, S.; Seideman, T.; Willig, F.; May, V. *J. Chem. Sci.* **2009**, *121*, 589.
- (536) Prezhdo, O. V.; Brooksby, C. *Phys. Rev. Lett.* **2001**, *86*, 3215.
- (537) Abuabara, S. G.; Cady, C. W.; Baxter, J. B.; Schmuttenmaer, C. A.; Crabtree, R. H.; Brudvig, G. W.; Batista, V. S. *J. Phys. Chem. C* **2007**, *111*, 11982.
- (538) Oviedo, M. B.; Zarate, X.; Negre, C. F. A.; Schott, E.; Arratia-Pérez, R.; Sánchez, C. G. *J. Phys. Chem. Lett.* **2012**, *3*, 2548.
- (539) Sánchez-de-Armas, R.; Oviedo, J.; San Miguel, M. A.; Sanz, J. F. *J. Phys. Chem. C* **2011**, *115*, 11293.
- (540) Rocca, D.; Gebauer, R.; De Angelis, F.; Nazeeruddin, M. K.; Baroni, S. *Chem. Phys. Lett.* **2009**, *475*, 49.
- (541) Sauvage, F.; Chhor, S.; Marchioro, A.; Moser, J.-E.; Graetzel, M. *J. Am. Chem. Soc.* **2011**, *133*, 13103.
- (542) Wang, M.; Chamberland, N.; Breau, L.; Moser, J.-E.; Humphry-Baker, R.; Marsan, B.; Zakeeruddin, S. M.; Grätzel, M. *Nat. Chem.* **2010**, *2*, 385.
- (543) Wang, H.; Nicholson, P. G.; Peter, L.; Zakeeruddin, S. M.; Grätzel, M. *J. Phys. Chem. C* **2010**, *114*, 14300.
- (544) Ondersma, J. W.; Hamann, T. W. *J. Phys. Chem. C* **2010**, *114*, 638.
- (545) Katzin, L. I.; Gebert, E. *J. Am. Chem. Soc.* **1955**, *77*, 5814.
- (546) Da Silva, R.; Rego, L. G. C.; Freire, J. A.; Rodriguez, J.; Laria, D.; Batista, V. S. *J. Phys. Chem. C* **2010**, *114*, 19433.
- (547) Boschloo, G.; Häggman, L.; Hagfeldt, A. *J. Phys. Chem. B* **2006**, *110*, 13144.
- (548) Koops, S. E.; O'Regan, B. C.; Barnes, P. R. F.; Durrant, J. R. *J. Am. Chem. Soc.* **2009**, *131*, 4808.
- (549) Zhang, C.; Huang, Y.; Huo, Z.; Chen, S.; Dai, S. *J. Phys. Chem. C* **2009**, *113*, 21779.



- (550) O'Regan, B. C.; López-Duarte, I.; Martínez-Díaz, M. V.; Forneli, A.; Albero, J.; Morandeira, A.; Palomares, E.; Torres, T.; Durrant, J. R. *J. Am. Chem. Soc.* **2008**, *130*, 2906.
- (551) O'Regan, B. C.; Walley, K.; Juozapavicius, M.; Anderson, A.; Matar, F.; Ghaddar, T.; Zakeeruddin, S. M.; Klein, C.; Durrant, J. R. *J. Am. Chem. Soc.* **2009**, *131*, 3541.
- (552) Hauch, A.; Georg, A. *Electrochim. Acta* **2001**, *46*, 3457.
- (553) Liu, Y.; Hagfeldt, A.; Xiao, X. R.; Lindquist, S. E. *Sol. Energy Mater. Sol. Cells* **1998**, *55*, 267.
- (554) Green, A. N. M.; Chandler, R. E.; Haque, S. A.; Nelson, J.; Durrant, J. R. *J. Phys. Chem. B* **2005**, *109*, 142.
- (555) Barnes, P. R. F.; Anderson, A. Y.; Juozapavicius, M.; Liu, L.; Li, X.; Palomares, E.; Forneli, A.; O'Regan, B. C. *Phys. Chem. Chem. Phys.* **2011**, *13*, 3547.
- (556) Nakade, S.; Kanzaki, T.; Kubo, W.; Kitamura, T.; Wada, Y.; Yanagida, S. *J. Phys. Chem. B* **2005**, *109*, 3480.
- (557) Bauer, C.; Boschloo, G.; Mukhtar, E.; Hagfeldt, A. *J. Phys. Chem. B* **2002**, *106*, 12693.
- (558) Montanari, L.; Nelson, J.; Durrant, J. R. *J. Phys. Chem. B* **2002**, *106*, 12203.
- (559) Fujishima, A.; Honda, K. *Bull. Chem. Soc. Jpn.* **1971**, *44*, 1148.
- (560) Inoue, T.; Fujishima, A.; Konishi, S.; Honda, K. *Nature* **1979**, *277*, 637.
- (561) Fujishima, A.; Rao, T. N.; Tryk, D. A. *J. Photochem. Photobiol., C* **2000**, *1*, 1.
- (562) Smestad, G. P.; Steinfeld, A. *Ind. Eng. Chem. Res.* **2012**, *51*, 11828.
- (563) Thompson, T. L.; Yates, J. T. *Chem. Rev.* **2006**, *106*, 4428.
- (564) Ni, M.; Leung, M. K. H.; Leung, D. Y. C.; Sumathy, K. *Renewable Sustainable Energy Rev.* **2007**, *11*, 401.
- (565) Ge, S.; Jia, H.; Zhao, H.; Zheng, Z.; Zhang, L. *J. Mater. Chem.* **2010**, *20*, 3052.
- (566) Vinodgopal, K.; Hotchandani, S.; Kamat, P. V. *J. Phys. Chem.* **1993**, *97*, 9040.
- (567) Syoufian, A.; Nakashima, K. *J. Colloid Interface Sci.* **2007**, *313*, 213.
- (568) Syoufian, A.; Nakashima, K. *J. Colloid Interface Sci.* **2008**, *317*, 507.
- (569) Koca, A.; Sahin, M. *Int. J. Hydrogen Energy* **2002**, *27*, 363.
- (570) Bamwenda, G. R.; Arakawa, H. *Sol. Energy Mater. Sol. Cells* **2001**, *70*, 14.
- (571) Kasahara, A.; Nukumizu, K.; Hitoki, G.; Takata, T.; Kondo, J. N.; Hara, M.; Kobayashi, H.; Domen, K. *J. Phys. Chem. A* **2002**, *106*, 6750.
- (572) Hirai, T.; Maeda, K.; Yoshida, M.; Kubota, J.; Ikeda, S.; Matsumura, M.; Domen, K. *J. Phys. Chem. C* **2007**, *111*, 18853.
- (573) Jensen, L. L.; Muckerman, J. T.; Newton, M. D. *J. Phys. Chem. C* **2008**, *112*, 3439.
- (574) Yoshida, M.; Hirai, T.; Maeda, K.; Saito, N.; Kubota, J.; Kobayashi, H.; Inoue, Y.; Domen, K. *J. Phys. Chem. C* **2010**, *114*, 15510.
- (575) Yoshino, M.; Kakihana, M.; Cho, W. S.; Kato, H.; Kudo, A. *Chem. Mater.* **2002**, *14*, 3369.
- (576) Sato, J.; Kobayashi, H.; Inoue, Y. *J. Phys. Chem. B* **2003**, *107*, 7970.
- (577) Sato, J.; Kobayashi, H.; Saito, N.; Nishiyama, H.; Inoue, Y. *J. Photochem. Photobiol., A* **2003**, *158*, 139.
- (578) Inoue, Y.; Kubokawa, T.; Sato, K. *J. Phys. Chem.* **1991**, *95*, 4059.
- (579) Ogura, S.; Kohno, M.; Sato, K.; Inoue, Y. *Appl. Surf. Sci.* **1997**, *121/122*, 521.
- (580) Sato, J.; Kobayashi, H.; Ikarashi, K.; Saito, N.; Nishiyama, H.; Inoue, Y. *J. Phys. Chem. B* **2004**, *108*, 4369.
- (581) Takahashi, H.; Kakihana, M.; Yamashita, Y.; Yoshida, K.; Ikeda, S.; Hara, M.; Domen, K. *J. Alloys Compd.* **1999**, *285*, 77.
- (582) Takata, T.; Furumi, Y.; Shinohara, K.; Tanaka, A.; Hara, M.; Kondo, J. N.; Domen, K. *Chem. Mater.* **1997**, *9*, 1063.
- (583) Domen, K.; Kondo, J. N.; Hara, M.; Takata, T. *Bull. Chem. Soc. Jpn.* **2000**, *73*, 1307.
- (584) Machida, M.; Mitsuyama, T.; Ikeue, K.; Matsushima, S.; Arai, M. *J. Phys. Chem. B* **2005**, *109*, 7801.
- (585) Ohno, T.; Bai, L.; Hisatomi, T.; Maeda, K.; Domen, K. *J. Am. Chem. Soc.* **2012**, *134*, 8254.
- (586) Nozik, A. J. *Annu. Rev. Phys. Chem.* **1978**, *29*, 189.
- (587) Li, Y.-F.; Liu, Z.-P. *J. Am. Chem. Soc.* **2011**, *133*, 15743.
- (588) Sayama, K.; Mukasa, K.; Abe, R.; Abe, Y.; Arakawa, H. *J. Photochem. Photobiol., A* **2002**, *148*, 71.
- (589) Abe, R.; Sayama, K.; Domen, K.; Arakawa, H. *Chem. Phys. Lett.* **2001**, *344*, 339.
- (590) Yun, H. J.; Lee, H.; Kim, N. D.; Lee, D. M.; Yu, S.; Yi, J. *ACS Nano* **2011**, *5*, 4084.
- (591) Iwase, A.; Ng, Y. H.; Ishiguro, Y.; Kudo, A.; Amal, R. *J. Am. Chem. Soc.* **2011**, *133*, 11054.
- (592) Fu, N.; Jin, Z.; Wu, Y.; Lu, G.; Li, D. *J. Phys. Chem. C* **2011**, *115*, 8586.
- (593) Hisatomi, T.; Miyazaki, K.; Takanabe, K.; Maeda, K.; Kubota, J.; Sakata, Y.; Domen, K. *ChemPhysChem* **2010**, *486*, 144.
- (594) Hisatomi, T.; Maeda, K.; Takanabe, K.; Kubota, J.; Domen, K. *J. Phys. Chem. C* **2009**, *113*, 21458.
- (595) Hisatomi, T.; Minegishi, T.; Domen, K. *Bull. Chem. Soc. Jpn.* **2012**, *85*, 647.
- (596) Enright, B.; Fitzmaurice, D. *J. Chem. Phys.* **1996**, *100*, 1027.
- (597) Kroeze, J. E.; Savenije, T. J.; Warman, J. M. *J. Am. Chem. Soc.* **2004**, *126*, 7608.
- (598) Tamaki, Y.; Hara, K.; Katoh, R.; Tachiya, M.; Furube, A. *J. Phys. Chem. C* **2009**, *113*, 11741.
- (599) Takata, T.; Domen, K. *J. Phys. Chem. C* **2009**, *113*, 19386.
- (600) He, H.; Liu, C.; Dubois, K. D.; Jin, T.; Louis, M. E.; Li, G. *Ind. Eng. Chem. Res.* **2012**, *51*, 11841.
- (601) White, J. C.; Dutta, P. K. *J. Phys. Chem. C* **2011**, *115*, 2938.
- (602) Tsuji, I.; Kato, H.; Kobayashi, H.; Kudo, A. *J. Am. Chem. Soc.* **2004**, *126*, 13406.
- (603) Subramanian, V.; Wolf, E.; Kamat, P. V. *J. Phys. Chem. B* **2001**, *105*, 11439.
- (604) Dawson, A.; Kamat, P. V. *J. Phys. Chem. B* **2001**, *105*, 960.
- (605) Maeda, K.; Teramura, K.; Lu, D.; Takata, T.; Saito, N.; Inoue, Y.; Domen, K. *Nature* **2006**, *440*, 295.
- (606) Ishikawa, A.; Takata, T.; Kondo, J. N.; Hara, M.; Kobayashi, H.; Domen, K. *J. Am. Chem. Soc.* **2002**, *124*, 13547.
- (607) Anpo, M.; Shima, T.; Kodama, S.; Kubokawa, Y. *J. Phys. Chem.* **1987**, *91*, 4305.
- (608) Matsuoka, M.; Anpo, M. *J. Photochem. Photobiol., C* **2003**, *3*, 225.
- (609) Su, Z.; Zhou, W. *J. Mater. Chem.* **2011**, *21*, 8955.
- (610) Shankar, K.; Basham, J. I.; Allam, N. K.; Varghese, O. K.; Mor, G. K.; Feng, X.; Paulose, M.; Seabold, J. A.; Choi, K.-S.; Grimes, C. A. *J. Phys. Chem. C* **2009**, *113*, 6327.
- (611) Mor, G. K.; Varghese, O. K.; Paulose, M.; Shankar, K.; Grimes, C. A. *Sol. Energy Mater. Sol. Cells* **2006**, *90*, 2011.
- (612) Naito, K.; Tachikawa, T.; Fujitsuka, M.; Majima, T. *J. Am. Chem. Soc.* **2009**, *131*, 934.
- (613) Zhou, L.; Smyth-Boyle, D.; O'Brien, P. J. *J. Am. Chem. Soc.* **2008**, *130*, 1309.
- (614) Zhang, D.; Li, G.; Wang, F.; Yu, J. C. *CrystEngComm* **2010**, *12*, 1759.
- (615) Lakshminarasimhan, N.; Kim, W.; Choi, W. *J. Phys. Chem. C* **2008**, *112*, 20451.
- (616) Gonzalez-Vazquez, J. P.; Morales-Flórez, V.; Anta, J. A. *J. Phys. Chem. Lett.* **2012**, *3*, 386.
- (617) Yang, H. G.; Sun, C. H.; Qiao, S. Z.; Zou, J.; Liu, G.; Smith, S. C.; Cheng, H. M.; Lu, G. Q. *Nature* **2008**, *453*, 638.
- (618) Bian, Z.; Tachikawa, T.; Majima, T. *J. Phys. Chem. Lett.* **2012**, *3*, 1422.
- (619) Nguyen, T.-V.; Wu, J. C. S.; Chiou, C.-H. *Catal. Commun.* **2008**, *9*, 2073.
- (620) Ozcan, O.; Yukruk, F.; Akkaya, E. U.; Uner, D. *Top. Catal.* **2007**, *44*, 523.

- (621) Ozcan, O.; Yukruk, F.; Akkaya, E.; Uner, D. *Appl. Catal., B* **2007**, *71*, 291.
- (622) Wanbayor, R.; Deák, P.; Frauenheim, T.; Ruangpornvisuti, V. *J. Chem. Phys.* **2011**, *134*, 104701.
- (623) Wei, G.-F.; Fang, Y.-H.; Liu, Z.-P. *J. Phys. Chem. C* **2012**, *116*, 12696.
- (624) Li, S.; Demuth, J.; Mirabal, A.; Wöste, L.; Siebert, T. *Phys. Chem. Chem. Phys.* **2012**, *14*, 148.
- (625) Suzuki, S.; Tsuneda, T.; Hirao, K. *J. Chem. Phys.* **2012**, *136*, 024706.
- (626) Hill, J. C.; Choi, K.-S. *J. Phys. Chem. C* **2012**, *116*, 7612.
- (627) Osterloh, F. E.; Parkinson, B. A. *MRS Bull.* **2011**, *36*, 17.
- (628) Shin, H.-J.; Jung, J.; Motobayashi, K.; Yanagisawa, S.; Morikawa, Y.; Kim, Y.; Kawai, M. *Nat. Mater.* **2010**, *9*, 442.
- (629) Valdés, A.; Qu, Z.-W.; Kroes, G.-J.; Rossmeisl, J.; Nørskov, J. K. *J. Phys. Chem. C* **2008**, *112*, 9872.
- (630) Valdés, A.; Kroes, G.-J. *J. Chem. Phys.* **2009**, *130*, 114701.
- (631) Valdés, A.; Kroes, G.-J. *J. Phys. Chem. C* **2010**, *114*, 1701.
- (632) Rossmeisl, J.; Dimitrievski, K.; Siegbahn, P.; Nørskov, J. K. *J. Phys. Chem. C* **2007**, *111*, 18821.
- (633) Cabrera-Sanfelix, P.; Fernández-Serra, M.; Arnau, A.; Sánchez-Portal, D. *Phys. Rev. B* **2010**, *82*, 125432.
- (634) Huang, Z.; Geletii, Y. V.; Musaev, D. G.; Hill, C. L.; Lian, T. *Ind. Eng. Chem. Res.* **2012**, *51*, 11850.
- (635) Chen, P.-T.; Sun, C.-L.; Hayashi, M. *J. Phys. Chem. C* **2010**, *114*, 18228.
- (636) Shen, X.; Allen, P. B.; Hybertsen, M. S.; Muckerman, J. T. *J. Phys. Chem. C* **2009**, *113*, 3365.
- (637) Li, Y.-F.; Liu, Z.-P.; Liu, L.; Gao, W. *J. Am. Chem. Soc.* **2010**, *132*, 13008.
- (638) Nakamura, R.; Nakato, Y. *J. Am. Chem. Soc.* **2004**, *126*, 1290.
- (639) Nakamura, R.; Ohashi, N.; Imanishi, A.; Osawa, T.; Matsumoto, Y.; Koinuma, H.; Nakato, Y. *J. Phys. Chem. B* **2005**, *109*, 1648.
- (640) Rossmeisl, J.; Qu, Z.-W.; Zhu, H.; Kroes, G.-J.; Nørskov, J. K. *J. Electroanal. Chem.* **2007**, *607*, 83.
- (641) Nozik, A. J.; Memming, R. *J. Phys. Chem.* **1996**, *100*, 13061.
- (642) Shen, X.; Small, Y. A.; Wang, J.; Allen, P. B.; Fernandez-Serra, M. V.; Hybertsen, M. S.; Muckerman, J. T. *J. Phys. Chem. C* **2010**, *114*, 13695.
- (643) Tripković, V.; Skúlason, E.; Siahrostami, S.; Nørskov, J. K.; Rossmeisl, J. *Electrochim. Acta* **2010**, *55*, 7975.
- (644) Fang, Y.-H.; Liu, Z.-P. *J. Am. Chem. Soc.* **2010**, *132*, 18214.
- (645) Chen, D.; Fang, Y.-H.; Liu, Z.-P. *Phys. Chem. Chem. Phys.* **2012**, *14*, 16612.
- (646) Nozik, A. J. *Nature* **1975**, *257*, 383.
- (647) Trasatti, S. *Electrochim. Acta* **1984**, *29*, 1503.
- (648) Hinnemann, B.; Moses, P. G.; Bonde, J.; Jørgensen, K. P.; Nielsen, J. H.; Horch, S.; Chorkendorff, L.; Nørskov, J. K. *J. Am. Chem. Soc.* **2005**, *127*, 5308.
- (649) Nørskov, J. K.; Bligaard, T.; Logadottir, A.; Kitchin, J. R.; Chen, J. G.; Pandelov, S.; Stimming, U. *J. Electrochem. Soc.* **2005**, *152*, J23.
- (650) Parsons, R. *Trans. Faraday Soc.* **1958**, *54*, 1053.
- (651) Hammer, B.; Nørskov, J. K. *Surf. Sci.* **1995**, *343*, 211.
- (652) Greeley, J.; Nørskov, J. K.; Kibler, L. A.; El-Aziz, A. M.; Kolb, D. M. *ChemPhysChem* **2006**, *7*, 1032.
- (653) Guerrini, E.; Trasatti, S. *Russ. J. Electrochem.* **2006**, *42*, 1017.
- (654) Castelli, P.; Trasatti, S.; Pollak, F. H.; O'Grady, W. E. *J. Electroanal. Chem.* **1986**, *210*, 189.
- (655) Shockley, W.; Queisser, H. J. *J. Appl. Phys.* **1961**, *32*, 510.